Cancellous bone and theropod dinosaur locomotion. Part I – An examination of cancellous bone architecture in the hindlimb bones of theropods (#22641)

First submission

Editor guidance

Please submit by **25 Jan 2018** for the benefit of the authors (and your $200 publishing discount).

Structure and Criteria
Please read the 'Structure and Criteria' page for general guidance.

Author notes
Have you read the author notes on the guidance page?

Raw data check
Review the raw data. Download from the location described by the author.

Image check
Check that figures and images have not been inappropriately manipulated.

Privacy reminder: If uploading an annotated PDF, remove identifiable information to remain anonymous.

Files
Download and review all files from the materials page.

44 Figure file(s)
2 Table file(s)

Structure and Criteria

2

Structure your review

The review form is divided into 5 sections.
Please consider these when composing your review:

1. **BASIC REPORTING**
2. **EXPERIMENTAL DESIGN**
3. **VALIDITY OF THE FINDINGS**
4. General comments
5. Confidential notes to the editor

You can also annotate this PDF and upload it as part of your review

When ready submit online.

Editorial Criteria

Use these criteria points to structure your review. The full detailed editorial criteria is on your guidance page.

BASIC REPORTING

- Clear, unambiguous, professional English language used throughout.
- Intro & background to show context. Literature well referenced & relevant.
- Structure conforms to PeerJ standards, discipline norm, or improved for clarity.
- Figures are relevant, high quality, well labelled & described.
- Raw data supplied (see PeerJ policy).

EXPERIMENTAL DESIGN

- Original primary research within Scope of the journal.
- Research question well defined, relevant & meaningful. It is stated how the research fills an identified knowledge gap.
- Rigorous investigation performed to a high technical & ethical standard.
- Methods described with sufficient detail & information to replicate.

VALIDITY OF THE FINDINGS

- Impact and novelty not assessed. Negative/inconclusive results accepted. *Meaningful* replication encouraged where rationale & benefit to literature is clearly stated.
- Data is robust, statistically sound, & controlled.
- Conclusions are well stated, linked to original research question & limited to supporting results.
- Speculation is welcome, but should be identified as such.

Standout reviewing tips

The best reviewers use these techniques

Tip	*Example*
Support criticisms with evidence from the text or from other sources	*Smith et al (J of Methodology, 2005, V3, pp 123) have shown that the analysis you use in Lines 241-250 is not the most appropriate for this situation. Please explain why you used this method.*
Give specific suggestions on how to improve the manuscript	*Your introduction needs more detail. I suggest that you improve the description at lines 57- 86 to provide more justification for your study (specifically, you should expand upon the knowledge gap being filled).*
Comment on language and grammar issues	*The English language should be improved to ensure that an international audience can clearly understand your text. Some examples where the language could be improved include lines 23, 77, 121, 128 – the current phrasing makes comprehension difficult.*
Organize by importance of the issues, and number your points	*1. Your most important issue* *2. The next most important item* *3. …* *4. The least important points*
Please provide constructive criticism, and avoid personal opinions	*I thank you for providing the raw data, however your supplemental files need more descriptive metadata identifiers to be useful to future readers. Although your results are compelling, the data analysis should be improved in the following ways: AA, BB, CC*
Comment on strengths (as well as weaknesses) of the manuscript	*I commend the authors for their extensive data set, compiled over many years of detailed fieldwork. In addition, the manuscript is clearly written in professional, unambiguous language. If there is a weakness, it is in the statistical analysis (as I have noted above) which should be improved upon before Acceptance.*

Cancellous bone and theropod dinosaur locomotion. Part I – An examination of cancellous bone architecture in the hindlimb bones of theropods

Peter Bishop Corresp., [1] , **Scott Hocknull** [1] , **Christofer Clemente** [2] , **John Hutchinson** [3] , **Andrew Farke** [4] , **Belinda Beck** [5] , **Rod Barrett** [5] , **David Lloyd** [5]

[1] Geosciences Program, Queensland Museum, Brisbane, Queensland, Australia

[2] School of Science and Engineering, University of the Sunshine Coast, Maroochydore, Queensland, Australia

[3] Department of Comparative Biomedical Sciences, Royal Veterinary College, Hatfield, Hertfordshire, United Kingdom

[4] Raymond M. Alf Museum of Paleontology at The Webb Schools, Claremont, California, United States of America

[5] School of Allied Health Sciences, Griffith University, Gold Coast, Queensland, Australia

Corresponding Author: Peter Bishop
Email address: peter.bishop@qm.qld.gov.au

The following three-part series investigates the architecture of cancellous ('spongy') bone in the main hindlimb bones of theropod dinosaurs, and uses cancellous bone architectural patterns to infer locomotor biomechanics in extinct non-avian species. Cancellous bone is widely known to be highly sensitive to its mechanical environment, and has previously been used to infer locomotor biomechanics in extinct tetrapod vertebrates, especially primates. Despite great promise, cancellous bone architecture has remained little utilized for investigating locomotion in many other extinct vertebrate groups, such as dinosaurs. Documentation and quantification of architectural patterns across a whole bone, and across multiple bones, can provide much information on cancellous bone architectural patterns and variation across species. Additionally, this also lends itself to analysis of the musculoskeletal biomechanical factors involved in a direct, mechanistic fashion.

On this premise, computed tomographic and image analysis techniques were used to describe and analyse the three-dimensional architecture of cancellous bone in the main hindlimb bones of theropod dinosaurs for the first time. A comprehensive survey across many extant and extinct species is produced, identifying several patterns of similarity and contrast between groups. For instance, more plesiomorphic non-avian theropods (e.g., ceratosaurs and tyrannosaurids) exhibit cancellous bone architectures more comparable to that present in humans, whereas species more closely related to birds (e.g., paravians) exhibit architectural patterns bearing greater similarity to those of extant birds. Many of the observed patterns may be linked to particular aspects of locomotor biomechanics, such as the degree of hip or knee flexion during stance and gait. A further important

observation was the abundance of markedly oblique trabeculae in the diaphyses of the femur and tibia of birds, which in large species produces spiralling patterns along the endosteal surface. Not only do these observations provide new insight into theropod anatomy and behaviour, they also provide the foundation for mechanistic testing of locomotor hypotheses via musculoskeletal biomechanical modelling.

Cancellous bone and theropod dinosaur locomotion. Part I – An examination of cancellous bone architecture in the hindlimb bones of theropods

P.J. Bishop[1,2,3,*], S.A. Hocknull[1,2,3], C.J. Clemente[4,5], J.R. Hutchinson[6], A.A. Farke[7], B.R. Beck[2,8], R.S. Barrett[2,3] and D.G. Lloyd[2,3].

[1]Geosciences Program, Queensland Museum, Brisbane, Queensland, Australia.
[2]School of Allied Health Sciences, Griffith University, Gold Coast, Queensland, Australia.
[3]Innovations in Health Technology, Menzies Health Institute Queensland.
[4]School of Science and Engineering, University of the Sunshine Coast, Maroochydore, Queensland, Australia.
[5]School of Biological Sciences, The University of Queensland, Brisbane, Queensland, Australia.
[6]Structure and Motion Laboratory, Department of Comparative Biomedical Sciences, Royal Veterinary College, Hatfield, Hertfordshire, UK.
[7]Raymond M. Alf Museum of Paleontology at The Webb Schools, Claremont, California, USA.
[8]Exercise and Human Performance, Menzies Health Institute Queensland.

*corresponding author: peter.bishop@qm.qld.gov.au.

I.1 Abstract

The following three-part series investigates the architecture of cancellous ('spongy') bone in the main hindlimb bones of theropod dinosaurs, and uses cancellous bone architectural patterns to infer locomotor biomechanics in extinct non-avian species. Cancellous bone is widely known to be highly sensitive to its mechanical environment, and has previously been used to infer locomotor biomechanics in extinct tetrapod vertebrates, especially primates. Despite great promise, cancellous bone architecture has remained little utilized for investigating locomotion in many other extinct vertebrate groups, such as dinosaurs. Documentation and quantification of architectural patterns across a whole bone, and across multiple bones, can provide much information on cancellous bone architectural patterns and variation across species. Additionally, this also lends itself to analysis of the musculoskeletal biomechanical factors involved in a direct, mechanistic fashion.

On this premise, computed tomographic and image analysis techniques were used to describe and analyse the three-dimensional architecture of cancellous bone in the main hindlimb bones of theropod dinosaurs for the first time. A comprehensive survey across many extant and extinct species is produced, identifying several patterns of similarity and contrast between groups. For instance, more plesiomorphic non-avian theropods (e.g., ceratosaurs and tyrannosaurids) exhibit cancellous bone architectures more comparable to that present in humans, whereas species more closely related to birds (e.g., paravians) exhibit architectural patterns bearing greater similarity to those of extant birds. Many of the observed patterns may be linked to particular aspects of locomotor biomechanics, such as the degree of hip or knee flexion during stance and gait. A further important observation was the abundance of markedly oblique trabeculae in the diaphyses of the femur and tibia of birds, which in large species produces spiralling patterns along the endosteal surface. Not only do these observations provide new insight into theropod anatomy and behaviour, they also provide the foundation for mechanistic testing of locomotor hypotheses via musculoskeletal biomechanical modelling.

I.2 Introduction

I.2.1 Background

Perhaps more than any other group of extinct vertebrates (except hominin primates), dinosaurs have been the subject of extensive research into a wide variety of aspects concerning their palaeobiology. One such aspect is their manner of locomotion, which has often been the topic of much debate. Locomotion has played an important role in arguments surrounding dinosaur physiology, behaviour and palaeoecology (Alexander 1989; Bakker 1980; Bakker 1986; Bell & Snively 2008; Horner & Lessem 1993; Molnar & Farlow 1990; Ostrom 1969; Paul 1988; Paul 2008; Pontzer et al. 2009; Thomas & Farlow 1997; Thulborn 1984). Movement has also been important to understanding dinosaur evolution. For example, approximately three-quarters of the features that distinguish dinosaurs from other animals relate to their erect (parasagittal), ancestrally bipedal posture and locomotion (Brusatte 2012; Novas 1996). Furthermore, much of dinosaur evolution was accompanied by major changes in locomotor morphology, and by inference, behaviour (Carrano 2000; Carrano 2005; Gatesy 2002; Gatesy & Middleton 1997; Hutchinson & Allen 2009; Maidment et al. 2014; Middleton & Gatesy 2000; Novas 1996).

In order to infer how extinct, non-avian dinosaurs may have locomoted, palaeontologists can only study the fossils left behind, either body fossils (bones) or trace fossils (footprints and trackways). Fossil footprints and trackways are the most direct line of evidence of locomotion in extinct dinosaurs (Farlow et al. 2012; Gatesy et al. 1999; Gillette & Lockley 1989; Lockley 1991; Thulborn 1990). However, footprints and trackways do not provide direct insight into the movement or coordination of individual limb segments except for the distal limb; moreover, they cannot be definitively assigned to a particular trackmaker (Hutchinson & Gatesy 2006; Lockley 1991; Thulborn 1990). In contrast, the associated bones of the animal's skeleton can be positively assigned to a given species, and if preserved well can provide insight into parts of the animal that never touched the substrate.

Owing to their often large size and comparatively detailed body fossil record, many investigations have examined how osteology may relate to locomotor behaviour in extinct dinosaurs. These studies have typically focused on externally visible features, such as bone

shapes or proportions (e.g., Carrano 1998; Carrano 2001; Carrano 2005; Christiansen 1999; Coombs 1978; Gatesy 1991b; Gatesy & Middleton 1997; Maidment & Barrett 2014; Maidment et al. 2012), joint range of motion (e.g., Mallison 2010a; Mallison 2010b; Paul 1998) or geometrical relationships between inferred muscle lines of action and joints (e.g., Bates et al. 2012; Carrano 2000; Hutchinson et al. 2005; Hutchinson et al. 2008; Maidment et al. 2014; Russell 1972). The insight such studies can provide are usually ~~only of a general nature~~, often having little bearing for understanding the posture or gait of any one species, and moreover carry the caveat of unknowns of soft tissue influences, which may be substantial (Bonnan et al. 2010; Hutchinson & Gatesy 2006; Tsai & Holliday 2015). Additionally, these studies may only be able to clarify the *range* of potential locomotor behaviours used by extinct dinosaurs, rather than the reconstruct the behaviours *actually* used.

A further line of osteological evidence that has been frequently investigated is the cross-sectional geometry of the mid-shaft of limb bones (e.g., Alexander 1985; Alexander 1989; Alexander 1991; Christiansen 1997; Christiansen 1998; Cubo et al. 2015; Fariña et al. 1997; Farke & Alicea 2009; Farlow et al. 1995; Heinrich et al. 1993; Lovejoy et al. 2002; Mazzetta et al. 1998; Wilson & Carrano 1999). The implicit assumption of such enquiry is that the manner in which cortical bone is distributed around a diaphyseal cross-section is related to the magnitude and direction of bending and torsional stresses it experiences (Biewener 1992; Brassey et al. 2013; Wainwright et al. 1976). Therefore, the geometry of a limb bone's cross-section at midshaft may provide insight into whole-bone loading mechanics, and by extension, locomotor behaviour. However, a growing body of experimental evidence indicates that there is no simple correlation between cortical bone morphology and ~~the nature~~ of bone loading, such as bending direction (Bertram & Biewener 1988; Biewener & Taylor 1986; Butcher et al. 2008; Demes 2007; Demes et al. 2001; Demes et al. 1998; Lieberman et al. 2004; Main & Biewener 2004; Pearson & Lieberman 2004; Thomason 1995; Wallace et al. 2014). Without a strong comparative framework derived from suitable extant species (if they exist) inferences drawn solely from mid-shaft cortical bone morphology should be viewed with caution (see also Farke & Alicea 2009).

I.2.2 Cancellous bone in brief

One aspect of osteology that has remained understudied by dinosaur palaeontologists is the nature of cancellous ('spongy') bone, the other main type of bone tissue found in limb bones. Cancellous bone is found throughout the vertebrate skeleton, including in the ends of long bones, vertebrae, throughout short bones (e.g., those of the wrist and ankle) and between the opposing cortices of many flat bones, such as those of the skull (Carter & Beaupré 2001; Currey 2002; Martin et al. 1998). This work will only consider cancellous bone in the endochondral bones of the appendicular skeleton. Furthermore, it will not consider medullary bone, the loosely packed bone that is periodically formed in birds (Dacke et al. 1993) and at least some dinosaurs (Hübner 2012; Lee & Werning 2008; Schweitzer et al. 2005), despite its superficial similarity to cancellous bone. Medullary bone is rapidly laid down to act as a calcium reservoir for the production of eggshells before they are laid, and consequently its tissue is not as mechanically competent as that of other, permanent bone tissues: its primary function is metabolic, rather than mechanical (Currey 2002).

The macroscopic architecture of cancellous bone is characterized by a complex, three-dimensional (3-D), lattice-like array of interlinking bony struts called trabeculae, from the Latin *trabecula*, meaning 'small beam' (Fig. 1). The shape of individual trabeculae may be rod-like, plate-like or some variant in between (Singh 1978). Despite being not as mechanically competent as cortical bone, cancellous bone forms a key component of the skeleton; in humans, it comprises some 70% of the whole skeleton by volume (Huiskes 2000).

The highly complex macrostructure of cancellous bone gives it an exceptionally high ratio of surface area to volume, which makes it a useful reservoir for calcium homeostasis (Clarke 2008; Swartz et al. 1998). More importantly, this high surface area also leads to a rate of remodelling that is an order of magnitude greater than that of cortical bone; in humans, some 25% by volume is remodelled per year, compared to 2–3% for cortical bone (Clarke 2008; Huiskes et al. 2000; Lane et al. 1996; Parfitt 1983). This rapid remodelling of cancellous bone allows it to adapt to changes in its mechanical environment more quickly than cortical bone. There is an every-

153 growing body of empirical evidence, derived from both experimental and comparative studies,
154 demonstrating how cancellous bone is highly sensitive and well adapted to its mechanical
155 environment. Moreover, when this mechanical environment changes, cancellous bone is able to
156 adapt its architecture in an accurate and predictable fashion. Much of this work has been recently
157 reviewed in detail by Kivell (2016), and will not be discussed further here.
158
159
160 ***I.2.3 The fabric of cancellous bone (and why cancellous bone shows directionality)***
161
162 A salient observation of previous studies is that the orientation of trabeculae (i.e., the fabric of the
163 cancellous bone architecture) is a fundamental component of how cancellous bone is adapted to
164 its environment. Indeed, fabric anisotropy is one of the most important parameters in determining
165 the mechanical behaviour of cancellous bone, second only to bone volume fraction, a measure of
166 porosity (Cowin 1997; Goldstein et al. 1993; Kabel et al. 1999; Maquer et al. 2015; Mittra et al.
167 2005; Odgaard et al. 1997; Turner 1992; Turner et al. 1990; Ulrich et al. 1999). Furthermore, the
168 principal material directions[1] in cancellous bone are very closely aligned with the principal fabric
169 directions of its architecture (Fig. 2); that is, the principal axes of the mechanical compliance
170 matrix and fabric tensors are closely aligned (Odgaard et al. 1997; Turner et al. 1990)[2].
171 Moreover, the degree of fabric anisotropy relates closely with the degree of anisotropy of the
172 mechanical properties: the relative magnitudes of eigenvalues of the fabric tensor closely match
173 that of their respective compliance matrix eigenvalues (Odgaard et al. 1997)[3].
174

[1] In an anisotropic continuous material, there exist a number of directions in which a given mechanical property (e.g., stiffness) is at its greatest or is lowest magnitude; these are its principal directions. In an orthotropic material such as bone (Cowin 1986; Keaveny et al. 2001; Pidaparti & Turner 1997), there are two such directions (one maximum, one minimum), which are orthogonal; there is also a third principal direction which is mutually orthogonal to the first two and is a minimax (intermediate). Perfectly isotropic materials have no principal directions, for each mechanical property is the same in every direction.

[2] The compliance matrix **C** of a volume of material is a square matrix of order six (generalized Hooke's Law for anisotropic materials) that describes its mechanical properties in terms of values of Young's modulus, shear modulus and Poisson's ratio. The fabric tensor **H** is a positive definite second-rank tensor that quantitatively describes the 3-D microstructural arrangement of trabeculae in a volume of cancellous bone (Cowin 1986). The principal axes of **C** and **H** are given by their *eigenvectors* (see next footnote).

[3] For a given matrix **A**, there are one or more vectors **v** which maintain their original direction when multiplied by the matrix, although they are dilated by some scaling factor: $\mathbf{Av} = \lambda\mathbf{v}$. These vectors **v** are the matrix's eigenvectors, and the scaling factors λ are the matrix's *eigenvalues*. The relative magnitudes of the eigenvalues describe the relative extent to which the matrix **A** is oriented in each direction given by the eigenvectors.

In a comparative context, many previous studies have also demonstrated that differences in cancellous bone fabric direction are indicative of differences in locomotor behaviour, presumably because different behaviours (e.g., joint kinematics) engender different loading regimes and directions thereof (Amson et al. 2017; Barak et al. 2013; Biewener et al. 1996; Carter & Beaupré 2001; Goldstein et al. 1991; Kamibayashi et al. 1995; Matarazzo 2015; Podsiadlo et al. 2008; Radin et al. 1982; Ryan & Ketcham 2005; van der Meulen et al. 2006). When the loading regimes change, cancellous bone fabric direction also changes, in a highly predictable fashion (Barak et al. 2011; Polk et al. 2008; Pontzer et al. 2006) (Fig. 3). These observations also appear to apply across species as well as within species, as demonstrated by work on several species of primate (Barak et al. 2013; Ryan & Ketcham 2005).

A strong correspondence between the directionality of cancellous bone and *in vivo* mechanical loading was first suggested more than 150 years ago (von Meyer 1867; Ward 1838). This became widely publicised by Wolff (1892) as the *trajectorial theory*, which was proposed as an overarching paradigm that related cancellous bone architecture to its mechanical environment. In its modern formulation (Cowin 2001), the trajectorial theory can be stated thus: at remodelling equilibrium (Cowin 1986), the principal material directions of a given volume of cancellous bone are aligned with principal stress trajectories[4], but only at spatial scales at which the cancellous bone can be treated as a continuous material (Fig. 4). The continuum scale is the scale at which the mechanical behaviour of a volume of cancellous bone structure can be replaced by a set of material properties that are averaged across the same volume. Only at this scale, or larger, can the averaged architecture and mechanical properties of cancellous bone be legitimately compared with the averaged network of principal stress trajectories (Cowin et al. 1992; Martin et al. 1998; Oxnard & Yang 1981; Tsubota et al. 2002; Tsubota et al. 2009). The spatial scale at which the continuum concept can be invoked for cancellous bone has been suggested to be at least three to five times trabecular spacing (Cowin 2001; Cowin et al. 1992; Harrigan et al. 1988).

[4] When a volume of material is under stress due to applied load, there will be three directions in which the shear component is zero; that is, only normal stresses (compressive or tensile) occur in these directions. The normal stresses in these directions are termed the principal stresses, and tangent lines to these directions form a network of principal stress trajectories. These trajectories essentially show how compressive and tensile forces are distributed throughout a body under loading.

The trajectorial theory of cancellous bone architecture has received strong support from many experimental (Biewener et al. 1996; Lanyon 1974; Su et al. 1999) and theoretical studies (Beaupré et al. 1990; Carter et al. 1989; Currey 2002; Gefen & Seliktar 2004; Giddings et al. 2000; Hayes & Snyder 1981; Jacobs 2000; Jacobs et al. 1997; Koch 1917; Miller et al. 2002; Pauwels 1980; Rudman et al. 2006; Sverdlova 2011; Vander Sloten & Van der Perre 1989), which have repeatedly shown striking similarity between cancellous bone fabric and principal stress trajectories generated from physiological loading. However, whilst it aptly describes the phenomenological association between cancellous bone architecture and its mechanical environment, the trajectorial theory does not link the two together via a mechanistic explanation. Such a mechanistic explanation was provided by Fyhrie & Carter (1986), who demonstrated that strain energy density (SED) in a given volume of cancellous bone is minimized when the architecture is anisotropic such that (i) the direction of maximum stiffness is parallel to that of the maximum principal stress, (ii) the direction of minimum stiffness is parallel to that of the minimum principal stress, and (iii) the direction of the intermediate stiffness is parallel to that of the intermediate principal stress. Thus, if SED is a stimulus for trabecular remodelling, cancellous bone adaptation at the continuum level can be mechanistically linked to remodelling activites at the cellular level.

More recent computational modelling studies have shown that SED, or a related measure such as strain or stress, is indeed likely an important driver of trabecular remodelling. Common to each is the notion of the 'mechanostat' of bone (Christen et al. 2014; Cresswell et al. 2016; Frost 1987; Frost 2003; Lambers et al. 2013; Schulte et al. 2013): bone remodels through the addition of bone tissue by osteoblasts to areas experiencing high strain (i.e., overloaded areas) and the removal of bone tissue by osteoclasts from areas experiencing low strain (i.e., underloaded areas) (Fig. 5A–D). By this process, at remodelling equilibrium all parts of the cancellous structure bear the same amount of strain, or more correctly, their SED is the same. By using a uniform SED as a remodelling objective, numerous continuum-level finite element computational models have predicted bulk density distributions and fabric patterns that accurately reflect reality (Beaupré et al. 1990; Carter & Beaupré 2001; Carter et al. 1989; Coelho et al. 2009; Jacobs et al. 1997; Kowalczyk 2010; Turner et al. 1997). More impressively, high-resolution simulations of cellular-level remodelling produce models that spontaneously 'self-trabeculate' from an initially isotropic

233 configuration (Martin et al. 1998). The result of such simulations is a cancellous structure with
234 trabeculae of realistic proportions, and in those models simulating whole bones, life-like whole-
235 bone architectures (Adachi et al. 2001; Boyle & Kim 2011; Huiskes et al. 2000; Jang & Kim
236 2008; Jang & Kim 2010a; Jang & Kim 2010b; Mullender & Huiskes 1995; Phillips 2012; Phillips
237 et al. 2015; Ruimerman et al. 2005; Smith et al. 1997; Tsubota et al. 2002; Tsubota et al. 2009;
238 Wang et al. 2012) (Fig. 5E,F). Moreover, these trabeculae, or more correctly, the fabric
239 directions, are aligned with the continuum-level principal stress trajectories, and when the
240 loading regime changes, the model re-adapts to produce a new cancellous architecture, where the
241 trabeculae are aligned with the new continuum-level principal stress trajectories (Adachi et al.
242 2001; Huiskes et al. 2000; Mullender & Huiskes 1995; Ruimerman et al. 2005; Wang et al.
243 2012). Hence, the trajectorial theory, which is a global pattern observable on the scale of whole
244 bones, may be considered emergent from the local actions of cells.
245
246 A rigid application of the trajectorial theory to cancellous bone would predict that trabeculae are
247 oriented at right angles to each other. However, this is often not the case; in fact, orthogonal
248 intersections seem to be the exception, rather than the rule (Murray 1936). The reason for this
249 apparent paradox is that most bones experience multiple, often diverse loading regimes. It is this
250 adaptation to multiple different loading regimes, each with different principal stress trajectories,
251 that produces the nonorthogonality observed in the majority of cancellous bone architectures
252 (Ben-Zvi et al. 2017; Heřt 1994; Pidaparti & Turner 1997; Skedros & Baucom 2007). Thus, only
253 in bones that tend to experience a single loading regime would an orthogonal 'trajectorial
254 structure' be expected in cancellous bone. One such example is the calcaneum of a number of
255 digitigrade mammals, such as sheep (Lanyon 1974), mule deer (Skedros & Baucom 2007;
256 Skedros et al. 2004; Skedros et al. 2007), horses (Vander Sloten & Van der Perre 1989),
257 macropod marsupials (Biewener et al. 1996) and cattle (Fig. 6). These bones are loaded in an
258 extremely consistent manner, by the pull on the distal end from the Achilles tendon and
259 superficial digital flexor tendons. A uniform ~~SED~~ distribution within a volume of cancellous
260 bone is hence not usually achieved in any single given loading regime (Jang & Kim 2008; van
261 Rietbergen et al. 2003; van Rietbergen et al. 1999). Rather, it is the *time-averaged distribution* of
262 SED, resulting from multiple daily loading regimes that a bone experiences, which is uniform
263 and which drives cancellous bone remodelling. This has been demonstrated by numerous

computational simulations of the bone remodelling process. Specifically, no one loading regime will lead to replication of all the observed architectural features in a bone; only when multiple loading regimes are considered can all of a bone's cancellous architecture be accounted for by the trajectorial theory (Beaupré et al. 1990; Boyle & Kim 2011; Carter & Beaupré 2001; Carter et al. 1989; Coelho et al. 2009; Jacobs et al. 1997; Jang & Kim 2008; Jang & Kim 2010a; Jang & Kim 2010b; Phillips et al. 2015; Sverdlova 2011; Tsubota et al. 2002; Tsubota et al. 2009; Turner et al. 1997).

I.2.4 Non-mechanical influences on cancellous bone architecture

Although the architecture of cancellous bone is clearly influenced by its mechanical environment, it may also be influenced by other factors, such as ontogeny and genetics. Epigenetic influences on cancellous bone mechanobiology may also exist, but exactly what these could be, and how much they are truly independent of genetic influences, remains unknown.

Many studies have demonstrated that the cancellous architecture in a particular region of a bone changes considerably throughout the ontogeny of an individual (Abel & Macho 2011; Gosman & Ketcham 2009; Gosman et al. 2011; Nafei et al. 2000a; Nafei et al. 2000b; Raichlen et al. 2015; Ryan & Krovitz 2006; Tanck et al. 2001; Townsley 1948; Volpato 2008; Wolschrijn & Weijs 2005). Such changes are necessitated by increases in absolute bone size, and it is therefore unsurprising that the most rapid changes occur early in ontogeny, during the growth of an individual (Gosman & Ketcham 2009; Gosman et al. 2011; Raichlen et al. 2015; Ryan & Krovitz 2006; Tanck et al. 2001). The timing of these ontogenetic changes in cancellous bone architecture often reflect the timing of ontogenetic changes in locomotor behaviour, especially the initial commencement of sustained locomotor-induced loading (Gosman & Ketcham 2009; Gosman et al. 2011; Raichlen et al. 2015; Ryan & Krovitz 2006; Tanck et al. 2001; Townsley 1948; Volpato 2008; Wolschrijn & Weijs 2005). Therefore, mechanical factors influence cancellous bone remodelling not only in the adult, but across the entire lifespan of an individual.

Given that the adaptation of cancellous bone to its mechanical environment occurs throughout the life of an individual, an interesting proposition arises if the rate at which bone remodels decreases through ontogeny (Christiansen et al. 2000; Keaveny & Yeh 2002; Lieberman et al. 2003;

295 Pearson & Lieberman 2004). That is, the adaptive response of cancellous bone in the adult may
296 not be as proficient as in earlier stages of life. If this occurs, the architecture observed in the adult
297 may reflect, to some degree, the habitual loading experienced during ontogeny, and not just the
298 current habitual loading environment (Carlson et al. 2006; Petterson et al. 2010; Pontzer et al.
299 2006). This phenomenon of *ontogenetic inertia* has not been investigated in great detail, but a
300 general consideration may nevertheless be made. The potential for ontogenetic inertia in
301 cancellous bone architecture will depend on at least four variables, namely (i) the absolute rate at
302 which cancellous bone remodels, (ii) the lifespan of the individual, (iii) the absolute increase in
303 bone size through ontogeny, and (iv) the degree to which locomotor-induced loading changes
304 through ontogeny.
305
306 Ontogenetic inertia will be minimal in species that have a high rate of bone remodelling
307 compared to their lifespan. For example, adult humans remodel about 25% by volume of their
308 cancellous bone per year (Huiskes et al. 2000; Parfitt 1983). Given the lengthy lifespan of
309 humans, this implies that cancellous bone will be turned over many times during the life of an
310 individual, erasing the 'signals' of locomotor-induced loading from earlier stages in life.
311 However, there may be a small, immediate component of ontogenetic inertia. This is because
312 bone (re)modelling can only occur on pre-existing bone surfaces (Carter & Beaupré 2001; Martin
313 et al. 1998; Mullender & Huiskes 1995), and hence there may be some lag left over between
314 successive 'bone generations'. Over the lifetime of an individual, however, this will be
315 inconsequential. A great increase in the absolute size of limb bones through ontogeny, as seen in
316 humans, will also result in the complete turning over of cancellous bone many times, reducing the
317 magnitude of ontogenetic inertia. If locomotor behaviour does not change appreciably throughout
318 ontogeny, then ontogenetic changes in locomotor-induced bone loading will be minimal.
319 Consequently, the cancellous bone architecture observed in the adult will reflect the current
320 habitual loading environment, because this environment has remained effectively unaltered for a
321 significant length of time. Such a pattern is also observed in humans, where locomotor behaviour
322 effectively matures by the age of four years (Sutherland 1997), and the cancellous bone
323 architecture in the human proximal femur and tibia is effectively unchanged from about nine
324 years of age onward (Gosman & Ketcham 2009; Ryan & Krovitz 2006). Minimal ontogenetic
325 inertia would also be expected for ostriches, which have a high rate of bone remodelling (Currey

2003), a sizeable lifespan (Davies 2002), exhibit great increase in bone size from chick to adult, and which show little ontogenetic change in locomotor behaviour as far as limb posture is concerned (Smith et al. 2010). One further consideration is that the magnitude of ontogenetic inertia may also depend on if the bone has experienced relatively 'novel' mechanical loading conditions in its recent past. In such a situation more rapid remodelling may occur in response to these novel loading conditions (Robling et al. 2006; Robling & Turner 2009), serving to 'erase' older ontogenetic signal and thereby decreasing the magnitude of ontogenetic inertia.

As regards genetic influences on cancellous bone architecture, these influences probably depend on the scale at which the topic is approached. Many studies have investigated the genetic effects on cancellous bone adaptation to mechanical loading, particularly in different strains of mice, and have shown that genetics can indeed modulate cancellous bone mechanobiology (e.g., Havill et al. 2010; Judex et al. 2004; Wallace et al. 2015; Wallace et al. 2012). However, the aforementioned investigations concern within-species differences, and concern very specific regions of a given bone. They hence do not illustrate how genetics influences the adaptation of entire bones, across the skeleton, and across species that load their bones in different manners.

In terms of the architecture of whole bones, genetic factors strongly influence a bone's initial development. The basic structure of the whole bone derives from the systematic expression of positional information encoded in the genome (Lanyon 1996; Lovejoy et al. 2002). Moreover, recent research has indicated that some aspects of the finer-scale architectural features may also be influenced by genetic factors, in addition to mechanical factors. For example, the gross architecture of cancellous bone (such as density distribution) in the adult human ilium appears quite early on during foetal development, well before the onset of locomotor-induced loading, suggestive of genetic influence (Abel & Macho 2011; Cunningham & Black 2009a; Cunningham & Black 2009b). However, such a phenomenon is not observed in the human proximal femur or tibia (Gosman & Ketcham 2009; Ryan & Krovitz 2006). The early appearance of an adult-like gross architecture may alternatively result from *in utero* muscular contractions, producing mechanical stimulation of the developing bone (Abel & Macho 2011; Cunningham & Black 2009a; Cunningham & Black 2009b; Lanyon 1974). Further insight is provided by a second example, namely the development of the calcaneum in artiodactyl ungulates. In both sheep

(Lanyon 1974) and mule deer (Skedros et al. 2004), the cancellous bone architecture observed in the adult calcaneum occurs in the foetus, paralleling the situation in the human ilium. However, when Lanyon and Goodship (reported by Skerry 2000) transected the Achilles tendon of a developing foetal lamb *in utero*, they found that subsequent prenatal growth resulted in a disorganized architecture in the experimental calcaneum, compared to the contralateral control. This suggests that in some situations at least, prenatal loading can be responsible for the cancellous bone architecture observed in a newborn animal, possibly diminishing the significance of genetic influences.

In general then, it appears that the influences on a bone's cancellous architecture shift during ontogeny, from a dominant role of genetic influences in early prenatal development (*in utero* or *in ovo*), to an increasingly important role for extragenetic stimuli, such as mechanical loading, in later development and postnatal ontogeny (Skedros et al. 2007). That is, a basic, genetically determined template lays out the gross architecture of cancellous bone, which is subsequently built upon and remodelled during postnatal ontogeny in response to mechanical loading.

Genetic influences on cancellous bone architecture may also extend across species. If the genetic control of cancellous bone architecture is strong enough, the potential arises that the cancellous architecture observed in a given bone in a particular species may not entirely reflect the loads experienced by the individual in life, but also the loads experienced by the homologous bone somewhere in the past of the species' evolutionary history. For example, if a species of primate that engages in quadrupedal locomotion recently evolved from a species which engaged in leaping locomotion, it may inherit some architectural characteristics from its ancestors. That is, whilst it is a quadruped, its cancellous bone architecture may be somewhat 'leaper-like' in nature (Ryan & Ketcham 2005). This phenomenon of *phylogenetic inertia* (Blomberg & Garland 2002) has received only limited attention in the context of cancellous bone architecture, but what research has been conducted shows only a weak effect, if any (Ryan & Shaw 2012; Ryan & Shaw 2013; Scherf et al. 2013; Tsegai et al. 2013). This possibly weak effect further suggests that the architecture of cancellous bone observed in the adult is largely, if not entirely, influenced by mechanical stimuli (Skedros et al. 2007).

The possibility of phylogenetic inertia can only exist if the genome itself is subject to the influences of the mechanical loading environment a bone experiences in life. That is, the genome that codes for the initial template of cancellous bone architecture is influenced by how the bone is loaded in life. Or, put another way, patterns of bone loading resulting from a particular locomotor behaviour lead to selection on the phenotype, which in turn influences the ~~genome (~~populational allele frequencies~~)~~ over generations, affecting the predetermination of gross architectural features prior to eventual bone use and loading in life (Lanyon 1974; Ryan & Shaw 2012; Ryan & Shaw 2013; Saparin et al. 2011; Townsley 1948). If epigenetic factors are involved, then ~~the~~ adaptation ~~of~~ the genome may possibly be achieved very quickly. It would indeed be advantageous to have some form of a blueprint in place for the gross architecture of cancellous bone, because this starts the bone 'off on the right foot' as soon as the animal is born (or hatches). In precocial species, the young have to start locomoting – and often have to keep up with the adults – as soon as they are born (or hatch); with the cancellous bone architecture already somewhat pre-adapted, this would make the bone more structurally efficient from the very first day of postnatal loading.

In light of the above considerations, there appear to be at least three pathways that the relationship between cancellous bone architecture and its mechanical environment can take (Fig. 7):

i. A direct pathway, whereby locomotor-induced bone loading leads to changes in cancellous bone architecture, via adaptive remodelling throughout the lifetime of an individual.
ii. An indirect pathway, whereby patterns of locomotor behaviour lead to selection on the genome (i.e., adaptation over generations), which in turn affects the genetic predetermination of gross architectural features prior to loading.
iii. A direct pathway, whereby prenatal muscular contractions produce bone loading, leading to adaptive remodelling prior to the commencement of postnatal, locomotor-induced loading.

If epigenetic factors are involved in cancellous bone mechanobiology, then a fourth, indirect, pathway would exist. These pathways are not mutually exclusive of each other, and it is likely that they all contribute to the final architecture observed in cancellous bone, to varying degrees. Pathway (i) can explain changes in cancellous bone architecture in response to changes in loading conditions within individuals, either naturally or experimentally. Pathways (i) and (ii) can explain how cancellous bone architecture reflects the loads experienced in post-natal life, and hence why

different cancellous bone architectures reflect different locomotor behaviours, such as those between different species. Pathways (ii) and (iii) can explain the presence of gross architectural features that are characteristic and reflective of adult locomotion, yet which are present in neonates before the onset of locomotor-induced loading.

I.2.5 The utility of cancellous bone in understanding locomotion in extinct, non-avian dinosaurs

Cancellous bone architecture clearly has great potential utility for better understanding locomotor biomechanics in extinct tetrapods. Most previous studies that have used cancellous bone to test hypotheses of behaviour have focused on extinct primates (Barak et al. 2013; D'Anastasio et al. 2013; DeSilva & Devlin 2012; Hébert et al. 2012; Macchiarelli et al. 1999; Rook et al. 1999; Ryan & Ketcham 2002a; Scherf 2008; Skinner et al. 2015; Su & Carlson 2017; Su et al. 2013), with few studies directed towards other tetrapod groups (Bishop et al. 2015; Moreno et al. 2007; Sues 1978; Thomason 1985). Yet, extinct, non-avian dinosaurs are a group that would be quite suitable for this kind of investigation. Non-avian dinosaurs lived for a very long period of time and in a wide variety of environments, exhibited a diverse array of locomotor morphologies, and their fossils are relatively abundant and often well-preserved. They are also inferred to have had high rates of bone growth and remodelling, comparable to that of extant mammals and birds (Brusatte 2012; Currey 2002; Reid 2012), in contrast to that observed in most extant reptiles (Currey 2002; de Ricqlès 1976; Enlow 1969). Especially in the larger species, they also had both lengthy lifespans and a large change in absolute bone size through ontogeny, having hatched from eggs less than 30 cm in diameter (Horner 2000). They would hence be expected to show minimal ontogenetic inertia in adults.

To the authors' knowledge, only two studies have examined cancellous bone architecture as it relates to aspects of non-avian dinosaur biomechanics, although technological limitations may be in part responsible for this. In the first (Sues 1978), 'trabeculae' were observed in the enlarged skull domes of pachycephalosaurs, appearing to be oriented appropriately for receiving the forces

that might be experienced during head-butting behaviour. However, these 'trabeculae' were later interpreted to be an ontogenetic transitory structure in the growth of the skull bones (Goodwin and Horner, 2004). More recently, cancellous bone in the pedal phalanges of various dinosaur species was imaged using clinical-grade X-ray computed tomographic scanning, and basic phenomenological interpretations were made (Moreno et al. 2007). Similarly, little investigation has been undertaken in the way of cancellous bone architecture in extant birds. In fact, aside from being qualitatively illustrated on several occasions (largely for show, e.g., Cracraft 1971; Owen 1866; Thompson 1942; Townsley 1948), and experimentally manipulated according to different loading patterns (Pontzer et al. 2006), the three-dimensional macrostructure of cancellous bone in the limb bones of birds is virtually unstudied.

A phenomenological approach has been the dominant theme of most previous studies of cancellous bone architecture in extinct vertebrates. Often, investigation has largely been limited to comparing the architecture of cancellous bone in a given extinct species to that of extant related species, essentially asking the question "what extant species is the extinct one closest to?" That is, similarity (or difference) in cancellous bone architecture implies similarity (or difference) in locomotor behaviour. Even then, comparisons are often limited to discrete sub-regions of the bone of interest, rather than architectural patterns throughout a whole bone. Whilst this approach may serve as a good starting point, it cannot by itself provide insight into questions of whole-bone loading or musculoskeletal mechanics. Furthermore, whilst such an approach may be useful when applied to a group of animals with close extant relatives of similar morphologies (such as primates), it may not be useful when investigating extinct animals that are quite different from any extant animal group (such as non-avian dinosaurs).

A more appropriate way of investigating cancellous bone architecture in any extinct species is through a holistic, whole-bone, biomechanically-informed approach. By considering the architecture of cancellous bone throughout an entire bone, more insight may potentially be gained, compared to focusing on a limited number of specific regions (Gross et al. 2014; Kivell 2016; Ryan & Test 2007; Saparin et al. 2011; Scherf 2008; Skinner et al. 2015; Stephens et al. 2016; Su et al. 2013; Tsegai et al. 2013; Tsegai et al. 2017). Even more insight may be possible by considering the architectural patterns of multiple bones, rather than just one (Saers et al. 2016;

Stephens et al. 2016; Tsegai et al. 2017). Most of the aforementioned whole-bone studies have focused on how scalar variables (e.g., bone volume fraction) vary throughout a bone. However, as the orientation of cancellous bone fabric is quite telling of loading conditions, and strongly reflects the mechanical performance of cancellous bone tissue as a whole, it is also deserving of considerable research attention. Importantly, cancellous bone fabric can also be related to bone loading mechanics across the scale of whole bones, via the trajectorial theory: principal material directions, and hence principal fabric directions, are aligned with continuum-level principal stresses engendered by physiological loading. Thus, when a whole-bone approach is taken, cancellous bone fabric can be linked with whole-limb musculoskeletal biomechanics in a mechanistic fashion, rather than just phenomenologically.

I.2.6 Outline of this study

In the present study, and the two subsequent parts of this series (Bishop et al. in review-b; Bishop et al. in review-c), cancellous bone architecture was investigated in one particular sub-group of dinosaurs, the theropods, to demonstrate how the investigation of microstructural characteristics across whole bones has the potential to provide unparalleled insight into questions of posture and loading mechanics. Theropoda include some of the most iconic of extinct animals, as well as the most species-rich group of modern-day terrestrial vertebrates, the birds (Bennett & Owens 2002; Chiappe & Witmer 2002; Gauthier 1986; Holtz 2012; Naish 2012; Sereno 1999; Weishampel et al. 2004). Over their 230 million year history, theropods have spanned an incredible range of body size, from the two gram *Mellisuga helenae* (bee hummingbird) to the eight tonne *Tyrannosaurus rex* (Dunning 2007; Henderson 1999; Hutchinson et al. 2011), and, despite being exclusively bipedal, have displayed a wide range of locomotor morphologies (Baumel & Witmer 1993; Carrano 1998; Gatesy & Middleton 1997; Middleton & Gatesy 2000; Paul 1988). This makes them excellent candidates for research into questions concerning the biomechanics of terrestrial locomotion, as well as the consequences of large body size on locomotor performance. Additionally, studies of theropod locomotion are critical to charting the evolution of locomotor behaviour on the line to modern birds, including the origin of a novel locomotor pattern, avian flight (Allen et al. 2009; Gatesy 2002; Heers & Dial 2012; Hutchinson & Gatesy 2000).

512

513 Terrestrial locomotion in theropods has received considerable attention over the past three
514 decades, and a substantially more detailed picture of non-avian theropod stance and gait, and its
515 evolution, has emerged. It is now well established that on the line to modern birds, many
516 profound anatomical changes occurred in theropods, including significant modifications of pelvic
517 and hindlimb osteology (Carrano 2000; Gatesy & Middleton 1997; Hutchinson 2001a;
518 Hutchinson 2001b), musculature and proportions (Carrano & Hutchinson 2002; Hutchinson
519 2001a; Hutchinson 2001b; Hutchinson 2002), changes to tail length and construction (Gatesy
520 1990; Gatesy 1995; Gatesy 2002; Pittman et al. 2013), and changes in the position of the whole-
521 body centre of mass (Allen et al. 2013). These are inferred to have influenced limb posture, from
522 more upright (less flexed hips and knees) in most forms to more crouched (more flexed hips and
523 knees) in the more derived forms (Bates et al. 2012; Carrano 1998; Gatesy 1990; Gatesy 1991b;
524 Gatesy 1995; Gatesy et al. 2009; Grossi et al. 2014; Hutchinson et al. 2005), as well as the
525 muscular strategies of limb support and propulsion (Gatesy 1990; Gatesy 1995; Gatesy 2002;
526 Hutchinson & Gatesy 2000). In turn, bone loading mechanics is also inferred to have changed
527 markedly through theropod evolution (Carrano 1998; Farke & Alicea 2009). All of these changes
528 were set against a backdrop of substantial body size evolution, with sustained miniaturisation
529 occuring along much of the stem lineage (Benson et al. in press; Lee et al. 2014; Turner et al.
530 2007), but also with many instances of secondary gigantism (Benson et al. in press; Carrano
531 2006; Lee et al. 2014). Studies of cancellous bone architecture have the potential to provide new
532 and improved insight on many of these changes.

533

534 Here, the three-dimensional (3-D) architecture of cancellous bone was investigated in the
535 principal hindlimb bones of a variety of extinct, non-avian theropod and extant ground-dwelling
536 bird species. Investigation focused mainly on the direction of the cancellous bone fabric and how
537 this varies spatially throughout a given bone. The reasoning for this is threefold:

538 1. The direction of fabric alignment is one of the more telling aspects of cancellous bone
539 architecture in terms of identifying differences in locomotor behaviour and bone loading (e.g.,
540 Barak et al. 2011; Barak et al. 2013; Goldstein et al. 1991; Polk et al. 2008; Pontzer et al.
541 2006; Ryan & Ketcham 2005).

2. When considered across the whole bone, the 3-D pattern of fabric directions can be analysed within the framework of the trajectorial theory. This provides greater power to an analysis, because this facilitates direct, mechanistic comparisons of cancellous bone architecture to whole-bone loading, as will be done in Parts II (Bishop et al. in review-b) and III (Bishop et al. in review-c).
3. Fabric direction is probably more reliably assessed for fossil specimens, as opposed to other features such as bone volume fraction, trabecular thickness or trabecular spacing. Although these other architectural features can also be useful for interpreting locomotor biomechanics (Kivell 2016), their investigation requires excellent preservation of the entire fossil and very high resolution imaging, the latter of which is difficult (if not impossible) for large bones. So long as the gross structure is preserved and able to be imaged, fabric direction can be assessed.

The observations made for theropod limb bones were also compared to those for theropod outgroups (crocodilians and lizards), as well as the other extant obligate biped, humans, which have been very well characterised with respect to cancellous bone architecture and locomotor biomechanics.

The research presented here in Part I includes first and foremost a comprehensive assessment of the gross architectural patterns in the hindlimb bones of many different theropod species, which constitutes a completely novel dataset. In addition to laying the foundations for future studies, it will facilitate the identification of major patterns of similarity and difference between species and between groups. This in turn can elucidate how cancellous bone architecture may have evolved in theropods, and provide new and unique insight into theropod locomotor biomechanics. The manner of loading that is associated with cancellous bone architecture, and how this may reflect differences in posture, muscle control or gross loading regimes (e.g., bending- *versus* torsion-dominant), will form the subject of Parts II (Bishop et al. in review-b) and III (Bishop et al. in review-c).

I.3 Materials and Methods

The sampling and methods used in the present study are outlined in full below. In brief, this study acquired X-ray computed tomographic (CT) scans of the main bones of the hindlimb of a range of avian and non-avian theropods, as well as extant reptilian species and humans, and used a variety of image processing and analysis techniques to help characterise the architecture of cancellous bone in these elements. Approximately 1.45 TB of CT scan data was obtained for over 160 bones, representing at least 44 species (Table 1). Owing to various logistical constraints, these bones were scanned using a variety of machines at a variety of resolutions. This, coupled with the fossilization of many of the specimens, required a number of different image processing protocols to extract the structural data. Likewise, a number of different analytical approaches were used, some more quantitative than others, to identify the predominant architectural patterns present. For some of the quantitative data, statistical analyses were also conducted to test for correlations of certain architectural features with body size. The whole procedure of data processing and analysis, undertaken on two computers with ≥32 GB of memory and a 2.4 GHz processor each, took approximately six months to complete.

I.3.1 Data acquisition

This study focused on the main bones of the hindlimb, the femur, tibia (tibiotarsus[5]) and fibula, in a variety of extant avian and non-avian theropods, as well as extant reptilian species, crocodilians and lizards (Table 1; institutional abbreviations for museum specimens are also detailed here). In addition, data were collected for a representative human specimen, to provide further comparative context; this was an adult male specimen used for teaching purposes, which showed no apparent pathologies. A schematic illustration of the higher-level phylogenetic relationships of the study species is given in Fig. 8. Only primarily ground-dwelling species of birds were investigated because, by virtue of spending most or all of their time on the ground, they have well-developed hindlimb locomotor systems. Where possible, only male bird specimens were

[5] The terms tibia and tibiotarsus are used in a specific fashion throughout this study. 'Tibia' refers to the bony element *per se*, whereas 'tibiotarsus' refers to the functional unit of the tibia and proximal tarsals (astragalus and calcaneum). Thus, 'tibiotarsus' is only meaningful when used in reference to theropods, in which the three comprising bones are tightly integrated, and in adult birds they become fused. In the other groups of animals studied, the presence of a tibiotarsal joint precludes the use of this term. As such, cancellous bone architecture in the proximal tarsals of theropods was also investigated.

chosen, so as to preclude the possibility of medullary bone being present and influencing the results (Dacke et al. 1993; but see below). Crocodilians were chosen as they represent the closest extant outgroup of Theropoda. Varanids (monitor lizards) were chosen to represent squamates because most are highly terrestrial species, and their large size better facilitates analysis of cancellous bone architecture compared to smaller species. Generally, only one or two individuals were sampled for a given species. As this study is the first detailed survey of cancellous bone architecture in theropods, and more broadly, saurians, preference was given to maximizing the number of species investigated, rather than achieving a larger number of samples for fewer species, in order to elucidate any general, broad-scale patterns that were present. It was hence not possible to quantify potential intraspecific variation in bone architecture, nor was it possible to examine finer-scale patterns as may occur in association with more subtle differences in anatomy, behaviour or habitat.

The 3-D cancellous bone architectural data was acquired through CT scanning of the limb bones. Scanning parameters varied depending on the size and bulk density of the specimen and the locally available scanning machine (details given in Table 1). In all cases, the highest possible resolution and contrast between bone and non-bone phases was sought. Regarding the non-avian theropods, more than 40 additional fossil specimens (including of other species) were scanned throughout the course of this study, but owing to various factors (e.g., high density, low contrast between bone and matrix, mineral-induced scanning artefacts, insufficient scanning power or resolution) their resulting scans were not useful and thus excluded. In addition to the data collected in the present study, data collected by previous studies were also used (Doube et al. 2012; Farke & Alicea 2009).

I.3.2 Image data processing

The CT scans of each bone were processed using the software ImageJ 1.47 (http://imagej.nih.gov/ij/) and Mimics 17.0 (Materialize NV, Belgium), so as to segment the bone from the non-bone phases. All image processing was undertaken by a single person (PJB). Five

different image processing protocols were used, depending on ~~the nature of~~ the specimens and ~~the manner in which~~ they were scanned (Table 1):

I.3.2.1 Protocol 1 – extant animal micro-CT scans (~70 bones)

Scans were segmented using the local thresholding algorithm of Bernsen (1986), as implemented in ImageJ (Landini 2008; Landini et al. 2016). The window radius was set to a low value (typically on the order of 5 pixels), whilst the contrast threshold was set to a fairly high value (typically in the range of 20–50), so as to reduce the possibility of relatively high density non-bone material (e.g., dried marrow tissue) from becoming segmented along with the bone phase. The specific values for each parameter varied from specimen to specimen, and were chosen based on iterative visual comparison of the segmented *versus* unsegmented scans. Subsequent to image segmentation, the scans were 'cleaned' in Mimics with the 'region growing tool', which removed extraneous matter that was included in the segmentation but was not connected to the cancellous bone network. That is, this process removed isolated ('floating') voxels that were not connected to any adjacent voxels in three dimensions; since cancellous bone is always connected to other bone material, this step did not cause any loss of cancellous bone material (but did remove voxels pertaining to marrow tissue, for example).

One extant bird femur (*Gallus gallus*) was found to possess material that was possibly medullary bone; it was processed according to Protocol 1 but only for the femoral head region, where the unidentified material essentially filled all the intertrabecular space and thus was able to be effectively isolated from the cancellous bone. Only the femoral head region was subsequently analysed in this particular specimen.

I.3.2.2 Protocol 2 – extant animal medical CT scans (~35 bones)

This protocol differs from protocol 1 only in that an additional step was undertaken prior to segmentation. As these scans were acquired with a medical-grade machine, the original dataset

660 was comprised of anisotropic voxels (slice thickness differed from in-plane pixel resolution),
661 which is not ideal for further architectural analyses. Moreover, the scans had a markedly lower
662 resolution compared to the micro-CT scans. As a result, protocol 1 would not result in accurate
663 segmentation of the cancellous structure. To negotiate this problem, the scans were first
664 resampled to triple the original in-plane pixel resolution, and simultaneously resampled along the
665 axial direction to produce isotropic voxels. The axial resampling factor is given as $3f$, where

666 $$f = \frac{\text{slice thickness}}{\text{pixel resolution}}. \quad (1)$$

667 This was performed in ImageJ using 3-D bicubic interpolation, after which the scans were
668 processed according to protocol 1.
669
670 The above process of resampling the CT scans is simply to facilitate a more complete and
671 accurate extraction of cancellous bone, without altering the underlying structure in the scan data
672 (Fig. 9). Despite a relatively low resolution to the scans, each individual trabecula was still
673 visible to the naked eye, owing to the partial volume effect (Ketcham & Carlson 2001; Ryan &
674 Ketcham 2002b). Here, pixels with intermediate grey-values reflect a volumetric averaging of the
675 high grey-values of bone and the low grey-values of intertrabecular spaces, and are interpreted by
676 the observer as reflecting intertrabecular spaces. However, as these intermediate-valued pixels are
677 adjacent to high-valued (bone) pixels, they may not be recognized as reflecting non-bone material
678 by a local segmentation algorithm because of insufficient contrast, and so become included in the
679 segmented bone phase, producing an erroneous result. By resampling the CT scans to a higher
680 resolution, the underlying structure in the data is retained, but the number of pixels associated
681 with each phase (bone and non-bone) of each part of the structure is increased (Fig. 9C). This
682 increases the ability of a local thresholding algorithm to distinguish the two phases from each
683 other, as there is higher local contrast, resulting in a more accurate segmentation. Theoretically,
684 the greater the degree to which the scan is resampled, the higher the accuracy of the resulting
685 segmentation. However, there will be a limit to the degree of resampling, beyond which any
686 further information extracted is not genuine, and is artefactual; furthermore, greater resampling
687 produces larger scan datasets, increasing computational requirements for all successive steps in
688 image processing and analysis. Experience has shown that, with the current scan dataset at least,
689 a resampling factor of three was sufficient to achieve accurate segmentation.

690
691
692 I.3.2.3 Protocol 3 – human CT scans (3 bones)
693
694 The human bone scans were collected using peripheral quantitative CT scanning; as with the
695 medical CT scans, the resulting scans often comprised anisotropic voxels. Since the in-plane
696 resolution was always lower than the slice thickness (if the two were not equal), the scans were
697 first resampled in the in-plane directions using bicubic interpolation in ImageJ, resulting in an
698 isotropic image stack. Next, a low-radius 3-D median filter of kernel radius 2 or 3 pixels was
699 applied, again in ImageJ, to remove high-frequency noise in the data (Ollion et al. 2013). Finally,
700 the steps outlined in protocol 1 were followed.
701
702
703 I.3.2.4 Protocol 4 – non-avian theropod micro-CT scans (15 bones)
704
705 Owing to a maximum capable peak tube voltage of 80 kV in the machine used, the resulting
706 scans of the fossil bones suffered from both high-frequency (i.e., short wavelength) and low
707 frequency (i.e., long wavelength) background noise that overprinted the actual structure in the
708 images. The former was manifest as speckled, 'salt and pepper' patterns, whilst the latter
709 stemmed from scanning artefacts such as beam hardening (Ketcham & Carlson 2001) and
710 differences in bulk density throughout a specimen. These two sources of noise were removed in
711 ImageJ in the following manner, and the process is illustrated in Fig. 10. First, a low-radius 3-D
712 median filter was applied to the original image stack, removing the high frequency noise; the
713 kernel radius used varied between 2–10 pixels, depending on the specimen. Secondly, a large-
714 radius 2D median filter was successively applied to the original image stack in all three directions
715 (x, y and z), to isolate the low-frequency noise; the kernel radius used was large in comparison to
716 the trabecular thickness, and varied between 10–40 pixels, depending on the specimen. A single
717 application of a large-radius 3-D median filter could have been used instead to obtain the same
718 effect, but owing to the larger number of calculations required and large kernel radius, it was
719 prohibitively slow. The low-frequency filtered image stack was then subtracted from the high-
720 frequency filtered stack. That is, this process removes the high-frequency noise, and then

removes the background noise. Whilst the resulting image stack was devoid of noise and captured the structure in the data, it nevertheless was texturally 'rough'. Consequently, a low-radius 3-D mean filter, of kernel radius 2 or 3 pixels, was applied to remove this roughness. As this filter was of a high frequency compared to the structure itself, this step did not alter the structure in the data (e.g., trabeculae were not removed, connections did not disappear). Lastly, a global segmentation, with a high-pass grey-value threshold set to 1 or 2, was applied to extract the cancellous bone structure.

It is important to note that the above approach did not result in the total removal of matrix from the medullary cavity, because the filtering parameters were chosen based on the results for regions of the specimen entirely occupied by cancellous bone. This did not pose a problem to analysis, however, because the remaining noise was essentially random and isotropic, and thus easily distinguished visually from the cancellous bone structure elsewhere. It was therefore easy to avoid the medullary canal in the architectural analyses.

I.3.2.5 Protocol 5 – non-avian theropod medical CT scans (~30 bones)

As with the other set of medical CT scans, the scans of the fossil non-avian theropod bones comprised anisotropic voxels. Moreover, the resolution of the scans, and spatial variation in density and preservation quality, prohibited the proper segmentation of the cancellous bone. Consequently, the scans were resampled in the axial direction only, to produce isotropic voxels; they were not resampled to a higher resolution, as per protocol 2. This also meant that the cancellous bone architecture was only able to be analysed qualitatively. One exception to this was the CT scans of the *Masiakasaurus* femora collected by Farke & Alicea (2009). Owing to the relatively high scan resolution and good preservation of the fossil bones, these scans were able to be processed as per protocol 2, and were subjected to quantitative analyses.

I.3.3 Architectural analyses

Owing to the varied resolution and quality of the CT scans obtained, several analytical techniques were used. In their own way, each helped to identify the dominant architectural direction in a given region of cancellous bone, and how this varied throughout an entire bony element. Quantitative fabric analysis (Section I.3.3.1) was able to be conducted for scans of most of the extant animal bones, as well as the fossil specimens imaged using micro-CT scanning, that is, most scans that were processed as per protocols 1–4 above. Most of the non-avian theropod scans processed as per protocol 5 above were only able to be analysed in a qualitative fashion (Section I.3.3.2), as were the scans of extant birds obtained by Farke & Alicea (2009). A small proportion of scans processed according to protocol 1, pertaining to small bird bones, were also analysed qualitatively. A subset of the results from the quantitative analyses were also subject to additional analysis to obtain further insight into two key regions of the femur, the femoral head and medial condyle (Section I.3.3.3). Lastly, the architecture of diaphyseal cancellous bone in birds was analysed in a semi-quantitative fashion, via a categorical scoring method (Section I.3.3.4).

I.3.3.1 Quantitative analyses

Quantitative analyses of cancellous bone architecture were conducted using the software Quant3D 2.3 (Ketcham & Ryan 2004; Ryan & Ketcham 2002a; Ryan & Ketcham 2002b). The 3-D fabric tensor (Cowin 1986; see also Fig. 2) for a given volume of cancellous bone was calculated from the segmented CT scans using the star volume distribution method (Cruz-Orive et al. 1992; Odgaard 1997; Odgaard 2001). This is a stereological technique that expresses how cancellous bone material is distributed in three dimensions, and the results of this approach have previously been demonstrated to show strong correlation with cancellous bone mechanical properties (Kabel et al. 1999; Odgaard et al. 1997; Turner et al. 1990; Ulrich et al. 1999). To examine how the fabric varied spatially throughout a given bone, analyses were conducted on numerous (sometimes > 700) discrete volumes of cancellous bone; each volume of interest (VOI) was spherical in shape, to avoid corner effects. The diameter of the VOIs was typically 5 or more times the mean trabecular spacing for a specimen, which is sufficiently large for the continuum assumption of cancellous bone behaviour to hold (Cowin 2001; Harrigan et al. 1988), thus permitting the calculation of a fabric tensor.

782

783 The ~~VOI~~s were arranged in the geometric pattern of cubic close-packed spheres (Fig. 11). This
784 arrangement maximizes the volume of cancellous bone analysed, and as no overlap occurs
785 between adjacent spheres, each part of cancellous bone was analysed only once. Hence, unlike
786 the results of Saparin et al. (2011), the results for each VOI were independent of one another. The
787 close-packed pattern was generated in the computer- aided design software Rhinoceros 4.0
788 (McNeel, USA) and scaled and fitted to each specimen as appropriate. By altering the VOI
789 positions relative to the whole bone in some test specimens, it was found that the exact location
790 of the VOIs did not influence the overall results. That is, the fabric vector field changed gradually
791 enough throughout a bone such that the exact location of VOIs did not alter the results, and no
792 part of the pattern of change was missed. Great care was taken to ensure that peripheral VOIs
793 included at most only minimal amounts of cortical bone or the medullary cavity. This was
794 achieved by manually removing VOIs that did not fall into cancellous bone regions, using 3-D
795 geometric models of each specimen in Rhinoceros (Fig. 11). Post-analysis inspection revealed
796 that inadvertently including small amounts of cortical bone or medullary cavity did not alter the
797 overall results. In the fossil specimens, cracks or other regions of obvious deformation were
798 avoided (Bishop et al. 2017); they were identified and their geometry subsequently mapped out in
799 the CT scans using Mimics, and the resulting geometry was used to remove VOIs from analysis
800 in Rhinoceros (Fig. 11).

801

802 For each ~~VOI~~ in a specimen, measurements were made for 2049 uniformly distributed
803 orientations at 4,000 points within the bone phase, with random rotation and dense vector
804 sampling (Ketcham & Ryan 2004). These were batch processed in Quant3D, controlled using a
805 custom script in MATLAB 8.0 (MathWorks, Natick, USA). For each VOI, Quant3D calculated
806 the fabric tensor, of which the three principal directions ($\mathbf{u}_1$, primary; $\mathbf{u}_2$, secondary; $\mathbf{u}_3$, tertiary)
807 corresponded to the principal fabric directions of cancellous bone in that particular VOI (i.e., the
808 principal directions of alignment). Additionally, the eigenvalues of this tensor (e_1, e_2, e_3)
809 expressed the degree to which the cancellous bone was aligned to each of these principal
810 directions. These parameters that described the fabric tensor were extracted from the Quant3D
811 outputs for each VOI using a custom MATLAB script, and were plotted and visualized in 3-D

relative to the whole bone using another custom MATLAB script. The vector results were also further visualized and interrogated with respect to the whole bone in Rhinoceros.

I.3.3.2 Qualitative analyses

There were ~~a small number of~~ bird specimens ~~for which~~ the quantitative architectural analyses described above ~~could not~~ be implemented. ~~This was due to their small size, especially for the distal ends.~~ Specifically, their bones were so small, and the trabeculae spaced far enough apart, that no VOI could be placed in the bone which would span at least five intertrabecular lengths. That is, the continuum assumption of cancellous bone behaviour (Cowin 2001; Harrigan et al. 1988) would not hold, preventing a quantitative fabric analysis. For these specimens, cancellous bone architecture was qualitatively assessed by 3-D visualization of the segmented CT scans using isosurface and volume renderings in Mimics and ImageJ, facilitating visual assessment of the predominant orientation of trabeculae in the different regions of a bone. This approach was also used for the scans of extant bird bones collected by Farke & Alicea (2009), ~~due to the~~ relatively low resolution ~~of these scans~~ or high voxel anisotropy. Additionally, 3-D visualization was performed on other specimens where quantitative architectural analysis was possible, to provide further insight into their architecture. Importantly, this also demonstrated that the physical morphologies observed by 3-D visualization correlated with the fabric directions calculated via quantitative analyses: the dominant orientation of trabeculae as assessed visually largely coincided with the primary fabric direction.

For the non-avian theropod specimens imaged using medical CT scans, 3-D visualization and assessment of cancellous bone architecture used the Volume Viewer 2.0 plugin for ImageJ (Barthel 2006). This allowed real-time re-slicing and racking of a CT scan image stack in any orientation. Not only did this permit visualization of the scans from any direction, it also helped identify architectural features that were difficult to see in any single static slice, but which were revealed upon dynamic racking through successive slices. It also allowed for the identification of scanning artifacts (Ketcham & Carlson 2001), and hence these could be ignored from assessments of architectural patterns. Based on these visualizations, the observed patterns were

mapped onto whole-bone models via geometric representations of the dominant architectural patterns and directions, using a combination of spline curves and deformable surfaces in Rhinoceros. The accuracy of these geometric models was assessed through constructing multiple cutting planes through the model in different orientations, and comparing the cut model geometry to the CT slices in the same orientation. The geometric models were iteratively developed and refined as appropriate until good visual agreement between the scan data and the model was achieved. In using these geometric models, it is implicitly assumed that they accurately capture the dominant fabric directions in a given region of cancellous bone. All qualitative assessments were initially undertaken by a single person (PJB), with later conferral provided by the other authors.

I.3.3.3 Anatomically explicit analyses of femora

The architectural directions identified by the quantitative and qualitative analyses above were largely interpreted in a qualitative fashion, in the context of whole-bone general osteology and spatial variation in cancellous bone fabric (i.e., the nature of the vector fields). However, strict quantitative focus was also directed towards the primary fabric direction of cancellous bone in the femoral head and medial femoral condyle, referenced to an explicit anatomical coordinates system defined by osteological landmarks. As extant birds employ a subhorizontal femoral posture, while most, if not all, non-avian theropods have been hypothesized to have employed a subvertical femoral posture (e.g., Carrano 1998; Farlow et al. 2000; Gatesy 1991b; Gatesy et al. 2009; Hutchinson 2006; Hutchinson & Allen 2009), it is logical that this may be reflected in the architecture of cancellous bone in these two regions. This is because flexion of the hip joint determines the degree of femoral crouch, and flexion of the knee joint will vary with femoral crouch such that the feet remain underneath the whole-body COM (Hutchinson & Allen 2009). To assess this conjecture, the mean orientation of the primary fabric vector in the femoral head and medial femoral condyle was determined for each specimen (except for the crocodylians and varanids, which are sprawling quadrupeds) using a custom MATLAB script, by calculating the vectorial mean of the primary fabric vectors for all VOIs in the relevant region (Allmendinger et al. 2013). The mean fabric direction was then referenced in a bone anatomical coordinate system,

874 which was defined in a consistent manner across all species (Fig. 12). This anatomical coordinate
875 system was based on two spheres fitted to the distal condyles, calculated using 3-Matic 9.0
876 (Materialize NV, Belgium), and the principal axis of inertia of the whole bone, calculated for
877 surface mesh of the bone using Meshlab 1.3.3 (http://meshlab.sourceforge.net/). The *z*-axis was
878 defined by the principal axis of inertia (i.e., the long axis of the bone; +*z* is proximal); the *y*-axis
879 defined as the cross-product of the *z*-axis and the vector joining the centres of the two condyle
880 spheres (+*y* is anterior); and the *x*-axis defined as the cross-product of the *y*- and *z*-axes (+*x* is
881 lateral). The anatomically referenced mean fabric directions were then assessed using a
882 stereographic projection (stereoplot) of the data (Amson et al. 2017; Ryan & Ketcham 2005).
883
884
885 I.3.3.4 Diaphyseal cancellous bone analyses
886
887 In both the bird and reptile specimens investigated, a significant amount of cancellous bone was
888 frequently observed to encroach from the ends of the bone in to the diaphysis (shaft), in both the
889 femur and tibia. In the regions nearer the ends, the amount was sometimes sufficient enough that
890 quantitative fabric analyses could be undertaken, particularly in the bones of larger species.
891 Usually, however, too little cancellous bone was present to permit such quantitative analysis.
892 Nevertheless, throughout the course of 3-D visualization, these bones were observed to show a
893 variety of interesting patterns, and so an attempt was made to characterize the variation in
894 architectures in the bird bones, by categorical scoring.
895
896 Categorical scoring was performed by five independent, volunteer observers (non-scientists who
897 all had varying levels of experience with vertebrate anatomy), who were blind to the objectives of
898 the present study.They were asked to inspect 3-D isosurface models of each bone, derived from
899 the segmented CT scans, assess them for three features and score each bone on a pre-defined,
900 categorical scale for each feature. The first feature was the bulk spatial extent of cancellous bone
901 in the diaphysis, with scores assigned on a four-point scale: 0 = essentially the whole diaphysis
902 was void of cancellous bone, 1 = less than half of the diaphysis was occupied by cancellous bone,
903 2 = half or more than half of the diaphysis was occupied by cancellous bone, 3 = essentially the
904 whole diaphysis was occupied by cancellous bone. The second feature was the average

orientation of trabeculae with respect to the long axis of the shaft, with scores assigned on a nine-point scale of 10° increments (Fig. 13A): 0 = 0 to 10°, 1 = 10 to 20°, 2 = 20 to 30°, and so on. The third feature was the tendency of trabeculae to be closely associated with other trabeculae, with scores assigned on a three-point scale (Fig. 13B): 0 = trabeculae mostly or always occur singly, well separated from any other trabeculae; 1 = trabeculae occur in small groups of two or three other, similarly situated trabeculae; 2 = trabeculae mostly or always occur in close association with many other similarly situated trabeculae. If a given bone was scored as '0' for the first feature, then it was not scored for the second or third ('n/a').

Following scoring, the mean score across the five observers was taken for each bone and for each morphological feature. For the second and third features, a given bone was sometimes scored as 'n/a' (if the first feature was scored as a '0'), and other times it was given an actual numeric score. If there were more 'n/a' scores than numeric scores assigned for a given specimen, then the mean score was taken as 'n/a', and that particular specimen did not contribute towards further analyses (detailed below). However, if the majority of scores assigned were numeric, then the mean score was taken as the mean of those numeric scores.

I.3.4 Statistics

Three datasets were examined to test for a relationship between measured parameters and body size in birds: the anterior inclination of the mean fabric direction in the femoral head, the posterior inclination of the mean fabric direction in the medial femoral condyle, and the results of categorical scoring of diaphyseal cancellous bone. The length of the relevant bone was taken here as a proxy for body size, and was measured as the total proximal distance between articular condyles (interarticular length), excluding crests and trochanters. A relationship with body size would normally be assessed using a standard parametric test of the slope of a major axis regression (Warton et al. 2006). However, the data often exhibited non-normal distribution of errors (non-normal probablility plot) and heteroscedasticity (Breusch-Pagan test), as determined in PAST 3.09 (Hammer et al. 2001). As such, a parametric test could not be implemented.

Instead, a permutation test of the slope with 100,000 replicates was used, implemented in a custom MATLAB script (Legendre & Legendre 2012); the significance level was set at $p = 0.05$.

In addition, the reliability of the scorers in the analysis of diaphyseal cancellous bone was assessed using the intraclass correlation coefficient (ICC). This was calculated in PAST 3.09, using the ICC(2,*k*) model of (Shrout & Fleiss 1979), where *k* in this instance is 5.The higher the value of the ICC, the more reliable the scorers. The ICC was only able to be calculated for bones that had received numeric scores by all five scorers. Furthermore, for features 2 and 3 of the tibiotarsus, an ICC could not be calculated, because there was only one specimen in each set that had received a numeric score by all five scorers. That is, for every other specimen, at least one scorer had scored feature 1 as '0', and then assigned the 'n/a' score to the remaining two features.

I.4 Results

Since the architecture of cancellous bone in all but one of the species investigated here (humans) has never been studied before, the results of this study are first and foremost descriptive, characterizing the ~~qualitative nature of~~ the whole-bone architectural patterns. Where quantitative data was produced, it is presented where appropriate. The presentation of data and observations is organized primarily by each bone investigated: the femur in Section I.4.3.1, the tibia (tibiotarsus) in Section I.4.2 and the fibula in Section I.4.3. For each bone, results are presented in sequential order, first with humans and birds (extant bipeds), then extant reptiles (theropod outgroups) and finally the non-avian theropods. Overall, birds were quite consistent in their observed architectural patterns, across all species studied, and it is therefore convenient to treat all species together, with specific differences noted where appropriate. The observations for non-avian theropods are presented in approximate phylogenetic order (i.e., clades progressively closer to crown-group birds). Furthemore, the observations reported for a given group pertain to all specimens studied for that group, unless otherwise indicated. It should also be noted that since this study was undertaken, a recent re-evaluation of North American troodontid taxonomy has cast doubt on the validity of the name *Troodon formosus* (van der Reest & Currie 2017). As such,

965 the troodontid material investigated here will be referred to as 'Troodontidae sp.', pending further
966 study.
967
968
969 ***I.4.1 Femur***
970
971
972 I.4.1.1 General remarks
973
974 Observations for the single human femur studied are consistent with previously published reports
975 (e.g., Elke et al. 1995; Garden 1961; Koch 1917; Singh et al. 1970; Takechi 1977; Tobin 1955;
976 Townsley 1944; von Meyer 1867), supporting the use of this specimen as a general reference for
977 humans. Cancellous bone occurs throughout both proximal and distal ends, but the majority of
978 the diaphysis is devoid of it. However, cancellous bone is present deep to and in the immediate
979 vicinity of the lesser trochanter on the proximal shaft, which is distinct from and non-homologous
980 with the lesser trochanter of theropods.
981
982 Cancellous bone is more extensive in the birds and reptiles than humans. It usually encroaches
983 into the diaphysis to a varied, and often large, extent, although moving towards mid-shaft it tends
984 to become progressively more sparse and restricted to the endosteal margin of the cortex. A more
985 detailed treatment of diaphyseal cancellous bone is given below (Section I.4.4). Pneumatized bird
986 femora are distinctly more 'loose-packed' compared to marrow-filled bird femora; that is,
987 pneumatized bones have greater trabecular spacing, a distinction that exists in both small and
988 large species (Fig. 14). Despite the modulating effect that pneumatization has on trabecular
989 spacing, no effect on the patterns of fabric direction was evident.
990
991 Similar to humans, in non-avian theropod femora the proximal and distal ends are fully occupied
992 by cancellous bone, but the majority of the diaphysis remains empty. As with the human lesser
993 trochanter, cancellous bone also occurs locally deep to the fourth trochanter, although this was
994 only observed in the larger species, where the fourth trochanter is prominently developed (both
995 on account of bone size and phylogenetic position: Gatesy 1990; Hutchinson 2001a). In larger

femora, cancellous bone can encroach further into the diaphysis, with a limited number of thick trabeculae extending from the metaphysis along the endosteal surface. This encroachment is most extensive in *Tyrannosaurus* femora, although the middle third to half of the bone still remains free of trabeculae. It is likely that this size-dependency of diaphyseal encroachment by cancellous bone is purely a function of allometry: in longer femora, the ends are larger and the diaphysis is relatively shorter in length.

I.4.1.2 Proximal femur

In the human proximal femur, the primary fabric direction ($\mathbf{u}_1$) in the head is essentially proximodistally oriented, with a gentle anteromedial inclination of about 5° from the proximodistal axis, which grades into a stronger medial inclination in the distal (inferior) part of the femoral neck (Fig. 15A). This corresponds to the widely recognized 'primary compressive group' noted in previous studies of humans (see also Fig. 4A), as well as other primates (Rafferty 1998; Scherf 2008). In the region of the greater trochanter (which is distinct from and non-homologous with the greater trochanter of theropods), $\mathbf{u}_1$ largely parallels the lateral margin of the trochanter, corresponding to the 'greater trochanter group' of previous studies (Fig. 15A). Within the main part of the metaphysis, a double-arcuate pattern of $\mathbf{u}_1$ occurs in the coronal plane (or more accurately, the plane containing the shaft and femoral neck), where it arcs from opposite sides of the metaphysis to intersect in the middle. Moreover, the secondary fabric direction ($\mathbf{u}_2$) in this region is also largely contained within (parallel to) the coronal plane. This double-arcuate pattern corresponds to the 'secondary compressive' and 'secondary tensile' groups of previous studies (Fig. 15B). The orientation of $\mathbf{u}_1$ in the distal metaphysis, underneath the lesser trochanter and in the transition to the diaphysis is subparallel to the long-axis of the bone (Fig. 15C).

The proximal femur of birds shows the same general pattern irrespective of size. In the femoral head, $\mathbf{u}_1$ is mainly proximodistally oriented, but there tends to be a variable degree of anteromedial inclination superimposed upon this (Fig. 16A–D). The anterior component of this inclination is often quite pronounced, ranging up to 60° from the proximodistal axis. This anteromedial inclination continues down into the distal femoral neck as well. Under the facies

antitrochanterica, $\mathbf{u}_1$ is largely proximodistally oriented, but often there is also a gentle posteromedial inclination (Fig. 16E–I). This orientation continues towards the trochanteric crest, where the medial and posterior inclination often becomes more pronounced (Fig. 16J–N). However, in the anteriormost part of the trochanter, there can sometimes be no posterior inclination at all. Progressing distally down the metaphysis, beyond the distal level of the femoral head and into the diaphysis, the orientations of $\mathbf{u}_1$ become more 'disorganised': they take on a more oblique orientation relative to the long-axis of the bone, and the change in direction across the bone is no longer a gradual transition (Fig. 16O,P). No double-arcuate pattern of $\mathbf{u}_1$ and $\mathbf{u}_2$, as described above for the human femur, was observed in any bird specimen. Moreover, $\mathbf{u}_2$ is generally subparallel to the axial plane, and in large bones they are also parallel to the bone periphery, forming a concentric pattern. Progressing distally through the metaphysis, however, the orientations of $\mathbf{u}_2$ become more obliquely oriented and disorganized, as with the orientations $\mathbf{u}_1$. Although fabric orientation could not be extensively quantified in the smaller bird femora, visualization of isosurface and volume renderings of the bones themselves shows that for a given region, the trabeculae are oriented in the same general direction as the $\mathbf{u}_1$ for larger bird femora (Fig. 16I, N).

In the extant reptile femora examined, the orientation of $\mathbf{u}_1$ is subparallel to the long-axis of the bone throughout the metaphysis (Fig. 17A–D), except in the region of the fourth trochanter, where it is largely parallel to the long-axis of the trochanter itself (Fig. 17B,D). Leading up to the head region, $\mathbf{u}_1$ fans out, away from the metaphysis and towards the articular surface (Fig. 17A–D). In the distal metaphysis and transitioning to the diaphysis, the orientation of $\mathbf{u}_1$ progressively becomes more obliquely oriented and disorganized, in the same fashion as the bird femora (Fig. 17E).

Only limited information could be gleaned for the proximal femur of the small non-avian theropod *Masiakasaurus*, owing to the small size of the specimens. The orientation of $\mathbf{u}_1$ throughout the proximal end is more or less proximodistally directed, leading from the base of the femoral neck up to the apex of the head (Fig. 18). A gentle medial inclination from the proximodistal axis is present in most specimens.

The proximal femur of both *Allosaurus* and the tyrannosaurids show a strikingly similar pattern to that of humans (Fig. 19A–E). There is a well-developed tract of dense, cancellous bone extending from the base of the femoral neck up towards the apex of the head of the femur, much like the 'primary compressive group' of humans (Fig. 19A–E, maroon). As in humans, too, this tract has a gentle anterior inclination relative to the proximodistal axis (Fig. 19F). Additionally, a double-arcuate pattern is evident in the tyrannosaurids, also similar to the human pattern. The 3-D visualization of CT scans suggests that whilst this pattern is most developed in the coronal plane, it does extend out of that plane somewhat, with the 'sheets' of trabeculae being partially concentric with the bone's periphery (Fig. 19A–E, maroon and green). A second double-arcuate pattern is also present in the lesser trochanter, again subparallel to the coronal plane (Fig. 19A–E, turqoise and purple). A modest quantity of cancellous bone is present in the fourth trochanter, and the dominant direction is directed posteroproximally, parallel to the distal margin of the trochanter (Fig. 19A–E, blue). In the distal metaphysis all observed cancellous bone (and sometimes individual trabeculae) is oriented subparallel to the bone's long-axis; there is no indication of marked obliquity or disorganization as seen in the bird and reptile femora.

In the femoral head of ornithomimids, the most conspicuous feature is that $\mathbf{u}_1$ is oriented predominantly in an anteroposterior direction, yet $\mathbf{u}_2$ is oriented proximodistally with a gentle medial inclination (directed towards the apex of the head), much like the orientation of $\mathbf{u}_1$ in the femoral head of humans, birds and (presumably) *Allosaurus* and the tyrannosaurids (Fig. 20A–D). In fact, a generally proximodistal orientation of $\mathbf{u}_2$ and a generally anteroposterior orientation of $\mathbf{u}_1$ also occurs throughout much of the proximal end of the femur. Only around the anterior and posterior peripheries of the bone does $\mathbf{u}_1$ assume the more typical proximodistal orientation, with a medial inclination in the region of the femoral head and neck. It also assumes a more proximodistal orientation progressing towards the greater trochanter and distal end of the metaphysis, but in the latter region is still shows a marked level of 'disorganization' (Fig. 20E). Along the anterior part of the lesser trochanter, $\mathbf{u}_1$ is aligned more or less parallel with the anterior margin in a generally proximodistal fashion (Fig. 20F). Further posteriorly into the main body of the trochanter, however, it takes on a more mediolateral orientation, which gradually becomes more anteroposteriorly directed as the trochanter merges with the main body of the proximal femur.

The single caenagnathid femur examined exhibits a pattern very much like that in the ornithomimids. The only notable difference occurs in relation to the lesser trochanter, which has decreased in size and become more unified with the greater trochanter. Here, the fabric pattern is essentially a continuation of what occurs elsewhere in the head and metaphysis, with $\mathbf{u}_1$ becoming anteromedially oriented, but still subparallel to the axial plane (Fig. 20G). The orientation of $\mathbf{u}_2$ remains predominantly proximodistal, although a small posterior component is also present.

In the therizinosauroid *Falcarius*, the spatial pattern of the orientation of $\mathbf{u}_1$ is largely comparable to that observed in humans, throughout the whole proximal end of the femur, save the lesser trochanter. In the head, $\mathbf{u}_1$ has a slight anteromedial component superimposed over an otherwise predominantly proximodistal orientation, which is directed toward the apex (Fig. 21A). In the middle of the metaphysis, $\mathbf{u}_1$ exhibits a weakly developed double-arcuate pattern that is parallel to the coronal plane (Fig. 21A). Additionally, in the distal metaphysis $\mathbf{u}_1$ is largely subparallel to the long-axis of the bone, showing little 'disorganization' as seen in the birds. In the lesser trochanter, both $\mathbf{u}_1$ and $\mathbf{u}_2$ are largely contained within the coronal plane. Towards the base of the trochanter, $\mathbf{u}_1$ is generally oriented proximodistally, and $\mathbf{u}_2$ is generally oriented mediolaterally; however, nearer the apex, $\mathbf{u}_1$ is generally oriented mediolaterally, and $\mathbf{u}_2$ is generally oriented proximodistally (Fig. 21B,C). One distinct difference to the pattern observed in humans is the orientation of $\mathbf{u}_2$ in much of the proximal end; here, it is anteroposteriorly aligned, much like $\mathbf{u}_1$ in the ornithomimid femora (Fig. 21D).

In the proximal femur of Troodontidae sp., the orientation of $\mathbf{u}_1$ is predominantly proximodistal. Relative to the proximodistal axis, it assumes a gentle medial inclination as it courses from the base of the femoral neck up towards the apex of the head; within the head, it also takes on an anterior inclination (Fig. 21E,F). Under the region homologous with the facies antitrochanterica of birds, and in the region of the greater trochanter, $\mathbf{u}_1$ has a posteromedial component to its orientation (Fig. 21G,H). In the anterior part of the proximal femur, $\mathbf{u}_1$ is largely contained within the coronal plane, but shows little preferred orientation within that plane; $\mathbf{u}_2$ is not contained within the coronal plane, unlike in the homologous region of the femur of *Falcarius* (base of

lesser trochanter). In the region of the lesser trochanter, which is small and proximally located in Troodontidae sp., $\mathbf{u}_1$ tends to take on a more mediolateral orientation (Fig. 21I). Progressing more distally through the metaphysis, the orientation of $\mathbf{u}_1$ becomes more disorganized and oblique to the bone's long axis, as seen in the proximal femur of birds and reptiles (Fig. 21J). No double-arcuate pattern of any form, as observed in humans, *Allosaurus*, tyrannosaurids or *Falcarius*, was observed in Troodontidae sp.

The mean orientation of $\mathbf{u}_1$ in the femoral head for each specimen analysed is presented in Fig. 22A. The ornithomimid and caenagnathid specimens were not included in this analysis, owing to their distinct fabric architecture; additionally, the femoral head of the caenagnathid specimen was incomplete. A general orientation was taken to represent *Allosaurus* and the tyrannosaurids, based on the geometric model developed to represent their architectural patterns. In almost all specimens, the mean fabric direction is oriented anteromedially. The human and *Masiakasaurus* specimens plot close to the pole of the stereoplot, indicating that their mean directions are oriented almost purely proximodistally. The plot for *Falcarius* and the general *Allosaurus*–tyrannosaurid pattern is a little further from the pole (more medially directed), but still has little anterior inclination. The bird results demonstrate a sizeable degree of spread in the northwest quadrant of the plot, and indeed variability occurs within the species or genera for which multiple individuals were studied (Fig. 22B). However, on the whole, birds exhibit a substantial anterior inclination to the mean fabric direction; the mean direction across all birds is inclined 21.6° anterior of the proximodistal axis in the sagittal plane. Major axis regression of the bird data set revealed that the sagittal inclination of the mean fabric direction did not vary significantly with femur length (slope = 0.059, intercept = 58.4, $r^2 = 0.100$, $p = 0.108$). The mean primary fabric direction in Troodontidae sp. is of an intermediate orientation between that of birds and the other non-avian theropods, having an anterior inclination in the sagittal plane of 15.8°.

I.4.1.3 Distal femur

Throughout distal femur of the human specimen, $\mathbf{u}_1$ is predominantly oriented subparallel to the long axis of the bone. In the central part of the metaphysis, $\mathbf{u}_1$ exhibits a double-arcuate pattern in

both the sagittal and coronal planes, with the individual fabric vectors tending to arc from the periphery of the bone in towards the centre (Fig. 23A,B). However, this double-arcuate pattern is not as strongly developed as in the proximal femur. In both the medial and lateral condyles, $\mathbf{u}_1$ has a largely proximodistal orientation (Fig. 23C). Additionally, $\mathbf{u}_2$ is largely parallel to the axial plane, and two prominent tracts or trajectories are evident, one in each condyle (Fig. 23D). These tracts, noted in previous studies (e.g., Takechi 1977) arc from the anterior aspect of their respective condyle back towards the posterior aspect, and together they form a distinctive 'butterfly pattern'.

In birds, the distal femur exhibits a fairly consistent set of patterns across species. The orientation of $\mathbf{u}_1$ in the metaphysis is largely proximodistally oriented. In the central metaphysis of larger birds, for which substantial quantification of fabric direction was possible, $\mathbf{u}_1$ exhibits a moderately developed double-arcuate pattern in the sagittal plane between the medial and lateral condyles, much as in humans (Fig. 24A). Also as observed in humans, the orientation of $\mathbf{u}_2$ in the condyles forms a butterfly pattern in the axial plane, or more correctly, the plane that passes through the centres of the condyles (Fig. 24B–D). Unlike humans, however, the orientation of $\mathbf{u}_1$ in the condyles often has a marked posterior inclination relative to the proximodistal axis, although it generally remains subparallel to the sagittal plane (Fig. 24E–K). Moreover, $\mathbf{u}_1$ sweeps a distinctly wide arc in the sagittal plane (often in excess of 100°), such that in the posterior and posterodistal extremities of the condyles, $\mathbf{u}_1$ can be perpendicular to the proximodistal axis. In large birds, this sweeping can also extend into the anterior parts of the condyles, where $\mathbf{u}_1$ is anterodistally directed (Fig. 24F). In the condyles of small bird femora for which only limited quantitative analysis was possible, both $\mathbf{u}_1$ and $\mathbf{u}_2$ are subparallel to the sagittal plane, and $\mathbf{u}_1$ is inclined posteriorly. In small bird femora for which quantitative analysis was not possible, much of the distal end is typically occupied by a small number of large but sparsely dispersed trabeculae. They vary from rod- to plate-shaped, but generally are parallel to the sagittal plane (Fig. 24D,K). As with the proximal femur, progressing towards the proximal metaphysis and into the diaphysis reveals a more oblique and disorganized nature to the individual vectors (Fig. 24L).

In the distal femur of reptiles, the orientation of $\mathbf{u}_1$ in the metaphysis is largely subparallel to the long-axis of the bone. In some specimens $\mathbf{u}_1$ becomes more disorganized and obliquely oriented

relative to the bone's long axis progressing towards the diaphysis, but this is not as pronounced as compared to the proximal femur, or as compared to birds. The orientation of $\mathbf{u}_2$ in the condyles is largely parallel to the axial plane, and exhibits the butterfly pattern seen in birds and humans (Fig. 25A,B). The main point of difference from birds arises in the orientation of $\mathbf{u}_1$ in the condyles: whilst $\mathbf{u}_1$ is posteriorly inclined in the sagittal plane, it does not display the large anteroposterior sweeping that is often present in birds, sweeping at most about 40° (Fig. 25C–F).

As with the proximal femur, only limited information could be gleaned for the distal femur of *Masiakasaurus*. The orientation of $\mathbf{u}_1$ throughout the distal end is more or less proximodistally oriented, generally with a slight posterior inclination in the sagittal plane.

In the distal femur of the tyrannosaurids, cancellous bone around the periphery of the metaphysis is oriented subparallel to the long axis of the bone. Additionally, there are two sets of paired, arcuate, sheet-like tracts of cancellous bone, which arc largely in the coronal plane (Fig. 26). The obliquity of these sheet-like tracts appears to change across the bone, such that one set of tracts radiates from the 'patellar' or intercondylar groove at the anterior margin of the bone (Fig. 26, maroon and turquoise), and the other set radiates from the popliteal area at the posterior margin of the bone (Fig. 26, green and purple). This feature was not observed in the *Allosaurus* specimens studied, for insufficient CT scan contrast or resolution did not reveal any information about the metaphysis. In the medial and lateral condyles of both *Allosaurus* and the tyrannosaurids, the dominant direction of cancellous bone is largely parallel to the sagittal plane, and parallel to the long axes of the condyles, thus producing a butterfly pattern in axial cross-section. Within the sagittal plane, the dominant direction has a marked posterior inclination relative to the proximodistal axis; it also exhibits some amount of anteroposterior sweeping, about 30° or so (Fig. 26, red).

In both the ornithomimid and caenagnathid specimens, the orientation of $\mathbf{u}_1$ is predominantly oriented subparallel to the long axis of the bone throughout much of the distal femur, particularly anteriorly. In much of the medial and lateral condyles, $\mathbf{u}_1$ is largely parallel to the sagittal plane and gently inclined posteriorly (Fig. 27A–D); anteroposterior sweeping in the sagittal plane is limited to about 20°. However, in the posterior parts of both condyles, the posterodistal

orientation gradually changes to become nearly perpendicular to the long-axis of the bone, and almost perpendicular to the local bone surface around the intercondylar sulcus (Fig. 27A–D, yellow). That is, in the posterior parts of the condyles, $\mathbf{u}_1$ appears to radiate away from the intercondylar sulcus, largely within the axial plane (Fig. 27E). In these regions, $\mathbf{u}_2$ is oriented largely proximodistally in the sagittal plane, but elsewhere in the condyles $\mathbf{u}_2$ forms the butterfly pattern observed in all other groups (Fig. 27F).

~~Owing to pervasive fracturing in~~ the central part of the *Falcarius* distal femur studied (UMNH VP 12360), little can be said concerning the metaphysis~~,~~ except that along the medial and lateral peripheries $\mathbf{u}_1$ is oriented largely parallel to the long axis of the bone. In both medial and lateral condyles, the orientation of $\mathbf{u}_1$ is gently inclined posteriorly and subparallel to the sagittal plane, with little anteroposterior sweeping evident (Fig. 28A,B). The orientation of $\mathbf{u}_2$ in the condyles is subparallel to the axial plane, and forms a typical butterfly pattern.

Throughout much of the distal femur of Troodontidae sp., the orientation of $\mathbf{u}_1$ is subparallel to the long-axis of the bone, although in the proximal metaphysis it tends to become more obliquely oriented and disorganized, as seen in birds (Fig. 28C). No indication of any arcing patterns in $\mathbf{u}_1$, as observed in humans and birds, was observed. Moreover, the radiating patterns (originating from the intercondylar sulcus) that were observed in the tyrannosaurids, ornithomimids and caenagnathid are not evident either. The orientation of $\mathbf{u}_1$ in the condyles is subparallel to the sagittal plane and gently inclined posteriorly (Fig. 28D,E); as in *Falcarius*, little anteroposterior sweeping is apparent. As with all other groups, $\mathbf{u}_2$ in the condyles is subparallel to the axial plane and forms a butterfly pattern (Fig. 28F).

The mean orientation of $\mathbf{u}_1$ in the medial femoral condyle for each specimen analysed is presented in Fig. 29A. Note that some of the smallest bird femora could not be analysed here, because they possessed too little cancellous bone to facilitate a quantitative analysis. As for the femoral head, a general orientation was taken to represent *Allosaurus* and the tyrannosaurids. In most specimens, the mean fabric direction is oriented posteriorly, with a small medial inclination. The human and *Masiakasaurus* specimens again plot close to the pole of the stereoplot, indicating an almost proximodistal mean direction. The plots for the ornithomimid, caenagnathid,

Falcarius and Troodontidae sp. are slightly further from the pole, and the general *Allosaurus*–tyrannosaurid pattern is a little further away again. As in the femoral head, the bird results demonstrate marked variation, although on the whole a substantial posterior inclination is present; the mean direction across all birds is inclined 24.7° posterior of the proximodistal axis in the sagittal plane. Furthermore, the mean primary fabric direction in smaller birds tends to be more posteriorly inclined in the sagittal plane compared to that in larger birds, as indicated by major axis regression (Fig. 29B).

I.4.2 Tibia or tibiotarsus

I.4.2.1 General remarks

As with the femur, observations for the single human tibia studied are comparable with previously published reports (e.g., Takechi 1977; von Meyer 1867), again supporting the use of this specimen as a general reference for humans. Cancellous bone is present throughout the entirety of both proximal and distal ends; a small amount also extends well into the diaphysis along the endocortical margin, but is mostly only one or two trabeculae thick (see Section I.4.4).

Cancellous bone is again generally more extensive in the birds and reptiles compared to humans, at least in the larger species. It usually encroaches into the diaphysis to a varied extent, although moving towards mid-shaft it becomes more sparse and restricted to the endosteal margin of the cortex. Compared to the femur, the tibiotarsus of birds is generally less invaded by cancellous bone; this is especially true of the smaller species. Indeed, in some of the smaller species of birds, the medullary cavity extends well into the proximal and distal ends, to the point that only a handful of large, well-spaced trabeculae remain, with many smaller trabeculae distributed around the periphery. There is virtually no cancellous bone under the tibiofibular crest in birds, regardless of body size. Rather, the crest mostly comprises thickened (but higher porosity) cortical bone. In those birds with a prominent tibiofibular crest (e.g., *Porphyrio*, *Gallinula*, *Ardeotis*, *Threskiornis*), some cancellous bone does exist, but trabeculae are still few in number.

Owing to logistical constraints, the tibia and proximal tarsals of non-avian theropods were not investigated as thoroughly as they were for the femur. In those specimens that were studied, the proximal and distal ends of the tibia are fully occupied by cancellous bone (as is the entirety of the astragalus and calcaneum), but the majority of the diaphysis remains empty. Proximally, cancellous bone encroaches as far distally as the beginning of the tibiofibular crest; distally, cancellous bone usually does not occur any further proximally than the point at which the tibia begins to flare out mediolaterally. In the large tyrannosaurids, however, the distal diaphysis contains a significant amount of cancellous bone proximal to the point of mediolateral widening, which is again probably an effect of allometry. Cancellous bone is also present under the tibiofibular crest for its entire length, with more being present in the larger species.

I.4.2.2 Proximal tibia

In the human proximal tibia, $\mathbf{u}_1$ is more or less proximodistally oriented throughout the entire end. Under the medial and lateral tibial condyles it has a slight (approximately 10°) posterior inclination relative to the proximodistal axis, and under the medial condyle there is also a slight medial component (Fig. 30). As with the femur of humans, in the distal metaphysis and transition into the diaphysis $\mathbf{u}_1$ remains proximodistally oriented, with little disorganization or obliquity.

In birds, the orientation of $\mathbf{u}_1$ throughout the proximal tibia is predominantly proximodistal, but there are marked departures from this locally throughout the bone. In the anterior cnemial crest, $\mathbf{u}_1$ has an anteroproximal inclination (Fig. 31A,B), which is much the same in the lateral cnemial crest, although a variable lateral component may also be present (Fig. 31C,D). In the thinnest parts of the crests where fabric was unable to be quantified, as well as in the cnemial crests of smaller bird tibiae, 3-D visualization of the CT scan data demonstrates that the individual trabeculae tend to maintain this general orientation, essentially following the anterior margins of the crests (Fig. 31E,F). Under the medial articular condyle, $\mathbf{u}_1$ projects proximally, up and away from the metaphyseal cortex and arcs posteriorly towards the articular surface, generally remaining subparallel to the sagittal plane (Fig. 31G–K). Immediately under the articular surface,

$\mathbf{u}_1$ has a posterior inclination of about 20–30° to the proximodistal of the bone. A similar pattern occurs for $\mathbf{u}_1$ under the lateral articular condyle, although there is also a strong lateral component to the inclination; sometimes the amount of lateral inclination exceeds the amount of posterior inclination (Fig. 31L–P). In the central part of the metaphysis, there is sometimes a double-arcuate pattern in $\mathbf{u}_1$ parallel to the sagittal plane; one 'tract' arcs from the posterior metaphysis to the cnemial crests, the other arcs from the anterior aspect towards the articular condyles (Fig. 31Q). Notably, this pattern was not observed in all specimens examined, not even in all specimens of the same species. Furthermore, the orientation of $\mathbf{u}_2$ is not constrained to being subparallel to the plane of the arcing, as is the case in the human proximal femur. Progressing distally through the tibial metaphysis and into the diaphysis brings about increased obliquity and disorganization to the orientation of $\mathbf{u}_1$ (Fig. 31R). Fabric orientation could not be extensively quantified in the tibiotarsus of many of the smaller bird bones (or even at all in the smallest ones). Nevertheless, 3-D visualization of the trabeculae themselves reveals that, in the regions of the cnemial crests and articular condyles, they tend to be oriented in the same general direction as $\mathbf{u}_1$ in the larger bird specimens (Fig. 31E,F,K,P). In the smallest species (e.g., *Coturnix chinensis*), there are hardly any trabeculae at all in the entire proximal end, with the medullary cavity extending almost to the proximal cortical surface. Additionally, little room for trabeculae exits in the cnemial crests between the two opposing cortices: the crests are either devoid of trabeculae, or there are very small trabeculae acting as spacers in a 'sandwich structure' (Currey 2002).

In the reptiles examined, $\mathbf{u}_1$ is generally oriented proximodistally throughout the entire proximal tibia, although it fans out proximally, away from the middle of the bone towards the articular surfaces (Fig. 32). There does not appear to be any appreciable increase in the degree of obliquity and disorganization of $\mathbf{u}_1$ in the more distal parts of the metaphysis, as observed in the femur.

The proximal tibiae of both *Allosaurus* and the tyrannosaurids again show similar patterns to each other, as with the femur. Under the medial condyle, strongly developed tracts of cancellous bone are parallel to the sagittal plane and gently inclined posteriorly relative to the proximodistal axis (by 5–10°); they also have a gentle lateral inclination as well (Fig. 33A,B). This continues into the region of the lateral condyle, but here the tracts assume a more marked lateral inclination, similar to the pattern described above for $\mathbf{u}_1$ in the birds (Fig. 33B,C). In the cnemial crest, the

dominant direction of cancellous bone is largely parallel to the anterior margin of the crest, and is oriented proximoanterolaterally, again similar to the pattern described above for $\mathbf{u}_1$ in the birds. In axial cross-section, the cancellous bone actually forms concentric, proximodistally oriented 'sheets' that are parallel to the external surface of the cnemial crest (Fig. 33D–J). Further posteriorly, towards the base of the cnemial crest, these sheet-like tracts become progressively more posteriorly inclined, directed toward the metaphysis. In the central metaphyseal region, a double-arcuate pattern is present, which roughly parallels the sagittal plane, where one set of tracts arcs up from the posterior periphery towards the cnemial crest (Fig. 33D–J, purple and turqoise), and the other set of curved sheets arcs up from the anterior periphery towards the articular condyles (Fig. 33D–J, green and maroon). Furthermore, 3-D visualization indicates that these tracts are curved, more or less concentric with the bone margins. Progressing proximally, the anterior and posterior sets of tracts gradually change inclination to merge with the tracts in the regions of the cnemial crest and articular condyles, respectively. The tyrannosaurids provide a few further details on cancellous bone in the proximal tibia, owing to better contrast in their CT scans compared to those of *Allosaurus*. Firstly, in the (incipient) lateral cnemial crest, cancellous bone is oriented parallel to the margin of the adjacent part of the main (anterior) cnemial crest (Fig. 33D–J, yellow) Secondly, in the fibular crest the cancellous bone forms a double-arcuate pattern parallel to the axis of the crest (Fig. 33D–J, red and orange); these arcs intersect proximally, and proximally they also curve inwards towards the diaphysis. Thirdly, there is no indication in the distal metaphysis that cancellous bone is anything but oriented parallel to the long axis of the bone.

In the single proximal ornithomimid tibia that was studied (TMP 93.066.0002), the region of the lateral condyle was characterized by a tract of cancellous bone with a slight posterolateral inclination, superimposed on an otherwise proximodistal orientation. This is comparable to the pattern ~~just described for~~ *Allosaurus* and the tyrannosaurs.

The proximal tibia of Troodontidae sp. largely shows the same general patterns for $\mathbf{u}_1$ as described in the birds. Under the medial and lateral condyles, $\mathbf{u}_1$ exhibits a gentle posterior inclination superimposed on an otherwise proximodistal alignment (Fig. 34A–D). However, only a slight lateral inclination occurs under the lateral condyle, in contrast to the often marked lateral

inclination observed in birds, as well as *Allosaurus* and the tyrannosaurids. In the cnemial crest, $\mathbf{u}_1$ is again oriented largely parallel to the anterior margin of the crest, inclined proximoanteriorly (Fig. 34E,F). This pattern is also present in the cnemial crest of *Saurornitholestes* (Fig. 34G). Throughout the metaphysis of Troodontidae sp., the orientation of $\mathbf{u}_1$ is largely proximodistal; a weakly developed double-arcuate pattern, parallel to the sagittal plane, is present in one specimen examined, but not the other (Fig. 34H). This is similar to the large birds studied, where only some specimens exhibited a comparable double-arcuate pattern.

I.4.2.3 Distal tibia or tibiotarsus

In the human distal tibia, $\mathbf{u}_1$ is largely proximodistally oriented throughout the entire bone. However, throughout most of the metaphysis, $\mathbf{u}_1$ has a slight (10° or so) inclination relative to the proximodistal axis towards the centreline of the bone, forming a conical pattern with the cone's apex pointing distally (Fig. 35A,B). The orientation of $\mathbf{u}_2$ is generally parallel to the axial plane; it has no orientation preference except in the periphery where it is generally subparallel to the local bone surface, forming a roughly concentric pattern (Fig. 35C).

The distal tibiotarsus of birds shows a very characteristic pattern regardless of size (Fig. 36). By and large, $\mathbf{u}_1$ is oriented proximodistally and parallel to the sagittal plane throughout the whole distal end of the bone. In large birds for which substantial quantification of fabric was possible, $\mathbf{u}_2$ is oriented more or less anteroposteriorly throughout most of the tibiotarsus, in stark contrast to the human pattern, although it can become more parallel to the bone margin towards the periphery (Fig. 36A–E). Within the condyles, $\mathbf{u}_1$ and $\mathbf{u}_2$ can also become 'rotated' within the sagittal plane to a variable degree. This distinctive pattern reflects the highly anisotropic and plate-like nature of the trabeculae (parallel to the sagittal plane) in this region of the bone, as evident in 3-D visualizations (Fig. 36F–H). In many of the smaller bird species, there was too little cancellous bone (too few trabeculae spaced too far apart) to permit an extensive quantitative fabric analysis, or any analysis at all in the smallest specimens. Nonetheless, 3-D visualization clearly shows that most of the distal tibiotarsus in these species is dominated by relatively large, usually plate-like trabeculae that are oriented more or less parallel to the sagittal plane,

qualitatively similar to the architecture observed in larger specimens (Fig. 36F–H). For those species in which fabric analysis was possible to some degree, the general pattern in $\mathbf{u}_1$ and $\mathbf{u}_2$ observed for larger birds was also observed here.

In the distal tibia of reptiles, $\mathbf{u}_1$ is predominantly oriented proximodistally, although in the varanids it also takes on a posterior inclination throughout much of the metaphysis (Fig. 37A–C). Distally, $\mathbf{u}_1$ tends to fan out towards the articular surface, much in the fashion as described for the proximal tibia. Similar to the human pattern, but unlike the birds, $\mathbf{u}_2$ is subparallel to the axial plane and largely concentric with the margins of the bone (Fig. 37D).

The distal tibia of both *Allosaurus* and the tyrannosaurids examined presents an intriguing cancellous bone architecture (Fig. 38A–G). In the axial plane, it is manifest as a two sets of double-arcuate patterns that are largely parallel to the margins of the bone (Fig. 38D, inset), yet in both the sagittal and coronal planes it is manifest as a more typical double-arcuate pattern, with the arcs from opposing sides of the bone intersecting distally. In three dimensions, this produces a set of 'Gothic arches' (Garden 1961). More distally, these arches progressively open up and become more distally directed, and the sheet-like tracts of cancellous bone become somewhat more anteroposteriorly oriented. They also start to fan away from the centreline of the bone, such that in the distal extremity of the tibia they are oriented medially on the medial side of the bone and are oriented laterally on the lateral side of the bone. Despite this opening up of the arches, a concentric pattern in the axial plane is somewhat retained. Within the astragalus and calcaneum, cancellous bone is only present in considerable quantities in the regions of the articular condyles. Here, the architecture is relatively simple, being strongly aligned in both the anteroposterior and proximodistal directions, paralleling the pattern for $\mathbf{u}_1$ and $\mathbf{u}_2$ in birds (Fig. 38H–J). This pattern also occurs in the fused astragalocalcaneum of *Ceratosaurus nasicornis* (UMNH VP 5278). Progressing distally, it also fans out and away slightly from the centreline. Unlike in the distalmost tibia, there is no indication of a concentric pattern of cancellous bone in the axial plane.

In contrast to the complex architectural patterns observed in ~~more plesiomorphic~~ theropods, the architecture in the distal tibia of Troodontidae sp. and *Saurornitholestes* is relatively simple (Fig.

39). The orientation of $\mathbf{u}_1$ throughout the distal tibia is largely subparallel to the proximodistal axis, and $\mathbf{u}_2$ is largely contained in the axial plane and aligned anteroposteriorly (except around the periphery), much like birds. Furthermore, 3-D visualization reveals that the cancellous bone architecture is dominated by plate-like trabeculae that are oriented more or less parallel to the sagittal plane, also like birds (Fig. 39C). Within the astragalus and calcaneum of Troodontidae sp., $\mathbf{u}_1$ and $\mathbf{u}_2$ become somewhat more disorganized, but importantly they largely remain parallel to sagittal plane. Thus, whilst the architecture of the distal tibia is decidedly different to that in the more plesiomorphic theropods examined, the architecture of the proximal tarsals is quite similar, as it is in birds.

I.4.3 Fibula

In humans, $\mathbf{u}_1$ is oriented proximodistally throughout the proximal and distal ends of the fibula (Fig. 40A,B). The same general pattern is also present in the reptiles examined, although $\mathbf{u}_1$ often fans out and away from the centerline leading towards the articular surfaces (Fig. 40C–F).

In all bird fibulae for which quantitative architectural analysis was possible, $\mathbf{u}_1$ is consistently oriented throughout the whole head, directed posteroproximally from the long-axis of the bone and subparallel to the local bone margin (Fig. 40G–I). In those specimens for which quantitative analysis was not possible, 3-D visualization revealed that the trabeculae themselves followed a similar orientation (Fig. 40J,K). There are typically very few trabeculae under the iliofibularis tubercle, even in the large birds, and none in the distal end, which is reduced to a splint of thin cortical bone.

In the fibular head of *Allosaurus* and the tyrannosaurids, as well as an indeterminate ornithomimid (TMP 2006.012.0065), cancellous bone is largely proximodistally orientated. It gently fans out away from the centreline of the bone in the sagittal plane, paralleling the anterior and posterior margins of the head and leading up towards the articular surface (Fig. 40L,M). In the distal fibula, the dominant architectural direction is largely parallel to the local centerline of the bone, and progressing distally this acquires a gentle lateral inclination (Fig. 40L,M). The

proximal fibula of Troodontidae sp. exhibited a pattern in $\mathbf{u}_1$ that was comparable to that observed in the other theropods examined (Fig. 40N); the distal end of the Troodontidae sp. fibula that was studied was not preserved.

I.4.4 Diaphyses

As noted above, the diaphysis of birds and reptiles often contains a significant quantity of cancellous bone, in both the femur and tibia. In bird femora, and to a lesser extent the tibia, the most conspicuous feature of this diaphyseal cancellous bone is the abundant trabeculae that are obliquely oriented relative to the long-axis of the bone, typically by 45° or more (Fig. 41). These trabeculae vary in individual form, displaying a range of rod-like to plate-like morphologies. They also vary in the degree to which they are connected to the adjacent cortex, ranging from being tightly appressed to the cortex (appearing little more than large 'wrinkles' in the endosteal surface), to being well separated from the cortex except at their ends, and arcing across the medullary cavity. When considered across the diaphysis as a whole, these oblique trabeculae tend to form conjugate helices that spiral along the endosteal margin of the cortex, especially in the bones of larger species (Fig. 41A,D,I). Markedly oblique trabeculae are also often present in the diaphysis of the reptile femora and tibiae examined, although they are not usually as abundant compared to the birds.

The results of the categorical scoring analyses of cancellous bone architecture in bird femora and tibiotarsi are presented in Table 2 and Fig. 42. The intraclass correlation coefficient (ICC) was relatively high for most features (0.46–0.85), suggesting that the assessments made by the five volunteers are reliable. In both the femur and tibiotarsus, the extent to which the diaphysis is occupied by cancellous bone (feature 1) tends to increase in larger bones, although in the tibiotarsus the increase is only really noticeable for the largest birds (Fig. 42A,B). The average orientation of the trabeculae relative to the long axis (feature 2) also changes with size in the

femur (Fig. 42C), but not the tibiotarsus (Fig. 42D). In the femur, it increases from approximately 45–50° in the largest birds to around 70° or more in the smallest birds. The average degree of association of trabeculae with other trabeculae (feature 3) appears to increase in larger femora and tibiotarsi (Fig. 42E,F); however, the results were not statistically significant. Thus, generally speaking, as bird femora get smaller, they become occupied by progressively less cancellous bone, the individual trabeculae of which are fewer in number and more widely spaced, and which have a more perpendicular orientation to the long axis of the bone. Additionally, as bird tibiotarsi get smaller, they also become occupied by progressively less cancellous bone, but the ~~nature~~ of individual trabeculae does not appear to change significantly.

Investigation of the human bones in this study revealed that a small amount of cancellous bone occurs along the endosteal surface of much of the tibial diaphysis. Whilst of insufficient quantity for quantitative fabric analysis, it is noteworthy that near the middle of the diaphysis, the cancellous bone architecture is dominated by trabeculae (or endosteal 'wrinkles') that are obliquely oriented, by about 10–20° to the long-axis of the bone (Fig. 43). Thus, some degree of similarity is present between the diaphyseal cancellous bone of humans and birds.

I.5 Discussion

This study had two primary objectives, first of which was the broad-scale comparative assessment of cancellous bone architecture in the main hindlimb bones of avian and non-avian theropods, as well as in humans and some large extant reptiles. This comparative assessment focused on the gross architectural features across the whole bone, and used both quantitative and qualitative observations. The second main objective of the study was to draw upon the comparative assessment to identify patterns of similarity and contrast between the different groups examined, which may be used to provide insight into bone loading and locomotor biomechanics.

I.5.1 Overarching patterns across taxa

Despite great differences in size, and to a lesser degree, phylogenetic heritage, all birds investigated showed largely consistent cancellous bone architecture for a given region of a given bone. The patterns illustrated by birds were often in stark contrast to that exhibited by humans. The extant reptiles examined (varanid lizards and crocodilians) were also largely consistent in their observed architectural patterns across taxa, and typically showed greater similarity to the architectural patterns of birds than humans.

Among non-avian theropods, there are a number of different patterns of cancellous bone architecture in the femur. In the non-maniraptoriform theropods examined (*Masiakasaurus*, *Allosaurus* and tyrannosaurids), the femur showed marked similarity to the architecture observed in humans. In the proximal end, a pronounced double-arcuate pattern occurs in the coronal plane (visible in the tyrannosaurid specimens), and the primary fabric direction of cancellous bone ($\mathbf{u}_1$) in the femoral head had little anterior inclination, much like humans but unlike birds. In the distal femur, the primary architectural direction in the condyles did not have the often large posterior inclination as observed in birds, but it was often still greater than in humans. Additionally, the primary architectural direction in the condyles did not show the large amount of anteroposterior sweeping as observed in birds. The derived non-avian theropod Troodontidae sp. had a femoral architecture more closely resembling that of birds than most other non-avian theropods examined: no coronal plane double-arcuate pattern was present, $\mathbf{u}_1$ in the femoral head had a significant anterior inclination, and in the diaphysis-ward parts of the metaphysis the primary fabric vectors were disorganized and often oblique to the long-axis of the bone. This latter feature, ubiquitous in the femora and tibiae of birds and reptiles, is interpreted to reflect the onset of markedly oblique trabecular spirals in the diaphysis (see Section I.5.3).

The ornithomimid and caenagnathid femora examined illustrated a distinct and intriguing pattern in the proximal end that was not observed in any extant groups studied. Most conspicuously, $\mathbf{u}_1$ was oriented predominantly in an anteroposterior direction, with the secondary fabric direction ($\mathbf{u}_2$) oriented more or less proximodistally. Additionally, $\mathbf{u}_1$ tended to exhibit some significant amount of obliquity and disorganization in the diaphysis-ward parts of the proximal and distal metaphyses, and in this respect was comparable to the pattern observed in birds and reptiles. The

femur of the basal therizinosauroid *Falcarius* shows some similarity to the ornithomimid and caenagnathid pattern in that the orientation of $\mathbf{u}_2$ in the central metaphysis and head was anteroposteriorly aligned, much like $\mathbf{u}_1$ in the ornithomimid femora. This is unlike the pattern observed in humans, or expected in *Allosaurus* and the tyrannosaurids based on the observed architectural patterns. However, the orientation of $\mathbf{u}_1$ in the diaphysis-ward parts of the proximal and distal metaphyses of *Falcarius* tended to be organized and subparallel to the long-axis of the bone, more comparable to humans and more plesiomorphic theropods. Distally, the femoral condyles of the ornithomimids, caenagnathid and *Falcarius* all had a gentle posterior inclination to the direction of $\mathbf{u}_1$, with little anteroposterior sweeping of the fabric, more like that in humans than birds.

The proximal tibia and fibula of the non-avian theropods showed a largely consistent architectural pattern, although it is acknowledged that these bones were not as extensively sampled as the femur. The architecture of the proximal tibia was quite comparable to that of birds, in both the cnemial crests and underneath the articular regions. A double-arcuate pattern, parallel to the sagittal plane, is present in the proximal end of the tibia of the large non-avian species, but is only occasionally present in Troodontidae sp. and large birds.

Cancellous bone architecture in the proximal tarsals (astragalus and calcaneum) was broadly comparable across all theropods examined, both avian and non-avian, being dominated by a strong anteroposterior-proximodistal alignment. In contrast, two distinctly different architectures were observed in the distal tibia (in non-avian theropods) or tibial component of the tibiotarsus (in birds). In the large non-maniraptoriform theropods (*Allosaurus* and tyrannosaurids), the distal tibia exhibited a complex double set of double-arcuate patterns, parallel to both the sagittal and coronal planes. In Troodontidae sp., *Saurornitholestes* and birds, however, the architecture was very much a continuation of that observed in the proximal tarsals, with a relatively simple pattern of anteroposterior-proximodistal alignment of $\mathbf{u}_1$ and $\mathbf{u}_2$.

Taken together, the various architectural patterns observed in the various bones of the non-avian theropods show a general correspondence with their phylogenetic relationships. The ~~more plesiomorphic theropods investigated~~ tended to possess architectures that were more broadly

comparable, and sometimes strikingly similar, to those in humans. In contrast, the paravians Troodontidae sp. and *Saurornitholestes* (as far as can be observed) possessed architectures more comparable to those of extant birds. Intriguingly, of all the non-avian theropods examined, *Allosaurus* and the tyrannosaurids had the greatest degree of posterior inclination in the fabric of the femoral condyles, most like birds. A further point of interest concerns the ornithomimid and caenagnathid specimens. Their femoral architectural patterns were similar to each other but distinctly different to those in other theropods studied, yet Ornithomimosauria and Oviraptorosauria are not thought to be each other's closest relatives, nor are they successively more derived nodes in theropod phylogeny (Zanno et al. 2009; Fig. 8). Thus, if taken at face value, the present set of observations suggest some amount of convergence in cancellous bone architectures, and by inference mechanical loading, between the two groups, or alternatively a reversion to a more plesiomorphic (tyrannosaurid-like) architecture in early therizinosaurs. Neither scenario can be tested until further specimens, of more species and more individuals of each species, are examined.

I.5.2 Biomechanical implications

As noted above, birds and humans demonstrate many distinct differences in cancellous bone architecture throughout their hindlimb bones. This was to be expected, since they exhibit very different bipedal locomotor biomechanics. Here, an attempt is made to correlate the salient differences in architectural patterns and biomechanics, and use these inferences to provide insight into the hindlimb locomotor biomechanics of the non-avian theropods studied.

I.5.2.1 Femoral head

The mean orientation of $\mathbf{u}_1$ in the femoral head of the human specimen had only a very small anterior inclination, whilst in birds the inclination was on the whole far more pronounced (Fig. 22A). This is interpreted to reflect the stark difference in femoral posture between humans and birds, with a large degree of flexion at the hip joint in birds leading to the hip joint reaction force

being more anteriorly directed relative to the femur (Fig. 44). It cannot be discounted at present that the differences in architecture may also reflect differences in trunk posture between humans (orthograde) and birds (pronograde), although how trunk posture may influence hip joint loading remains unexplored. Most non-avian theropods examined had a minor anterior component to the mean orientation of $\mathbf{u}_1$, as in the human, suggesting that these species also held their femur in a similar, subvertical orientation. However, the mean orientation of $\mathbf{u}_1$ in Troodontidae sp. lay between that of birds and the other non-avian theropods, suggesting that its femoral orientation was intermediate between the subvertical posture of humans and the subhorizontal posture of birds.

I.5.2.2 Medial femoral condyle

Much as in the femoral head, the mean orientation of $\mathbf{u}_1$ in the medial femoral condyle is telling of postural differences between humans and birds, paralleling the results of previous experimental studies (Polk et al. 2008; Pontzer et al. 2006). In the human, it had only a small posterior inclination, whereas in birds the posterior inclination was generally substantial (Fig. 29A), which is inferred to reflect the greater degree of habitual knee flexion in birds (Fig. 44). This is supported by the results for the reptiles studied, which also exhibited a marked posterior inclination to $\mathbf{u}_1$ (although this was not strictly quantified), reflecting a marked level of habitual knee flexion during locomotion (Blob & Biewener 2001; Clemente et al. 2013; Gatesy 1991a). It was also demonstrated that the mean orientation of $\mathbf{u}_1$ in smaller birds tends to be more posteriorly inclined compared to larger birds (Fig. 29B). This reflects the fact that smaller birds tend to have a larger degree of postural crouch (Bishop et al. in review-a; Gatesy & Biewener 1991), which can be brought about by greater flexion of the knee joint. The non-avian theropods examined showed a variable amount of posterior inclination in the mean orientation of $\mathbf{u}_1$, although on the whole it was usually less compared to birds (less than 20°; Fig. 29A), suggesting a level of habitual knee flexion intermediate between that of humans and birds. No phylogenetic

pattern was apparent, and curiously the *Allosaurus*–tyrannosaurid architecture had the greatest posterior inclination of all.

A further point of difference between birds and the other groups investigated here is the degree to which the orientation of $\mathbf{u}_1$ swept throughout the condyles in the anteroposterior plane. In birds, this sweeping often exceeded 100°, yet it was less than 40° in all other groups (although this was not strictly quantified). This may reflect the greater degree of habitual knee flexion birds, but it may also correlate to the greater *range* of knee flexion-extension employed by birds during the stride cycle compared to other groups (Andrada et al. 2013; Blob & Biewener 2001; Clemente et al. 2013; Cracraft 1971; Gatesy 1991a; Gatesy 1999; Kambic et al. 2014; Kambic et al. 2015; Reilly 2000; Rubenson et al. 2007; Stoessel & Fischer 2012; Winter 2009). It should be noted that, owing to the fact that $\mathbf{u}_1$ swept throughout the condyles, the mean direction results reported for the medial condyle above need to be viewed with some caution. This is because significant sweeping in the anterior part of the condyles, particularly in larger species, could influence the calculated mean direction.

I.5.2.3 Proximal and distal femur

The pronounced double-arcuate architecture of cancellous bone in the coronal plane of the human proximal femur has been widely recognized for nearly two centuries (Ward 1838) and much discussion has focused upon the mechanical significance of this for almost as long (see reviews by Cowin 2001; Skedros & Baucom 2007). Despite the various interpretations that have been proposed over time, the inescapable fact remains that this bears strong resemblance to the principal stress trajectories that would be engendered under mediolateral bending, via a load applied to the head of the femur (the 'trajectorial theory'; see Introduction and Fig. 4). Such a loading regime, with compression dominating medially and tension laterally, is supported by *in vivo* strain gauge data (Aamodt et al. 1997). Moreover, the 'primary compressive group' that runs from the base of the femoral neck up to the head has been widely considered as reflecting transmission of the hip joint reaction force, away from the hip and down toward the rest of the femur (Skedros & Baucom 2007). The presence of a strikingly similar double-arcuate pattern, also parallel to the coronal plane, in the proximal femur of the tyrannosaurids suggests that very

much the same loading environment as occurs in humans also occurred in these species. Mediolateral bending of the femur is also suggested by another double-arcuate pattern, parallel to the coronal plane, in the distal femoral metaphysis.

An additional point of note is that the 'primary compressive group' in *Allosaurus* and the tyrannosaurids is directed towards the apex of the femoral head. By analogy with the proximal femur of humans, this suggests that the hip joint reaction force was principally applied there, implying that the articulation with the acetabulum was centred about the apex of the femoral head. This interpretation differs from previous suggestions, that the articulation was more lateral and involved at least part of the trochanteric region (e.g., Hotton 1980; Hutchinson & Allen 2009). The exact nature of non-avian theropod hip articulations is therefore worthy of further study. Indeed, the nature of contact between the femur and acetabulum may have varied both within and between various behaviours (e.g.,differing degrees of hip abduction). These dynamic articulations could have possibly varied with different morphologies (e.g., different degrees of inclination of the femoral neck), and probably changed appreciably on the line from basal theropods to extant birds.

I.5.2.4 Lesser trochanter

A second double-arcuate architecture in the lesser trochanter of the femur of the tyrannosaurids, also parallel to the coronal plane, further suggests that the trochanter also was loaded predominantly in mediolateral bending. This could conceivably occur via the medial pull (or medial component thereof) of the muscle(s) that inserted there, such as the iliotrochantericus caudalis (Hutchinson 2001a). In such a situation it would be predicted that the medial arcade would be loaded in compression, and the lateral arcade in tension.

I.5.2.5 Proximal tibia

The orientation of $\mathbf{u}_1$ in the proximal tibia of the human is largely proximodistally oriented throughout the entire end, whereas it shows considerable variation throughout the bone in birds.

Under the articular condyles, birds exhibit a more marked posterior inclination compared to that in the human (up to 30°, *versus* about 10°), as well as a strong lateral component under the lateral condyles, which does not occur in humans. Anteriorly, $\mathbf{u}_1$ can take on a distinct anterior inclination as it parallels the leading margin of the cnemial crests, which are absent in humans. Within the metaphysis, a double-arcuate pattern in $\mathbf{u}_1$, parallel to the sagittal plane, may also occur in the proximal tibia of birds, which is also absent in humans. In these respects, the proximal tibia of all the non-avian theropods studied is more similar to that of birds. This similarity in cancellous bone architecture is undoubtedly due in part to the greater similarity in morphologies (e.g., prominent cnemial crest) and nature of the knee articulation (with the fibula being involved laterally) between the two groups. However, it does suggest that anteroposterior bending may be a more significant loading regime in the theropod tibia than the human tibia.

I.5.2.6 Distal tibia or tibiotarsus

The distal tibia of *Allosaurus* and the tyrannosaurids has two well-developed sets of double-arcuate patterns, one parallel to the sagittal plane, the other parallel to the coronal plane. By analogy with the proximal femur, this suggests that both anteroposterior bending and mediolateral bending were important loading regimes in this part of the bone. These two different loading regimes may possibly have been engendered during different behaviours, or at different instances during the one behaviour, such as different points throughout the stride cycle. Conspicuously, these complex patterns do not continue into the astragalus and calcaneum. Equally conspicuous is the different cancellous bone architecture in the distal tibia of Troodontidae sp., *Saurornitholestes* and birds, which is continuous with the architecture in the astragalus and calcaneum (in Troodontidae sp. and birds at least). Not only does this suggest tighter mechanical unity between the three bones in life in the case of Troodontidae sp. (indeed, the astragalus and calcaneum fuse in adults), but it also suggests that the distal tibiotarsus of Troodontidae sp. and *Saurornitholestes* experienced a different set of loading regimes compared to *Allosaurus* and the tyrannosaurids, but similar to that of extant birds.

I.5.3 Oblique trabeculae in the diaphyses

One of the more interesting results of this study was the observation of markedly oblique trabeculae in the diaphysis of the femur and tibia of birds and reptiles. Aside from some pterosaur wing bones (Wellnhofer 1991), the authors are not aware of this feature being reported previously for any other tetrapod group. Interestingly, however, it also appears to be present in the proximal humeral diaphysis of orangutans (*Pongo pygmaeus*), judging from a figure published by Scherf et al. (2013, figure 1a). In the present study, the observed oblique trabeculae tended to form helices that spiralled along the endosteal margin, especially in the bones of larger bird species. This feature is interpreted to be responsible for the progressive increase in obliquity and disorganization of the orientation of $\mathbf{u}_1$ in the diaphysis-ward part of the metaphysis in birds and reptiles. Essentially, the more ordered architecture of the main part of the metaphysis gradually breaks down and transitions to a sparser architecture of oblique trabeculae in the diaphysis.

Application of the trajectorial theory to the oblique trabeculae of the diaphysis of bird and reptile femora and tibia would suggest that these bones are loaded predominantly in torsion, or at the very least experience a significant amount of torsion during daily use. This is because for a cylinder under pure torsion, both maximum (tensile) and minimum (compressive) principal stresses are parallel to the margin and oriented at 45° to it, forming conjugate spirals (Beer et al. 2012; Carrano 1998). *In vivo* strain gauge studies fully support this interpretation: the femora and tibiae of both birds and reptiles are loaded predominantly by torsion during locomotion (Biewener et al. 1986; Blob & Biewener 1999; Butcher et al. 2008; Carrano 1998; Carrano & Biewener 1999; Main & Biewener 2007; Verner et al. 2016). Oblique trabeculae were also observed to occur in the diaphysis of the human tibia, although not as strongly oblique to the bone's long-axis compared to birds and reptiles (about 10–20°). This also concurs with *in vivo* data showing that a considerable torsional component to bone loading occurs during part of the stance phase of locomotion (Lanyon et al. 1975; Yang et al. 2014). The increase in obliquity and disorganization of $\mathbf{u}_1$ observed in the diaphysis-ward parts of the femoral metaphyses of Troodontidae sp., and to a lesser extent the ornithomimids and caenagnathid, therefore suggests that torsion was a more important (but not necessarily predominant) loading regime in the femur of these species. By contrast, the lack of any noticeable obliquity in $\mathbf{u}_1$ in the femora of the other

non-avian theropods studied implies that torsion was minimally important. This too concurs with observations of the human femur, whereby $\mathbf{u}_1$ is subparallel to the long-axis of the bone in the diaphysis-ward parts of the metaphyses.

Whilst spiralling trabeculae in the femoral and tibial diaphyses of large birds is consistent with predictions of the trajectorial theory, the agreement breaks down in the bones of smaller birds. Specifically, in smaller birds the trabeculae tended to acquire an increasingly oblique orientation relative to the long-axis, approaching 70° or more; indeed, in some specimens, there were individual trabeculae that were almost orthogonal to the long-axis. Presumably, these smaller bird bones are also loaded predominantly in torsion, as are the bones of their larger relatives, on account of there being no evidence to the contrary, by way of anatomical, kinematic or kinetic observations. It would therefore be expected that principal stresses would still be approaching 45° to the long-axis of the bones. The lack of congruence between trabecular orientation and predictions of the trajectorial theory warrants explanation.

One possible explanation for the observed architectural patterns in smaller bird bones is that these bones are probably more liable to undergo failure through torsion-induced buckling, compared to the bones of larger species. In torsional loading, the critical shear stress needed to initiate buckling in a thin-walled cylindrical tube is given by

$$\tau_{\text{crit}} = \frac{k\pi^2 D}{l^2 t}, \tag{2}$$

where k is a constant depending on the comprising material, l is the length and t is the thickness of the cylinder wall (Batdorf 1947; Batdorf et al. 1947; Donnell 1933; Weingarten et al. 1968). D is the flexural stiffness per unit length along the circumference, given as

$$D = \frac{Et^3}{12(1-\nu^2)}, \tag{3}$$

where E is Young's modulus and ν is Poisson's ratio for the material concerned. Moreover, the stress in a thin-walled tube loaded in torsion is related to the applied torque T as

$$\tau = \frac{T}{2tA}, \tag{4}$$

where A is the area of the cross-section (Beer et al. 2012); for a circular geometry, this means that

$$\tau = \frac{2T}{\pi d^2 t}, \quad (5)$$

where d is the diameter. Therefore, the critical torque required to initiate buckling may be expressed as

$$T_{\text{crit}} = \frac{K\pi^3 d^2 t^3}{2l^2}, \quad (6)$$

where K is a constant reflecting the material comprising the tube. Thus, the propensity for a thin-walled cylindrical tube to undergo torsion-induced buckling is proportional to the square of its length and inversely proportional to the square of its diameter. Previous studies of bird allometry have demonstrated that at smaller size, their hindlimb bones become progressively more slender (Alexander 1983; Brassey et al. 2013; Carrano 1998; Doube et al. 2012; Gatesy 1991b; Olmos et al. 1996). Conversely, for a given size-normalized cross-sectional geometry, bones that are smaller in absolute terms will be longer in relative terms. The femora and tibiotarsi of smaller bird species are therefore more prone to torsion-induced buckling. One way by which to mitigate buckling in a thin-walled tube is to support the tube walls against excessive transverse deflection, through the addition of structural stiffeners inside the tube (Chitale & Gupta 2011). It is therefore hypothesized that the high-angle trabeculae in the femora (and less frequently, the tibiotarsus) of small birds are present mainly to provide cross-bracing support, to prevent the dimensions of the bone from changing too much that may initiate buckling, which could lead to catastrophic failure at the whole-bone level.

I.5.4 Future work

It is worth reiterating the main limitations of the present study, and noting that these may be addressed in future investigations. The foremost limitation concerns that of sampling. In investigating phenomena not studied previously, the work presented here was very much exploratory ~~in nature~~. Logistical constraints restricted the number of species that were studied, as well as the number of replicates for each species and each bone. It was therefore not possible in many instances to provide a more precise, quantitative assessment of architectural variation, in terms of inter- or intraspecific variability, or how architectural patterns may relate to finer-scale differences in anatomy, behaviour or habitat. In addition, although large specimens were sought for the extinct, non-avian theropods, this nevertheless could not fully control for possible

ontogenetic influences, as recognizing skeletally mature adults in the fossil record can be problematic (Hone et al. 2016). Furthermore, a number of major non-avian theropod groups were not investigated, such as basalmost tetanurans (e.g., megalosaurs), coelophysoids or alvarezsaurids. Increased sampling of non-avian species, as well as the number of individuals or bones for each species, is therefore an important objective for future studies, and will likely lead to greater refinement of the general patterns identified here. Likewise, it will also be important to increase sampling of avian species, including those outside of the crown group, although as many fossils of stem-group birds are taphonomically flattened, this will admittedly be difficult. In addition, it may be worthwhile expanding the scope of study to include other bones as well; for instance, investigating cancellous bone architectural patterns in the ilium may provide further insight on hip joint loading mechanics and posture (cf. sections I.5.2.1 and I.5.2.3 above).

It would also be very worthwhile investigating potential effects of body size in non-avian theropods, by conducting denser sampling within lineages that display marked variation in body size (e.g., dromaeosaurids, tyrannosauroids). This can not only provide further illumination on the range of postures and locomotor biomechanics used by non-avian theropods, but may also help disentangle the relative influence of body size from other factors, such as phylogeny, musculoskeletal anatomy or the location of the whole-body centre of mass. For instance, the greatest amount of posterior inclination of the mean orientation of $\mathbf{u}_1$ in the medial femoral condyle was observed in *Allosaurus* and the tyrannosaurids, which were also the largest species studied. This observation is counter to what would be predicted from extant birds (Fig. 29B), and so may reflect other (yet to be ascertained) factors. Alternatively, this observation may indeed reflect their very large size, where at such large body size other factors become relevant, factors that are not important at smaller sizes.

A second limitation of this study concerns the fact that focus was directed primarily towards the directionality of cancellous bone fabric. Whilst architectural directionality is an important indicator of loading mechanics (see Section I.2.3 above), studies of extant species have demonstrated that other architectural parameters can also be useful, such as bone volume fraction, trabecular thickness and trabecular spacing. Future investigation of these parameters may therefore yield further insights. A serious obstacle to this line of enquiry, however, is being able

to achieve sufficient CT scan contrast and resolution with fossil specimens, which currently is only possible for smaller specimens. Additionally, such study also requires excellent preservation of an entire fossil specimen.

One final limitation worth noting here is that the quantitative architectural analyses performed were not able to be used in as extensive a fashion – if at all – in very small bird bones. This was because these analyses rested on the continuum assumption, which breaks down at small spatial scales. Essentially, there were too few trabeculae present to permit rigorous quantitative analysis. A goal for future studies may hence be to explore alternative ways of quantitatively characterising cancellous bone architecture in very small bones. One possible avenue is to use micro-finite element modelling (Ryan & van Rietbergen 2005; van Rietbergen et al. 2003; van Rietbergen et al. 1999) to examine the principal material directions of the cancellous bone structure directly, although this can be computationally very expensive.

A further avenue for future work concerns the oblique or spiralling patterns of trabeculae observed in the femoral and tibial diaphyses of many birds, as well as other species. These patterns have hitherto never been reported outside of pterosaurs (Wellnhofer 1991), and so it would be interesting to investigate how widely distributed they actually are among various tetrapod groups. Moreover, given the mechanical significance hypothesized above for these spiralling patterns, it would also be interesting to investigate whether their presence correlates with certain aspects of locomotor biomechanics.

I.6 Conclusion

This study has used new approaches for analysing and quantifying how the 3-D architecture of cancellous bone varies throughout a limb bone, as well as new ways of comparing this between species. In doing so, it has produced a broad survey of the major architectural features present in the main hindlimb bones of a variety of extinct, non-avian theropod species, as well as a variety of extant, ground-dwelling birds.

Qualitative and quantitative comparisons between non-avian theropods, birds, reptiles and humans have identified several patterns of similarity and contrast between these groups. Many of the observed patterns can be mechanistically linked to various aspects of locomotor biomechanics in the extant species, such as the degree of hip or knee flexion. This has in turn provided insight into locomotor biomechanics in non-avian theropods. Although explicit quantitative comparisons were conducted only for two regions of the femur in the present study, the approach used here can be expanded to the analysis of other regions of this and other bones in the future. Not only will this enable a more rigorous characterization of cancellous bone architectural variation in the various species, but it may also provide further bearing on interpretations of locomotor biomechanics, especially with increased sample sizes.

Cancellous bone architecture in the hindlimb bones of birds is quite consistent across the species studied. When variations were apparent, they could be related to differences in size, or the presence or absence of pneumatization. Although variation due to phylogeny was not explicitly tested for in this study, no evidence for this was apparent. For instance, comparably-sized kiwis and chickens exhibited similar architectural patterns, as did comparably-sized tinamous and quail.

Broadly speaking, the cancellous bone architecture in more plesiomorphic theropods (ceratosaurs, *Allosaurus* and tyrannosaurids) is comparable to that in humans in many respects, but is often distinctly different from that observed in birds. The architectural patterns observed in Troodontidae sp. (and *Saurornitholestes*, where it was possible to assess), ~~is~~ typically intermediate between those of humans and birds. However, some features, such as the architecture of the distal tibiotarsus, are essentially identical to that of birds. Ornithomimid and caenagnathid femora both show a fairly distinct architectural pattern, different from all other groups studied.

Cancellous bone architecture in the hindlimb bones of non-avian theropods clearly varies between the different species studied, implying differences in locomotor biomechanics. Observed architectural features in the more plesiomorphic theropods studied suggest a manner of locomotion not too dissimilar from humans, with a subvertical femoral posture and mediolateral bending being the dominant loading regime in the femur. In contrast, Troodontidae sp. is inferred

to have had ~~a suite of~~ locomotor biomechanics intermediate between those of the more plesiomorphic theropods and extant birds, befitting its phylogenetic position.

A particularly interesting architectural feature observed in the present study is the abundance of markedly oblique trabeculae in the diaphyses of the femur and tibia of birds, and to a lesser extent, ~~reptiles~~. In the bones of large species, this produces spiralling patterns along the endosteal surface of the diaphysis. It is hypothesized that this feature reflects a prominence of torsional loading in these bones during normal use. If this is correct, the presence of oblique or spiralling trabeculae can be used as an indicator of high-torsion limb bone loading in future studies of other extinct vertebrate species.

I.7 Acknowledgements

The staff of the Geosciences Program of the Queensland Museum is thanked for the provision of workspace and access to literature: A. Rozefelds, K. Spring, R. Lawrence, P. Tierney, J. Wilkinson and D. Lewis. A very special thanks is extended to the staff and associated colleagues of the institutions that provided access to the material studied here: D. Henderson, B. Strlisky, G. Housego, R. Russel, T. Courtenay, B. Sanchez and F. Therrien (Royal Tyrell Museum of Palaeontology, Drumheller); R. Irmis, C. Levitt-Bussian, C. Webb and P. Policelli (Natural History Museum of Utah, Salt Lake City); J. Horner, J. Scannella, D. Varricchio, D. Strosnider, C. Woodruff, D. Fowler and T. Carr (Museum of the Rockies, Bozeman); K. Spring, H. Janetzki, A. Amey, P. Couper and S. Van Dyck (Queensland Museum, Brisbane); K. Roberts (Museum Victoria, Melbourne); R. Sadlier (Australian Museum, Sydney); and M. Forwood (Griffith University, Gold Coast). Many of the above people also provided helpful discussion on various aspects of theropod biology, and also helped transport specimens for CT scanning. The efforts of those who facilitated or performed the scanning itself are also much appreciated: S. Purdy and D. Wetter (Canada Diagnostic Centres, Calgary); K. Ugrin and D. Van Why (Bozeman Deaconess Hospital, Bozeman); M. Bauman, A. Price, S. Matinkhah and K. Sanders (University of Utah Hospital, Salt Lake City); S. Merchant, E. Hsu and J. Morgan (HSC Cores Research Facility, University of Utah, Salt Lake City); I. Mitchell and N. Newman (Queensland X-ray, Brisbane);

K. Mardon (Centre for Advanced Imaging, The University of Queensland, Brisbane); and R. Lawrence (Queensland Museum, Brisbane). Great thanks are also due to the volunteers who undertook scoring of diaphyseal cancellous bone architecture: R. Lawrence, J. Rasmussen, J. Macmillan, D. O'Boyle and N. Bishop. SCANCO Medical AG kindly provided the scan image presented in Figure 4A, and Figures 1 and 6A were prepared with the assistance of N. Bishop and P. Tierney. This series of studies is derived from doctoral work undertaken by P.J.B.; the thorough and constructive comments of the examiners of P.J.B.'s thesis are greatly appreciated, and substantially improved the clarity and content of the research presented here. All scripts and data used are held in the Geosciences Collection of the Queensland Museum, and will be made available upon request to the Collections Manager. Additionally, a complete copy of the fossil CT scan data obtained in the present study is housed with the respective institutions from which the specimens were sourced.

I.8 References

Aamodt A, Lund-Larsen J, Eine J, Andersen E, Benum P, and Schnell Husby O. 1997. *In Vivo* Measurements Show Tensile Axial Strain in the Proximal Lateral Aspect of the Human Femur. *Journal of Orthopaedic Research* 15:927-931.

Abel R, and Macho GA. 2011. Ontogenetic changes in the internal and external morphology of the ilium in modern humans. *Journal of Anatomy* 218:324-335.

Adachi T, Tsubota K, Tomita Y, and Hollister SJ. 2001. Trabecular Surface Remodeling Simulation for Cancellous Bone Using Microstructural Voxel Finite Element Models. *Journal of Biomechanical Engineering* 123:403-409.

Alexander RM. 1983. Allometry of the leg bones of moas (Dinornithes) and other birds. *Journal of Zoology* 200:215-231.

Alexander RM. 1985. Mechanics of posture and gait of some large dinosaurs. *Zoological Journal of the Linnean Society* 83:1-25.

Alexander RM. 1989. *Dynamics of Dinosaurs and Other Extinct Giants*. New York: Columbia University Press.

Alexander RM. 1991. Doubts and assumptions in dinosaur mechanics. *Interdisciplinary Science Reviews* 16:175-181.

Allen V, Bates KT, Li Z, and Hutchinson JR. 2013. Linking the evolution of body shape and locomotor biomechanics in bird-line archosaurs. *Nature* 497:104–107.

Allen V, Paxton H, and Hutchinson JR. 2009. Variation in Center of Mass Estimates for Extant Sauropsids and its Importance for Reconstructing Inertial Properties of Extinct Archosaurs. *The Anatomical Record* 292:1442-1461.

Allmendinger RW, Cardozo NC, and Fisher D. 2013. *Structural Geology Algorithms: Vectors and Tensors*. Cambridge: Cambridge University Press.

1991 Amson E, Arnold P, van Heteren AH, Canoville A, and Nyakatura JA. 2017. Trabecular
1992 architecture in the forelimb epiphyses of extant xenarthrans (Mammalia). *Frontiers in*
1993 *Zoology* 14:52.
1994 Andrada E, Nyakatura JA, Bergmann F, and Blickhan R. 2013. Adjustments of global and local
1995 hindlimb properties during terrestrial locomotion of the common quail (*Coturnix*
1996 *coturnix*). *Journal of Experimental Biology* 216:3906-3916.
1997 Bakker RT. 1980. Dinosaur heresy-dinosaur renaissance: Why we need endothermic archosaurs
1998 for a comprehensive theory of bioenergetic evolution. In: Thomas RDK, and Olson EC,
1999 eds. *A Cold Look at the Warm Blooded Dinosaurs*. Boulder: Westview Press, Inc.
2000 Bakker RT. 1986. *The Dinosaur Heresies*. New York: William Morrow & Company, Inc.
2001 Barak MM, Lieberman DE, and Hublin J-J. 2011. A Wolff in sheep's clothing: Trabecular bone
2002 adaptation in response to changes in joint loading orientation. *Bone* 49:1141-1151.
2003 Barak MM, Lieberman DE, Raichlen DA, Pontzer H, Warrener AG, and Hublin J-J. 2013.
2004 Trabecular Evidence for a Human-Like Gait in *Australopithecus africanus*. *PLoS ONE*
2005 8:e77687.
2006 Barthel KU. 2006. 3D-Data Representation with ImageJ. Proceedings of the First ImageJ User
2007 and Developer Conference. Luxembourg: The Centre de Recherche Public Henri Tudor.
2008 p 1-4.
2009 Batdorf SB. 1947. A simplified method of elastic-stability analysis for thin cylindrical shells. II -
2010 modified equilibrium equation. *National Advisory Committee for Aeronautics Technical*
2011 *Note* 1342:1-32.
2012 Batdorf SB, Stein M, and Schildcrout M. 1947. Critical stress of thin-walled cylinders in torsion.
2013 *National Advisory Committee for Aeronautics Technical Note* 1344:1-26.
2014 Bates KT, Benson RBJ, and Falkingham PL. 2012. A computational analysis of locomotor
2015 anatomy and body mass evolution in Allosauroidea (Dinosauria: Theropoda).
2016 *Paleobiology* 38:486-507.
2017 Baumel JJ, and Witmer LM. 1993. Osteologia. In: Baumel JJ, King AS, Breazile JE, Evans HE,
2018 and Vanden Berge JC, eds. *Handbook of Avian Anatomy: Nomina Anatomica Avium*. 2
2019 ed. Cambridge: Nuttall Ornithological Club, 45-132.
2020 Beaupré GS, Orr TE, and Carter DR. 1990. An Approach for Time-Dependent Bone Modeling
2021 and Remodeling – Application: A Preliminary Remodeling Simulation. *Journal of*
2022 *Orthopaedic Research* 8:662-670.
2023 Beer FP, Johnston ER, Jr, DeWolf JT, and Mazurek DF. 2012. *Mechanics of Materials*. New
2024 York: McGraw-Hill.
2025 Bell PR, and Snively E. 2008. Polar dinosaurs on parade: a review of dinosaur migration.
2026 *Alcheringa* 32:271-284.
2027 Ben-Zvi Y, Reznikov N, Shahar R, and Weiner S. 2017. 3D architecture of Trabecular Bone in
2028 the Pig Mandible and Femur: Inter-Trabecular angle Distributions. *Frontiers in Materials*
2029 4:29.
2030 Bennett PM, and Owens IPF. 2002. *Evolutionary Ecology of Birds*. Oxford: Oxford University
2031 Press.
2032 Benson RBJ, Hunt G, Carrano MT, and Campione NE. in press. Cope's Rule and the adaptive
2033 landscape of dinosaur body size evolution. *Palaeontology*.
2034 Bernsen J. 1986. Dynamic Thresholding of Grey-Level Images. Proceedings of the 8th
2035 International Conference on Pattern Recognition. Paris, France. p 1251-1255.

2036 Bertram JEA, and Biewener AA. 1988. Bone curvature: sacrificing strength for load
2037 predictability? *Journal of Theoretical Biology* 131:75-92.
2038 Biewener AA. 1992. Overview of structural mechanics. In: Biewener AA, ed. *Biomechanics:*
2039 *Structures and Systems – A Practical Approach*. Oxford: Oxford University Press, 1-20.
2040 Biewener AA, Fazzalari NL, Konieczynski DD, and Baudinette RV. 1996. Adaptive Changes in
2041 Trabecular Architecture in Relation to Functional Strain Patterns and Disuse. *Bone* 19:1-
2042 8.
2043 Biewener AA, Swartz SM, and Bertram JEA. 1986. Bone Modelling During Growth: Dynamics
2044 Strain Equilibrium in the Chick Tibiotarsus. *Calcified Tissue International* 39:390-395.
2045 Biewener AA, and Taylor CR. 1986. Bone strain: a determinant of gait and speed? *Journal of*
2046 *Experimental Biology* 123:383-400.
2047 Bishop PJ, Clemente CJ, Graham DF, Lamas LP, Hutchinson JR, Rubenson J, Hancock JA,
2048 Wilson RS, Hocknull SA, Barrett RS, and Lloyd DG. in review-a. The Influence of
2049 Speed and Size on Avian Terrestrial Locomotor Biomechanics: Predicting Locomotion in
2050 Extinct Theropod Dinosaurs. *PLoS ONE*.
2051 Bishop PJ, Clemente CJ, Hocknull SA, Barrett RS, and Lloyd DG. 2017. The effects of cracks
2052 on the quantification of the cancellous bone fabric tensor in fossil and archaeological
2053 specimens: a simulation study. *Journal of Anatomy* 230:461-470.
2054 Bishop PJ, Hocknull SA, Clemente CJ, Hutchinson JR, Barrett RS, and Lloyd DG. in review-b.
2055 Cancellous bone architecture and theropod dinosaur locomotion. Part II – A new
2056 approach to reconstructing posture and locomotor biomechanics in extinct tetrapod
2057 vertebrates. *PeerJ*.
2058 Bishop PJ, Hocknull SA, Clemente CJ, Hutchinson JR, Farke AA, Barrett RS, and Lloyd DG. in
2059 review-c. Cancellous bone architecture and theropod dinosaur locomotion. Part III –
2060 Inferring posture and locomotor biomechanics in extinct theropods, and its evolution on
2061 the line to birds. *PeerJ*.
2062 Bishop PJ, Walmsley CW, Phillips MJ, Quayle MR, Boisvert CA, and McHenry CR. 2015.
2063 Oldest Pathology in a Tetrapod Bone Illuminates the Origin of Terrestrial Vertebrates.
2064 *PLoS ONE* 10:e0125723.
2065 Blob RW, and Biewener AA. 1999. *In vivo* locomotor strain in the hindlimb bones of *Alligator*
2066 *mississippiensis* and *Iguana iguana*: implications for the evolution of limb bone safety
2067 factor and non-sprawling limb posture. *Journal of Experimental Biology* 202:1023-1046.
2068 Blob RW, and Biewener AA. 2001. Mechanics of limb bone loading during terrestrial
2069 locomotion in the green iguana (*Iguana iguana*) and American alligator (*Alligator*
2070 *mississippiensis*). *Journal of Experimental Biology* 204:1099-1122.
2071 Blomberg SP, and Garland T, Jr. 2002. Tempo and mode in evolution: phylogenetic inertia,
2072 adaptation and comparative methods. *Journal of Evolutionary Biology* 15:899-910.
2073 Bonnan MF, Sandrik JL, Nishiwaki T, Wilhite DR, Elsey RM, and Vittore C. 2010. Calcified
2074 Cartilage Shape in Archosaur Long Bones Reflects Overlying Joint Shape in Stress-
2075 Bearing Elements: Implications for Nonavian Dinosaur Locomotion. *The Anatomical*
2076 *Record* 293:2044-2055.
2077 Boyle C, and Kim IY. 2011. Three-dimensional micro-level computational study of Wolff's law
2078 via trabecular bone remodeling in the human proximal femur using design space topology
2079 optimization. *Journal of Biomechanics* 44:935-942.

2080 Brassey CA, Kitchener AC, Withers PJ, Manning PL, and Sellers WI. 2013. The Role of Cross-
2081 Sectional Geometry, Curvature, and Limb Posture in Maintaining Equal Safety Factors:
2082 A Computed Tomography Study. *The Anatomical Record* 296:395-413.
2083 Brusatte SL. 2012. *Dinosaur Paleobiology*. West Sussex: John Wiley and Sons, Ltd.
2084 Butcher MT, Espinoza NR, Cirilo SR, and Blob RW. 2008. *In vivo* strains in the femur of river
2085 cooter turtles (*Pseudemys concinna*) during terrestrial locomotion: tests of force-platform
2086 models of loading mechanics. *Journal of Experimental Biology* 211:2397-2407.
2087 Cardozo NC, and Allmendinger RW. 2013. Spherical projections with OSXStereonet.
2088 *Computers & Geosciences* 51:193-205.
2089 Carlson KJ, Doran-Sheehy DM, Hunt KD, Nishida T, Yamanaka A, and Boesch C. 2006.
2090 Locomotor behaviour and long bone morphology in individual free-ranging chimpanzees.
2091 *Journal of Human Evolution* 50:394-404.
2092 Carrano MT. 1998. Locomotion in non-avian dinosaurs: integrating data from hindlimb
2093 kinematics, in vivo strains, and bone morphology. *Paleobiology* 24:450-469.
2094 Carrano MT. 2000. Homoplasy and the evolution of dinosaur locomotion. *Paleobiology* 26:489-
2095 512.
2096 Carrano MT. 2001. Implications of limb bone scaling, curvature and eccentricity in mammals
2097 and non-avian dinosaurs. *Journal of Zoology* 254:41-55.
2098 Carrano MT. 2005. The Evolution of Sauropod Locomotion: Morphological Diversity of a
2099 Secondarily Quadrupedal Radiation. In: Curry Rogers KA, and Wilson JA, eds. *The*
2100 *Sauropods: Evolution and Paleobiology*. Berkeley: University of California Press, 229-
2101 251.
2102 Carrano MT. 2006. Body-Size Evolution in the Dinosauria. In: Carrano MT, Gaudin TJ, Blob
2103 RW, and Wible JR, eds. *Amniote Paleobiology: Perspectives on the Evolution of*
2104 *Mammals, Birds, and Reptiles*. Chicago: University of Chicago Press, 225-268.
2105 Carrano MT, Benson RBJ, and Sampson SD. 2012. The phylogeny of Tetanurae (Dinosauria:
2106 Theropoda). *Journal of Systematic Palaeontology* 10:211-300.
2107 Carrano MT, and Biewener AA. 1999. Experimental Alteration of Limb Posture in the Chicken
2108 (*Gallus gallus*) and its Bearing on the Use of Birds as Analogs for Dinosaur Locomotion.
2109 *Journal of Morphology* 240:237-249.
2110 Carrano MT, and Hutchinson JR. 2002. Pelvic and hindlimb musculature of *Tyrannosaurus rex*
2111 (Dinosauria: Theropoda). *Journal of Morphology* 253:207-228.
2112 Carter DR, and Beaupré GS. 2001. *Skeletal Function and Form: Mechanobiology of Skeletal*
2113 *Development, Aging, and Regeneration*. Cambridge: Cambridge University Press.
2114 Carter DR, Orr TE, and Fyhrie DP. 1989. Relationships between loading history and femoral
2115 cancellous bone architecture. *Journal of Biomechanics* 22:231-244.
2116 Chiappe LM, and Witmer LM. 2002. Mesozoic Birds: Above the Heads of the Dinosaurs.
2117 Berkeley: University of California Press.
2118 Chitale AK, and Gupta RC. 2011. *Product Design and Manufacturing*. New Delhi: PHI Learning
2119 Private Limited.
2120 Christen P, Ito K, Ellouz R, Boutroy S, Sornay-Rendu E, Chapurlat RD, and van Rietbergen B.
2121 2014. Bone remodelling in humans is load-driven but not lazy. *Nature Communications*
2122 5:4855.
2123 Christiansen M, Kveiborg M, Kassem M, Clark BFC, and Rattan SIS. 2000. CBFA1 and
2124 Topoisomerase I mRNA Levels Decline During Cellular Aging of Human Trabecular
2125 Osteoclasts. *Journal of Gerontology* 55A:B194-B200.

2126 Christiansen P. 1997. Locomotion in sauropod dinosaurs. *Gaia* 14:45-75.
2127 Christiansen P. 1998. Strength indicator values of theropod long bones, with comments on limb
2128 proportions and cursorial potential. *Gaia* 15:241-255.
2129 Christiansen P. 1999. Long bone scaling and limb posture in non-avian theropods: evidence for
2130 differential allometry. *Journal of Vertebrate Paleontology* 19:666-680.
2131 Clarke B. 2008. Normal Bone Anatomy and Physiology. *Clinical Journal of the American*
2132 *Society of Nephrology* 3:S131-S139.
2133 Clemente CJ, Withers PC, Thompson GG, and Lloyd DG. 2013. Lizard tricks: overcoming
2134 conflicting requirements of speed *versus* climbing ability by altering biomechanics of the
2135 lizard stride. *Journal of Experimental Biology* 216:3854-3862.
2136 Coelho PG, Fernandes PR, Rodrigues HC, Cardoso JB, and Guedes JM. 2009. Numerical
2137 modeling of bone tissue adaptation—A hierarchical approach for bone apparent density
2138 and trabecular structure. *Journal of Biomechanics* 42:830-837.
2139 Coombs WP, Jr. 1978. Theoretical aspects of cursorial adaptations in dinosaurs. *Quarterly*
2140 *Review of Biology* 53:393-418.
2141 Cowin SC. 1986. Wolff's Law of Trabecular Architecture at Remodelling Equilibrium. *Journal*
2142 *of Biomechanical Engineering* 108:83-88.
2143 Cowin SC. 1997. Remarks on the paper entitled 'Fabric and elastic principal directions of
2144 cancellous bone are closely related'. *Journal of Biomechanics* 30:1191-1192.
2145 Cowin SC. 2001. The false premise in Wolff's Law. In: Cowin SC, ed. *Bone Biomechanics*
2146 *Handbook*. 2 ed. Boca Raton: CRC Press, 30-31–30-15.
2147 Cowin SC, Sadegh AM, and Luo GM. 1992. An Evolutionary Wolff's Law for Trabecular
2148 Architecture. *Journal of Biomechanical Engineering* 114:129-136.
2149 Cracraft J. 1971. The functional morphology of the hind limb of the domestic pigeon, *Columba*
2150 *livia*. *Bulletin of the American Museum of Natural History* 144:171-268.
2151 Cresswell EN, Goff MG, Nguyen TM, Lee WX, and Hernandez CJ. 2016. Spatial relationships
2152 between bone formation and mechanical stress within cancellous bone. *Journal of*
2153 *Biomechanics* 49:222-228.
2154 Cruz-Orive LM, Karlsson LM, Larsen SE, and Wainschtein F. 1992. Characterizing anisotropy:
2155 a new concept. *Micron and Microscopica Acta* 23:75-76.
2156 Cubo J, Woodward H, Wolff E, and Horner JR. 2015. First Reported Cases of Biomechanically
2157 Adaptive Bone Modeling in Non-Avian Dinosaurs. *PLoS ONE* 10:e131131.
2158 Cunningham CA, and Black SM. 2009a. Anticipating bipedalism: trabecular organization in the
2159 newborn ilium. *Journal of Anatomy* 214:817-829.
2160 Cunningham CA, and Black SM. 2009b. Development of the fetal ilium – challenging concepts
2161 of bipedality. *Journal of Anatomy* 214:91-99.
2162 Currey JD. 2002. *Bones: Structure and Mechanics*. Princeton: Princeton University Press.
2163 Currey JD. 2003. The many adaptations of bone. *Journal of Biomechanics* 36:1487-1495.
2164 D'Anastasio R, Wroe S, Tuniz C, Mancini L, Cesana DT, Dreossi D, Ravichandiran M, Attard
2165 M, Parr WCH, Agur A, and Capasso L. 2013. Micro-Biomechanics of the Kebara 2
2166 Hyoid and Its Implications for Speech in Neanderthals. *PLoS ONE* 8:e82261.
2167 Dacke CG, Arkle S, Cook DJ, Wormstone IM, Jones S, Zaidi M, and Bascal ZA. 1993.
2168 Medullary bone and avian calcium regulation. *Journal of Experimental Biology* 184:63-
2169 88.
2170 Davies SJJF. 2002. *Ratites and Tinamous*. Oxford: Oxford University Press.

de Ricqlès AJ. 1976. On bone histology of fossil and living reptiles, with comments on its functional and evolutionary importance. In: Bellairs AdA, and Cox CB, eds. *Morphology and Biology of Reptiles*. London: Academic Press, 123-150.
Demes B. 2007. In vivo bone strain and bone functional adaptation. *American Journal of Physical Anthropology* 133:717-722.
Demes B, Qin Y-X, Stern JT, Jr, Larson SG, and Rubin CT. 2001. Patterns of strain in the macaque tibia during functional activity. *American Journal of Physical Anthropology* 116:257-265.
Demes B, Stern JT, Jr, Hausman MR, Larson SG, McLeod KJ, and Rubin CT. 1998. Patterns of strain in the macaque ulna during functional activity. *American Journal of Physical Anthropology* 106:87-100.
DeSilva JM, and Devlin MJ. 2012. A comparative study of the trabecular bony architecture of the talus in humans, non-human primates, and *Australopithecus*. *Journal of Human Evolution* 63:536-551.
Donnell LH. 1933. Stability of thin-walled tubes under torsion. *National Advisory Committee for Aeronautics Technical Report* 479:95-116.
Doube M, Kłosowski MM, Arganda-Carreras I, Cordelières FP, Dougherty RP, Jackson JS, Schmid B, Hutchinson JR, and Shefelbine SJ. 2010. BoneJ: Free and extensible bone image analysis in ImageJ. *Bone* 47:1076-1079.
Doube M, Yen SCW, Kłosowski MM, Farke AA, Hutchinson JR, and Shefelbine SJ. 2012. Whole-bone scaling of the avian pelvic limb. *Journal of Anatomy* 221:21-29.
Dunning JB, Jr. 2007. *CRC Handbook of Avian Body Masses*. Boca Raton: CRC Press.
Elke RPE, Cheal EJ, Simmons C, and Poss R. 1995. Three-Dimensional Anatomy of the Cancellous Structures within the Proximal Femur from Computed Tomography Data. *Journal of Orthopaedic Research* 13:513-523.
Enlow DH. 1969. The Bone of Reptiles. In: Gans C, Bellairs AdA, and Parsons TS, eds. *Biology of the Reptilia*. London: Academic Press, 45-80.
Fariña RA, Vizcaíno SF, and Blanco RE. 1997. Scaling of the indicator of athletic capability in fossil and extant land tetrapods. *Journal of Theoretical Biology* 185:441-446.
Farke AA, and Alicea J. 2009. Femoral strength and posture in terrestrial birds and non-avian theropods. *The Anatomical Record* 292:1406-1411.
Farlow JO, Chapman RE, Breithaupt BH, and Matthews N. 2012. The Scientific Study of Dinosaur Footprints. In: Brett-Surman MK, Holtz TR, Jr, and Farlow JO, eds. *The Complete Dinosaur*. 2 ed. Bloomington: Indiana University Press, 712–759.
Farlow JO, Gatesy SM, Holtz TR, Jr, Hutchinson JR, and Robinson JM. 2000. Theropod Locomotion. *American Zoologist* 40:640-663.
Farlow JO, Smith MB, and Robinson JM. 1995. Body mass, bone "strength indicator," and cursorial potential of *Tyrannosaurus rex*. *Journal of Vertebrate Paleontology* 15:713-725.
Frost HM. 1987. Bone mass and the mechanostat – a proposal. *The Anatomical Record* 219:1-9.
Frost HM. 2003. Bone's mechanostat: a 2003 update. *The Anatomical Record* 275A:1081-1101.
Fyhrie DP, and Carter DR. 1986. A Unifying Principle Relating Stress to Trabecular Bone Morphology. *Journal of Orthopaedic Research* 4:304-317.
Garden RS. 1961. The structure and function of the proximal end of the femur. *Journal of Bone and Joint Surgery* 43B:576-589.

2216 Gatesy SM. 1990. Caudofemoral musculature and the evolution of theropod locomotion.
2217 *Paleobiology* 16:170-186.
2218 Gatesy SM. 1991a. Hind limb movements of the American alligator (*Alligator mississippiensis*)
2219 and postural grades. *Journal of Zoology* 224:577-588.
2220 Gatesy SM. 1991b. Hind Limb Scaling in Birds and Other Theropods: Implications for
2221 Terrestrial Locomotion. *Journal of Morphology* 209:83-96.
2222 Gatesy SM. 1995. Functional evolution of the hindlimb and tail from basal theropods to birds. In:
2223 Thomason JJ, ed. *Functional Morphology in Vertebrate Paleontology*. New York:
2224 Cambridge University Press, 219–234.
2225 Gatesy SM. 1999. Guineafowl Hindlimb Function I: Cineradiographic Analysis and Speed
2226 Effects. *Journal of Morphology* 240:115–125.
2227 Gatesy SM. 2002. Locomotor Evolution on the Line to Modern Birds. In: Chiappe LM, and
2228 Witmer LM, eds. *Mesozoic Birds: Above the Heads of the Dinosaurs*. Berkeley:
2229 University of California Press, 432–447.
2230 Gatesy SM, Bäker M, and Hutchinson JR. 2009. Constraint-based exclusion of limb poses for
2231 reconstructing theropod dinosaur locomotion. *Journal of Vertebrate Paleontology*
2232 29:535-544.
2233 Gatesy SM, and Biewener AA. 1991. Bipedal locomotion: effects of speed, size and limb posture
2234 in birds and humans. *Journal of Zoology* 224:127-147.
2235 Gatesy SM, and Middleton KM. 1997. Bipedalism, flight, and the evolution of theropod
2236 locomotor diversity. *Journal of Vertebrate Paleontology* 17:308-329.
2237 Gatesy SM, Middleton KM, Jenkins FA, Jr, and Shubin NH. 1999. Three-dimensional
2238 preservation of foot movements in Triassic theropod dinosaurs. *Nature* 399:141-144.
2239 Gauthier JA. 1986. Saurischian monophyly and the origin of birds. *Memoirs of the California*
2240 *Academy of Sciences* 8:1-55.
2241 Gefen A, and Seliktar R. 2004. Comparison of the trabecular architecture and the isostatic stress
2242 flow in the human calcaneus. *Medical Engineering & Physics* 26:119-129.
2243 Giddings VL, Beaupré GS, Whalen RT, and Carter DR. 2000. Calcaneal loading during walking
2244 and running. *Medicine & Science in Sports & Exercise* 32:627-634.
2245 Gillette DD, and Lockley MG. 1989. Dinosaur Tracks and Traces. Cambridge: Cambridge
2246 University Press.
2247 Goldstein SA, Goulet R, and McCubbrey D. 1993. Measurement and Significance of Three-
2248 Dimensional Architecture to the Mechanical Integrity of Trabecular Bone. *Calcified*
2249 *Tissue International* 53 (suppl. 1):S127–S133.
2250 Goldstein SA, Matthews LS, Kuhn JL, and Hollister SJ. 1991. Trabecular bone remodelling: an
2251 experimental model. *Journal of Biomechanics* 24 (suppl. 1):135-150.
2252 Gosman JH, and Ketcham RA. 2009. Patterns in Ontogeny of Human Trabecular Bone From
2253 SunWatch Village in the Prehistoric Ohio Valley: General Features of Microarchitectural
2254 Change. *American Journal of Physical Anthropology* 138:318-332.
2255 Gosman JH, Stout SD, and Larsen CS. 2011. Skeletal Biology Over the Life Span: A View From
2256 the Surfaces. *Yearbook of Physical Anthropology* 54:86-98.
2257 Gross T, Kivell TL, Skinner MM, Nguyen NH, and Pahr DH. 2014. A CT-image-based
2258 framework for the holistic analysis of cortical and trabecular bone morphology.
2259 *Palaeontologia Electronica* 17:33A.

2260 Grossi B, Iriarte-Díaz J, Larach O, Canals M, and Vásquez RA. 2014. Walking Like Dinosaurs:
2261 Chickens with Artificial Tails Provide Clues about Non-Avian Theropod Locomotion.
2262 *PLoS ONE* 9:e88458.
2263 Hackett SJ, Kimball RT, Reddy S, Bowie RCK, Braun EL, Braun MJ, Chojnowski JL, Cox WA,
2264 Han K-L, Harshman J, Huddleston CJ, Marks BD, Miglia KJ, Moore WS, Sheldon FH,
2265 Steadman DW, Witt CC, and Yuri T. 2008. A Phylogenomic Study of Birds Reveals
2266 Their Evolutionary History. *Science* 320:1763-1768.
2267 Haddrath O, and Baker AJ. 2012. Multiple nuclear genes and retroposons support vicariance and
2268 dispersal of the palaeognaths, and an Early Cretaceous origin of modern birds.
2269 *Proceedings of the Royal Society of London, Series B* 279:4617-4625.
2270 Hammer Ø, Harper DAT, and and Ryan PD. 2001. PAST: Paleontological Statistics Software
2271 Package for Education and Data Analysis. *Palaeontologia Electronica* 4:4.
2272 Harrigan TP, Jasty M, Mann RW, and Harris WH. 1988. Limitations of the continuum
2273 assumption in cancellous bone. *Journal of Biomechanics* 21:269-275.
2274 Havill LM, Allen MR, Bredbenner TL, Burr DB, Nicolella DP, Turner CH, Warren DM, and
2275 Mahaney MC. 2010. Heritability of lumbar trabecular bone mechanical properties in
2276 baboons. *Bone* 46:835-840.
2277 Hayes WC, and Snyder B. 1981. Toward a quantitative formulation of Wolff's Law in trabecular
2278 bone. In: Cowin SC, ed. *Mechanical Properties of Bone*. New York: American Society of
2279 Mechanical Engineers, 43-68.
2280 Hébert D, Lebrun R, and Marivaux L. 2012. Comparative Three-Dimensional Structure of the
2281 Trabecular Bone in the Talus of Primates and Its Relationship to Ankle Joint Loads
2282 Generated During Locomotion. *The Anatomical Record* 295:2069-2088.
2283 Heers AM, and Dial KP. 2012. From extant to extinct: locomotor ontogeny and the evolution of
2284 avian flight. *Trends in Ecology and Evolution* 27:296-305.
2285 Heinrich RE, Ruff CB, and Weishampel DB. 1993. Femoral ontogeny and locomotor
2286 biomehcnaics of *Dryosaurus lettowvorbecki* (Dinosauria, Iguanodontia). *Zoological*
2287 *Journal of the Linnean Society* 108:179-196.
2288 Henderson DM. 1999. Estimating the masses and centers of mass of extinct animals by 3-D
2289 mathematical slicing. *Paleobiology* 25:88-106.
2290 Heřt J. 1994. A new attempt at the interpretation of the functional architecture of the cancellous
2291 bone. *Journal of Biomechanics* 27:239-242.
2292 Holtz TR, Jr. 2012. Theropods. In: Brett-Surman MK, Holtz TR, Jr, and Farlow JO, eds. *The*
2293 *Complete Dinosaur*. 2 ed. Bloomington: Indiana University Press, 346-378.
2294 Hone DWE, Farke AA, and Wedel MJ. 2016. Ontogeny and the fossil record: what, if anything,
2295 is an adult dinosaur? *Biology Letters* 12:20150947.
2296 Horner JR. 2000. Dinosaur Reproduction and Parenting. *Annual Review of Earth and Planetary*
2297 *Sciences* 28:19-45.
2298 Horner JR, and Lessem D. 1993. *The Complete T. rex*. New York: Simon and Schuster, Inc.
2299 Hotton NH, III. 1980. An Alternative to Dinosaur Endothermy: The Happy Wanderers. In:
2300 Thomas RDK, and Olson EC, eds. *A Cold Look at the Warm-Blooded Dinosaurs*.
2301 Boulder: Westview Press, Inc., 311-350.
2302 Hübner TR. 2012. Bone Histology in *Dysalotosaurus lettowvorbecki* (Ornithischia:
2303 Iguanodontia) – Variation, Growth, and Implications. *PLoS ONE* 7:e29958.
2304 Huiskes R. 2000. If bone is the answer, then what is the question? *Journal of Anatomy* 197:145-
2305 156.

2306 Huiskes R, Ruimerman R, van Lenthe GH, and Janssen JD. 2000. Effects of mechanical forces
2307 on maintenance and adaptation of form in trabecular bone. *Nature* 405:704-706.
2308 Hutchinson JR. 2001a. The evolution of femoral osteology and soft tissues on the line to extant
2309 birds (Neornithes). *Zoological Journal of the Linnean Society* 131:169-197.
2310 Hutchinson JR. 2001b. The evolution of pelvic osteology and soft tissues on the line to extant
2311 birds (Neornithes). *Zoological Journal of the Linnean Society* 131:123-168.
2312 Hutchinson JR. 2002. The evolution of hindlimb tendons and muscles on the line to crown-group
2313 birds. *Comparative Biochemistry and Physiology, Part A* 133:1051-1086.
2314 Hutchinson JR. 2006. The evolution of locomotion in archosaurs. *Comptes Rendus Palevol*
2315 5:519-530.
2316 Hutchinson JR, and Allen V. 2009. The evolutionary continuum of limb function from early
2317 theropods to birds. *Naturwissenschaften* 96:423-448.
2318 Hutchinson JR, Anderson FC, Blemker SS, and Delp SL. 2005. Analysis of hindlimb muscle
2319 moment arms in *Tyrannosaurus rex* using a three-dimensional musculoskeletal computer
2320 model: implications for stance, gait, and speed. *Paleobiology* 31:676-701.
2321 Hutchinson JR, Bates KT, Molnar J, Allen V, and Makovicky PJ. 2011. A Computational
2322 Analysis of Limb and Body Dimensions in Tyrannosaurus rex with Implications for
2323 Locomotion, Ontogeny and Growth. *PLoS ONE* 6:e26037.
2324 Hutchinson JR, and Gatesy SM. 2000. Adductors, abductors, and the evolution of archosaur
2325 locomotion. *Paleobiology* 26:734-751.
2326 Hutchinson JR, and Gatesy SM. 2006. Dinosaur locomotion: Beyond the bones. *Nature* 440:292-
2327 294.
2328 Hutchinson JR, Miller CE, Fritsch G, and Hildebrandt T. 2008. The Anatomical Foundation for
2329 Multidisciplinary Studies of Animal Limb Function: Examples from Dinosaur and
2330 Elephant Limb Imaging Studies. In: Endo H, and Frey R, eds. *Anatomical Imaging:*
2331 *Towards a New Morphology*. Tokyo: Springer, 23-38.
2332 Jacobs CR. 2000. The mechanobioogy of cancellous bone structural adaptation. *Journal of*
2333 *Rehabilitation Research and Development* 37:209-216.
2334 Jacobs CR, Simo JC, Beaupré GS, and Carter DR. 1997. Adaptive bone remodeling
2335 incorporating simultaneous density and anisotropy considerations. *Journal of*
2336 *Biomechanics* 30:603-613.
2337 Jang IG, and Kim IY. 2008. Computational study of Wolff's law with trabecular architecture in
2338 the human proximal femur using topology optimization. *Journal of Biomechanics*
2339 41:2353-2361.
2340 Jang IG, and Kim IY. 2010a. Application of design space optimization to bone remodeling
2341 simulation of trabecular architecture in human proximal femur for higher computational
2342 efficiency. *Finite Elements in Analysis and Design* 46:311-319.
2343 Jang IG, and Kim IY. 2010b. Computational simulation of cortical and trabecular bone change in
2344 human proximal femur during bone remodelling. *Journal of Biomechanics* 43:294-301.
2345 Jarvis ED, Mirarab S, Aberer AJ, Li B, Houde P, Li C, Ho SYW, Faircloth BC, Nabholz B,
2346 Howard JT, Suh A, Weber CC, da Fonseca RR, Li J, Zhang F, Li H, Zhou L, Narula N,
2347 Liu L, Ganapathy G, Boussau B, Bayzid MS, Zavidovych V, Subramanian S, Gabalbón
2348 T, Capella-Gutiérrez S, Huerta-Cepas J, Rekepalli B, Munch K, Schierup M, Lindow B,
2349 Warren WC, Ray D, Green RE, Bruford MW, Zhan X, Dixon A, Li S, Li N, Huang Y,
2350 Derryberry EP, Bertelsen FF, Sheldon FH, Brumfield RT, Mello CV, Lovell PV, Wirthlin
2351 M, Schneider MPC, Prosdocimi F, Samaniego JA, Velazquez AMV, Alfaro-Núñez A,

Campos PF, Petersen B, Sicheritz-Ponten T, Pas A, Bailey T, Scofield RP, Bunce M, Lambert DM, Zhou Q, Perelman P, Driskell AC, Shapiro B, Xiong Z, Zeng Y, Liu S, Li Z, Liu B, Wu K, Xiao J, Yinqi X, Zheng Q, Zhang Y, Yang H, Wang J, Smeds L, Rheindt FE, Braun M, Fjeldsa J, Orlando L, Barker FK, Jønsson KA, Johnson W, Koepfli K-P, O'Brien S, Haussler D, Ryder OA, Rahbek C, Willerslev E, Graves GR, Glenn TC, McCormack J, Burt D, Ellegren H, Alström P, Edwards SV, Stamatakis A, Mindell DP, Cracraft J, Braun EL, Warnow T, Jun W, Gilbert MTP, and Zhang G. 2014. Whole-genome analyses resolve early branches in the tree of life of modern birds. *Science* 346:1320-1331.

Jetz W, Thomas GH, Joy JB, Hartmann K, and Mooers AO. 2012. The global diversity of birds in space and time. *Nature* 491:444-448.

Judex S, Garman R, Squire M, Donahue L-R, and Rubin CT. 2004. Genetically Based Influences on the Site-Specific Regulation of Trabecular and Cortical Bone Morphology. *Journal of Bone and Mineral Research* 19:600-606.

Kabel J, van Rietbergen B, Odgaard A, and Huiskes R. 1999. Constitutive Relationships of Fabric, Density, and Elastic Properties in Cancellous Bone Architecture. *Bone* 25:481-486.

Kambic RE, Roberts TJ, and Gatesy SM. 2014. Long-axis rotation: a missing degree of freedom in avian bipedal locomotion. *Journal of Experimental Biology* 217:2770-2782.

Kambic RE, Roberts TJ, and Gatesy SM. 2015. Guineafowl with a twist: asymmetric limb control in steady bipedal locomotion. *Journal of Experimental Biology* 218:3836-3844.

Kamibayashi L, Wyss UP, Cooke TDV, and Zee B. 1995. Changes in Mean Trabecular Orientation in the Medial Condyle of the Proximal Tibia in Osteoarthritis. *Calcified Tissue International* 57:69-73.

Keaveny TM, Morgan EF, Niebur GL, and Yeh OC. 2001. Biomechanics of Trabecular Bone. *Annual Review of Biomedical Engineering* 3:307-333.

Keaveny TM, and Yeh OC. 2002. Architecture and trabecular bone – Toward an improved understanding of the biomechanical effects of age, sex and osteoporosis. *Journal of Musculoskeletal and Neuronal Interactions* 2:205-208.

Ketcham RA, and Carlson WD. 2001. Acquisition, optimization and interpretation of X-ray computed tomographic imagery: applications to the geosciences. *Computers & Geosciences* 27:381-400.

Ketcham RA, and Ryan TM. 2004. Quantification and visualization of anisotropy in trabecular bone. *Journal of Microscopy* 213:158-171.

Kivell TL. 2016. A review of trabecular bone functional adaptation: what have we learned from trabecular analyses in extant hominoids and what can we apply to fossils? *Journal of Anatomy* 228:569-594.

Koch JC. 1917. The laws of bone architecture. *American Journal of Anatomy* 21:177-298.

Kowalczyk P. 2010. Simulation of orthotropic microstructure remodelling of cancellous bone. *Journal of Biomechanics* 43:563-569.

Ksepka DT. 2009. Broken gears in the avian molecular clock: new phylogenetic analyses support stem galliform status for *Gallinuloides wyomingensis* and rallid affinities for *Amitabha urbsinterdictensis*. *Cladistics* 25:173-197.

Ksepka DT, and Phillips MJ. 2015. Avian diversification patterns across the K-Pg boundary: influence of calibrations, datasets, and model misspecification. *Annals of the Missouri Botanic Garden* 100:300-328.

2398 Lambers FM, Koch K, Kuhn G, Ruffoni D, Weigt C, Schulte FA, and Müller R. 2013.
2399 Trabecular bone adapts to long-term cyclic loading by increasing stiffness and
2400 normalization of dynamic morphometric rates. *Bone* 55:325-334.
2401 Landini G. 2008. Advanced shape analysis with ImageJ. Proceedings of the Second ImageJ User
2402 and Developer Conference. Luxembourg: The Centre de Recherche Public Henri Tudor.
2403 p 116-121.
2404 Landini G, Randell DA, Fouad S, and Galton A. 2016. Automatic thresholding from the
2405 gradients of region boundaries. *Journal of Microscopy* In Press.
2406 Lane JM, Riley EH, and Wirganowicz PZ. 1996. Osteoporosis: Diagnosis and Treatment.
2407 *Journal of Bone and Joint Surgery* 78A:618-166.
2408 Lanyon LE. 1974. Experimental support for the trajectorial theory of bone structure. *Journal of*
2409 *Bone and Joint Surgery* 56B:160-166.
2410 Lanyon LE. 1996. Locomotor Loading and Functional Adaptation in Limb Bones. *Symposium of*
2411 *the Zoological Society of London* 48:305-329.
2412 Lanyon LE, Hampson WGJ, Goodship AE, and Shah JS. 1975. Bone deformation recorded in
2413 vivo from strain gauges attached to the human tibial shaft. *Acta Orthopaedica*
2414 *Scandinavica* 46:256-268.
2415 Lee AH, and Werning S. 2008. Sexual maturity in growing dinosaurs does not fit reptilian
2416 growth models. *Proceedings of the National Academy of Sciences* 105:582-587.
2417 Lee MSY, Cau A, Naish D, and Dyke GJ. 2014. Sustained miniaturization and anatomical
2418 innovation in the dinosaurian ancestors of birds. *Science* 345:562-566.
2419 Legendre P, and Legendre L. 2012. *Numerical Ecology, Third English Edition*. Amsterdam:
2420 Elsevier.
2421 Lieberman DE, Pearson OM, Polk JD, Demes B, and Crompton AW. 2003. Optimization of
2422 bone growth and remodelling in response to loading in tapered mammalian limbs.
2423 *Journal of Experimental Biology* 206:3125-3138.
2424 Lieberman DE, Polk JD, and Demes B. 2004. Predicting Long Bone Loading From Cross-
2425 Sectional Geometry. *American Journal of Physical Anthropology* 123:156-171.
2426 Lockley MG. 1991. *Tracking Dinosaurs*. Cambridge: Cambridge University Press.
2427 Lovejoy CO, Meindl RS, Ohman JC, Heiple KG, and White TD. 2002. The Maka Femur and Its
2428 Bearing on the Antiquity of Human Walking: Applying Contemporary Concepts of
2429 Morphogenesis to the Human Fossil Record. *American Journal of Physical Anthropology*
2430 119:97-133.
2431 Macchiarelli R, Bondioli L, Galichon V, and Tobias PV. 1999. Hip bone trabecular architecture
2432 shows uniquely distinctive locomotor behaviour in South African australopithecines.
2433 *Journal of Human Evolution* 36:211-232.
2434 Maidment SCR, and Barrett PM. 2014. Osteological correlates for quadrupedality in
2435 ornithischian dinosaurs. *Acta Palaeontologica Polonica* 59:53-70.
2436 Maidment SCR, Bates KT, Falkingham PL, VanBuren C, Arbour V, and Barrett PM. 2014.
2437 Locomotion in ornithischian dinosaurs: an assessment using three-dimensional
2438 computational modelling. *Biological Reviews* 89:588-617.
2439 Maidment SCR, Linton DH, Upchurch P, and Barrett PM. 2012. Limb-Bone Scaling Indicates
2440 Diverse Stance and Gait in Quadrupedal Ornithischian Dinosaurs. *PLoS ONE* 7:e36904.
2441 Main RP, and Biewener AA. 2004. Ontogenetic patterns of limb loading, *in vivo* bone strains and
2442 growth in the goat radius. *Journal of Experimental Biology* 207:2577-2588.

Main RP, and Biewener AA. 2007. Skeletal strain patterns and growth in the emu hindlimb during ontogeny. *Journal of Experimental Biology* 210:2676-2690.
Mallison H. 2010a. CAD assessment of the posture and range of motion of *Kentrosaurus aethiopicus* Hennig 1915. *Swiss Journal of Geosciences* 103:211-233.
Mallison H. 2010b. The digital *Plateosaurus* II: An assessment of the range of motion of the limbs and vertebral column and of previous reconstructions using a digital skeletal mount. *Acta Palaeontologica Polonica* 55:433-458.
Maquer G, Musy SN, Wandel J, Gross T, and Zysset PK. 2015. Bone Volume Fraction and Fabric Anisotropy Are Better Determinants of Trabecular Bone Stiffness than Other Morphological Variables. *Journal of Bone and Mineral Research* 30:1000-1008.
Martin RB, Burr DB, and Sharkey NA. 1998. *Skeletal Tissue Mechanics*. New York: Springer.
Matarazzo SA. 2015. Trabecular Architecture of the Manual Elements Reflects Locomotor Patterns in Primates. *PLoS ONE* 10:e0120436.
Mazzetta GV, Fariña RA, and Vizcaíno SF. 1998. On the palaeobiology of the South American horned theropod *Carnotaurus sastrei* Bonaparte. *Gaia* 15:185-192.
Middleton KM, and Gatesy SM. 2000. Theropod forelimb design and evolution. *Zoological Journal of the Linnean Society* 128:149-187.
Miller Z, Fuchs MB, and Arcan M. 2002. Trabecular bone adaptation with an orthotropic material model. *Journal of Biomechanics* 35:247-256.
Mitchell KJ, Llamas B, Soubrier J, Rawlence NJ, Worthy TH, Wood J, Lee MSY, and Cooper A. 2014. Ancient DNA reveals elephant birds and kiwi are sister taxa and clarifies ratite bird evolution. *Science* 344:898-900.
Mittra E, Rubin CT, and Qin Y-X. 2005. Interrelationship of trabecular mechanical and microstructural properties in sheep trabecular bone. *Journal of Biomechanics* 38:1229-1237.
Molnar RE, and Farlow JO. 1990. Carnosaur Paleobiology. In: Weishampel DB, Dodson P, and Osmólska H, eds. *The Dinosauria*. 1 ed. Berkeley: University of California Press, 210–224.
Moreno K, Carrano MT, and Snyder R. 2007. Morphological Changes in Pedal Phalanges Through Ornithopod Dinosaur Evolution: A Biomechanical Approach. *Journal of Morphology* 268:50-63.
Morgan-Richards M, Trewick SA, Bartosch-Härlid A, Kardailsky O, Phillips MJ, McLenachan P, and Penny D. 2008. Bird evolution: testing the Metaves clade with six new mitochondrial genomes. *BMC Evolutionary Biology* 8:20.
Mullender MG, and Huiskes R. 1995. Proposal for the Regulatory Mechanism of Wolff's Law. *Journal of Orthopaedic Research* 13:503-512.
Murray PDF. 1936. *Bones: A Study of the Development and Structure of the Vertebrate Skeleton*. Cambridge: Cambridge University Press.
Nafei A, Danielsen CC, Linde F, and Hvid I. 2000a. Properties of growing trabecular ovine bone, part I: mechanical and physical properties. *Journal of Bone and Joint Surgery* 82B:910-920.
Nafei A, Kabel J, Odgaard A, Linde F, and Hvid I. 2000b. Properties of growing trabecular ovine bone, part II: architectural and mechanical properties. *Journal of Bone and Joint Surgery* 82B:921-927.
Naish D. 2012. Birds. In: Brett-Surman MK, Holtz TR, Jr, and Farlow JO, eds. *The Complete Dinosaur*. 2 ed. Bloomington: Indiana University Press, 379-423.

2489 Novas FE. 1996. Dinosaur monophyly. *Journal of Vertebrate Paleontology* 16:723-741.
2490 Odgaard A. 1997. Three-Dimensional Methods for Quantification of Cancellous Bone
2491 Architecture. *Bone* 20:315-328.
2492 Odgaard A. 2001. Quantification of Cancellous Bone Architecture. In: Cowin SC, ed. *Bone*
2493 *Biomechanics Handbook*. 2 ed. Boca Raton: CRC Press, 14-11–14-19.
2494 Odgaard A, Kabel J, van Rietbergen B, Dalstra M, and Huiskes R. 1997. Fabric and elastic
2495 principal directions of cancellous bone are closely related. *Journal of Biomechanics*
2496 30:487-495.
2497 Ollion J, Cochennec J, Loll F, Escudé C, and Boudier T. 2013. TANGO: A Generic Tool for
2498 High-throughput 3D Image Analysis for Studying Nuclear Organization. *Bioinformatics*
2499 29:1840-1841.
2500 Olmos M, Casinos A, and Cubo J. 1996. Limb allometry in birds. *Annales des Sciences*
2501 *naturelles, Zoologie, Paris* 17:39-49.
2502 Ostrom JH. 1969. Osteology of *Deinonychus antirrhopus*, and unusual theropod from the Lower
2503 Cretaceous of Montana. *Bulletin of the Peabody Museum of Natural History* 30:1-165.
2504 Owen R. 1866. On the Osteology of the Dodo (*Didus ineptus*, Linn.). *Transactions of the*
2505 *Zoological Society of London* 5:49-85.
2506 Oxnard CE, and Yang HC. 1981. Beyond biometrics: studies of complex biological patterns.
2507 *Symposium of the Zoological Society of London* 46:127.
2508 Parfitt AM. 1983. The physiologic and clinic significance of bone histomorphometric data. In:
2509 Recker RR, ed. *Bone Histomorphometry: Techniques and Interpretation*. Boca Raton:
2510 CRC Press, 143-223.
2511 Paul GS. 1988. *Predatory Dinosaurs of the World*. New York: Simon & Schuster.
2512 Paul GS. 1998. Limb design, function and running performance in ostrich-mimics and
2513 tyrannosaurs. *Gaia* 15:257-270.
2514 Paul GS. 2008. The Extreme Lifestyles and Habits of the Gigantic Tyrannosaurid Superpredators
2515 of the Late Cretaceous of North America and Asia. In: Larsen PL, and Carpenter K, eds.
2516 *Tyrannosaurus rex, the Tyrant King*. Bloomington: Indiana University Press, 307-354.
2517 Pauwels F. 1980. *Biomechanics of the Locomotor Apparatus*. Berlin: Springer-Verlag.
2518 Pearson OM, and Lieberman DE. 2004. The Aging of Wolff's "Law": Ontogeny and Responses
2519 to Mechanical Loading in Cortical Bone. *Yearbook of Physical Anthropology* 47:63-99.
2520 Petterson U, Nilsson M, Sundh V, Mellström D, and Lorentzon M. 2010. Physical activity is the
2521 strongest predictor of calcaneal peak bone mass in young Swedish men. *Osteoporosis*
2522 *International* 21:447-455.
2523 Phillips ATM. 2012. Structural optimisation: biomechanics of the femur. *Proceedings of the*
2524 *Institution of Civil Engineers – Engineering and Computational Mechanics* 165:147-154.
2525 Phillips ATM, Villette CC, and Modenese L. 2015. Femoral bone mesoscale structural
2526 architecture prediction using musculoskeletal and finite element modelling. *International*
2527 *Biomechanics* 2:43-61.
2528 Phillips MJ, Gibb GC, Crimp EA, and Penny D. 2010. Tinamous and Moa Flock Together:
2529 Mitochondrial Genome Sequence Analysis Reveals Independent Losses of Flight among
2530 Ratites. *Systematic Biology* 59:90-107.
2531 Pidaparti RMV, and Turner CH. 1997. Cancellous bone architecture: advantages of
2532 nonorthogonal trabecular alignment under multidirectional joint loading. *Journal of*
2533 *Biomechanics* 30:979-983.

2534 Pittman M, Gatesy SM, Upchurch P, Goswani A, and Hutchinson JR. 2013. Shake a Tail
2535 Feather: The Evolution of the Theropod Tail into a Stiff Aerodynamic Surface. *PLoS*
2536 *ONE* 8:e63115.
2537 Podsiadlo P, Dahl L, Englund M, Lohmander LS, and Stachowiak GW. 2008. Differences in
2538 trabecular bone texture between knees with and without radiographic osteoarthritis
2539 detected by fractal methods. *Osteoarthritis and Cartilage* 16:323-329.
2540 Polk JD, Blumenfeld J, and Ahluwalia D. 2008. Knee Posture Predicted From Subchondral
2541 Apparent Density in the Distal Femur: An Experimental Validation. *The Anatomical*
2542 *Record* 16:323-329.
2543 Pontzer H, Allen V, and Hutchinson JR. 2009. Biomechanics of Running Indicates Endothermy
2544 in Bipedal Dinosaurs. *PLoS ONE* 4:e7783.
2545 Pontzer H, Lieberman DE, Momin E, Devlin MJ, Polk JD, Hallgrímsson B, and Cooper DML.
2546 2006. Trabecular bone in the bird knee responds with high sensitivity to changes in load
2547 orientation. *Journal of Experimental Biology* 209:57-65.
2548 Prum RO, Berv JS, Dornburg A, Field DJ, Townsend JP, lemmon EM, and Lemmon AR. 2015.
2549 A comprehensive phylogeny of birds (Aves) using targeted next-generation DNA
2550 sequencing. *Nature* 526:569-573.
2551 Radin EL, Orr RB, Kelman JL, Paul IL, and Rose RM. 1982. Effect of prolonged walking on
2552 concrete on the knees of sheep. *Journal of Biomechanics* 15:487-492.
2553 Rafferty KL. 1998. Structural design of the femoral neck in primates. *Journal of Human*
2554 *Evolution* 34:361-383.
2555 Raichlen DA, Gordon AD, Foster AD, Webber JT, Sukhdeo SM, Scott RS, Gosman JH, and
2556 Ryan TM. 2015. An ontogenetic framework linking locomotion and trabecular bone
2557 architecture with applications for reconstructing hominin life history. *Journal of Human*
2558 *Evolution* 81:1-12.
2559 Reid REH. 2012. “Intermediate” Dinosaurs: The Case Updated. In: Brett-Surman MK, Holtz TR,
2560 Jr, and Farlow JO, eds. *The Complete Dinosaur*. 2 ed. Bloomington: Indiana University
2561 Press, 873-921.
2562 Reilly SM. 2000. Locomotion in the Quail (*Coturnix japonica*): The Kinematics of Walking and
2563 Increasing Speed. *Journal of Morphology* 243:173-185.
2564 Robling AG, Castillo AB, and Turner CH. 2006. Biomechanical and Molecular Regulation of
2565 Bone Remodeling. *Annual Review of Biomedical Engineering* 8:455-498.
2566 Robling AG, and Turner CH. 2009. Mechanical Signaling for Bone Modeling and Remodeling.
2567 *Critical Reviews in Eukaryote Gene Expression* 19:319-338.
2568 Rook L, Bondioli L, Köhler M, Moyà-Solà S, and Macchiarelli R. 1999. Oreopithecus was a
2569 bipedal ape after all: Evidence from the iliac cancellous architecture. *Proceedings of the*
2570 *National Academy of Sciences* 96:8795-8799.
2571 Rubenson J, Lloyd DG, Besier TF, Heliams DB, and Fournier PA. 2007. Running in ostriches
2572 (*Stuthio camelus*): three-dimensional joint axes alignment and joint kinematics. *Journal*
2573 *of Experimental Biology* 210:2548-2562.
2574 Rudman KE, Aspden RM, and Meakin JR. 2006. Compression or tension? The stress distribution
2575 in the proximal femur. *BioMedical Engineering OnLine* 5:12.
2576 Ruimerman R, Hilbers P, van Rietbergen B, and Huiskes R. 2005. A theoretical framework for
2577 strain-related trabecular bone maintenance and adaptation. *Journal of Biomechanics*
2578 38:931-941.

2579 Russell DA. 1972. Ostrich Dinosaurs from the Late Cretaceous of Western Canada. *Canadian*
2580 *Journal of Earth Sciences* 9:375-402.
2581 Ryan TM, and Ketcham RA. 2002a. Femoral head trabecular bone structure in two omomyid
2582 primates. *Journal of Human Evolution* 43:241-263.
2583 Ryan TM, and Ketcham RA. 2002b. The three-dimensional structure of trabecular bone in the
2584 femoral head of strepsirrhine primates. *Journal of Human Evolution* 43:1-26.
2585 Ryan TM, and Ketcham RA. 2005. Angular Orientation of Trabecular Bone in the Femoral Head
2586 and Its Relationship to Hip Joint Loads in Leaping Primates. *Journal of Morphology*
2587 265:249-263.
2588 Ryan TM, and Krovitz GE. 2006. Trabecular bone ontogeny in the human proximal femur.
2589 *Journal of Human Evolution* 51:591-602.
2590 Ryan TM, and Shaw CN. 2012. Unique Suites of Trabecular Bone Features Characterize
2591 Locomotor Behavior in Human and Non-Human Anthropoid Primates. *PLoS ONE*
2592 7:e41037.
2593 Ryan TM, and Shaw CN. 2013. Trabecular bone microstructure scales allometrically in the
2594 primate humerus and femur. *Proceedings of the Royal Society of London, Series B*
2595 280:20130172.
2596 Ryan TM, and Test M. 2007. Methodological Issues in Comparative Analyses of Trabecular
2597 Bone Morphology. Eighth International Conference of Vertebrate Morphology, July 16–
2598 21, 2007. Paris, France. p 1126-1127.
2599 Ryan TM, and van Rietbergen B. 2005. Mechanical Significance of Femoral head Trabecular
2600 Bone structure in *Loris* and *Galago* Evaluated Using Micromechanical Finite Element
2601 Models. *American Journal of Physical Anthropology* 126:82-96.
2602 Saers JPP, Cazorla-Bak Y, Shaw CN, Stock JT, and Ryan TM. 2016. Trabecular bone structural
2603 variation throughout the human lower limb. *Journal of Human Evolution* 97:97-108.
2604 Saparin P, Scherf H, Hublin J-J, Fratzl P, and Weinkamer R. 2011. Structural Adaptation of
2605 Trabecular Bone Revealed by Position Resolved Analysis of Proximal Femora of
2606 Different Primates. *The Anatomical Record* 294:55-67.
2607 Scherf H. 2008. Locomotion-related Femoral Trabecular Architectures in Primates – High
2608 Resolution Computed Tomographies and Their Implications for Estimations of
2609 Locomotor Preferences of Fossil Primates. In: Endo H, and Frey R, eds. *Anatomical*
2610 *Imaging: Towards a New Morphology*. Tokyo: Springer, 39-59.
2611 Scherf H, Harvati K, and Hublin J-J. 2013. A comparison of proximal humeral cancellous bone
2612 of great apes and humans. *Journal of Human Evolution* 65:29-38.
2613 Schulte FA, Ruffoni D, Lambers FM, Christen D, Webster DJ, Kuhn G, and Müller R. 2013.
2614 Local mechanical stimuli regulate bone formation and resorption in mice at the tissue
2615 level. *PLoS ONE* 8:e62172.
2616 Schweitzer MH, Wittmeyer JL, and Horner JR. 2005. Gender-Specific Reproductive Tissue in
2617 Ratites and *Tyrannosaurus rex*. *Science* 308:1456-1460.
2618 Sereno PC. 1999. The evolution of dinosaurs. *Science* 284:2137-2147.
2619 Shrout PE, and Fleiss JL. 1979. Intraclass Correlations: Uses in Assessing Rater Reliability.
2620 *Psychological Bulletin* 86:420-428.
2621 Singh I. 1978. The architecture of cancellous bone. *Journal of Anatomy* 127:305-310.
2622 Singh M, Nagrath AR, and Maini PS. 1970. Changes in trabecular pattern of the upper end of the
2623 femur as an index of osteoporosis. *Journal of Bone and Joint Surgery* 52B:457-467.

2624 Skedros JG, and Baucom SL. 2007. Mathematical analysis of trabecular 'trajectories' in apparent
2625 trajectorial structures: The unfortunate historical emphasis on the human proximal femur.
2626 *Journal of Theoretical Biology* 244:15-45.
2627 Skedros JG, Hunt KJ, and Bloebaum RD. 2004. Relationships of Loading History and Structural
2628 and Material Characteristics of Bone: Development of the Mule Deer Calcaneus. *Journal*
2629 *of Morphology* 259:281-307.
2630 Skedros JG, Sorenson SM, Hunt KJ, and Holyoak JD. 2007. Ontogenetic Structural and Material
2631 Variations in Ovine Calcanei: A Model for Interpreting Bone Adaptation. *The*
2632 *Anatomical Record* 290:284-300.
2633 Skerry T. 2000. Biomechanical influences on skeletal growth and development. In: O'Higgins P,
2634 and Cohn MJ, eds. *Development, Growth, and Evolution: Implications for the Study of*
2635 *the Hominid Skeleton*. San Diego: Academic Press, 29-39.
2636 Skinner MM, Stephens NB, Tsegai ZJ, Foote AC, Nguyen NH, Gross T, Pahr DH, Hublin J-J,
2637 and Kivell TL. 2015. Human-like hand use in Australopithecus africanus. *Science*
2638 347:395-399.
2639 Smith JV, Braun EL, and Kimball RT. 2013. Ratite Nonmonophyly: Independent Evidence from
2640 40 Novel Loci. *Systematic Biology* 62:35-49.
2641 Smith NC, Jespers KJ, and Wilson AM. 2010. Ontogenetic scaling of locomotor kinetics and
2642 kinematics of the ostrich (*Struthio camelus*). *Journal of Experimental Biology* 213:1347-
2643 1355.
2644 Smith TS, Martin RB, Hubbard M, and Bay BK. 1997. Surface Remodeing of Trabecular Bone
2645 Using a Tissue Level Model. *Journal of Orthopaedic Research* 15:593-600.
2646 Stephens NB, Kivell TL, Gross T, Pahr DH, Lazenby RA, Hublin J-J, Hershkovitz I, and Skinner
2647 MM. 2016. Trabecular architecture in the thumb of *Pan* and *Homo*: implications for
2648 investigating hand use, loading, and hand preference in the fossil record. *American*
2649 *Journal of Physical Anthropology* 161:603-619.
2650 Stoessel A, and Fischer MS. 2012. Comparative intralimb coordination in avian bipedal
2651 locomotion. *Journal of Experimental Biology* 215:4055-4069.
2652 Su A, and Carlson KJ. 2017. Comparative analysis of trabecular bone structure and orientation in
2653 South African hominin tali. *Journal of Human Evolution* 106:1-18.
2654 Su A, Wallace IJ, and Nakatsukasa M. 2013. Trabecular bone anisotropy and orientation in an
2655 Early Pleistocene hominin talus from East Turkana, Kenya. *Journal of Human Evolution*
2656 64:667-677.
2657 Su SC, Skedros JG, Bachus KN, and Bloebaum RD. 1999. Loading conditions and cortical bone
2658 construction of an artiodactyl calcaneus. *Journal of Experimental Biology* 202:3239-
2659 3254.
2660 Sues H-D. 1978. Functional morphology of the dome in pachycephalosaurid dinosaurs. *Neus*
2661 *Jahrbuch fur Geologie und Palaontologie* 1978:459-472.
2662 Sutherland D. 1997. The development of mature gait. *Gait & Posture* 6:163-170.
2663 Sverdlova N. 2011. Tensile trabeculae - Myth or Reality? *Journal of Musculoskeletal and*
2664 *Neuronal Interactions* 11:1-7.
2665 Swartz SM, Parker A, and Huo C. 1998. Theoretical and empirical scaling patterns and
2666 topological homology in bone trabeculae. *Journal of Experimental Biology* 201:573-590.
2667 Takechi H. 1977. Trabecular architecture of the knee joint. *Acta Orthopaedica Scandinavica*
2668 48:673-681.

2669 Tanck E, Homminga J, van Lenthe GH, and Huiskes R. 2001. Increase in Bone Volume Fraction
2670 Precedes Architectural Adaptation in Growing Bone. *Bone* 28:650-654.
2671 Thomas DA, and Farlow JO. 1997. Tracking a Dinosaur Attack. *Scientific American* 277:74-79.
2672 Thomason JJ. 1985. The relationship of trabecular architecture to inferred loading patterns in the
2673 third metacarpals of the extinct equids *Merychippus* and *Mesohippus*. *Paleobiology*
2674 11:323-335.
2675 Thomason JJ. 1995. To what extent can the mechanical environment of a bone be inferred from
2676 its internal architecture? In: Thomason JJ, ed. *Functional Morphology in Vertebrate*
2677 *Paleontology*. New York: Cambridge University Press, 249-263.
2678 Thompson DW. 1942. *On Growth and Form*. Cambridge: Cambridge University Press.
2679 Thulborn RA. 1984. Preferred gaits of bipedal dinosaurs. *Alcheringa* 8:243-252.
2680 Thulborn T. 1990. *Dinosaur Tracks*. London: Chapman and Hall.
2681 Tobin WJ. 1955. The internal architecture of the femur and its clinical significance: the upper
2682 end. *Journal of Bone and Joint Surgery* 37A:57-72.
2683 Townsley W. 1944. The architectural structure of the upper end of the femur in various
2684 pathological conditions. *Journal of Pathology* 56:199-207.
2685 Townsley W. 1948. The influence of mechanical factors on the development and structure of
2686 bone. *American Journal of Physical Anthropology* 6:25-46.
2687 Tsai HP, and Holliday CM. 2015. Articular Soft Tissue Anatomy of the Archosaur Hip Joint:
2688 Structural Homology and Functional Implications. *Journal of Morphology* 276:601-630.
2689 Tsegai ZJ, Kivell TL, Gross T, Nguyen NH, Pahr DH, Smaers JB, and Skinner MM. 2013.
2690 Trabecular Bone Structure Correlates with Hand Posture and Use in Hominoids. *PLoS*
2691 *ONE* 8:e78781.
2692 Tsegai ZJ, Skinner MM, Gee AH, Pahr DH, Treece GM, Hublin J-J, and Kivell TL. 2017.
2693 Trabecular and cortical bone structure of the talus and distal tibia in *Pan* and *Homo*.
2694 *American Journal of Physical Anthropology* 163:784-805.
2695 Tsubota K, Adachi T, and Tomita Y. 2002. Functional adaptation of cancellous bone in human
2696 proximal femur predicted by trabecular surface remodeling simulation toward uniform
2697 stress state. *Journal of Biomechanics* 35:1541-1551.
2698 Tsubota K, Suzuki Y, Yamada T, Hojo M, Makinouchi A, and Adachi T. 2009. Computer
2699 simulation of trabecular remodelling in human proximal femur using large-scale voxel
2700 FE models: Approach to understanding Wolff's law. *Journal of Biomechanics* 42:1088-
2701 1094.
2702 Turner AH, Makovicky PJ, and Norell MA. 2012. A review of dromaeosaurid systematics and
2703 paravian phylogeny. *Bulletin of the American Museum of Natural History* 371:1-206.
2704 Turner AH, Pol D, Clarke JA, Erickson GM, and Norell MA. 2007. A Basal Dromaeosaurid and
2705 Size Evolution Preceding Avian Flight. *Science* 317:1378-1381.
2706 Turner CH. 1992. On Wolff's Law of trabecular architecture. *Journal of Biomechanics* 25:1-9.
2707 Turner CH, Anne V, and Pidaparti RMV. 1997. A uniform strain criterion for trabecular bone
2708 adaptation: do continuum-level strain gradients drive adaptation? *Journal of*
2709 *Biomechanics* 30:555-563.
2710 Turner CH, Cowin SC, Rho JY, Ashman RB, and Rice JC. 1990. The fabric dependence of the
2711 orthotropic elastic constants of cancellous bone. *Journal of Biomechanics* 23:549-561.
2712 Ulrich D, van Rietbergen B, Laib A, and Rüegsegger P. 1999. The Ability of Three-Dimensional
2713 Structural Indices to Reflect Mechanical Aspects of Trabecular Bone. *Bone* 25:55-60.

van der Meulen MCH, Morgan TG, Yang X, Baldini TH, Myers ER, Wright TM, and Bostrom MPG. 2006. Cancellous bone adaptation to in vivo loading in a rabbit model. *Bone* 38:871-877.

van der Reest AJ, and Currie PJ. 2017. Troodontids (Theropoda) from the Dinosaur Park Formation, Alberta, with a description of a unique new taxon: implications for deinonychosaur diversity in North America. *Canadian Journal of Earth Sciences* 54:919-935.

van Rietbergen B, Huiskes R, Eckstein F, and Rüegsegger P. 2003. Trabecular Bone Tissue Strains in the Healthy and Osteoporotic Human Femur. *Journal of Bone and Mineral Research* 18:1781-1788.

van Rietbergen B, Müller R, Ulrich D, Rüegsegger P, and Huiskes R. 1999. Tissue stresses and strain in trabeculae of a canine proximal femur can be quantified from computer simulations. *Journal of Biomechanics* 32:165-173.

Vander Sloten J, and Van der Perre G. 1989. Trabecular structure compared to stress trajectories in the proximal femur and calcaneus. *Journal of Biomedical Engineering* 11:203-208.

Verner KA, Lehner M, Lamas LP, and Main RP. 2016. Experimental tests of planar strain theory for predicting cross-sectional longitudinal and shear strains. *Journal of Experimental Biology* 219:3082-3090.

Volpato V. 2008. Morphogenèse de l'endostructure osseuse de l'ilion humain. *Comptes Rendus Palevol* 7:463-471.

von Meyer GH. 1867. Die Architektur der Spongiosa. *Archiv für Anatomie, Physiologie und Wissenschaftliche Medicin* 34:615-628.

Wainwright SA, Biggs WD, Currey JD, and Gosline JM. 1976. *Mechanical Design in Organisms*. London: Edward Arnold (Publishers) Limited.

Wallace IJ, Demes B, C. M, Pearson OM, Polk JD, and Lieberman DE. 2014. Exercise-Induced Bone Formation is Poorly Linked to Local Strain Magnitude in the Sheep Tibia. *PLoS ONE* 9:e99108.

Wallace IJ, Judex S, and Demes B. 2015. Effects of load-bearing exercise on skeletal structure andmechanics differ between outbred populations of mice. *Bone* 72:1-8.

Wallace IJ, Tommasini SM, Judex S, Garland T, Jr, and Demes B. 2012. Genetic Variations and Physical Activity as Determinants of Limb Bone Morphology: An Experimental Approach Using a Mouse Model. *American Journal of Physical Anthropology* 148:24-35.

Wang H, Ji B, Liu XS, Guo XE, Huang Y, and Hwang K-C. 2012. Analysis of microstructural and mechanical alterations of trabecular bone in a simulated three-dimensional remodelling process. *Journal of Biomechanics* 45:2417-2425.

Ward FO. 1838. *Outlines of Human Osteology*. London: Henry Renshaw.

Warton DI, Wright IJ, Falster DS, and Westoby M. 2006. Bivariate line-fitting methods for allometry. *Biological Reviews* 81:259-291.

Weingarten VI, Seide P, and Petersen JP. 1968. Buckling of thin-walled circular cylinders. *NASA Space Vehicle Design Criteria (Structures) Monographs* SP-8007:1-49.

Weishampel DB, Dodson P, and Osmólska H. 2004. The Dinosauria. 2 ed. Berkeley: University of California Press.

Wellnhofer P. 1991. *The Illustrated Encyclopedia of Pterosaurs*. New York: Crescent Books.

Wilson JA, and Carrano MT. 1999. Titanosaurs and the origin of "wide-gauge" trackways: a biomechanical and systematic perspective on sauropod locomotion. *Paleobiology* 25:252-267.

Winter DA. 2009. *Biomechanics and Motor Control of Human Movement*. Hoboken: John Wiley & Sons, Inc.
Wolff J. 1892. *Das Gesetz der Transformation der Knochen*. Berlin: August Hirschwald.
Wolschrijn CF, and Weijs WA. 2005. Development of the Subchondral Bone Layer of the Medial Coronoid Process of the Canine Ulna. *The Anatomical Record* 284A:439-445.
Yang P-F, Sanno M, Ganse B, Koy T, Brüggemann G-P, Müller LP, and Rittweger J. 2014. Torsion and Antero-Posterior Bending in the *In Vivo* Human Tibia Loading Regimes during Walking and Running. *PLoS ONE* 9:e94525.
Yuri T, Kimball RT, Harshman J, Bowie RCK, Braun MJ, Chojnowski JL, Han K-L, Hackett SJ, Huddleston CJ, Moore WS, Reddy S, Sheldon FH, Steadman DW, Witt CC, and Braun EL. 2013. Parsimony and Model-Based Analyses of Indels in Avian Nuclear Genes Reveal Congruent and Incongruent Phylogenetic Signals. *Biology* 2:419-444.
Zanno LE, Gillette DD, Albright LB, and Titus AL. 2009. A new North American therizinosaurid and the role of herbivory in 'predatory' dinosaur evolution. *Proceedings of the Royal Society of London, Series B* 276:3505-3511.

I.9 Figure captions

Figure 1. Cancellous bone occurrence and macrostructure, as illustrated here with the femur of a cow (*Bos tauros*), sectioned in the coronal plane. Cancellous bone occurs in the proximal and distal ends of the bone (as indicated by the braces), underlying the thin cortical bone capping the epiphyses and apophyses, as well as the metaphyses. A close up view of the cancellous bone (right) reveals the highly porous nature of the tissue, giving it a spongy appearance.

Figure 2. Cancellous bone fabric as represented by its principal architectural directions. (A) A cube of cancellous bone of side length 5.33 mm, from the proximal femur of a freshwater crocodile (*Crocodylus johnstoni*), with the principal directions of the bone's architecture superimposed. As an orthotropic material, cancellous bone fabric is completely described by three principal directions. (B) The fabric ellipsoid representation for this cube of cancellous bone is derived from the vectors that describe the principal architectural directions. The ellipsoid's major, semimajor and minor axes are given by the primary ($\mathbf{u}_1$), secondary ($\mathbf{u}_2$) and tertiary ($\mathbf{u}_3$) directions of the cancellous bone architecture, which correspond to the eigenvectors of the fabric tensor. The relative lengths of each axis depend on the relative magnitudes of the principal directions, which correspond to the eigenvalues of the fabric tensor. The degree of anisotropy

(DA) describes the extent to which the trabeculae are aligned within a sample, and is given as the relative magnitude of the primary and tertiary eigenvalues (i.e., DA = e_1/e_3); in this instance DA = 1.44. The cancellous bone geometry was derived via micro-computed X-ray tomographic scanning (Siemens Inveon, 80 kV, 500 μA, 900 ms exposure, 53.3 μm isotropic resolution) and 3-D visualization (Mimics 17.0, Materialise NV, Belgium). The material directions were calculated using the mean intercept length method as implemented in the software Quant3D 2.3 (see Ketcham & Ryan 2004).

Figure 3. Cancellous bone fabric direction can change in response to experimentally induced changes in mechanical loading. (A–C) The study of Goldstein et al. (1991). In the distal femur of normal dogs (A), the principal directions of cancellous bone fabric (arrows) vary throughout the bone. After 38 weeks following surgical implantation of load cells (B, arrows indicate direction of applied principal compressive stress), the principal directions of the cancellous fabric were greatly altered, and were reoriented to align with the compressive stress applied by the load cells (C). (D–F) The study of Pontzer et al. (2006). Subjecting guineafowl to running on inclined treadmills caused them to move with a more flexed knee posture compared to running on the level (the angle θ is reduced). The postural change resulted in an altered relative orientation of the joint force that the distal femur experienced (E, F, red arrow), which after 45 days was found to produce a changed orientation of peak trabecular density (dotted arrow).

Figure 4. Trabeculae tend to align themselves with the orientation of principal stresses resulting from *in vivo* loading. (A) Coronal micro-computed tomographic section through a human proximal femur, illustrating the architecture of cancellous bone. Image provided courtesy of SCANCO Medical AG. (B) A typical loading regime experienced by the proximal femur during locomotion, here the single-legged stance phase of walking (after Rudman et al. 2006). This consists of the joint reaction force applied by the acetabulum (JRF), the force of the adductor muscles pulling on the trochanter (add) and the small forces applied by the capsular ligaments (c). (C) Principal stress trajectories resulting from the loading regime in B, as calculated by a two-dimensional finite element analysis (after Rudman et al. 2006). Note the striking correspondence of the main tracts of trabeculae in A and the principal stress trajectories in C.

2827

2828

2829 **Figure 5.** Cancellous bone remodelling at the cellular level can bring about changes in the entire
2830 architecture at the whole-bone level. (A–D) Schematic illustration of the mechanostat of
2831 cancellous bone. Given an initial architecture in A, a change in the loading regime will lead to
2832 some parts becoming overloaded (high stress, dotted) and others becoming underloaded (low
2833 stress, horizontal hatching) in B. Surface remodelling by osteoblasts and osteoclasts (C) acts to
2834 deposit additional bone material in those overloaded areas (dark grey) and remove bone material
2835 from those underloaded areas (light grey); arrows show direction in which local bone surface
2836 moves. This continues *ad infinitum* until all bone tissue is neither too highly strained nor too little
2837 strained. (E, F) An illustration of the application of the mechanostat principal on the level of the
2838 whole bone, via computational modelling (adapted from Jang & Kim 2008; Jang & Kim 2010a).
2839 In this example of the human proximal femur, with loads simulating both the joint reaction force
2840 and forces from the abductor muscles, the initially isotropic architecture (E) undergoes
2841 remodelling until equilibrium is reached. The resulting equilibrium architecture (F) is extremely
2842 similar to that observed in the real specimen (cf. Fig. 4A)

2843

2844

2845 **Figure 6.** Orthogonal arrangements of trabeculae usually reflect a highly consistent loading
2846 regime experienced by a bone. (A) Sagittal section through the calcaneum of a cow, with the pull
2847 of the Achilles tendon on the distal end indicated by the arrow. (B) A force applied to the free
2848 end of a cantilever beam is comparable to the loading regime experienced by the cow calcaneum
2849 during locomotion. The bending of the cantilever beam produces principal stress trajectories that
2850 are very similar to the overall arrangement of trabeculae in the calcaneum (solid lines are
2851 trajectories of compressive stress; dashed lines are trajectories of tensile stress). Since the
2852 calcaneum is only loaded in this fashion, the two systems of trabeculae (one curving from up, one
2853 curving down) tend to intersect at right angles.

2854

2855

2856 **Figure 7.** Three different ways in which the architecture of cancellous bone can be influenced by
2857 its mechanical environment. See main text for full discussion. The dashed grey pathway for

epigenetics signifies that it currently remains unknown as to if and how epigenetics may influence cancellous bone mechanobiology.

Figure 8. Phylogenetic interrelationships of the major groups of animals studied. Interrelationships of non-avian theropods are based on Zanno et al. (2009), Carrano et al. (2012) and Turner et al. (2012); interrelationships of birds are based on Hackett et al. (2008), Morgan-Richards et al. (2008), Ksepka (2009), Phillips et al. (2010), Haddrath & Baker (2012), Jetz et al. (2012), Smith et al. (2013), Yuri et al. (2013), Mitchell et al. (2014), Jarvis et al. (2014), Ksepka & Phillips (2015) and Prum et al. (2015). The interrelationships of the neoavian species studied here are currently not well agreed upon, and so Neoaves is shown as an unresolved polytomy. Silhouettes depict exemplar members or each group, and are not to scale. The individual determinate species of non-avian theropod studied are listed in the inset box, and their phylogenetic position signified by superscripts.

Figure 9. Resampling the medical CT scans, as per protocol 2, helps produce a more accurate segmentation of the cancellous bone structure. This is illustrated here with a CT slice of the proximal femur of a cassowary (*Casuarius casuarius*, QMO 31137). (A) The raw CT slice. (B) A local segmentation algorithm, as per protocol 1, is applied to the slice in A, with window radius 8 pixels and contrast threshold of 25; notice that it performs poorly, with some trabeculae becoming disconnected and some intertrabecular spaces being obliterated. (C) The same CT slice as in A, but resampled to triple the resolution, that is, voxel dimensions are now ⅓ of original in-plane pixel resolution. (D) A local segmentation is applied to the resampled slice in C, using the same parameters as in B; notice that it performs far better in extracting the cancellous structure. Bicubic interpolation results in smoother boundaries to the segmented scans, in contrast to lower-order (e.g., bilinear) interpolation. The location of the insets in each panel is shown in C.

Figure 10. Schematic illustration of the image processing protocol used for the non-avian theropod micro-CT scans. (A) The original image, affected by both high and low frequency noise; segmentation of this image by global or local thresholding techniques will not work. (B) A

low-radius median filter is applied to remove high-frequency noise. (C) A large-radius median filter is applied to isolate the low-frequency (background) noise. (D) The low-frequency filtered image in C is subtracted from the high-frequency filtered image in B. (E) A low-radius mean filter is applied, followed by a global high-pass segmentation to produce the final image.

Figure 11. The arrangement of VOIs for quantitative analysis of cancellous bone architecture follows the geometric pattern of cubic close-packed spheres. This is illustrated here for the proximal right femur of Troodontidae sp. (MOR 748). Each spherical VOI has a diameter of 5 mm. In this arrangement, each VOI is just touching its neighbouring VOIs, and each sphere can be in contact with up to 12 other VOIs. (A,B) Shown in medial view. (C, D) Shown in oblique anteromedial view. Notice in C and D that VOI placement avoids the medullary cavity (orange) and cracks (green).

Figure 12. Definition of the anatomical coordinate system for the femur used in this study. This is illustrated here with the right femur of a bustard (*Ardeotis australis*, MVB 20408), and is defined by the principal axis of inertia of the bone (dashed line) and the centres of two spheres fit to the distal condyles (white circles). For left femora, their geometry and calculated mean orientation of the primary fabric vector were mirrored prior to construction of an anatomical coordinate system.

Figure 13. Schematic illustration of two of the features of diaphyseal cancellous bone that were subject to categorical scoring. (A) The orientation of trabeculae with respect to the long axis of the shaft. (B) The tendency of trabeculae to be closely associated with other trabeculae. Upper row is oblique view, lower row is section-on view. These illustrations were given to the scorers to provide them with a point of reference.

Figure 14. Pneumatization modulates trabecular spacing in the femur of both large and small birds. This is illustrated here with processed CT scan slices located approximately midway

through the femoral head in the axial plane. (A) A marrow-filled femur of *Casuarius casuarius* (QMO 30105), with mean trabecular spacing = 0.638 mm. (B) A pneumatized femur of *Dromaius novaehollandiae* (QMO 16140) with mean trabecular spacing = 1.128 mm. (C) A marrow-filled femur of *Gallus gallus* (PJB coll.), with mean trabecular spacing = 0.320 mm. (D) A pneumatized femur of *Alectura lathami* (PJB coll.), with mean trabecular spacing = 0.999 mm. Reported trabecular spacing values were calculated (for illustrative purposes) for the femoral head using the BoneJ 1.3.11 plugin for ImageJ (Doube et al. 2010). A and B are shown at the same scale, as are C and D. Scale bars are 10 mm, and yellow asterisks denote pneumatopores.

Figure 15. The main architectural features of cancellous bone in the human proximal femur. (A) Vector field of $\mathbf{u}_1$ in the head, inferior neck and greater trochanter regions, plotted on a translucent rendering of the external bone geometry; view is in the coronal plane. Schematic inset illustrates close correspondence with the principal compressive (PC) and greater trochanter (GT) groups of previous studies. (B) Vector field of $\mathbf{u}_1$ (red) and $\mathbf{u}_2$ (blue) in the middle of the metaphysis, viewed in the coronal plane. Schematic inset illustrates close correspondence with the secondary compressive (SC) and secondary tensile (ST) groups of previous studies. Note that both $\mathbf{u}_1$ and $\mathbf{u}_2$ are largely parallel to the coronal plane. (C) Vector field of $\mathbf{u}_1$ in the distal metaphysis and lesser trochanter (in oblique proximomedial view), which is largely parallel to the bone's long-axis. In this and all subsequent illustrations of fabric vector fields, the length of each fabric vector is proportional to its corresponding fabric eigenvalue. Additionally, all images are of bones from the right side of the body.

Figure 16. The main architectural features of cancellous bone in the proximal femur of birds. (A–D) Vector field of $\mathbf{u}_1$ in the femoral head and inferior neck of *Dromaius novaehollandiae* (QMO 16140; A, B) and *Struthio camelus* (MV R.2385; C, D). (E–H) Vector field of $\mathbf{u}_1$ under the facies antitrochanterica of *Rhea americana* (QMO 23517; E, F) and *Gallus gallus* (PJB coll.; G, H). (I) Isosurface rendering of cancellous bone under the facies antitrochanterica of *Gallinula tenebrosa* (PJB coll., between arrows), sectioned in the sagittal plane. (J–M) Vector field of $\mathbf{u}_1$ in the trochanteric crest of *Casuarius casuarius* (QMO 30105; J, K) and *Struthio camelus* (MV R.2385,

L, M). (N) Isosurface rendering of cancellous bone in the trochanteric crest of *Anseranus semipalmata* (QMO 29529, between arrows), sectioned in the sagittal plane. (O, P) Vector field of $\mathbf{u}_1$ throughout the entire proximal femur of *Dromaius novaehollandiae* (QMO 16140, O) and *Casuarius casuarius* (QMO 30105, P), which illustrates the increasing obliquity and disorganization of vectors in the distal metaphysis and transition to the diaphysis, shown in regions with braces. A, C, J and L are anterior views; B and D are medial views; E and G are posterior views; F, H, K and M are lateral views; O is an oblique anterolateral view; P is an oblique anteromedial view. For reference, silhouettes of the animals depicted are provided in this figure and those that follow.

Figure 17. The main architectural features of cancellous bone in the proximal femur of reptiles. (A, B) Vector field of $\mathbf{u}_1$ in the proximal femur of *Crocodylus johnstoni* (QMJ 47916). (C, D) Vector field of $\mathbf{u}_1$ in the proximal femur of *Varanus spenceri* (QMJ 84416). (E) Vector field of $\mathbf{u}_1$ throughout the proximal femur of *Varanus komodoensis* (AM R.106933), which illustrates the increasing obliquity and disorganization of vectors in the distal metaphysis and transition to the diaphysis, shown in region with braces. A and C are anterior views ('dorsal view' of herpetologists); B and D are lateral views ('posterior view' of herpetologists); E is an oblique anterolateral view. For clarity, the vectors of $\mathbf{u}_1$ in the fourth trochanter are not visible in A, C and E.

Figure 18. The orientation of $\mathbf{u}_1$ throughout the femoral head of *Masiakasaurus knopfleri*, here exemplified by FMNH PR 2117. (A) Anterior view. (B) Lateral view.

Figure 19. The main architectural features of cancellous bone in the proximal femur of both *Allosaurus* and the tyrannosaurids. These are illustrated here with a 3-D geometric model of the observed architecture, mapped to the femur of *Daspletosaurus torosus* (TMP 2001.036.0001). (A–E) Five progressive rotations of the bone, in 30° increments, from anteromedial to anterolateral views (C is a purely anterior view). (F) The observed orientation of the dominant

tract of cancellous bone in the femoral head (blue) has a gentle anterior inclination; bone shown in medial view. For explanation of the features and colour coding, refer to the main text. Inset below C is a CT slice through the proximal femur of *Tyrannosaurus rex* (MOR 1128), parallel to the coronal plane and through the middle of the femoral head. This illustrates the very characteristic tract of cancellous bone that extends from the base of the femoral neck up towards the apex of the head, highly comparable to the tract present in humans (cf. Fig. 4A).

Figure 20. The main architectural features of cancellous bone in the proximal femur of ornithomimids and caenagnathids. (A–D) Vector field of $\mathbf{u}_1$ (A, C) and $\mathbf{u}_2$ (B, D) in the femoral head and proximal metaphysis of an inteterminate ornithomimid (TMP 85.36.276), in oblique anteromedial (A, B) and oblique anterolateral (C, D) views. Note that the vector field along the anterior and posterior peripheries of the femoral head are not shown here (for clarity), where they are more typically oriented as in birds and humans. (E) Vector field of $\mathbf{u}_1$ in the greater trochanter region and distal metaphysis of an indeterminate ornithomimid (TMP 85.36.276), in oblique anterolateral view; note the increased obliquity and disorganization of vectors in the distal metaphysis (region with braces). (F) Vector field of $\mathbf{u}_1$ in the lesser trochanter of an indeterminate ornithomimid (TMP 91.36.569), in oblique anteromedial view. (G) Vector field of $\mathbf{u}_1$ in the proximal femur of an indeterminate caenagnathid (TMP 86.36.323), in a 3-D slice parallel to the axial plane and through the femoral head and lesser trochanter. Main image is shown in axial view (anterior is toward bottom of page), with inset illustrating the region illustrated in context of the whole bone. The medialmost part of the femoral head is missing (dotted line).

Figure 21. The main architectural features of cancellous bone in the proximal femur of *Falcarius utahensis* and Troodontidae sp. (A) Vector field of $\mathbf{u}_1$ in the proximal femur of *Falcarius* (UMNH VP 12361), viewed as a 3-D slice parallel to the coronal plane and through the middle of the bone. Schematic inset illustrates three main trajectories in this image, which are not too dissimilar from the patterns observed in humans and large non-avian theropods (cf. Figs 15, 19). (B, C) Vector field of $\mathbf{u}_1$ (B) and $\mathbf{u}_2$ (C) in the lesser trochanter of *Falcarius*, in oblique anterolateral view. (D) Vector field of $\mathbf{u}_2$ in the proximal femur of *Falcarius*, in a 3-D slice

parallel to the axial plane and through the femoral head. Main image is shown in axial view (anterior is toward bottom of page), with inset illustrating the region illustrated in context of the whole bone. (E, F) Vector field of $\mathbf{u}_1$ in the femoral head and inferior neck of Troodontidae sp. (MOR 748) in anterior (E) and medial (F) views. (G, H) Vector field of $\mathbf{u}_1$ in the region of the greater trochanter of Troodontidae sp. (MOR 553s-7.28.91.239) in posterior (G) and lateral (H) views. (I) Orientation of $\mathbf{u}_1$ in the lesser trochanter, or immediate region thereof, of Troodontidae sp., in oblique anterolateral view (main image illustrates MOR 748; inset illustrates MOR 553s-7.28.91.239). (J) Vector field of $\mathbf{u}_1$ throughout the metaphysis of Troodontidae sp. (MOR 553s-7.28.91.239), illustrating increasing obliquity and disorganization of vectors in the distal metaphysis and transition to the diaphysis (region with braces).

Figure 22. The mean orientation of $\mathbf{u}_1$ in the femoral head, referenced in the femur anatomical coordinate system. This is plotted on an equal-angle stereoplot, with northern hemisphere projection (using StereoNet 9.5Allmendinger et al. 2013; Cardozo & Allmendinger 2013). (A) Results for all specimens analysed. Note that for the fossil specimens, only those that were complete and well-preserved, and enabled an anatomical coordinate system to be defined, were analysed. Colour codes: black = birds, pink = human, blue = *Masiakasaurus* (FMNH PR 2153, UA 8384), orange = *Falcarius*, green = Troodontidae sp. (MOR 748), purple = general orientation for *Allosaurus* and the tyrannosaurids, red = mean orientation across birds. (B) Results for species or genera that were multiply sampled often displayed significant instraspecific or intrageneric variation, ranging up to 30.6°. Colour codes: black = *Struthio camelus*, blue = *Casuarius casuarius*, orange = *Dromaius novaehollandiae*, red = *Gallus gallus*, green = *Apteryx* spp.

Figure 23. The main architectural features of cancellous bone in the human distal femur. (A) Vector field of $\mathbf{u}_1$ in a 3-D slice parallel to the coronal plane, made through the middle of the condyles. Schematic inset illustrates weakly developed double-arcuate pattern. (B) Vector field of $\mathbf{u}_1$ in a 3-D slice parallel to the sagittal plane, made between the condyles. Schematic inset illustrates weakly developed double-arcuate pattern. (C) Vector field of $\mathbf{u}_1$ in the medial condyle,

shown for a 3-D slice parallel to the sagittal plane, made through the middle of the condyle. (D) Vector field of $\mathbf{u}_2$ at the level of the condyles, shown for a 3-D slice parallel to the axial plane, made through the middle of the condyles; anterior is toward top of page. Schematic inset illustrates the two distinctive tracts that comprise a 'butterfly pattern'.

Figure 24. The main architectural features of cancellous bone in the distal femur of birds. (A) Vector field of $\mathbf{u}_1$ in the central metaphysis of *Casuarius casuarius* (QMO 30105), in a 3-D slice, parallel to the sagittal plane and between the condyles, shown in lateral view. Note the weakly developed double arcuate pattern. (B, C) Vector field of $\mathbf{u}_2$ in a 3-D slice through the middle of the condyles in *Struthio camelus* (MV R.2385, B) and *Dromaius novaehollandiae* (QMO 11685, C), shown in distal view. Note the 'butterfly pattern' in both examples. (D) Isosurface rendering of cancellous bone in the distal condyles of *Coturnix japonica* (PJB coll.), sectioned in the axial plane; notice the 'butterfly pattern' between the arrows. (E–H) Vector field of $\mathbf{u}_1$ in the medial condyle of *Dromaius novaehollandiae* (QMO 16140, E, F) and *Casuarius casuarius* (QMO 30604, G, H), shown in anterior (E, G) and medial (F, H) views. (I, J) Vector field of $\mathbf{u}_1$ in the lateral condyle of *Gallus gallus* (PJB coll.), shown in anterior (I) and lateral (J) views. (K) Isosurface rendering of cancellous bone in the medial condyle of *Porphyrio porphyrio* (PJB coll.), sectioned in the sagittal plane. (L) Vector field of $\mathbf{u}_1$ throughout the entire distal femur of *Casuarius casuarius* (QMO 31137), illustrating increasing obliquity and disorganization of vectors in the proximal metaphysis and transition to the diaphysis (region with braces).

Figure 25. The main architectural features of cancellous bone in the distal femur of reptiles. (A, B) Vector field of $\mathbf{u}_2$ in a 3-D slice through the middle of the condyles in *Crocodylus porosus* (QMJ 48127, A) and *Varanus komodoensis* (AM R.106933, B), shown in proximal view. (C, D) Vector field of $\mathbf{u}_1$ in the medial condyle of *Crocodylus porosus* (QMJ 48127), shown in anterior (C) and medial (D) views. (E, F) Vector field of $\mathbf{u}_1$ in the lateral condyle of *Varanus spenceri* (QMJ 484416), shown in anterior (E) and lateral (F) views.

Figure 26. The main architectural features of cancellous bone in the distal femur of both *Allosaurus* and the tyrannosaurids. These are illustrated here with a 3-D geometric model of the observed architecture, mapped to the femur of *Daspletosaurus torosus* (TMP 2001.036.0001). (A–G) **S**even progressive rotations of the bone, in 30° increments, from medial to lateral views (D is a purely anterior view). Note that the architecture of the metaphysis was not observed in the *Allosaurus* specimens studied, owing to insufficient contrast or resolution in the CT scans failing to reveal any information about the metaphysis. For explanation of the features and colour coding, refer to the main text.

Figure 27. The main architectural features of cancellous bone in the distal femur of ornithomimids and caenagnathids. (A, B) Vector field of $\mathbf{u}_1$ in the lateral condyle of an indeterminate ornithomimid (TMP 99.55.337) in posterior (A) and lateral (B) views. (C, D) Vector field of $\mathbf{u}_1$ in the medial condyle of an indeterminate caenagnathid (TMP 86.36.323) in posterior (C) and medial (D) views. (E, F) Vector field of $\mathbf{u}_1$ (E) and $\mathbf{u}_2$ (F) in the distal femur of an indeterminate ornithomimid (TMP 91.36.569) at the level of the distal condyles, shown in proximal view for a 3-D slice parallel to the axial plane (inset shows location of slice). In A–D, the highlighted yellow vectors in the posterior extremities of the condyles have a much more mediolateral orientation compared to elsewhere in the condyle. This is also seen in E, where vectors that appear longer are more parallel to the axial plane, and vectors that appear shorter are more proximodistally oriented.

Figure 28. The main architectural features of cancellous bone in the distal femur of *Falcarius utahensis* and Troodontidae sp. (A, B) Vector field of $\mathbf{u}_1$ in the medial condyle of *Falcarius* (UMNH VP 12360) in anterior (A) and medial (B) views. (C) Vector field of $\mathbf{u}_1$ throughout the distal femur of Troodontidae sp. (MOR 553s-7.28.91.239), illustrating increasing obliquity and disorganization of vectors in the proximal metaphysis and transition to the diaphysis (region with braces). (D, E) Vector field of $\mathbf{u}_1$ in the lateral condyle of Troodontidae sp. (MOR 748) in anterior (D) and lateral (E) views. (F) Vector field of $\mathbf{u}_2$ in the condyles of Troodontidae sp. (MOR 748), shown as a 3-D slice through the middle of the condyles in axial view; anterior is toward top of page.

Figure 29. The mean orientation of $\mathbf{u}_1$ in the medial femoral condyle, referenced in the femur anatomical coordinate system. This is plotted on an equal-angle stereoplot, with southern hemisphere projection (using StereoNet 9.5). (A) The results for all specimens analysed; for clarity, only the posteromedial quadrant of the plot is shown. Note that for the fossil specimens, only those that were complete and well-preserved, and enabled an anatomical coordinate system to be defined, were analysed. Colour codes: black = birds, pink = human, blue = *Masiakasaurus* (FMNH PR 2153, UA 8384), orange = *Falcarius*, green = Troodontidae sp., purple = general orientation for *Allosaurus* and the tyrannosaurids, yellow = indeterminate ornithomimid (TMP 91.36.569), brown = indeterminate caenagnathid, red = mean orientation across birds. (B) Comparison of posterior inclination of $\mathbf{u}_1$ in sagittal plane *versus* femur length in birds, with major axis regression line (and associated statistics) plotted.

Figure 30. The main architectural feature of cancellous bone in the human proximal tibia is the gentle posterior inclination of $\mathbf{u}_1$ underneath the medial and lateral condyles. (A) Vector field of $\mathbf{u}_1$ under the lateral condyle, in lateral view. (B) Vector field of $\mathbf{u}_1$ under both condyles, in anterior view. (C) Vector field of $\mathbf{u}_1$ under the medial condyle, in medial view.

Figure 31. The main architectural features of cancellous bone in the proximal tibia of birds. (A, B) Vector field of $\mathbf{u}_1$ in the anterior (cranial) cnemial crest of *Dromaius novaehollandiae* (QMO 11686, A) and *Meleagris gallopavo* (RVC turkey 1, B), shown in medial view. (C, D) Vector field of $\mathbf{u}_1$ in the lateral cnemial crest of *Casuarius casuarius* (QMO 30105), shown in anterior (C) and lateral (D) views. (E) Isosurface rendering of cancellous bone in the anterior cnemial crest of *Threskiornis moluccus* (PJB coll., between arrows), sectioned in the sagittal plane. (F) Isosurface rendering of cancellous bone in the lateral cnemial crest of *Numida meleagris* (PJB coll., between arrows), sectioned in the plane of the crest. (G–J) Vector field of $\mathbf{u}_1$ under the medial condyle of *Struthio camelus* (MV R.2385, G, H) and *Gallus gallus* (PJB coll., I, J), shown in posterior (G, I) and medial (H, J) views. (K) Isosurface rendering of cancellous bone under the

medial condyle of *Eudromia elegans* (UMZC 404.e, between arrows), sectioned in the sagittal plane. (L–O) Vector field of $\mathbf{u}_1$ under the lateral condyle of *Struthio camelus* (MV R.2711, L, M) and *Dromaius novaehollandiae* (QMO 11686, N, O), shown in posterior (L, N) and lateral (M, O) views. (P) Isosurface rendering of cancellous bone under the lateral condyle of *Apteryx owenii* (UMZC 378.iii, between arrows), sectioned in the coronal plane. (Q) Vector field of $\mathbf{u}_1$ in a 3-D slice through the middle of the proximal metaphysis, cnemial crests and condyles of *Dromaius novaehollandiae* (QMO 11686), parallel to the sagittal plane. Schematic inset illustrates the moderately developed double-arcuate pattern present. (R) Vector field of $\mathbf{u}_1$ throughout the entire proximal tibia of *Dromaius novaehollandiae* (QMO 11686), illustrating increasing obliquity and disorganization of vectors in the distal metaphysis and transition to the diaphysis (region with braces).

Figure 32. The main architectural features of cancellous bone in the proximal tibia of reptiles, as exemplified by *Crocodylus porosus* (QMJ 48127). (A) Vector field of $\mathbf{u}_1$ in anterior view. (B) Vector field of $\mathbf{u}_1$ in medial view.

Figure 33. The main architectural features of cancellous bone in the proximal tibia of both *Allosaurus* and the tyrannosaurids. These are illustrated here with a 3-D geometric model of the observed architecture, mapped to the tibia of *Daspletosaurus torosus* (TMP 2001.036.0001). (A) The dominant orientation of cancellous bone in the medial condyle, in medial view. (B) The dominant orientation of cancellous bone in the medial and lateral condyles, in posterior view. (C) The dominant orientation of cancellous bone in the lateral condyle, in lateral view. (D–J) Seven progressive rotations of the bone, in 30° increments, from proximally oblique medial to lateral views. For explanation of the features and colour coding, refer to the main text.

Figure 34. The main architectural features of cancellous bone in the proximal tibia of Troodontidae sp. and *Saurornitholestes langstoni*. (A, B) Vector field of $\mathbf{u}_1$ under the medial condyle of Troodontidae sp. (MOR 553s-7.11.91.41) in posterior (A) and medial (B) views. (C,

D) Vector field of $\mathbf{u}_1$ under the lateral condyle of Troodontidae sp. (MOR 748) in posterior (C) and lateral (D) views. (E, F) Vector field of $\mathbf{u}_1$ in the cnemial crest of Troodontidae sp. (MOR 748) in lateral (E) and anterior (F) views. (G) Vector field of $\mathbf{u}_1$ in the cnemial crest of *Saurornitholestes* (MOR 660) in lateral view. (H) Vector field of $\mathbf{u}_1$ in a 3-D slice, parallel to the sagittal plane, through the central metaphysis of Troodontidae sp. (MOR 553s-7.28.91.239), shown in medial view. Schematic inset illustrates the moderately developed double-arcuate pattern present.

Figure 35. The main architectural features of cancellous bone in the human distal tibia. (A) Vector field of $\mathbf{u}_1$ in a 3-D slice, parallel to the coronal plane, through the middle of the bone, shown in anterior view. (B) Vector field of $\mathbf{u}_1$ in a 3-D slice, parallel to the sagittal plane, through the middle of the bone, shown in lateral view. (C) Vector field of $\mathbf{u}_2$ in a 3-D slice, parallel to the axial plane, through the distal end of the bone, shown in proximal view (anterior is toward top of page). Inset shows location of slice.

Figure 36. The main architectural features of cancellous bone in the distal tibiotarsus of birds. (A–D) Vector field of $\mathbf{u}_1$ (A, C) and $\mathbf{u}_2$ (B, D) in the distal tibiotarsus of *Dromaius novaehollandiae* (QMO 16140) in oblique anterolateral (A, B) and oblique anteromedial (C, D) views. (E) Vector field of $\mathbf{u}_1$ (red) and $\mathbf{u}_2$ (blue) in the condyles of *Dromaius novaehollandiae* (QMO 16140) in proximal view (anterior is toward top of page). Note how both $\mathbf{u}_1$ and $\mathbf{u}_2$ are strongly aligned parallel to the sagittal plane. This particular specimen exemplifies a very stereotypical pattern that is observed in all large birds; the general pattern illustrated here was also observed in smaller species for which only limited fabric analysis was possible. (F) Isosurface rendering of cancellous bone in the distal tibiotarsus of *Casuarius casuarius* (QMO 30105), shown in oblique anteromedial view, with multiple cuts through the bone to illustrate 3-D architecture. (G) Isosurface rendering of cancellous bone in the distal tibiotarsus of *Ardeotis australis* (MVB 20408), shown in oblique anterolateral view, with multiple cuts through the bone to illustrate 3-D architecture. (H) Isosurface rendering of cancellous bone in the distal tibiotarsus of *Coturnix chinensis* (PJB coll.), sectioned in the axial plane through the middle of the condyles

and shown in proximal view (anterior is toward top of page). In F and G, cut surfaces are coloured red to better show ~~the nature of~~ the cancellous bone architecture, in particular, the plate-like ~~nature~~ of many of the trabeculae, largely aligned parallel to the sagittal plane.

Figure 37. The main architectural features of cancellous bone in the distal tibiotarsus of reptiles. (A, B) Vector field of $\mathbf{u}_1$ in *Varanus komodoensis* (AM R.106933) in anterior (A) and medial (B) views. (C) Vector field of $\mathbf{u}_1$ in *Crocodylus porosus* (QMJ 48127) in anteromedial view. (D) Vector field of $\mathbf{u}_2$ in a 3-D slice through the distal end of the tibia of *Crocodylus porosus* (QMJ 48127), shown in proximal view (anterior is toward top of page). Inset shows location of slice.

Figure 38. The main architectural features of cancellous bone in the distal tibiotarsus of basal theropods. These are illustrated here with a 3-D geometric model of the observed architecture, mapped to the tibiotarsus of *Daspletosaurus torosus* (TMP 2001.036.0001; note that calcaneum was digitally sculpted based on other tyrannosaurid calcanei). (A–G) Seven progressive rotations of the tibia, in 30° increments, from proximally oblique medial to lateral views. Schematic inset in D illustrates generic cross-sectional pattern at the level indicated. (H–J) Three views of the astragalus and calcaneum, corresponding to those in C–E, respectively. The various colours are used to help visualize the various tracts of cancellous bone more clearly.

Figure 39. The main architectural features of cancellous bone in the distal tibiotarsus of Troodontidae sp. and *Saurornitholestes langstoni*. (A, B) Vector field of $\mathbf{u}_1$ (red) and $\mathbf{u}_2$ (blue) in the distal tibiotarsus of Troodontidae sp. (MOR 748) in anterior (A) and proximal (B) views; in B, anterior is toward top of page. Note how both $\mathbf{u}_1$ and $\mathbf{u}_2$ are generally aligned parallel to the sagittal plane. (C) Isosurface rendering of cancellous bone in the medial distal tibia of *Saurornitholestes* (MOR 660), shown in oblique anteromedial view, with multiple cuts through the bone (cut surfaces are coloured red) to illustrate 3-D architecture.

Figure 40. The main architectural features of cancellous bone in the fibula. (A, B) Vector field of $\mathbf{u}_1$ in the human fibula, in anterior (A) and lateral (B) views. (C, D) Vector field of $\mathbf{u}_1$ in *Crocodylus johnstoni* (QMJ 47916), in anterior (C) and lateral (D) views. (E, F) Vector field of $\mathbf{u}_1$ in *Varanus panoptes* (QMJ 91981), in anterior (E) and lateral (F) views. (G–I) Vector field of $\mathbf{u}_1$ in the fibular head of *Dromaius novaehollandiae* (QMO 11686, G), *Rhea americana* (QMO 23517, H) and *Gallus gallus* (PJB coll., I), in lateral view. (J, K) Isosurface rendering of cancellous bone in the proximal fibula of *Leipoa ocellata* (MVB 20194, J) and *Coturnix chinensis* (PJB coll., K), sectioned in the plane of the head and shown in lateral view. (L, M) The dominant architectural direction of cancellous bone in the fibula of *Allosaurus* and tyrannosaurids, shown in anterior (L) and lateral (M) views. This is illustrated here with a 3-D geometric model of the observed architecture, mapped to the fibula of *Daspletosaurus torosus* (TMP 2001.036.0001). (N) Vector field of $\mathbf{u}_1$ in the proximal fibula of Troodontidae sp. (MOR 553s-8.17.92.265), in lateral view.

Figure 41. Oblique trabeculae in the diaphyses of birds and reptiles. These are illustrated here with a number of examples demonstrating the variety of forms the individual trabeculae can assume. (A) Femoral mid-shaft of *Dromaius novaehollandiae* (QMO 16140). (B) Proximal femoral shaft of *Meleagris gallopavo* (PJB coll.). (C) Distal femoral shaft of *Leipoa ocellata* (MVB 20194). (D) Proximal femoral shaft of *Dromaius novaehollandiae* (QMO 11686). (E) Proximal femoral shaft of *Alectura lathami* (PJB coll.). (F) Proximal femoral shaft of *Eudromia elegans* (UMZC 404.e). (G) Femoral mid-shaft of *Varanus panoptes* (QMJ 91981). (H) Distal femoral shaft of *Crypturellus soui* (MVB 23647). (I) Tibial mid-shaft of *Struthio camelus* (MV R.2385). In all figures, proximal is towards the top of the page.

Figure 42. Size-dependent variation in the ~~nature of~~ diaphyseal cancellous bone architecture in the femora and tibiae of birds. These plots compare the results of the categorical scoring of each bone against its length. (A, B) Feature 1 (extent of cancellous bone) in the femur (A) and tibia (B); a higher score indicates greater extent. (C, D) Feature 2 (average orientation of trabeculae) in the femur (C) and tibia (D); a higher score indicates that trabeculae are more perpendicular to the

bone's long-axis. (E, F) Feature 3 (degree of association of trabeculae) in the femur (E) and tibia (F); a higher score indicates that trabeculae tend to be more closely associated with other similar trabeculae. Major axis regression lines are also plotted when correlations were statistically significant. *N* signifies number of species represented, and *n* signifies number of individuals. Other statistical metrics for each comparison are reported in Table 2.

Figure 43. Gently oblique trabeculae in the tibial diaphysis of a human. Inset shows location of section relative to the whole bone. Although the trabeculae (or endosteal 'wrinkles') are less obliquely oriented compared to the birds or reptiles, they are nonetheless consistently oriented in an oblique fashion.

Figure 44. Schematic demonstrating the effect of differences in the degree of hip and knee flexion on the joint forces experienced by the femur. This is illustrated with right lateral views of a human (left) and a typical bird (right) in approximate mid-stance postures. In the more flexed posture of birds, the hip joint force is more anteriorly oriented relative to the long-axis of the femur (dotted line) compared to humans. Further, the knee joint force is more posteriorly oriented relative to the long-axis of the femur compared to humans.

Table 1(on next page)

The specimens investigated, detailing the higher-level taxonomy of the species studied, the settings used in acquiring the CT scan data and the protocol used to process the CT images.

Table 1. The specimens investigated. In addition to providing the higher-level taxonomy of the species studied (cf. Figure 8), this table also lists the settings used in acquiring the CT scan data for each specimen, as well as the protocol used to process the raw CT images for subsequent analysis.

Higher-order taxonomy	Species	Specimen number*	Element	CT scan settings						Study	Image processing protocol
				Machine	Peak tube voltage (kV)	Tube current (mA)	Exposure time (ms)	In-plane pixel resolution (mm)	Slice thickness (mm)		
Mammalia, Hominidae	*Homo sapiens*	GU S-0013	Femur^{p}	Stratec XCT 3000	61.3	0.203	100,000	0.161	0.1	This study	3
Mammalia, Hominidae	*Homo sapiens*	GU S-0013	Femur^{d}	Stratec XCT 3000	61.3	0.203	100,000	0.137	0.1	This study	3
Mammalia, Hominidae	*Homo sapiens*	GU S-0013	Tibia^{p}	Stratec XCT 3000	61.3	0.203	100,000	0.137	0.1	This study	3
Mammalia, Hominidae	*Homo sapiens*	GU S-0013	Tibia^{d}	Stratec XCT 3000	61.3	0.203	100,000	0.137	0.1	This study	3
Mammalia, Hominidae	*Homo sapiens*	GU S-0013	Tibia^{s}	Stratec XCT 3000	61.3	0.203	100,000	0.137	0.1	This study	3
Mammalia, Hominidae	*Homo sapiens*	GU S-0013	Fibula^{p}	Stratec XCT 3000	61.3	0.203	100,000	0.137	0.1	This study	3
Mammalia, Hominidae	*Homo sapiens*	GU S-0013	Fibula^{d}	Stratec XCT 3000	61.3	0.203	100,000	0.137	0.1	This study	3
Sauria, Squamata	*Varanus komodoensis*	AM R.106933	Femur	Siemens Inveon	80	0.45	1000	0.053	0.053	This study	1
Sauria, Squamata	*Varanus komodoensis*	AM R.106933	Tibia	Siemens Inveon	80	0.45	1000	0.053	0.053	This study	1
Sauria, Squamata	*Varanus komodoensis*	AM R.106933	Fibula	Siemens Inveon	80	0.45	1000	0.053	0.053	This study	1
Sauria, Squamata	*Varanus spenceri*	QMJ 84416	Femur	Siemens Inveon	80	0.5	900	0.053	0.053	This study	1
Sauria, Squamata	*Varanus spenceri*	QMJ 84416	Tibia	Siemens Inveon	80	0.5	900	0.053	0.053	This study	1

Table 1 (continued).

Higher-order taxonomy	Species	Specimen number*	Element	CT scan settings						Study	Image processing protocol
				Machine	Peak tube voltage (kV)	Tube current (mA)	Exposure time (ms)	In-plane pixel resolution (mm)	Slice thickness (mm)		
Sauria, Squamata	*Varanus spenceri*	QMJ 84416	Fibula	Siemens Inveon	80	0.5	900	0.053	0.053	This study	1
Sauria, Squamata	*Varanus panoptes*	QMJ 91981	Femur	Siemens Inveon	80	0.5	900	0.053	0.053	This study	1
Sauria, Squamata	*Varanus panoptes*	QMJ 91981	Tibia	Siemens Inveon	80	0.5	900	0.053	0.053	This study	1
Sauria, Squamata	*Varanus panoptes*	QMJ 91981	Fibula	Siemens Inveon	80	0.5	900	0.053	0.053	This study	1
Archosauria, Crocodylia	*Crocodylus johnstoni*	QMJ 47916	Femur	Siemens Inveon	80	0.5	900	0.053	0.053	This study	1
Archosauria, Crocodylia	*Crocodylus johnstoni*	QMJ 47916	Tibia	Siemens Inveon	80	0.5	900	0.053	0.053	This study	1
Archosauria, Crocodylia	*Crocodylus johnstoni*	QMJ 47916	Fibula	Siemens Inveon	80	0.5	900	0.053	0.053	This study	1
Archosauria, Crocodylia	*Crocodylus porosus*	QMJ 48127	Femur	Siemens Inveon	80	0.45	1000	0.053	0.053	This study	1
Archosauria, Crocodylia	*Crocodylus porosus*	QMJ 48127	Tibia	Siemens Inveon	80	0.45	1000	0.053	0.053	This study	1
Archosauria, Crocodylia	*Crocodylus porosus*	QMJ 48127	Fibula	Siemens Inveon	80	0.45	1000	0.053	0.053	This study	1
Non-avian theropod, Ceratosauria	*Ceratosaurus nasicornis*	UMNH VP 5278	Tibia + astragalus + calcaneum	Siemens Somatom Definition Flash	80, 140	480	500	0.504	0.5	This study	5
Non-avian theropod, Ceratosauria	*Masiakasaurus knopfleri*	FMNH PR 2117	Femur	GE Lightspeed 16	100	70	1297	0.1875	1	Farke and Alicea (2009)	2
Non-avian theropod, Ceratosauria	*Masiakasaurus knopfleri*	FMNH PR 2153	Femur	GE Lightspeed 16	100	100	2101	0.1875	1.338	Farke and Alicea (2009)	2

Table 1 (continued).

Higher-order taxonomy	Species	Specimen number*	Element	CT scan settings						Study	Image processing protocol
				Machine	Peak tube voltage (kV)	Tube current (mA)	Exposure time (ms)	In-plane pixel resolution (mm)	Slice thickness (mm)		
Non-avian theropod, Ceratosauria	*Masiakasaurus knopfleri*	FMNH PR 2208	Femur	GE Lightspeed 16	100	70	1297	0.1875	1	Farke and Alicea (2009)	2
Non-avian theropod, Ceratosauria	*Masiakasaurus knopfleri*	UA 8684	Femur	GE Lightspeed 16	100	70	1297	0.1875	1	Farke and Alicea (2009)	2
Non-avian theropod, Allosauroidea	*Allosaurus* sp.	MOR 693	Femora × 2	Toshiba Aquilion 64	135	250	750	0.625	0.5	This study	5
Non-avian theropod, Allosauroidea	*Allosaurus* sp.	MOR 693	Tibiae × 2	Toshiba Aquilion 64	135	300	750	0.468	0.4	This study	5
Non-avian theropod, Allosauroidea	*Allosaurus* sp.	MOR 693	Fibulae × 2	Toshiba Aquilion 64	135	250	750	0.625	0.5	This study	5
Non-avian theropod, Allosauroidea	*Allosaurus* sp.	MOR 693	Astragalus	Toshiba Aquilion 64	135	250	750	0.625	0.5	This study	5
Non-avian theropod, Allosauroidea	*Allosaurus* sp.	MOR 693	Calcaneum	Toshiba Aquilion 64	135	250	750	0.625	0.5	This study	5
Non-avian theropod, Allosauroidea	*Allosaurus fragilis*	DNM 2560	Femur	Siemens Somatom Definition Flash	80, 140	315	500	0.549	0.5	This study	5
Non-avian theropod, Allosauroidea	*Allosaurus fragilis*	DNM 2560	Tibia + astragalus + calcaneum	Siemens Somatom Definition Flash	80, 140	360	500	0.637	0.5	This study	5

Table 1 (continued).

Higher-order taxonomy	Species	Specimen number*	Element	CT scan settings						Study	Image processing protocol
				Machine	Peak tube voltage (kV)	Tube current (mA)	Exposure time (ms)	In-plane pixel resolution (mm)	Slice thickness (mm)		
Non-avian theropod, Allosauroidea	*Allosaurus fragilis*	UMNH VP 7884	Femur	Siemens Somatom Definition Flash	80, 140	630	500	0.529	0.5	This study	5
Non-avian theropod, Allosauroidea	*Allosaurus fragilis*	UMNH VP 7885	Femur	Siemens Somatom Definition Flash	80, 140	225	500	0.387	0.5	This study	5
Non-avian theropod, Allosauroidea	*Allosaurus fragilis*	UMNH VP 7889	Femur[p]	Siemens Somatom Definition Flash	80, 140	630	500	0.523	0.5	This study	5
Non-avian theropod, Allosauroidea	*Allosaurus fragilis*	UMNH VP 7928	Tibia	Siemens Somatom Definition Flash	80, 140	630	500	0.355	0.5	This study	5
Non-avian theropod, Allosauroidea	*Allosaurus fragilis*	UMNH VP 9480	Femur	Siemens Somatom Definition Flash	80, 140	80	500	0.217	0.5	This study	5
Non-avian theropod, Allosauroidea	*Allosaurus fragilis*	UMNH VP 20363	Femur	Siemens Somatom Definition Flash	80, 140	315	500	0.664	0.5	This study	5
Non-avian theropod, Allosauroidea	*Allosaurus fragilis*	UMNH VP 24326	Tibia[p]	Siemens Somatom Definition Flash	80, 140	200	500	0.459	0.5	This study	5
Non-avian theropod, Tyrannosauridae	*Tyrannosaurus rex*	MOR 009	Femur[p]	Toshiba Aquilion 64	135	500	500	0.782	0.4	This study	5

Table 1 (continued).

Higher-order taxonomy	Species	Specimen number*	Element	CT scan settings						Study	Image processing protocol
				Machine	Peak tube voltage (kV)	Tube current (mA)	Exposure time (ms)	In-plane pixel resolution (mm)	Slice thickness (mm)		
Non-avian theropod, Tyrannosauridae	*Tyrannosaurus rex*	MOR 1125	Femur	Toshiba Aquilion 64	135	350	500	1.178	0.5	This study	5
Non-avian theropod, Tyrannosauridae	*Tyrannosaurus rex*	MOR 1125	Tibia	Toshiba Aquilion 64	135	350	500	0.976	0.5	This study	5
Non-avian theropod, Tyrannosauridae	*Tyrannosaurus rex*	MOR 1125	Fibulae × 2	Toshiba Aquilion 64	135	350	500	0.873	0.8	This study	5
Non-avian theropod, Tyrannosauridae	*Tyrannosaurus rex*	MOR 1128	Femur	Toshiba Aquilion 64	135	350	500	0.976	2	This study	5
Non-avian theropod, Tyrannosauridae	*Tyrannosaurus rex*	MOR 1128	Tibia[d]	Toshiba Aquilion 64	135	350	500	0.961	0.5	This study	5
Non-avian theropod, Tyrannosauridae	Tyrannosauridae indet.	MOR 1192	Fibula	Toshiba Aquilion 64	135	150	1000	0.976	2	This study	5
Non-avian theropod, Tyrannosauridae	*Gorgosaurus libratus*	TMP 1994.012.0602	Femur	GE Lightspeed Ultra	120	160	1195	0.723	1.25	This study	5
Non-avian theropod, Tyrannosauridae	*Gorgosaurus libratus*	TMP 1994.012.0602	Tibia + astragalus + calcaneum	GE Lightspeed Ultra	140	150	1195	0.703	1.25	This study	5
Non-avian theropod, Tyrannosauridae	*Daspletosaurus torosus*	TMP 2001.036.0001	Femur	GE Lightspeed Ultra	140	150	1195	0.838	1.25	This study	5
Non-avian theropod, Tyrannosauridae	*Daspletosaurus torosus*	TMP 2001.036.0001	Tibia	GE Lightspeed Ultra	120	245	1195	0.832	1.25	This study	5

Table 1 (continued).

Higher-order taxonomy	Species	Specimen number*	Element	CT scan settings						Study	Image processing protocol
				Machine	Peak tube voltage (kV)	Tube current (mA)	Exposure time (ms)	In-plane pixel resolution (mm)	Slice thickness (mm)		
Non-avian theropod, Tyrannosauridae	*Daspletosaurus torosus*	TMP 2001.036.0001	Fibula	GE Lightspeed Ultra	120	245	1195	0.832	1.25	This study	5
Non-avian theropod, Tyrannosauridae	*Daspletosaurus torosus*	TMP 2001.036.0001	Astragalus	GE Lightspeed Ultra	140	155	1195	0.879	1.25	This study	5
Non-avian theropod, Ornithomimidae	Ornithomimidae indet.	TMP 1985.036.0276	Femur[p]	Siemens Inveon	80	500	825	0.05	0.05	This study	4
Non-avian theropod, Ornithomimidae	Ornithomimidae indet.	TMP 1991.036.0569	Femur	Siemens Inveon	80	250	1500	0.05	0.05	This study	4
Non-avian theropod, Ornithomimidae	Ornithomimidae indet.	TMP 1991.036.0854	Femur[p]	GE Lightspeed Ultra	140	150	1195	0.943	1.25	This study	5
Non-avian theropod, Ornithomimidae	Ornithomimidae indet.	TMP 1992.036.0696	Femur[p]	GE Lightspeed Ultra	140	150	1195	0.943	1.25	This study	5
Non-avian theropod, Ornithomimidae	Ornithomimidae indet.	TMP 1993.066.0002	Tibia[p]	GE Lightspeed Ultra	140	155	1195	0.879	1.25	This study	5
Non-avian theropod, Ornithomimidae	Ornithomimidae indet.	TMP 1999.055.0337	Femur[d]	Siemens Inveon	80	250	1500	0.05	0.05	This study	4
Non-avian theropod, Ornithomimidae	Ornithomimidae indet.	TMP 2006.012.0065	Fibula	GE Lightspeed Ultra	120	185	1195	0.738	1.25	This study	5
Non-avian theropod, Therizinosauria	*Falcarius utahensis*	UMNH VP 12360	Femur[d]	Siemens Inveon	80	250	1600	0.05	0.05	This study	4

Table 1 (continued).

Higher-order taxonomy	Species	Specimen number*	Element	CT scan settings						Study	Image processing protocol
				Machine	Peak tube voltage (kV)	Tube current (mA)	Exposure time (ms)	In-plane pixel resolution (mm)	Slice thickness (mm)		
Non-avian theropod, Therizinosauria	*Falcarius utahensis*	UMNH VP 12361	Femur[p]	Siemens Inveon	80	250	1700	0.05	0.05	This study	4
Non-avian theropod, Caenagnathidae	Caenagnathidae indet.	TMP 1986.036.0323	Femur	Siemens Inveon	80	250	1600	0.05	0.05	This study	4
Non-avian theropod, Dromaeosauridae	*Saurornitholestes langstoni*	MOR 660	Tibiae × 2	Siemens Inveon	80	250	1600	0.05	0.05	This study	4
Non-avian theropod, Troodontidae	Troodontidae sp.	MOR 553s-7.11.91.41	Tibia	Siemens Inveon	80	200	1900	0.04	0.04	This study	4
Non-avian theropod, Troodontidae	Troodontidae sp.	MOR 553s-7.28.91.239	Femur	Siemens Inveon	80	200	1800	0.04	0.04	This study	4
Non-avian theropod, Troodontidae	Troodontidae sp.	MOR 553s-8.17.92.265	Fibula	Siemens Inveon	80	250	1600	0.04	0.04	This study	4
Non-avian theropod, Troodontidae	Troodontidae sp.	MOR 748	Femur	Siemens Inveon	80	200	1900	0.04	0.04	This study	4
Non-avian theropod, Troodontidae	Troodontidae sp.	MOR 748	Tibia + astragalus + calcaneum	Siemens Inveon	80	200	1900	0.04	0.04	This study	4
Aves, Struthioniformes	*Struthio camelus*	MV R.2385	Femur	GE BrightSpeed	120	55	1681	0.488	0.3	This study	2
Aves, Struthioniformes	*Struthio camelus*	MV R.2385	Tibiotarsus	Siemens Somatom Definition AS+	120	199	1000	0.363	0.4	This study	2

Table 1 (continued).

Higher-order taxonomy	Species	Specimen number*	Element	CT scan settings						Study	Image processing protocol
				Machine	Peak tube voltage (kV)	Tube current (mA)	Exposure time (ms)	In-plane pixel resolution (mm)	Slice thickness (mm)		
Aves, Struthioniformes	*Struthio camelus*	MV R.2385	Fibula	GE BrightSpeed	120	55	1681	0.488	0.3	This study	2
Aves, Struthioniformes	*Struthio camelus*	MV R.2711	Femur	GE BrightSpeed	120	55	1681	0.488	0.3	This study	2
Aves, Struthioniformes	*Struthio camelus*	MV R.2711	Tibiotarsus	GE BrightSpeed	120	55	1681	0.488	0.3	This study	2
Aves, Struthioniformes	*Struthio camelus*	MV R.2711	Fibula	GE BrightSpeed	120	55	1681	0.488	0.3	This study	2
Aves, Struthioniformes	*Struthio camelus*	YPM 2124	Femur	GE Lightspeed 16	100	70	1297	0.311	1.25	Farke and Alicea (2009)	none**
Aves, Struthioniformes	*Struthio camelus*	RVC Ostrich 2	Femur	Picker PQ5000	120	200	1000	0.391	2	Doube et al. (2012)	2
Aves, Struthioniformes	*Struthio camelus*	RVC Ostrich 2	Tibiotarsus	Picker PQ5000	120	200	1000	0.313	4	Doube et al. (2012)	2
Aves, Struthioniformes	*Struthio camelus*	RVC Ostrich 2	Fibula	Picker PQ5000	120	200	1000	0.313	4	Doube et al. (2012)	2
Aves, Struthioniformes	*Struthio camelus*	RVC-JRH-OST 1	Femur	GE LightSpeed Pro 16	120	200	800	0.273	0.625	This study	2
Aves, Struthioniformes	*Struthio camelus*	RVC-JRH-OST 1	Tibiotarsus	GE LightSpeed Pro 16	120	200	800	0.369	1.25	This study	2
Aves, Struthioniformes	*Struthio camelus*	RVC-JRH-OST 1	Fibula	GE LightSpeed Pro 16	120	200	800	0.369	1.25	This study	2

Table 1 (continued).

Higher-order taxonomy	Species	Specimen number*	Element	CT scan settings						Study	Image processing protocol
				Machine	Peak tube voltage (kV)	Tube current (mA)	Exposure time (ms)	In-plane pixel resolution (mm)	Slice thickness (mm)		
Aves, Rheiformes	*Rhea americana*	QMO 23517	Femur	GE BrightSpeed	120	80	1584	0.488	0.3	This study	2
Aves, Rheiformes	*Rhea americana*	QMO 23517	Tibiotarsus	GE BrightSpeed	120	80	1584	0.488	0.3	This study	2
Aves, Rheiformes	*Rhea americana*	QMO 23517	Fibula	GE BrightSpeed	120	80	1584	0.488	0.3	This study	2
Aves, Tinamiformes	*Crypturellus soui*	MVB 23647	Femur	Siemens Inveon	80	0.35	1400	0.035	0.035	This study	1
Aves, Tinamiformes	*Crypturellus soui*	MVB 23647	Tibiotarsus	Siemens Inveon	80	0.35	1400	0.035	0.035	This study	1
Aves, Tinamiformes	*Crypturellus soui*	MVB 23647	Fibula	Siemens Inveon	80	0.35	1400	0.035	0.035	This study	1
Aves, Tinamiformes	*Eudromia elegans*	UMZC 404.e	Femur	Nikon HMX ST 225				0.034	0.034	Doube et al. (2012)	1
Aves, Tinamiformes	*Eudromia elegans*	UMZC 404.e	Tibiotarsus	Nikon HMX ST 225				0.047	0.047	Doube et al. (2012)	1
Aves, Tinamiformes	*Eudromia elegans*	UMZC 404.e	Fibula	Nikon HMX ST 225				0.047	0.047	Doube et al. (2012)	1
Aves, Apterygiformes	*Apteryx owenii*	UMZC 378.iii	Femur	Nikon HMX ST 225				0.046	0.046	Doube et al. (2012)	1
Aves, Apterygiformes	*Apteryx owenii*	UMZC 378.iii	Tibiotarsus	Nikon HMX ST 225				0.061	0.061	Doube et al. (2012)	1
Aves, Apterygiformes	*Apteryx owenii*	UMZC 378.iii	Fibula	Nikon HMX ST 225				0.061	0.061	Doube et al. (2012)	1

Table 1 (continued).

Higher-order taxonomy	Species	Specimen number*	Element	CT scan settings						Study	Image processing protocol
				Machine	Peak tube voltage (kV)	Tube current (mA)	Exposure time (ms)	In-plane pixel resolution (mm)	Slice thickness (mm)		
Aves, Apterygiformes	*Apteryx haastii*	UMZC 378.p	Femur	Nikon HMX ST 225				0.044	0.044	Doube et al. (2012)	1
Aves, Casuariiformes	*Dromaius novaehollandiae*	QMO 11685	Femur	GE BrightSpeed	120	55	1681	0.379	0.3	This study	2
Aves, Casuariiformes	*Dromaius novaehollandiae*	QMO 11686	Femur	GE BrightSpeed	120	80	1584	0.326	0.3	This study	2
Aves, Casuariiformes	*Dromaius novaehollandiae*	QMO 11686	Tibiotarsus	GE BrightSpeed	120	55	1681	0.488	0.3	This study	2
Aves, Casuariiformes	*Dromaius novaehollandiae*	QMO 11686	Fibula	GE BrightSpeed	120	55	1681	0.326	0.3	This study	2
Aves, Casuariiformes	*Dromaius novaehollandiae*	QMO 16140	Femur	GE BrightSpeed	120	55	1681	0.232	0.3	This study	2
Aves, Casuariiformes	*Dromaius novaehollandiae*	QMO 16140	Tibiotarsus	GE BrightSpeed	120	55	1681	0.232	0.3	This study	2
Aves, Casuariiformes	*Dromaius novaehollandiae*	QMO 16140	Fibula	GE BrightSpeed	120	55	1681	0.188	0.3	This study	2
Aves, Casuariiformes	*Casuarius casuarius*	QMO 30105	Femur	GE BrightSpeed	120	55	1681	0.215	0.3	This study	2
Aves, Casuariiformes	*Casuarius casuarius*	QMO 30105	Tibiotarsus	GE BrightSpeed	120	55	1681	0.219	0.3	This study	2
Aves, Casuariiformes	*Casuarius casuarius*	QMO 30105	Fibula	GE BrightSpeed	120	55	1681	0.215	0.3	This study	2
Aves, Casuariiformes	*Casuarius casuarius*	QMO 30604	Femur	GE BrightSpeed	120	80	1584	0.467	0.3	This study	2
Aves, Casuariiformes	*Casuarius casuarius*	QMO 30604	Tibiotarsus	GE BrightSpeed	120	80	1584	0.488	0.3	This study	2
Aves, Casuariiformes	*Casuarius casuarius*	QMO 30604	Fibula	GE BrightSpeed	120	80	1584	0.488	0.3	This study	2
Aves, Casuariiformes	*Casuarius casuarius*	QMO 31137	Femur	GE BrightSpeed	120	55	1681	0.213	0.3	This study	2

Table 1 (continued).

Higher-order taxonomy	Species	Specimen number*	Element	CT scan settings						Study	Image processing protocol
				Machine	Peak tube voltage (kV)	Tube current (mA)	Exposure time (ms)	In-plane pixel resolution (mm)	Slice thickness (mm)		
Aves, Casuariiformes	*Casuarius casuarius*	QMO 31137	Tibiotarsus	GE BrightSpeed	120	80	1584	0.488	0.3	This study	2
Aves, Casuariiformes	*Casuarius casuarius*	QMO 31137	Fibula	GE BrightSpeed	120	80	1584	0.488	0.3	This study	2
Aves, Casuariiformes	*Dromaius novaehollandiae*	YPM 2128	Femur	GE Lightspeed 16	100	70	1297	0.188	0.5	Farke and Alicea (2009)	none**
Aves, Galliformes	*Alectura lathami*	PJB	Femur	Siemens Inveon	80	0.45	1000	0.053	0.053	This study	1
Aves, Galliformes	*Alectura lathami*	PJB	Tibiotarsus	Siemens Inveon	80	0.45	1000	0.053	0.053	This study	1
Aves, Galliformes	*Alectura lathami*	PJB	Fibula	Siemens Inveon	80	0.45	1000	0.053	0.053	This study	1
Aves, Galliformes	*Leipoa ocellata*	MVB 20194	Femur	Siemens Inveon	80	0.45	1000	0.053	0.053	This study	1
Aves, Galliformes	*Leipoa ocellata*	MVB 20194	Tibiotarsus	Siemens Inveon	80	0.45	1000	0.053	0.053	This study	1
Aves, Galliformes	*Leipoa ocellata*	MVB 20194	Fibula	Siemens Inveon	80	0.45	1000	0.053	0.053	This study	1
Aves, Galliformes	*Numida meleagris*	PJB	Femur	Siemens Inveon	80	0.45	1000	0.053	0.053	This study	1
Aves, Galliformes	*Numida meleagris*	PJB	Tibiotarsus	Siemens Inveon	80	0.45	1000	0.053	0.053	This study	1
Aves, Galliformes	*Numida meleagris*	PJB	Fibula	Siemens Inveon	80	0.45	1000	0.053	0.053	This study	1
Aves, Galliformes	*Colinus virginianus*	PJB	Femur	Siemens Inveon	80	0.35	1400	0.035	0.035	This study	1
Aves, Galliformes	*Colinus virginianus*	PJB	Tibiotarsus	Siemens Inveon	80	0.45	1000	0.053	0.053	This study	1

Table 1 (continued).

Higher-order taxonomy	Species	Specimen number*	Element	CT scan settings						Study	Image processing protocol
				Machine	Peak tube voltage (kV)	Tube current (mA)	Exposure time (ms)	In-plane pixel resolution (mm)	Slice thickness (mm)		
Aves, Galliformes	*Colinus virginianus*	PJB	Fibula	Siemens Inveon	80	0.45	1000	0.053	0.053	This study	1
Aves, Galliformes	*Coturnix chinensis*	PJB	Femur	Siemens Inveon	80	0.35	1400	0.035	0.035	This study	1
Aves, Galliformes	*Coturnix chinensis*	PJB	Tibiotarsus	Siemens Inveon	80	0.35	1400	0.035	0.035	This study	1
Aves, Galliformes	*Coturnix chinensis*	PJB	Fibula	Siemens Inveon	80	0.35	1400	0.035	0.035	This study	1
Aves, Galliformes	*Coturnix japonica*	PJB	Femur	Siemens Inveon	80	0.35	1400	0.035	0.035	This study	1
Aves, Galliformes	*Coturnix japonica*	PJB	Tibiotarsus	Siemens Inveon	80	0.45	1000	0.053	0.053	This study	1
Aves, Galliformes	*Coturnix japonica*	PJB	Fibula	Siemens Inveon	80	0.45	1000	0.053	0.053	This study	1
Aves, Galliformes	*Gallus gallus*	PJB	Femur	Siemens Inveon	80	0.45	1000	0.053	0.053	This study	1
Aves, Galliformes	*Gallus gallus*	PJB	Tibiotarsus	Siemens Inveon	80	0.45	1000	0.053	0.053	This study	1
Aves, Galliformes	*Gallus gallus*	PJB	Fibula	Siemens Inveon	80	0.45	1000	0.053	0.053	This study	1
Aves, Galliformes	*Gallus gallus*	PJB	Femur	Siemens Inveon	80	0.45	1000	0.053	0.053	This study	1 (for head only)
Aves, Galliformes	*Meleagris gallopavo*	PJB	Femur	Siemens Inveon	80	0.45	1000	0.053	0.053	This study	1
Aves, Galliformes	*Meleagris gallopavo*	PJB	Tibiotarsus	Siemens Inveon	80	0.45	1000	0.053	0.053	This study	1
Aves, Galliformes	*Meleagris gallopavo*	PJB	Fibula	Siemens Inveon	80	0.45	1000	0.053	0.053	This study	1
Aves, Galliformes	*Meleagris gallopavo*	RVC turkey 1	Tibiotarsus	Nikon HMX ST 225				0.122	0.122	Doube et al. (2012)	1

Table 1 (continued).

Higher-order taxonomy	Species	Specimen number*	Element	CT scan settings						Study	Image processing protocol
				Machine	Peak tube voltage (kV)	Tube current (mA)	Exposure time (ms)	In-plane pixel resolution (mm)	Slice thickness (mm)		
Aves, Galliformes	*Meleagris gallopavo*	RVC turkey 1	Fibula	Nikon HMX ST 225				0.122	0.122	Doube et al. (2012)	1
Aves, Galliformes	*Meleagris gallopavo*	YPM 2113	Femur	GE Lightspeed 16	100	70	1297	0.188	0.5	Farke and Alicea (2009)	none**
Aves, Galliformes	*Argusianus argus*	YPM 2100	Femur	GE Lightspeed 16	100	70	1297	0.188	0.5	Farke and Alicea (2009)	none**
Aves, Anseriformes	*Anseranus semipalmata*	QMO 29529	Femur	Siemens Inveon	80	0.45	1000	0.053	0.053	This study	1
Aves, Anseriformes	*Anseranus semipalmata*	QMO 29529	Tibiotarsus	Siemens Inveon	80	0.45	1000	0.053	0.053	This study	1
Aves, Anseriformes	*Anseranus semipalmata*	QMO 29529	Fibula	Siemens Inveon	80	0.45	1000	0.053	0.053	This study	1
Aves, Otidiformes	*Ardeotis australis*	MVB 20408	Femur	Siemens Inveon	80	0.45	1000	0.053	0.053	This study	1
Aves, Otidiformes	*Ardeotis australis*	MVB 20408	Tibiotarsus	Siemens Inveon	80	0.45	1000	0.053	0.053	This study	1
Aves, Otidiformes	*Ardeotis australis*	MVB 20408	Fibula	Siemens Inveon	80	0.45	1000	0.053	0.053	This study	1
Aves, Gruiformes	*Porphyrio porphyrio*	PJB	Femur	Siemens Inveon	80	0.45	1000	0.053	0.053	This study	1
Aves, Gruiformes	*Porphyrio porphyrio*	PJB	Tibiotarsus	Siemens Inveon	80	0.45	1000	0.053	0.053	This study	1
Aves, Gruiformes	*Porphyrio porphyrio*	PJB	Fibula	Siemens Inveon	80	0.45	1000	0.053	0.053	This study	1
Aves, Gruiformes	*Gallinula tenebrosa*	PJB	Femur	Siemens Inveon	80	0.45	1000	0.053	0.053	This study	1

Table 1 (continued).

Higher-order taxonomy	Species	Specimen number*	Element	CT scan settings						Study	Image processing protocol
				Machine	Peak tube voltage (kV)	Tube current (mA)	Exposure time (ms)	In-plane pixel resolution (mm)	Slice thickness (mm)		
Aves, Gruiformes	*Gallinula tenebrosa*	PJB	Tibiotarsus	Siemens Inveon	80	0.45	1000	0.053	0.053	This study	1
Aves, Gruiformes	*Gallinula tenebrosa*	PJB	Fibula	Siemens Inveon	80	0.45	1000	0.053	0.053	This study	1
Aves, Pelecaniformes	*Threskiornis moluccus*	PJB	Femur	Siemens Inveon	80	0.45	1000	0.053	0.053	This study	1
Aves, Pelecaniformes	*Threskiornis moluccus*	PJB	Tibiotarsus	Siemens Inveon	80	0.45	1000	0.053	0.053	This study	1
Aves, Pelecaniformes	*Threskiornis moluccus*	PJB	Fibula	Siemens Inveon	80	0.45	1000	0.053	0.053	This study	1
Aves, Cuculiformes	*Geococcyx californianus*	UMZC 429.p	Femur	Nikon HMX ST 225				0.032	0.032	Doube et al. (2012)	1
Aves, Cuculiformes	*Geococcyx californianus*	UMZC 429.p	Tibiotarsus	Nikon HMX ST 225				0.049	0.049	Doube et al. (2012)	1
Aves, Cuculiformes	*Geococcyx californianus*	UMZC 429.p	Fibula	Nikon HMX ST 225				0.049	0.049	Doube et al. (2012)	1
Aves, Columbiformes	*Pezophaps solitaria*	YPM 1154	Femur	GE Lightspeed 16	120	70	1297	0.188	0.5	Farke and Alicea (2009)	none**
Aves, Columbiformes	*Raphus cucullatus*	YPM 2064	Femur	GE Lightspeed 16	120	70	1297	0.188	0.5	Farke and Alicea (2009)	none**
Aves, Accipitriformes	*Sagittarius serpentarius*	YPM 1797	Femur	GE Lightspeed 16	100	70	1297	0.188	0.5	Farke and Alicea (2009)	none**
Aves, Accipitriformes	*Sagittarius serpentarius*	YPM 14150	Femur	GE Lightspeed 16	120	70	1297	0.188	0.5	Farke and Alicea (2009)	none**

* Collection number abbreviations: AM R., Australian Museum; DNM, UMNH VP; Natural History Museum of Utah; FMNH PR, Field Museum of Natural History; GU, Griffith University teaching collection; MOR, Museum of the Rockies; MVB, MV R., Museum Victoria; PJB, P.J.B. personal collection (housed within Queensland Museum collections); QMJ, QMO, Queensland Museum; RVC, Royal Veterinary College; TMP, Royal Tyrrell Museum of Palaeontology; UA, Université d'Antananarivo; UMZC, Cambridge University Museum of Zoology; YPM, Yale Peabody Museum of Natural History.

** The scans of these specimens were qualitatively analysed only, and did not require any further processing.

^{p} = proximal end, ^{d} = distal end, ^{s} = shaft.

Table 2(on next page)

Statistical results of categorical scoring analyses of cancellous bone architecture in bird femora and tibiotarsi versus bone length.

Table 2. Statistical results of categorical scoring analyses of cancellous bone architecture in bird femora and tibiotarsi *versus* bone length.

Element	Feature	Slope	Intercept	r^2	*p*-value	ICC
Femur	1 (extent)	0.004123	0.3668	0.3846	0.0002	0.8533
	2 (orientation)	-0.0061	6.5355	0.2196	0.0245	0.8064
	3 (association)	0.00198	0.92015	0.1577	0.0609	0.6909
Tibiotarsus	1 (extent)	0.001268	0.14686	0.2263	0.0168	0.4642
	2 (orientation)	-0.006	6.6016	0.2807	0.1438	***
	3 (association)	0.001055	1.0996	0.2239	0.2110	***

***For features 2 and 3 of the tibiotarsus, an ICC was unable to be calculated, because there was only one specimen in each set that had actually received a numeric score by all five scorers.

Figure 1 (on next page)

Cancellous bone occurrence and macrostructure, as illustrated here with the femur of a cow (*Bos tauros*), sectioned in the coronal plane.

Cancellous bone occurs in the proximal and distal ends of the bone (as indicated by the braces), underlying the thin cortical bone capping the epiphyses and apophyses, as well as the metaphyses. A close up view of the cancellous bone (right) reveals the highly porous nature of the tissue, giving it a spongy appearance.

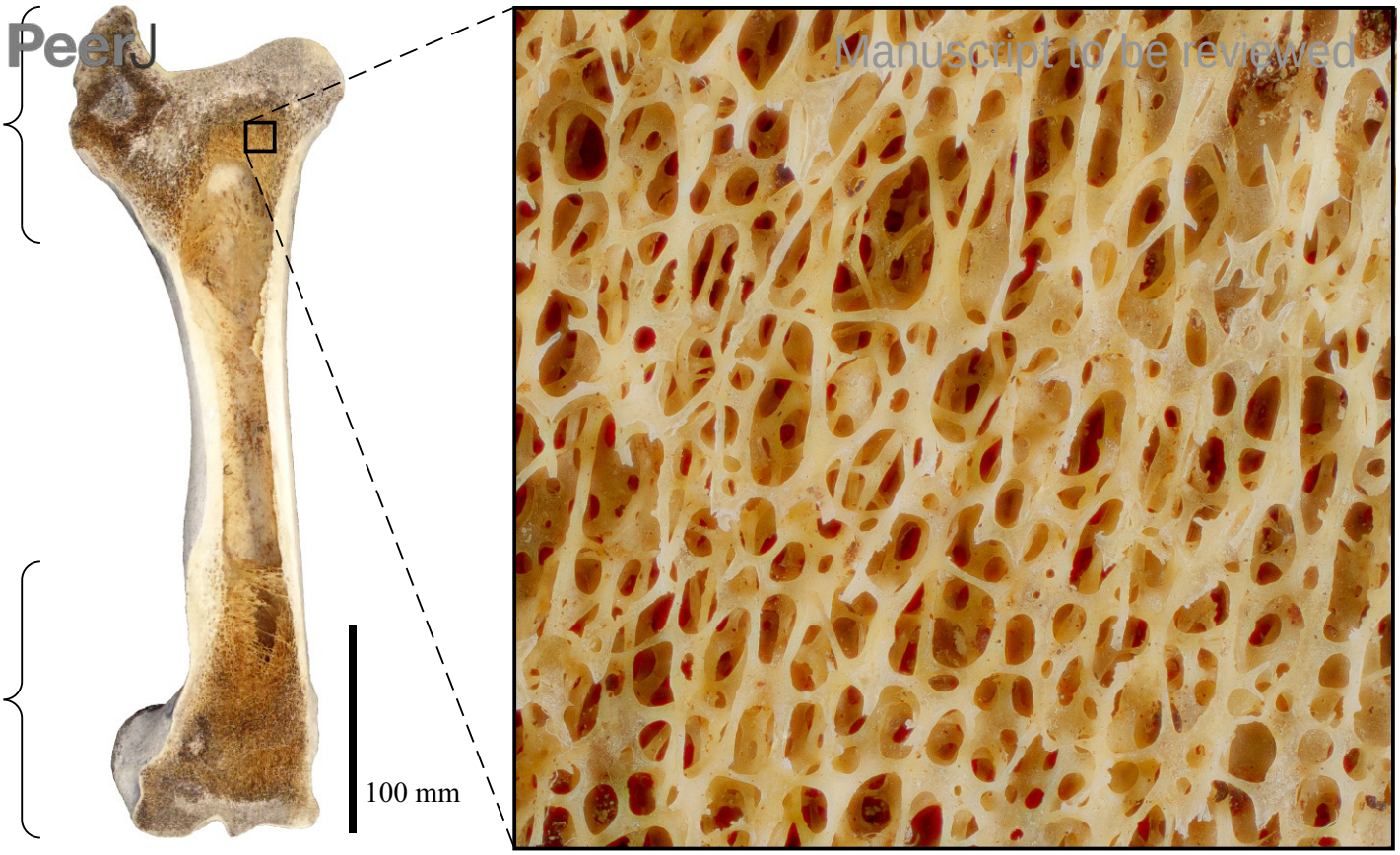

Figure 2(on next page)

Cancellous bone fabric as represented by its principal architectural directions.

(A) A cube of cancellous bone of side length 5.33 mm, from the proximal femur of a freshwater crocodile (*Crocodylus johnstoni*), with the principal directions of the bone's architecture superimposed. As an orthotropic material, cancellous bone fabric is completely described by three principal directions. (B) The fabric ellipsoid representation for this cube of cancellous bone is derived from the vectors that describe the principal architectural directions. The ellipsoid's major, semimajor and minor axes are given by the primary ($\mathbf{u}_1$), secondary ($\mathbf{u}_2$) and tertiary ($\mathbf{u}_3$) directions of the cancellous bone architecture, which correspond to the eigenvectors of the fabric tensor. The relative lengths of each axis depend on the relative magnitudes of the principal directions, which correspond to the eigenvalues of the fabric tensor. The degree of anisotropy (DA) describes the extent to which the trabeculae are aligned within a sample, and is given as the relative magnitude of the primary and tertiary eigenvalues (i.e., DA = e_1 / e_3); in this instance DA = 1.44. The cancellous bone geometry was derived via micro-computed X-ray omographic scanning (Siemens Inveon, 80 kV, 500 µA, 900 ms exposure, 3.3 µm isotropic resolution) and 3-D visualization (Mimics 17.0, Materialise NV, Belgium). The material directions were calculated using the mean intercept length method as implemented in the software Quant3D 2.3 (see Ketcham & Ryan 2004) .

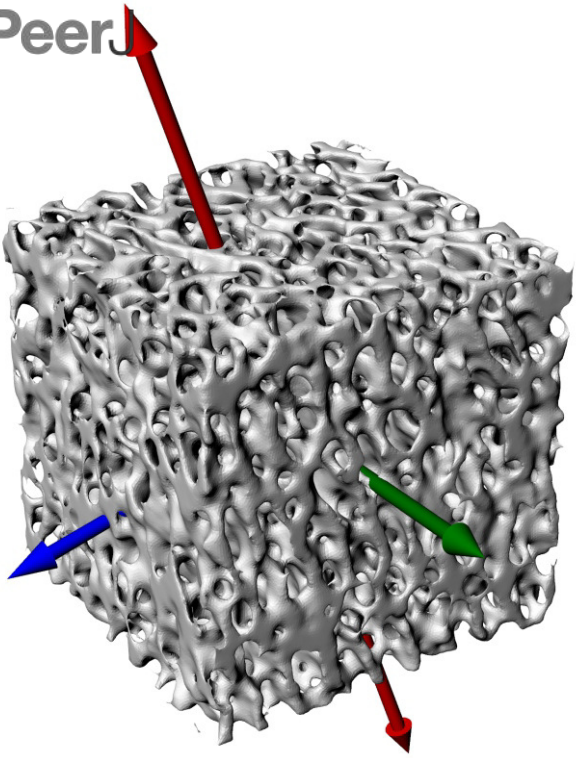

A

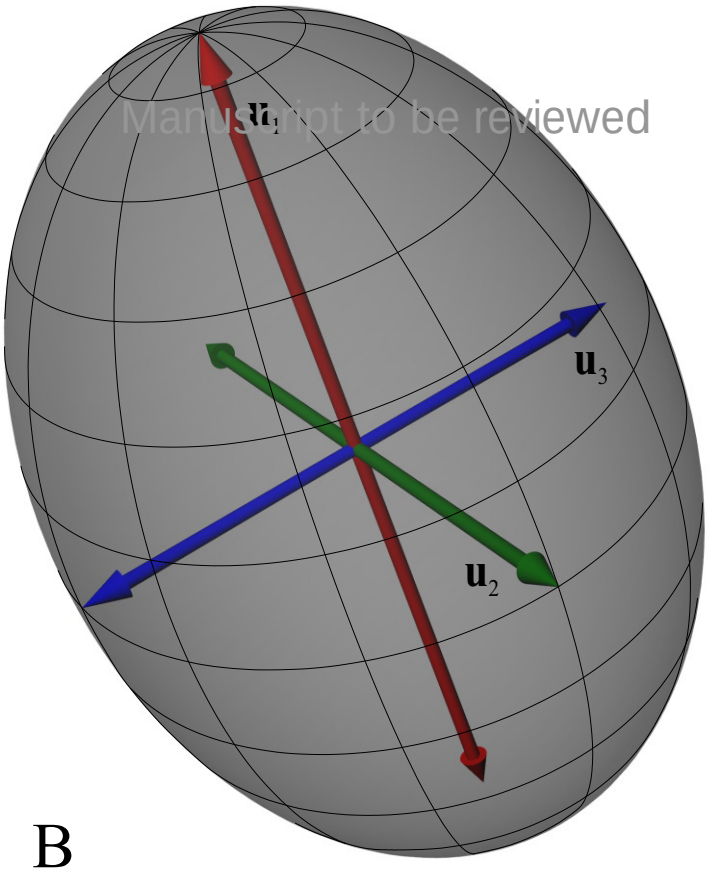

B

Figure 3(on next page)

Cancellous bone fabric direction can change in response toexperimentally induced changes in mechanical loading.

(A–C) The study of Goldstein et al. (1991) . In the distal femur of normal dogs (A), the principal directions of cancellous bone fabric (arrows) vary throughout the bone. After 38 weeks following surgical implantation of load cells (B, arrows indicate direction of applied principal compressive stress), the principal directions of the cancellous fabric were greatly altered, and were reoriented to align with the compressive stress applied by the load cells (C). (D–F) The study of Pontzer et al. (2006) . Subjecting guineafowl to running on inclined treadmills caused them to move with a more flexed knee posture compared to running on the level (the angle θ is reduced). The postural change resulted in an altered relative orientation of the joint force that the distal femur experienced (E, F, red arrow), which after 45 days was found to produce a changed orientation of peak trabecular density (dotted arrow).

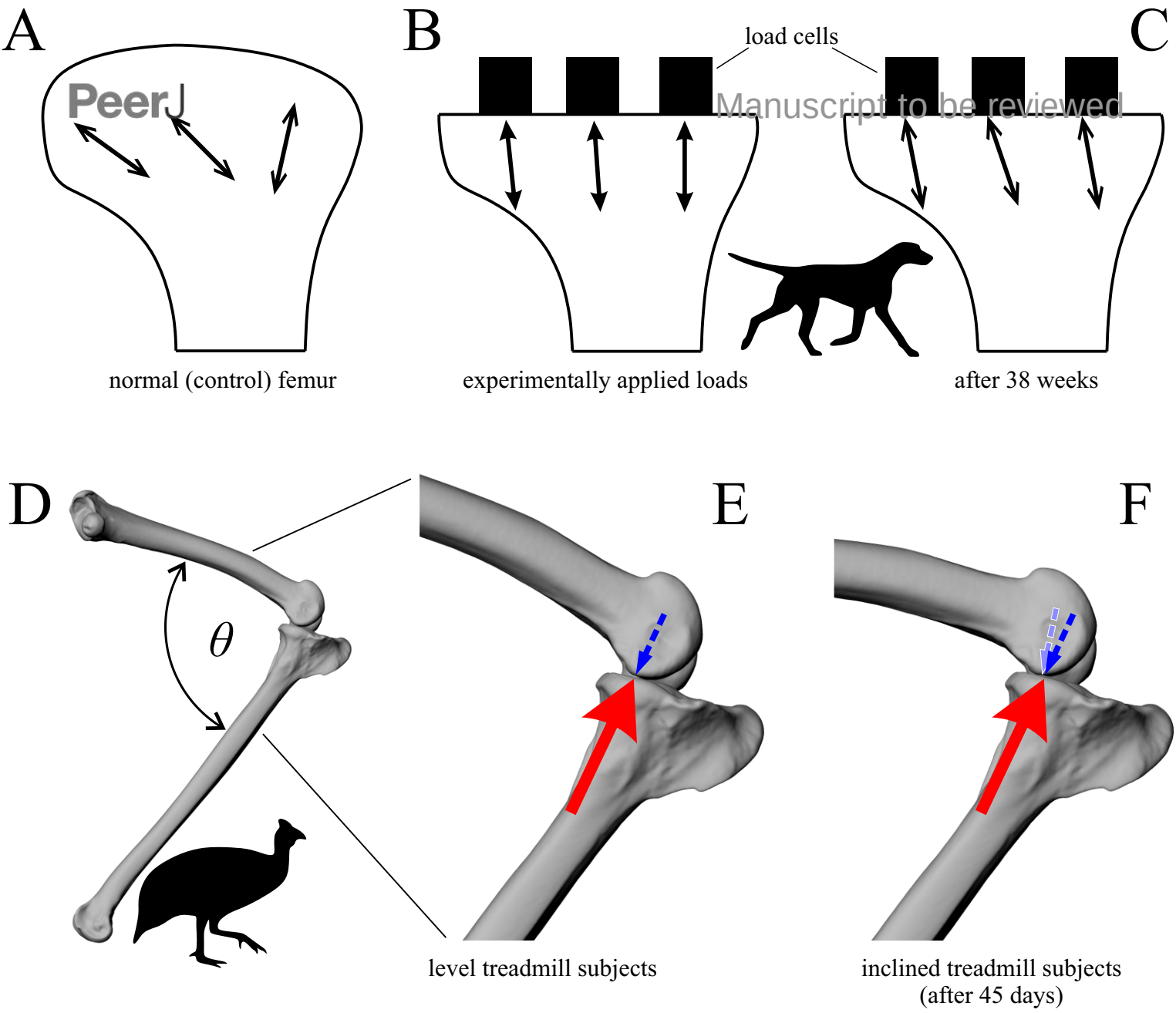
A
B
C
load cells
PeerJ
Manuscript to be reviewed
normal (control) femur
experimentally applied loads
after 38 weeks
D
E
F
θ
level treadmill subjects
inclined treadmill subjects
(after 45 days)

Figure 4(on next page)

Trabeculae tend to align themselves with the orientation ofprincipal stresses resulting from in vivo loading.

(A) Coronal micro-computed tomographic section through a human proximal femur, illustrating the architecture of cancellous bone. Image provided courtesy of SCANCO Medical AG. (B) A typical loading regime experienced by the proximal femur during locomotion, here the single-legged stance phase of walking (after Rudman et al. 2006) . This consists of the joint reaction force applied by the acetabulum (JRF), the force of the adductor muscles pulling on the trochanter (add) and the small forces applied by the capsular ligaments (c). (C) Principal stress trajectories resulting from the loading regime in B, as calculated by a two-dimensional finite element analysis (after Rudman et al. 2006) . Note the striking correspondence of the main tracts of trabeculae in A and the principal stress trajectories in C.

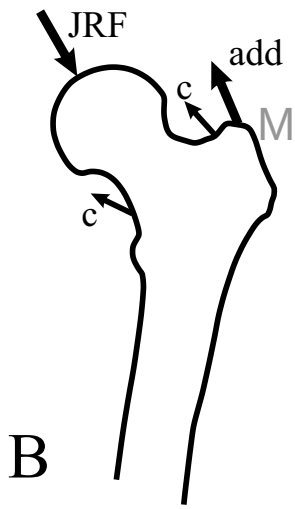

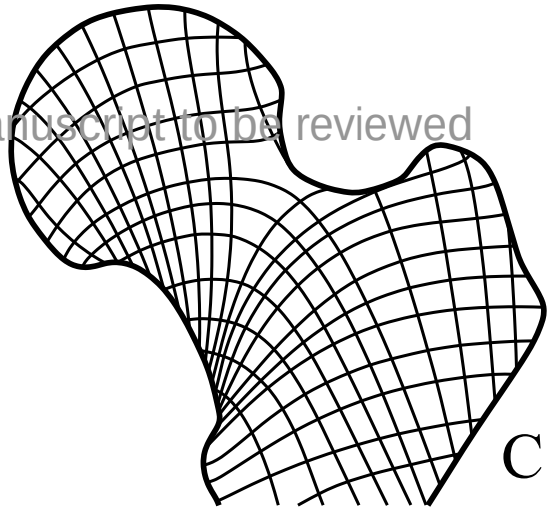

Figure 5(on next page)

Cancellous bone remodelling at the cellular level can bringabout changes in the entire architecture at the whole-bone level.

(A–D) Schematic illustration of the mechanostat of cancellous bone. Given an initial architecture in A, a change in the loading regime will lead to some parts becoming overloaded (high stress, dotted) and others becoming underloaded (low stress, horizontal hatching) in B. Surface remodelling by osteoblasts and osteoclasts (C) acts to deposit additional bone material in those overloaded areas (dark grey) and remove bone material from those underloaded areas (light grey); arrows show direction in which local bone surface moves. This continues *ad infinitum* until all bone tissue is neither too highly strained nor too little strained. (E, F) An illustration of the application of the mechanostat principal on the level of the whole bone, via computational modelling (adapted from Jang & Kim 2008; Jang & Kim 2010a) . In this example of the human proximal femur, with loads simulating both the joint reaction force and forces from the abductor muscles, the initially isotropic architecture (E) undergoes remodelling until equilibrium is reached. The resulting equilibrium architecture (F) is extremely similar to that observed in the real specimen (cf. Fig. 4A).

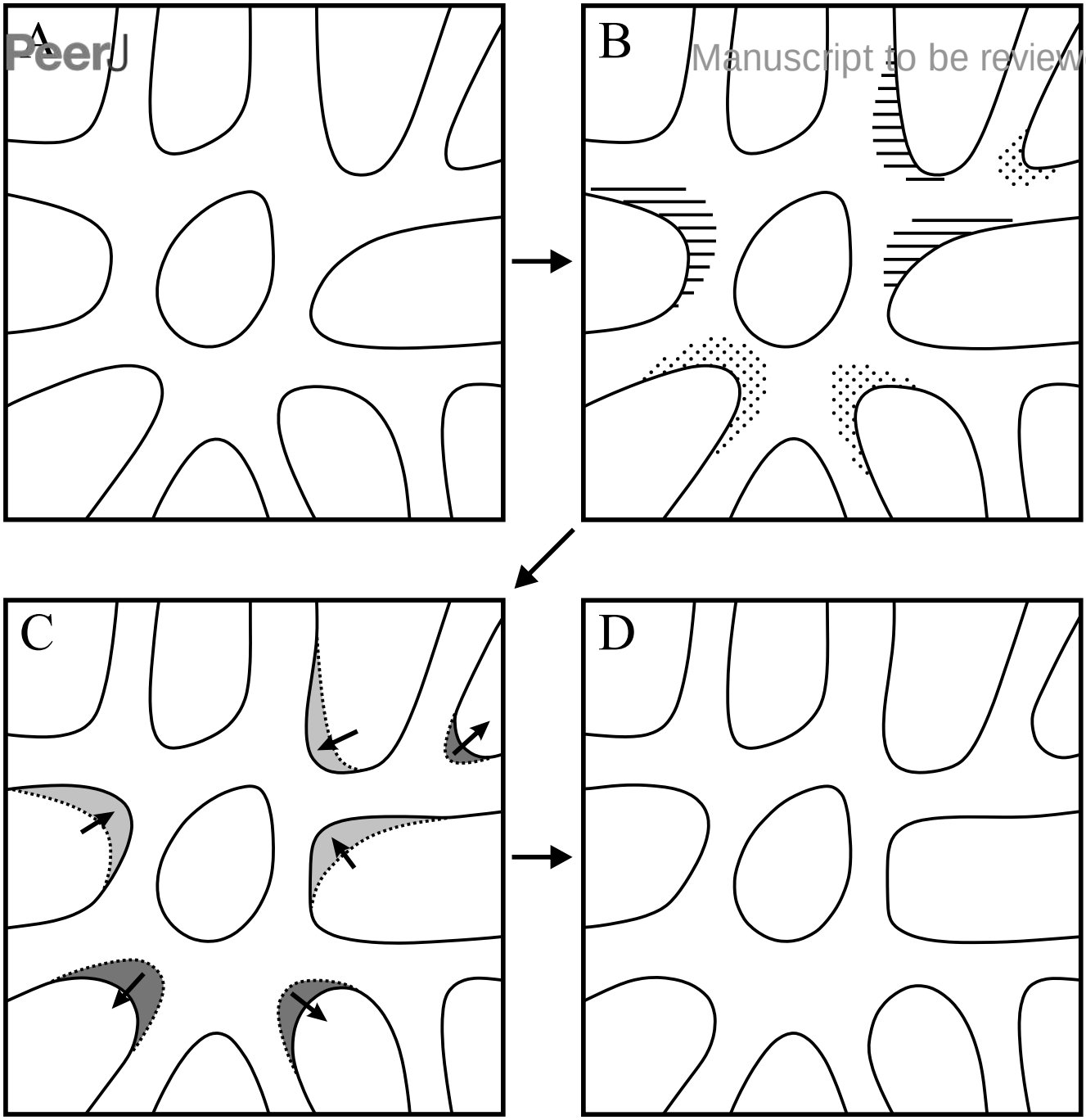

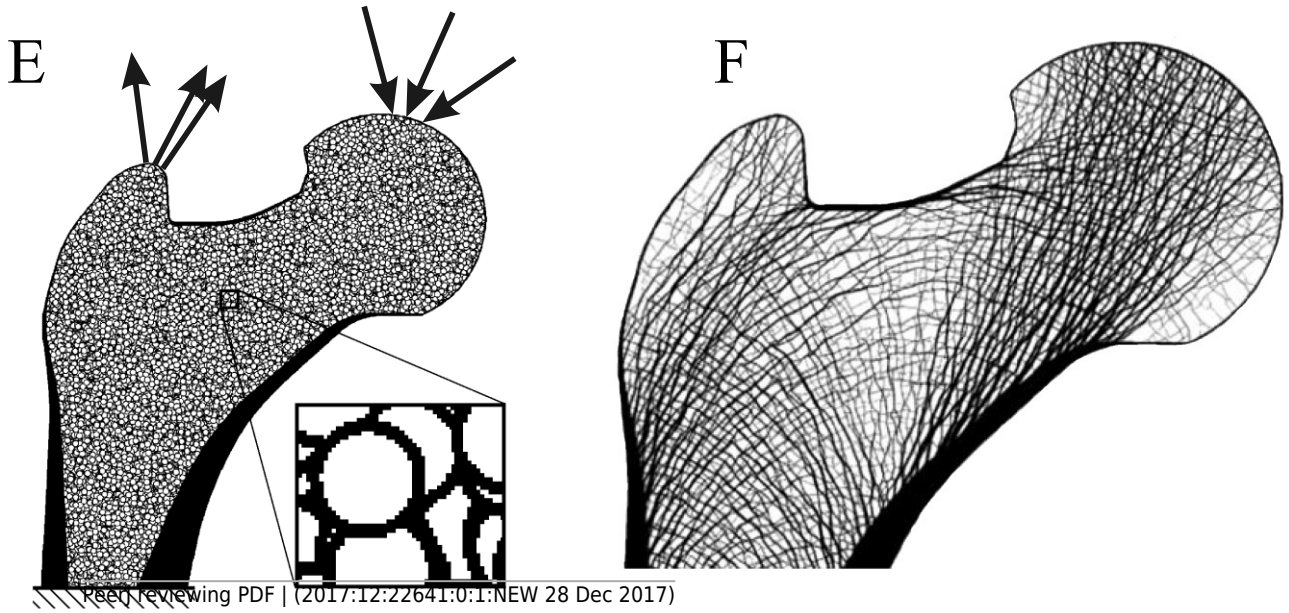

Figure 6(on next page)

Orthogonal arrangements of trabeculae usually reflect ahighly consistent loading regime experienced by a bone.

(A) Sagittal section through the calcaneum of a cow, with the pull of the Achilles tendon on the distal end indicated by the arrow. (B) A force applied to the free end of a cantilever beam is comparable to the loading regime experienced by the cow calcaneum during locomotion. The bending of the cantilever beam produces principal stress trajectories that are very similar to the overall arrangement of trabeculae in the calcaneum (solid lines are trajectories of compressive stress; dashed lines are trajectories of tensile stress). Since the calcaneum is only loaded in this fashion, the two systems of trabeculae (one curving from up, one curving down) tend to intersect at right angles.

A

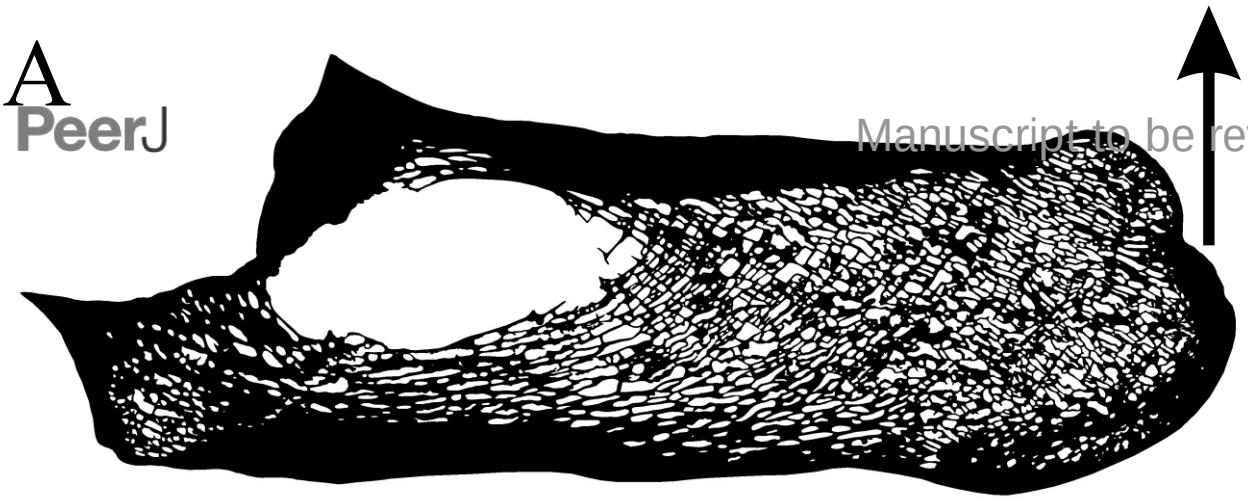

2 cm

B

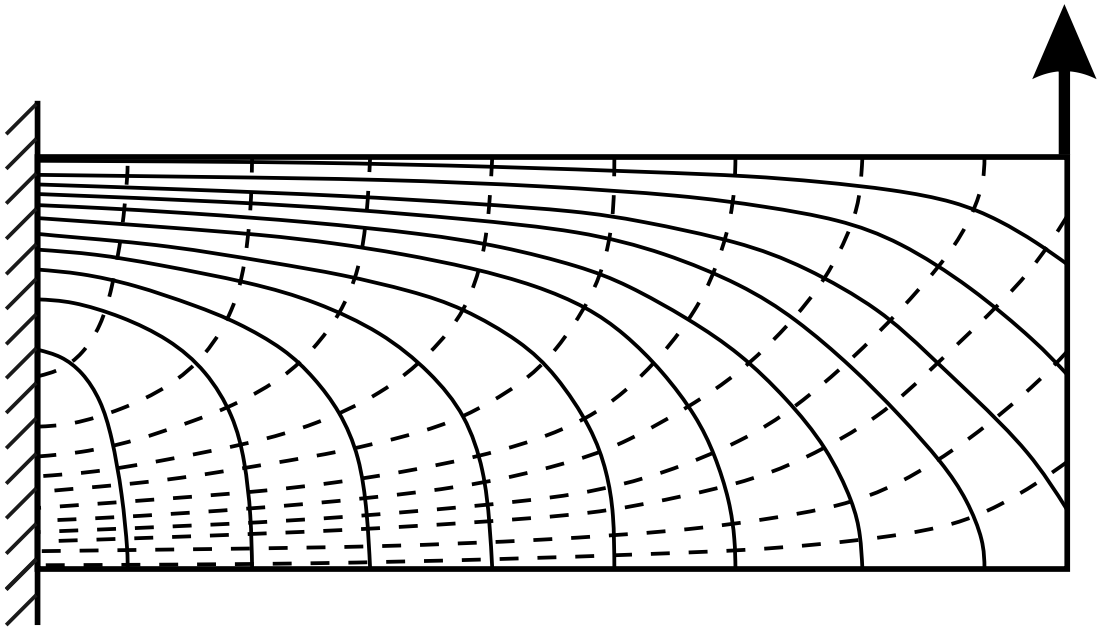

Figure 7 (on next page)

Three different ways in which the architecture of cancellousbone can be influenced by its mechanical environment.

See main text for full discussion. The dashed grey pathway for epigenetics signifies that it currently remains unknown as to if and how epigenetics may influence cancellous bone mechanobiology.

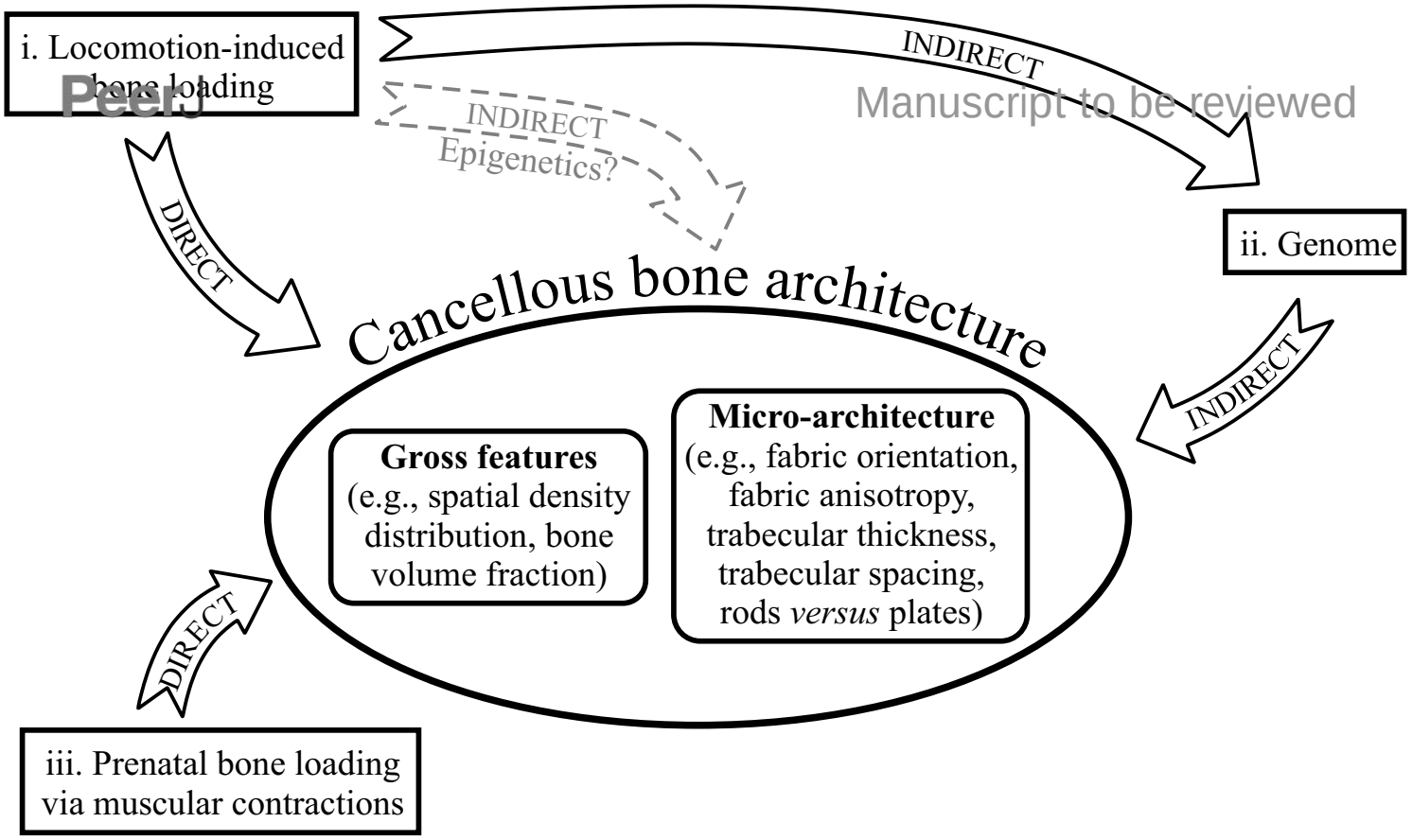

Figure 8(on next page)

Phylogenetic interrelationships of the major groups ofanimals studied.

Interrelationships of non-avian theropods are based on Zanno et al. (2009) , Carrano et al. (2012) and Turner et al. (2012) ; interrelationships of birds are based on Hackett et al. (2008) , Morgan-Richards et al. (2008) , Ksepka (2009) , Phillips et al. (2010) , Haddrath & Baker (2012) , Jetz et al. (2012) , Smith et al. (2013) , Yuri et al. (2013) , Mitchell et al. (2014) , Jarvis et al. (2014) , Ksepka & Phillips (2015) and Prum et al. (2015) . The interrelationships of the neoavian species studied here are currently not well agreed upon, and so Neoaves is shown as an unresolved polytomy. Silhouettes depict exemplar members or each group, and are not to scale. The individual determinate species of non-avian theropod studied are listed in the inset box, and their phylogenetic position signified by superscripts.

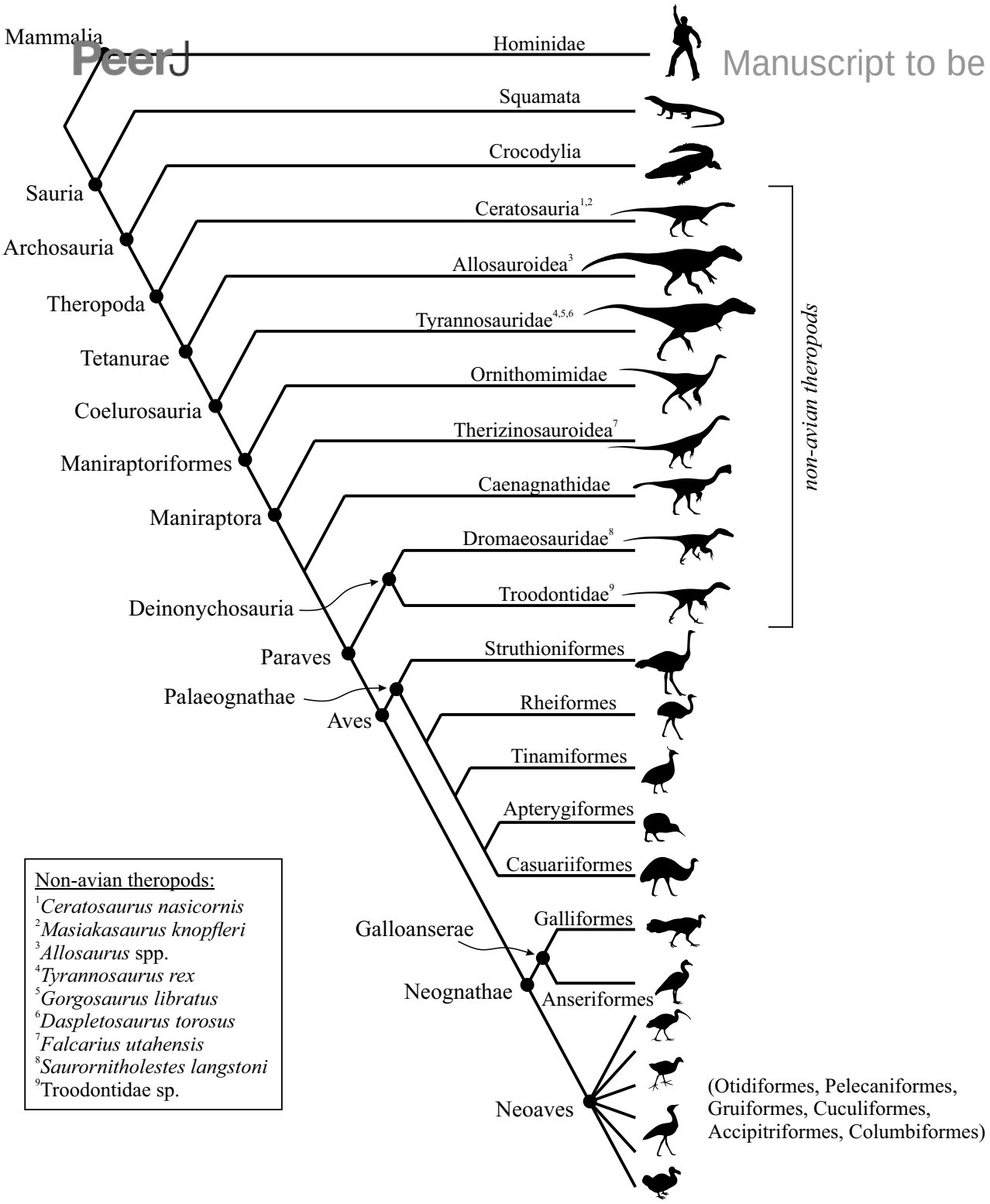

Non-avian theropods:
[1]*Ceratosaurus nasicornis*
[2]*Masiakasaurus knopfleri*
[3]*Allosaurus* spp.
[4]*Tyrannosaurus rex*
[5]*Gorgosaurus libratus*
[6]*Daspletosaurus torosus*
[7]*Falcarius utahensis*
[8]*Saurornitholestes langstoni*
[9]Troodontidae sp.

Figure 9(on next page)

Resampling the medical CT scans, as per protocol 2, helpsproduce a more accurate segmentation of the cancellous bone structure.

This is illustrated here with a CT slice of the proximal femur of a cassowary (*Casuarius casuarius*, QMO 31137). (A) The raw CT slice. (B) A local segmentation algorithm, as per protocol 1, is applied to the slice in A, with window radius 8 pixels and contrast threshold of 25; notice that it performs poorly, with some trabeculae becoming disconnected and some intertrabecular spaces being obliterated. (C) The same CT slice as in A, but resampled to triple the resolution, that is, voxel dimensions are now ⅓ of original in-plane pixel resolution. (D) A local segmentation is applied to the resampled slice in C, using the same parameters as in B; notice that it performs far better in extracting the cancellous structure. Bicubic interpolation results in smoother boundaries to the segmented scans, in contrast to lower-order (e.g., bilinear) interpolation. The location of the insets in each panel is shown in C.

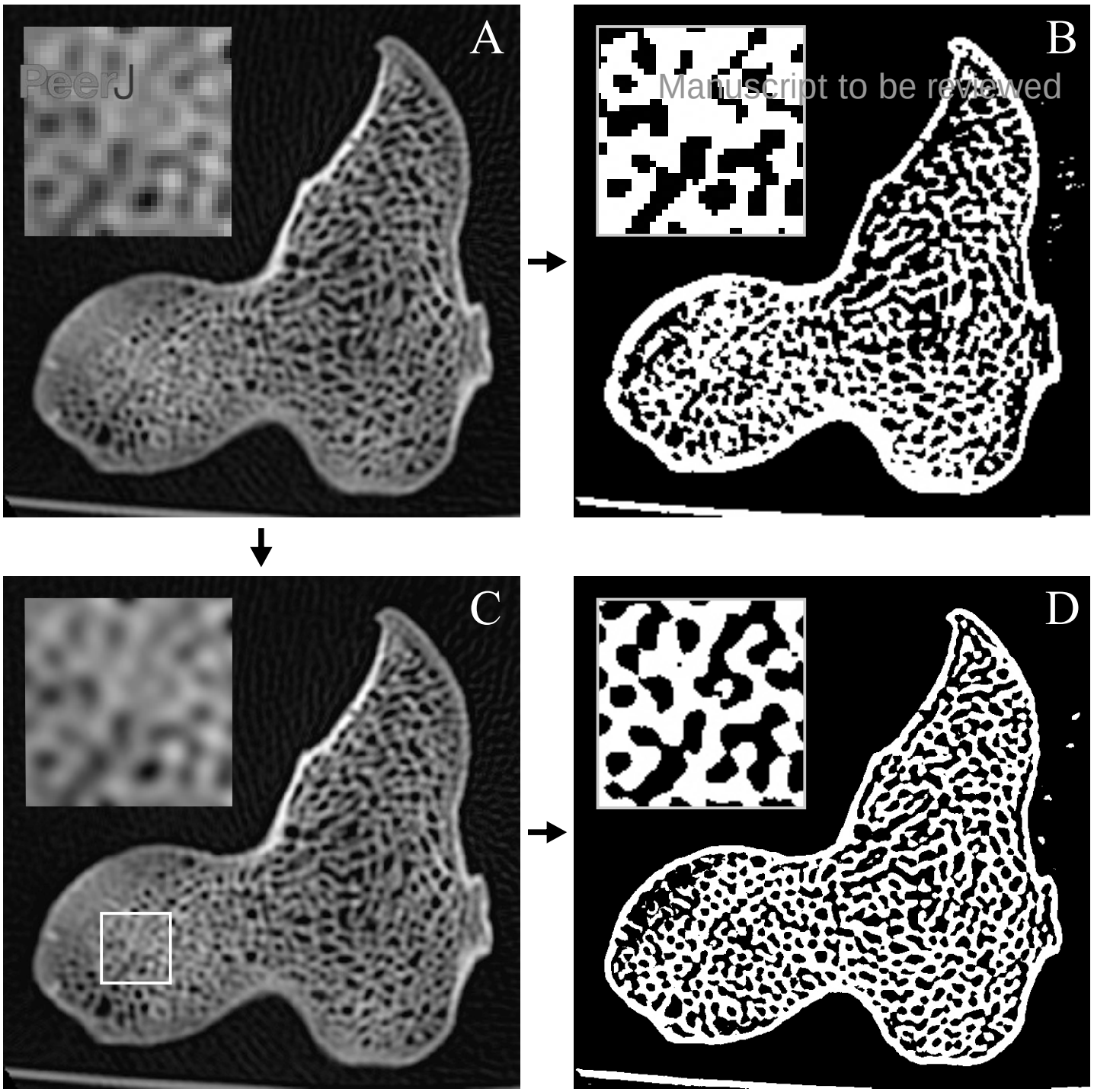

Figure 10 (on next page)

Schematic illustration of the image processing protocol usedfor the non-avian theropod micro-CT scans.

(A) The original image, affected by both high and low frequency noise; segmentation of this image by global or local thresholding techniques will not work. (B) A low-radius median filter is applied to remove high-frequency noise. (C) A large-radius median filter is applied to isolate the low-frequency (background) noise. (D) The low-frequency filtered image in C is subtracted from the high-frequency filtered image in B. (E) A low-radius mean filter is applied, followed by a global high-pass segmentation to produce the final image.

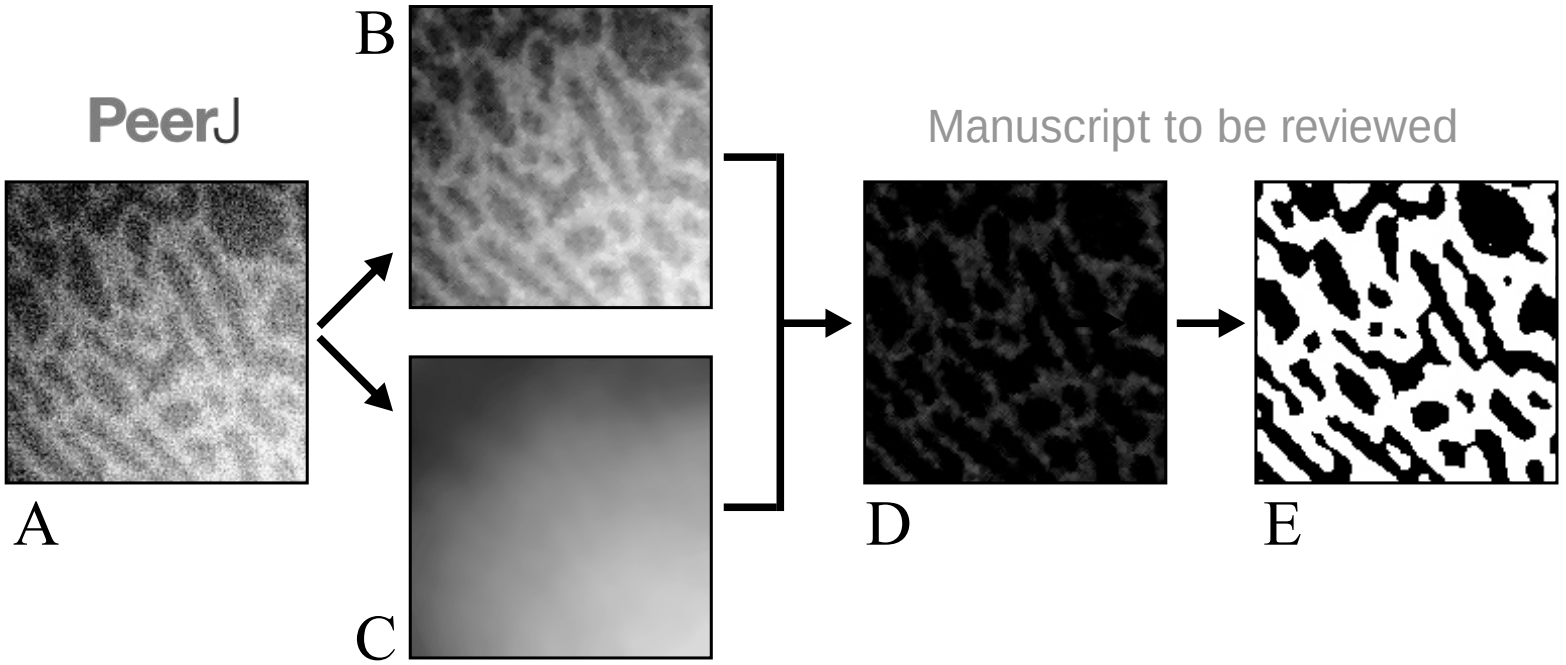

Figure 11 (on next page)

The arrangement of VOIs for quantitative analysis ofcancellous bone architecture follows the geometric pattern of cubicclose-packed spheres.

This is illustrated here for the proximal right femur of Troodontidae sp. (MOR 748). Each spherical VOI has a diameter of 5 mm. In this arrangement, each VOI is just touching its neighbouring VOIs, and each sphere can be in contact with up to 12 other VOIs. (A,B) Shown in medial view. (C, D) Shown in oblique anteromedial view. Notice in C and D that VOI placement avoids the medullary cavity (orange) and cracks (green).

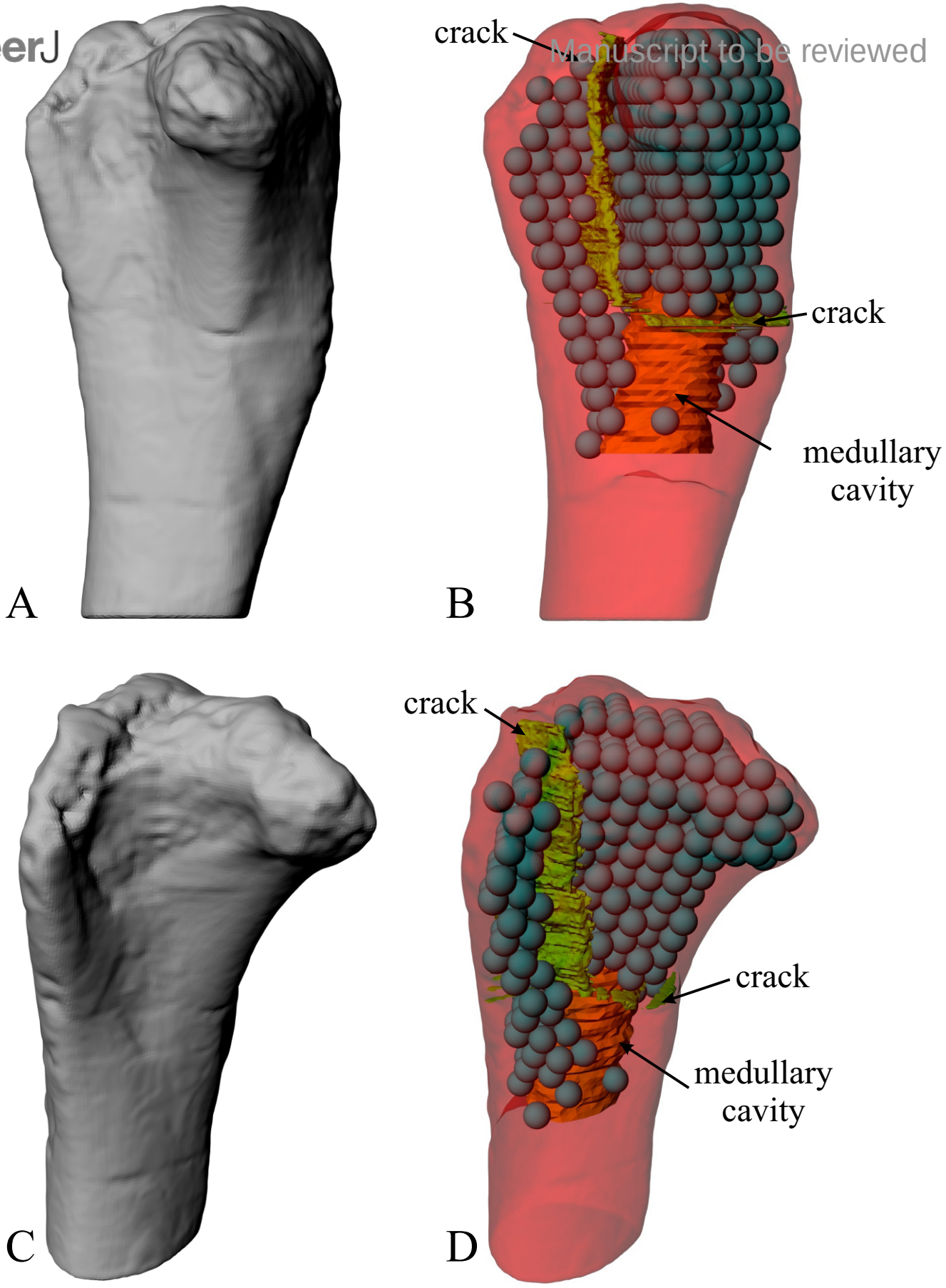

Figure 12 (on next page)

Definition of the anatomical coordinate system for the femurused in this study.

This is illustrated here with the right femur of a bustard (*Ardeotis australis*, MVB 20408), and is defined by the principal axis of inertia of the bone (dashed line) and the centres of two spheres fit to the distal condyles (white circles). For left femora, their geometry and calculated mean orientation of the primary fabric vector were mirrored prior to construction of an anatomical coordinate system.


whole-bone principal
axis of inertia
+z
+x
+y

Figure 13 (on next page)

Schematic illustration of two of the features of diaphysealcancellous bone that were subject to categorical scoring.

(A) The orientation of trabeculae with respect to the long axis of the shaft. (B) The tendency of trabeculae to be closely associated with other trabeculae. Upper row is oblique view, lower row is section-on view. These illustrations were given to the scorers to provide them with a point of reference.

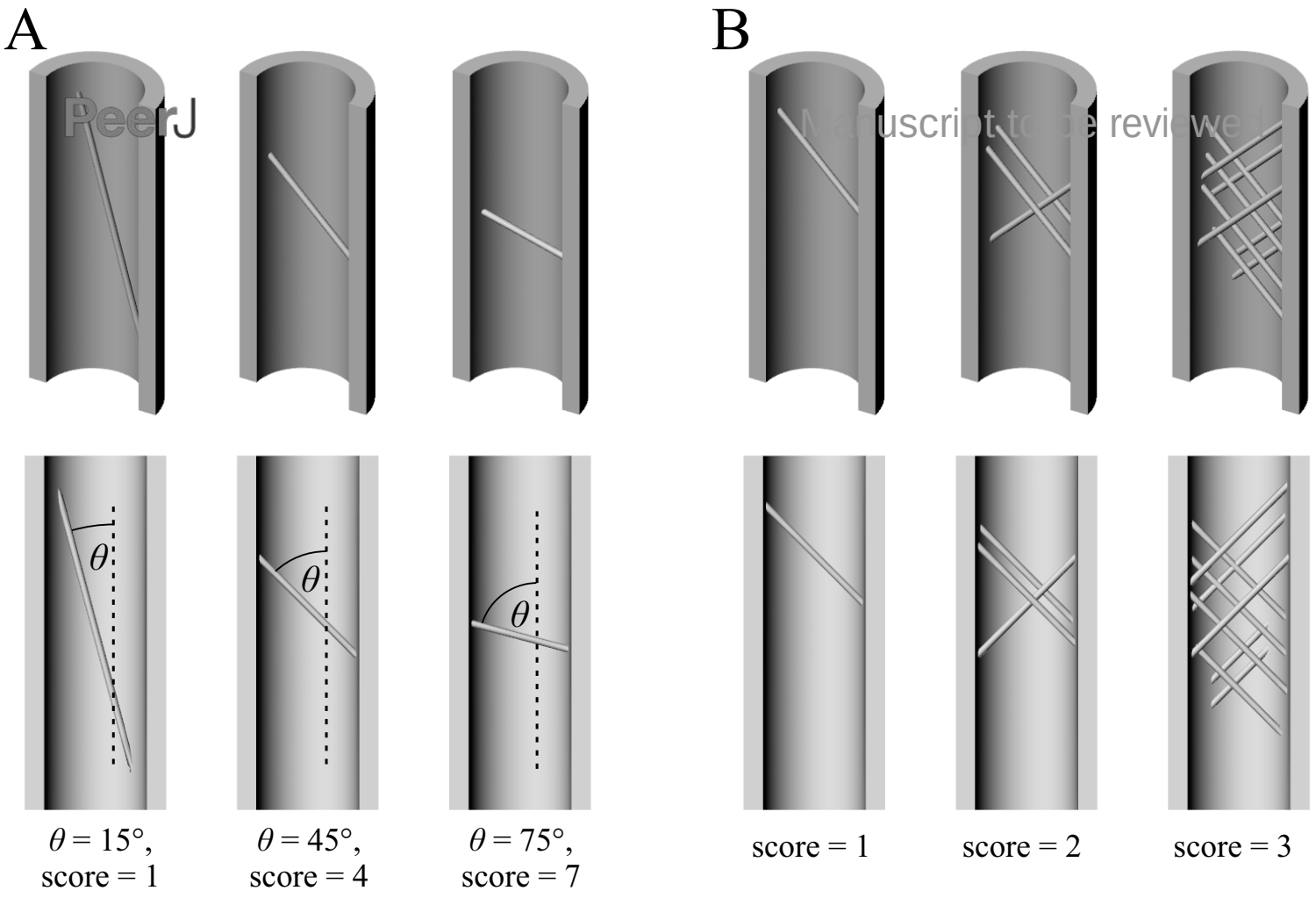

Figure 14(on next page)

Pneumatization modulates trabecular spacing in the femur ofboth large and small birds.

This is illustrated here with processed CT scan slices located approximately midway through the femoral head in the axial plane. (A) A marrow-filled femur of *Casuarius casuarius* (QMO 30105), with mean trabecular spacing = 0.638 mm. (B) A pneumatized femur of *Dromaius novaehollandiae* (QMO 16140) with mean trabecular spacing = 1.128 mm. (C) A marrow-filled femur of *Gallus gallus* (PJB coll.), with mean trabecular spacing = 0.320 mm. (D) A pneumatized femur of *Alectura lathami* (PJB coll.), with mean trabecular spacing = 0.999 mm. Reported trabecular spacing values were calculated (for illustrative purposes) for the femoral head using the BoneJ 1.3.11 plugin for ImageJ (Doube et al. 2010) . A and B are shown at the same scale, as are C and D. Scale bars are 10 mm, and yellow asterisks denote pneumatopores.

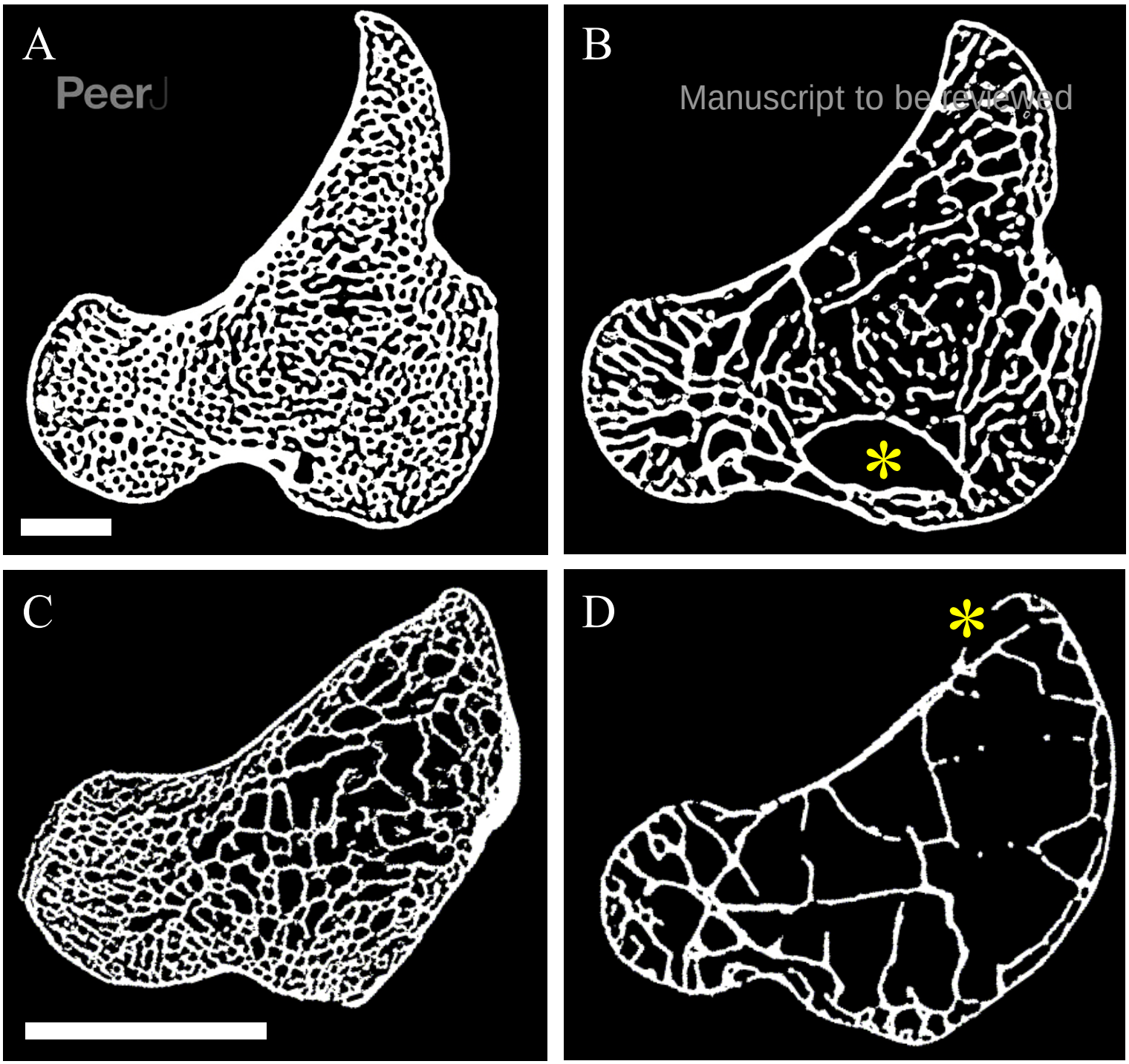

Figure 15(on next page)

The main architectural features of cancellous bone in thehuman proximal femur.

(A) Vector field of $\mathbf{u}_1$ in the head, inferior neck and greater trochanter regions, plotted on a translucent rendering of the external bone geometry; view is in the coronal plane. Schematic inset illustrates close correspondence with the principal compressive (PC) and greater trochanter (GT) groups of previous studies. (B) Vector field of $\mathbf{u}_1$ (red) and $\mathbf{u}_2$ (blue) in the middle of the metaphysis, viewed in the coronal plane. Schematic inset illustrates close correspondence with the secondary compressive (SC) and secondary tensile (ST) groups of previous studies. Note that both $\mathbf{u}_1$ and $\mathbf{u}_2$ are largely parallel to the coronal plane. (C) Vector field of $\mathbf{u}_1$ in the distal metaphysis and lesser trochanter (in oblique proximomedial view), which is largely parallel to the bone's long-axis. In this and all subsequent illustrations of fabric vector fields, the length of each fabric vector is proportional to its corresponding fabric eigenvalue. Additionally, all images are of bones from the right side of the body.

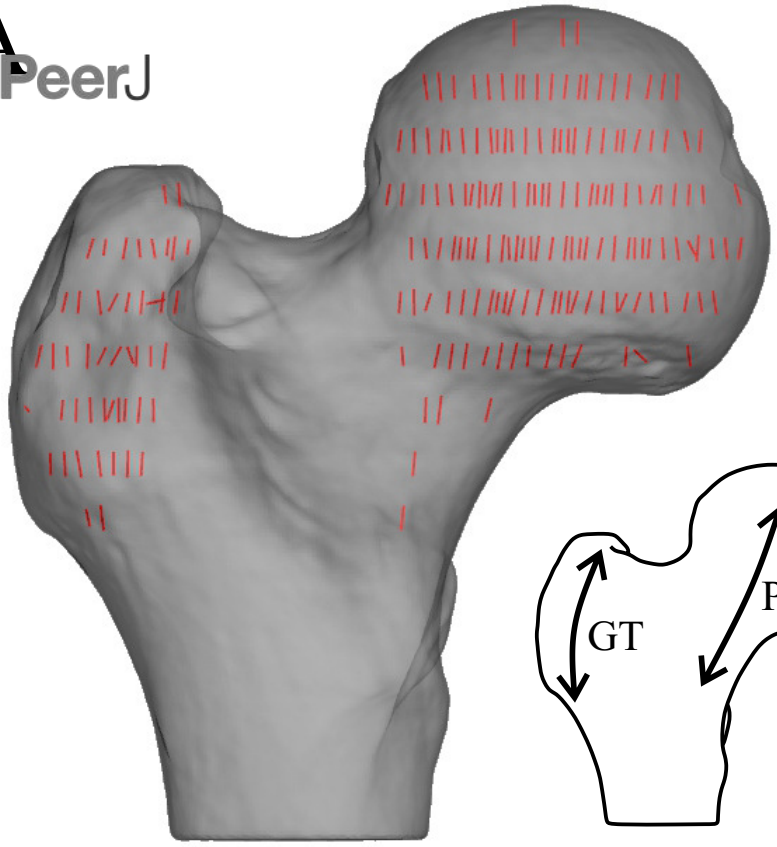

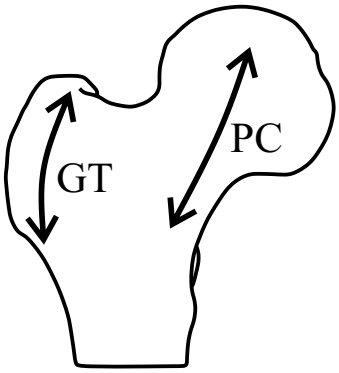

20 mm

B

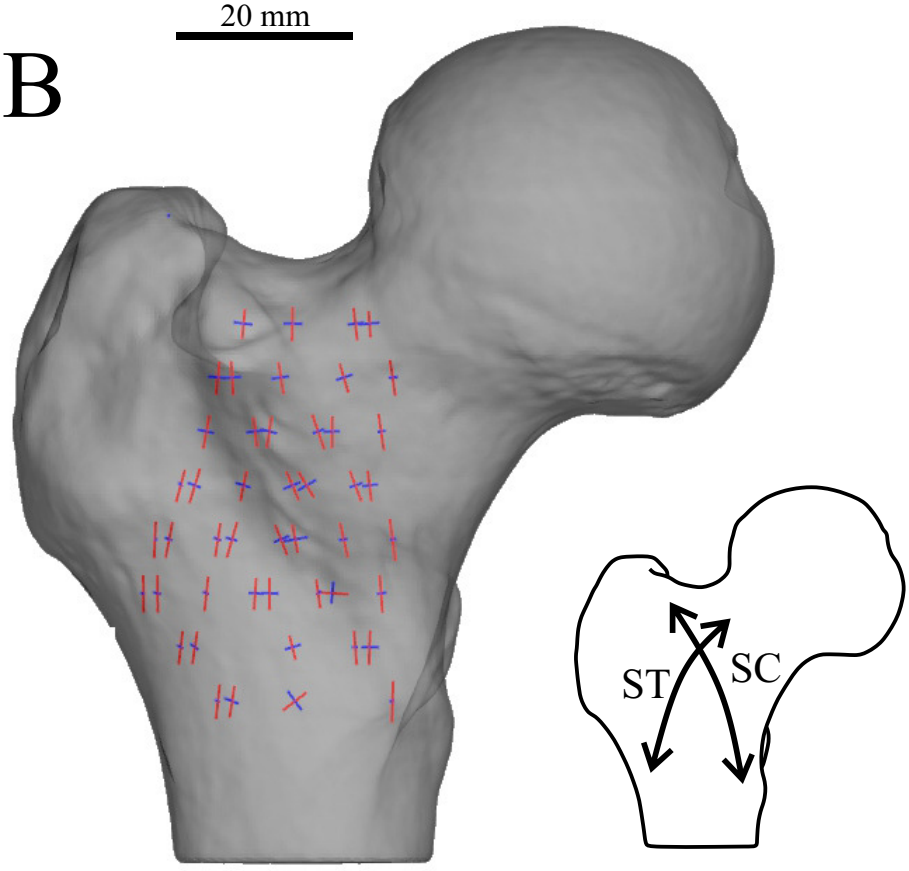

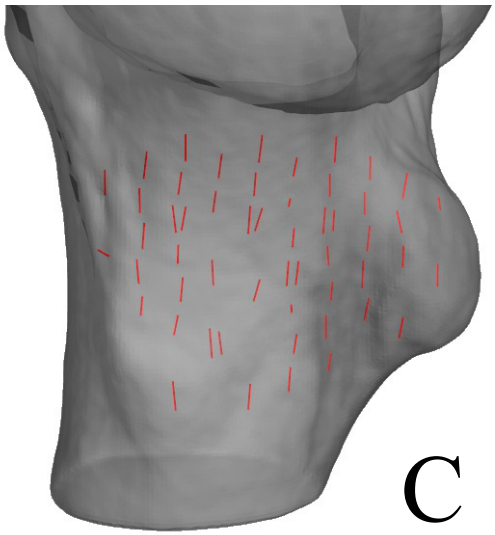

C

Figure 16(on next page)

The main architectural features of cancellous bone in theproximal femur of birds.

(A–D) Vector field of $\mathbf{u}_1$ in the femoral head and inferior neck of Dromaius novaehollandiae (QMO 16140; A, B) and Struthio camelus (MV R.2385; C, D). (E–H) Vector field of $\mathbf{u}_1$ under the facies antitrochanterica of Rhea americana (QMO 23517; E, F) and Gallus gallus (PJB coll.; G, H). (I) Isosurface rendering of cancellous bone under the facies antitrochanterica of Gallinula tenebrosa (PJB coll., between arrows), sectioned in the sagittal plane. (J–M) Vector field of $\mathbf{u}_1$ in the trochanteric crest of Casuarius casuarius (QMO 30105; J, K) and Struthio camelus (MV R.2385, L, M). (N) Isosurface rendering of cancellous bone in the trochanteric crest of Anseranus semipalmata (QMO 29529, between arrows), sectioned in the sagittal plane. (O, P) Vector field of $\mathbf{u}_1$ throughout the entire proximal femur of Dromaius novaehollandiae (QMO 16140, O) and Casuarius casuarius (QMO 30105, P), which illustrates the increasing obliquity and disorganization of vectors in the distal metaphysis and transition to the diaphysis, shown in regions with braces. A, C, J and L are anterior views; B and D are medial views; E and G are posterior views; F, H, K and M are lateral views; O is an oblique anterolateral view; P is an oblique anteromedial view. For reference, silhouettes of the animals depicted are provided in this figure and those that follow.

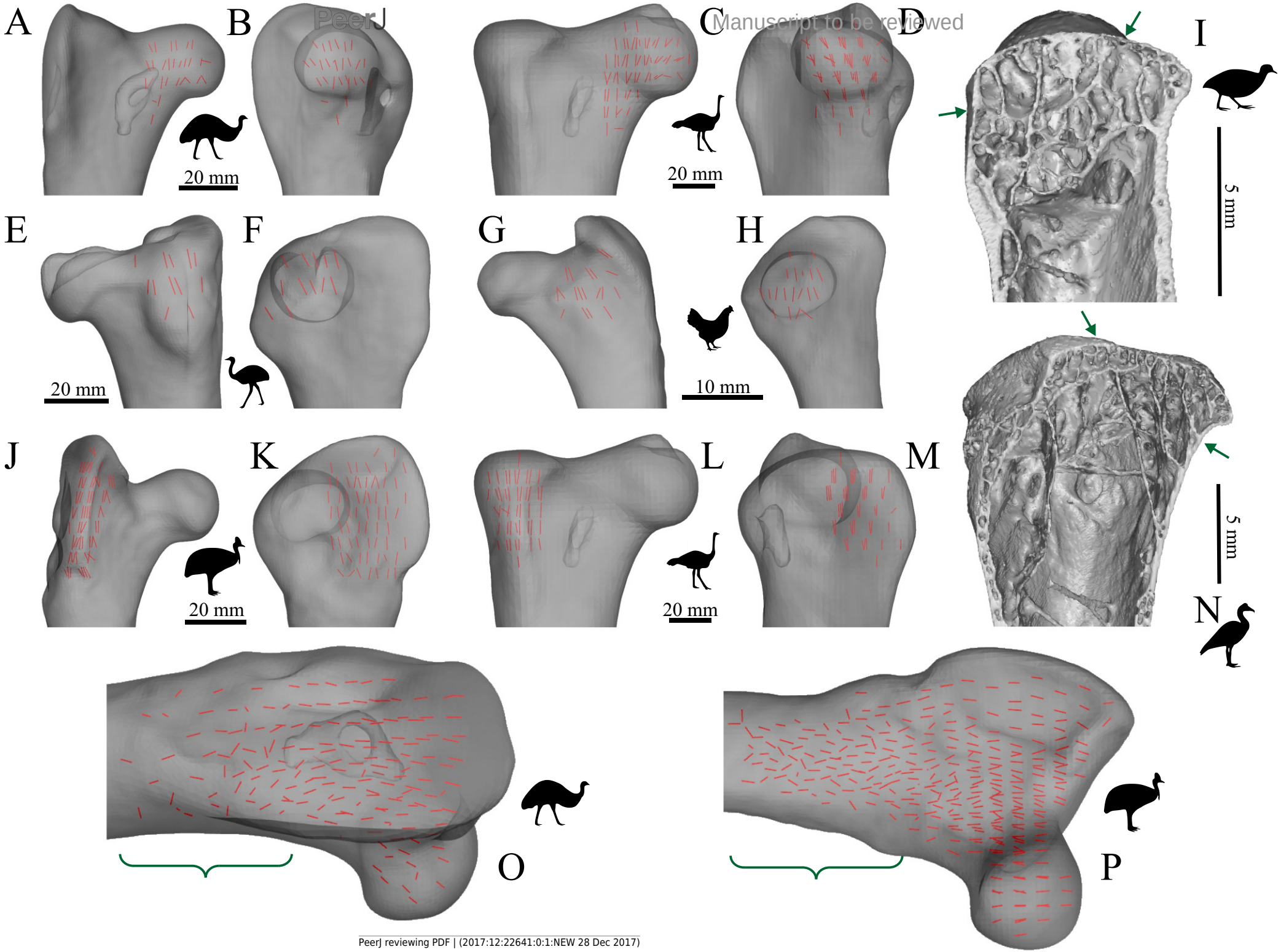

Figure 17 (on next page)

The main architectural features of cancellous bone in theproximal femur of reptiles.

(A, B) Vector field of $\mathbf{u}_1$ in the proximal femur of Crocodylus johnstoni (QMJ 47916). (C, D) Vector field of $\mathbf{u}_1$ in the proximal femur of Varanus spenceri (QMJ 84416). (E) Vector field of $\mathbf{u}_1$ throughout the proximal femur of Varanus komodoensis (AM R.106933), which illustrates the increasing obliquity and disorganization of vectors in the distal metaphysis and transition to the diaphysis, shown in region with braces. A and C are anterior views (‘dorsal view’ of herpetologists); B and D are lateral views (‘posterior view’ of herpetologists); E is an oblique anterolateral view. For clarity, the vectors of $\mathbf{u}_1$ in the fourth trochanter are not visible in A, C and E.

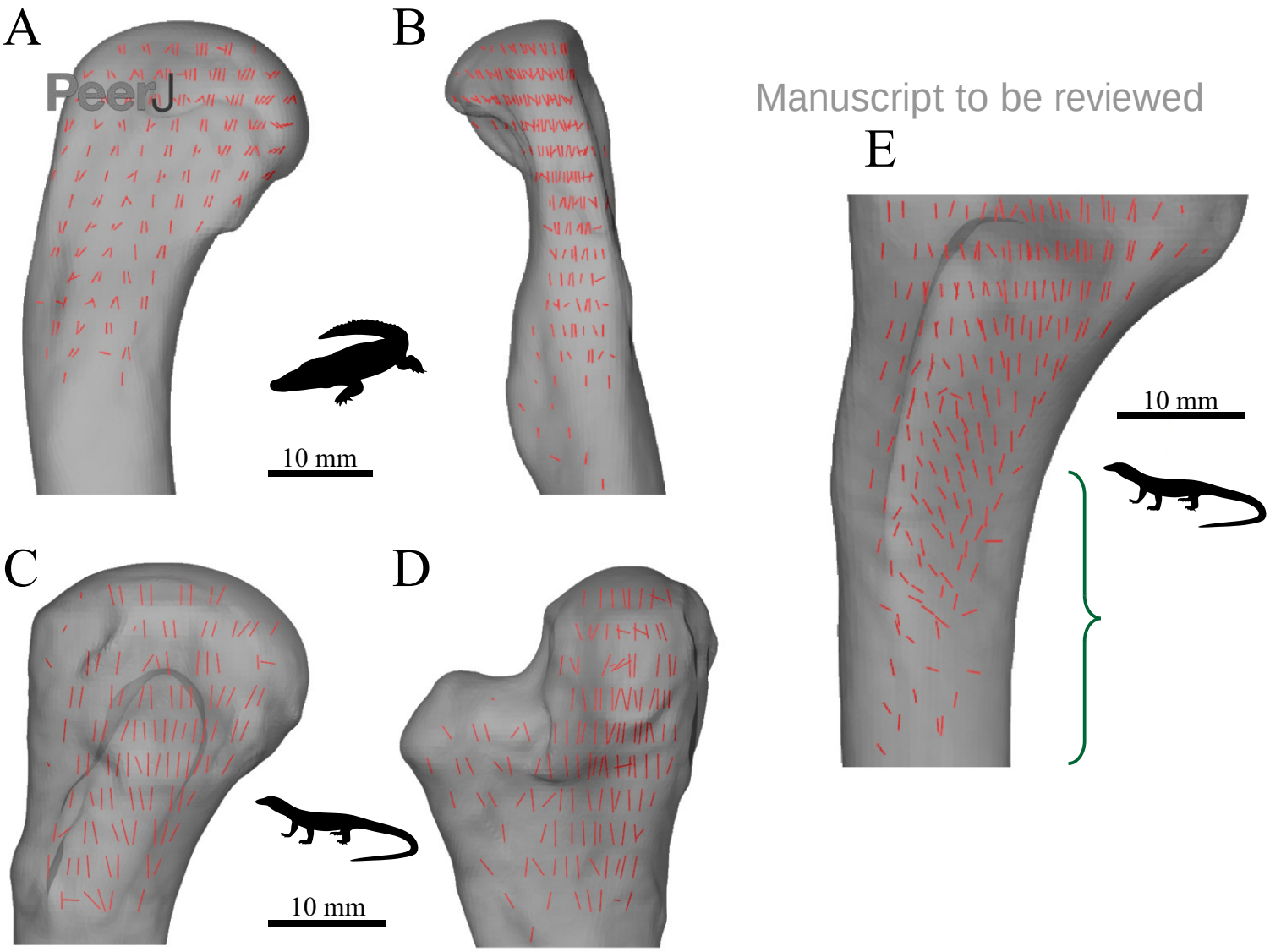

Figure 18(on next page)

The orientation of $\mathbf{u}_1$ throughout the femoral head of Masiakasaurus knopfleri , here exemplified byFMNH PR 2117.

(A) Anterior view. (B) Lateral view.

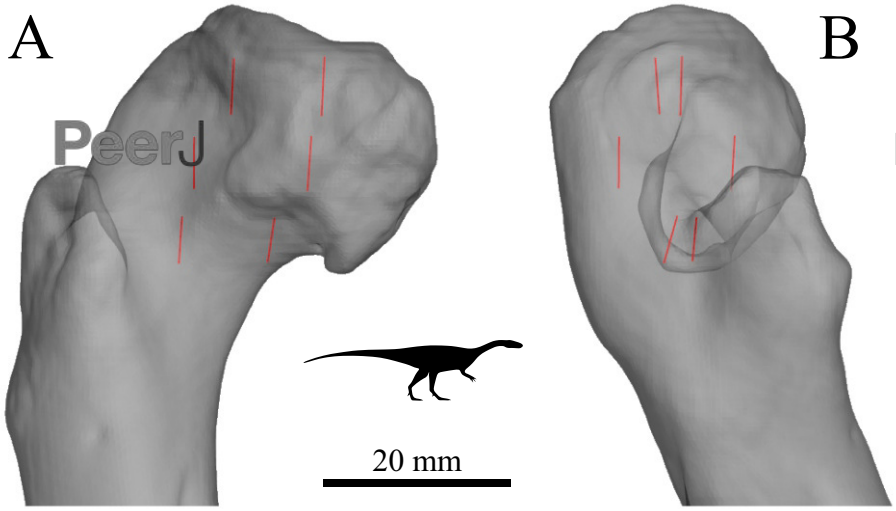

Figure 19 (on next page)

The main architectural features of cancellous bone in the proximal femur of both Allosaurus and the tyrannosaurids.

These are illustrated here with a 3-D geometric model of the observed architecture, mapped to the femur of ~~Daspletosaurus torosus~~ (TMP 2001.036.0001). (A–E) Five progressive rotations of the bone, in 30° increments, from anteromedial to anterolateral views (C is a purely anterior view). (F) The observed orientation of the dominant tract of cancellous bone in the femoral head (blue) has a gentle anterior inclination; bone shown in medial view. For explanation of the features and colour coding, refer to the main text. Inset below C is a CT slice through the proximal femur of Tyrannosaurus rex (MOR 1128), parallel to the coronal plane and through the middle of the femoral head. This illustrates the very characteristic tract of cancellous bone that extends from the base of the femoral neck up towards the apex of the head, highly comparable to the tract present in humans (cf. Fig. 4A).

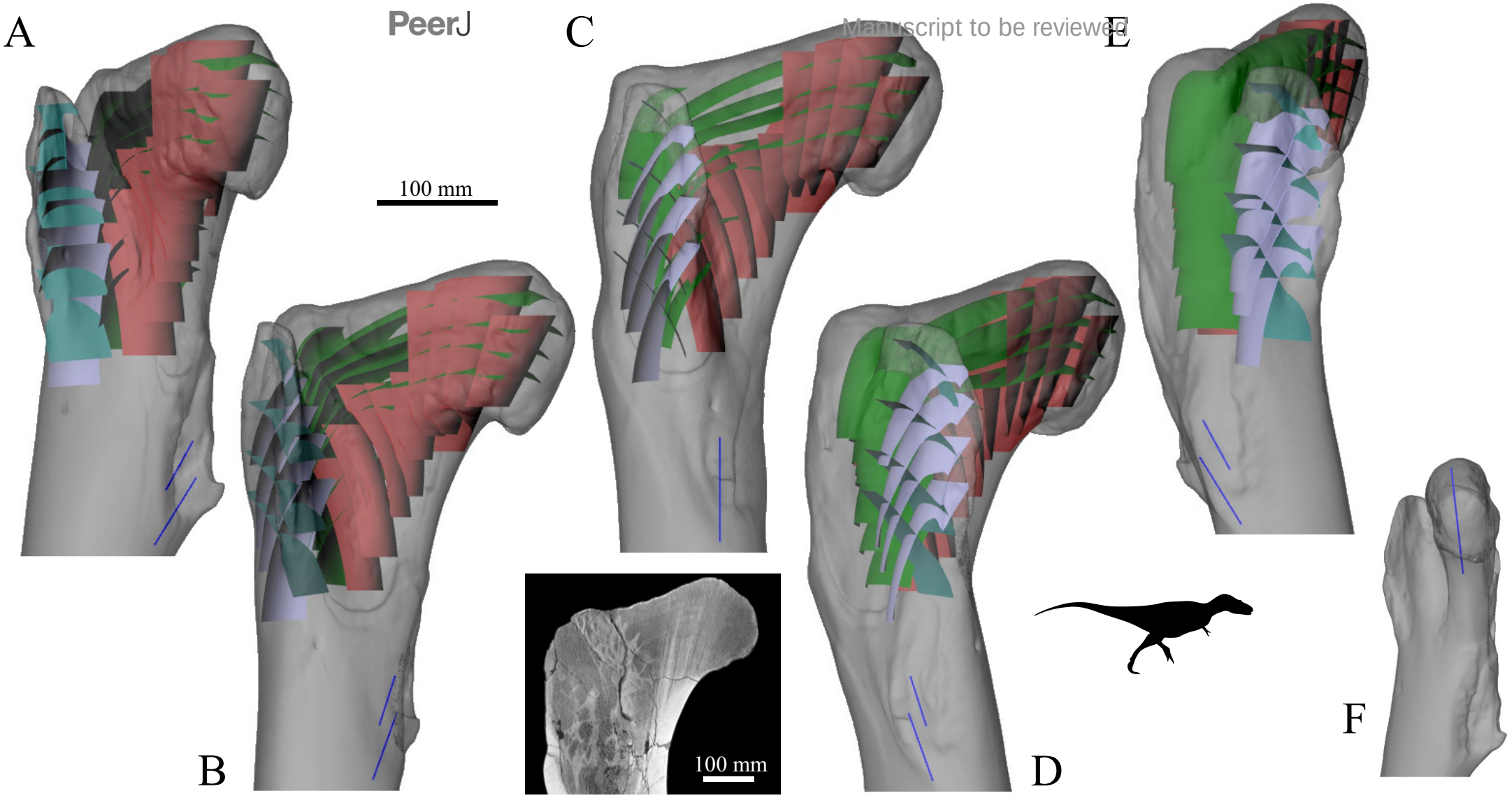

Figure 20(on next page)

The main architectural features of cancellous bone in theproximal femur of ornithomimids and caenagnathids.

(A–D) Vector field of $\mathbf{u}_1$ (A, C) and $\mathbf{u}_2$ (B, D) in the femoral head and proximal metaphysis of an inteterminate ornithomimid (TMP 85.36.276), in oblique anteromedial (A, B) and oblique anterolateral (C, D) views. Note that the vector field along the anterior and posterior peripheries of the femoral head are not shown here (for clarity), where they are more typically oriented as in birds and humans. (E) Vector field of $\mathbf{u}_1$ in the greater trochanter region and distal metaphysis of an indeterminate ornithomimid (TMP 85.36.276), in oblique anterolateral view; note the increased obliquity and disorganization of vectors in the distal metaphysis (region with braces). (F) Vector field of $\mathbf{u}_1$ in the lesser trochanter of an indeterminate ornithomimid (TMP 91.36.569), in oblique anteromedial view. (G) Vector field of $\mathbf{u}_1$ in the proximal femur of an indeterminate caenagnathid (TMP 86.36.323), in a 3-D slice parallel to the axial plane and through the femoral head and lesser trochanter. Main image is shown in axial view (anterior is toward bottom of page), with inset illustrating the region illustrated in context of the whole bone. The medialmost part of the femoral head is missing (dotted line).

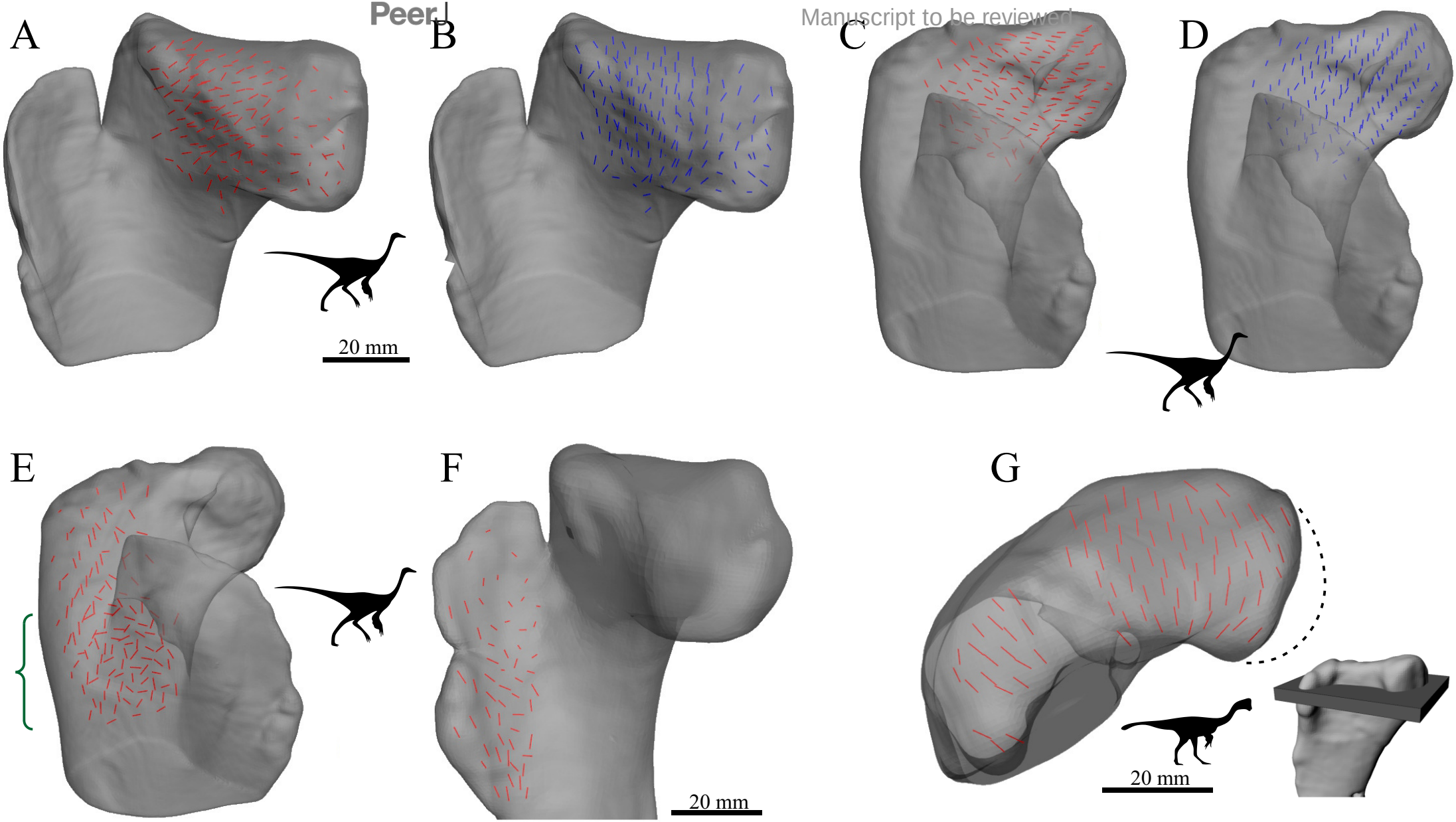

Figure 21(on next page)

The main architectural features of cancellous bone in theproximal femur of Falcarius utahensis and Troodontidaesp.

(A) Vector field of $\mathbf{u}_1$ in the proximal femur of Falcarius (UMNH VP 12361), viewed as a 3-D slice parallel to the coronal plane and through the middle of the bone. Schematic inset illustrates three main trajectories in this image, which are not too dissimilar from the patterns observed in humans and large non-avian theropods (cf. Figs 15, 19). (B, C) Vector field of $\mathbf{u}_1$ (B) and $\mathbf{u}_2$ (C) in the lesser trochanter of Falcarius , in oblique anterolateral view. (D) Vector field of $\mathbf{u}_2$ in the proximal femur of Falcarius, in a 3-D slice parallel to the axial plane and through the femoral head. Main image is shown in axial view (anterior is toward bottom of page), with inset illustrating the region illustrated in context of the whole bone. (E, F) Vector field of $\mathbf{u}_1$ in the femoral head and inferior neck of Troodontidae sp. (MOR 748) in anterior (E) and medial (F) views. (G, H) Vector field of $\mathbf{u}_1$ in the region of the greater trochanter of Troodontidae sp. (MOR 553s-7.28.91.239) in posterior (G) and lateral (H) views. (I) Orientation of $\mathbf{u}_1$ in the lesser trochanter, or immediate region thereof, of Troodontidae sp. , in oblique anterolateral view (main image illustrates MOR 748; inset illustrates MOR 553s-7.28.91.239). (J) Vector field of $\mathbf{u}_1$ throughout the metaphysis of Troodontidae sp. (MOR 553s-7.28.91.239), illustrating increasing obliquity and disorganization of vectors in the distal metaphysis and transition to the diaphysis (region with braces).

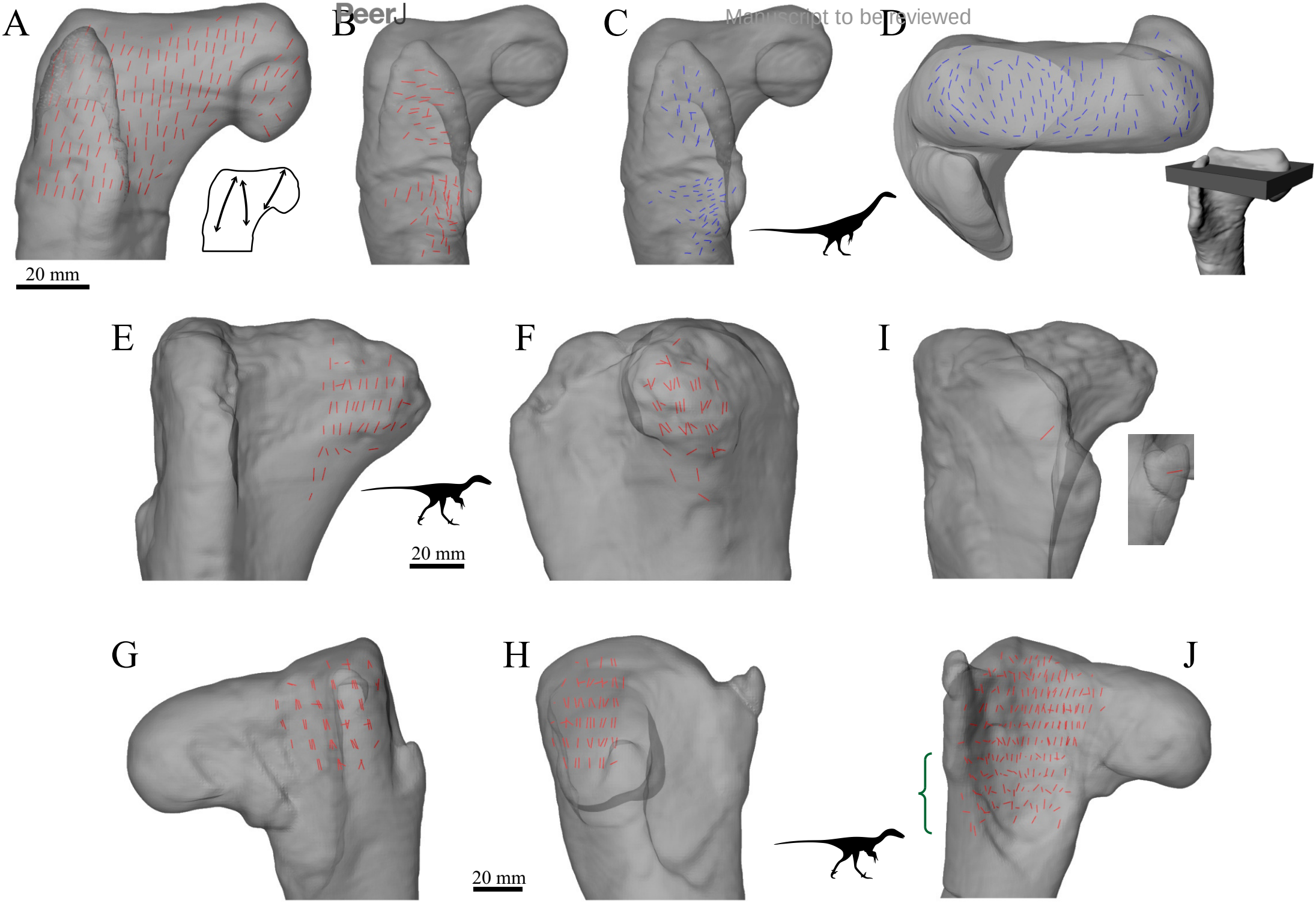

Figure 22 (on next page)

The mean orientation of $\mathbf{u}_1$ in the femoral head, referenced in the femur anatomical coordinate system.

This is plotted on an equal-angle stereoplot, with northern hemisphere projection (using StereoNet 9.5Allmendinger et al. 2013; Cardozo & Allmendinger 2013) . (A) Results for all specimens analysed. Note that for the fossil specimens, only those that were complete and well-preserved, and enabled an anatomical coordinate system to be defined, were analysed. Colour codes: black = birds, pink = human, blue = Masiakasaurus (FMNH PR 2153, UA 8384), orange = Falcarius , green = Troodontidae sp. (MOR 748), purple = general orientation for Allosaurus and the tyrannosaurids, red = mean orientation across birds. (B) Results for species or genera that were multiply sampled often displayed significant instraspecific or intrageneric variation, ranging up to 30.6°. Colour codes: black = Struthio camelus , blue = Casuarius casuarius , orange = Dromaius novaehollandiae , red = Gallus gallus , green = Apteryx spp.

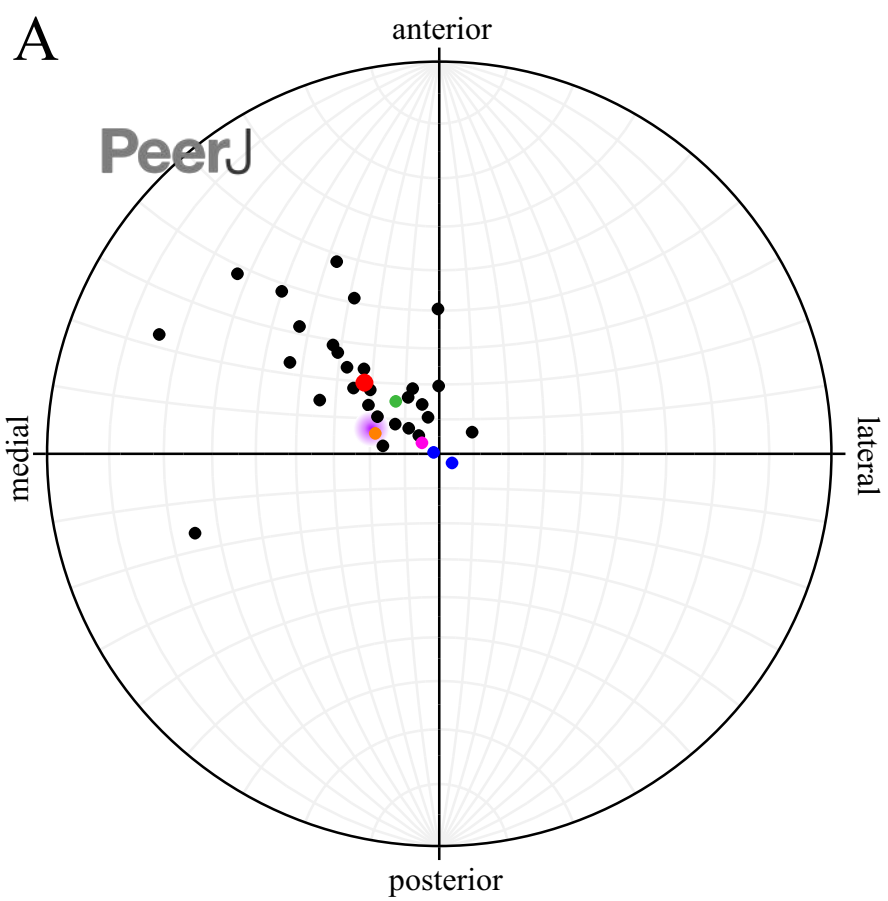

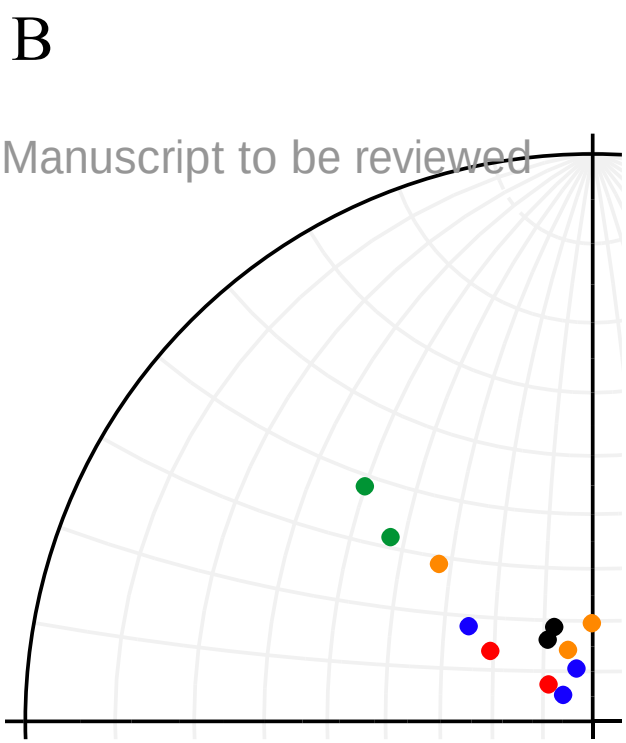

Figure 23(on next page)

The main architectural features of cancellous bone in thehuman distal femur.

(A) Vector field of $\mathbf{u}_1$ in a 3-D slice parallel to the coronal plane, made through the middle of the condyles. Schematic inset illustrates weakly developed double-arcuate pattern. (B) Vector field of $\mathbf{u}_1$ in a 3-D slice parallel to the sagittal plane, made between the condyles. Schematic inset illustrates weakly developed double-arcuate pattern. (C) Vector field of $\mathbf{u}_1$ in the medial condyle, shown for a 3-D slice parallel to the sagittal plane, made through the middle of the condyle. (D) Vector field of $\mathbf{u}_2$ at the level of the condyles, shown for a 3-D slice parallel to the axial plane, made through the middle of the condyles; anterior is toward top of page. Schematic inset illustrates the two distinctive tracts that comprise a ‘butterfly pattern’.

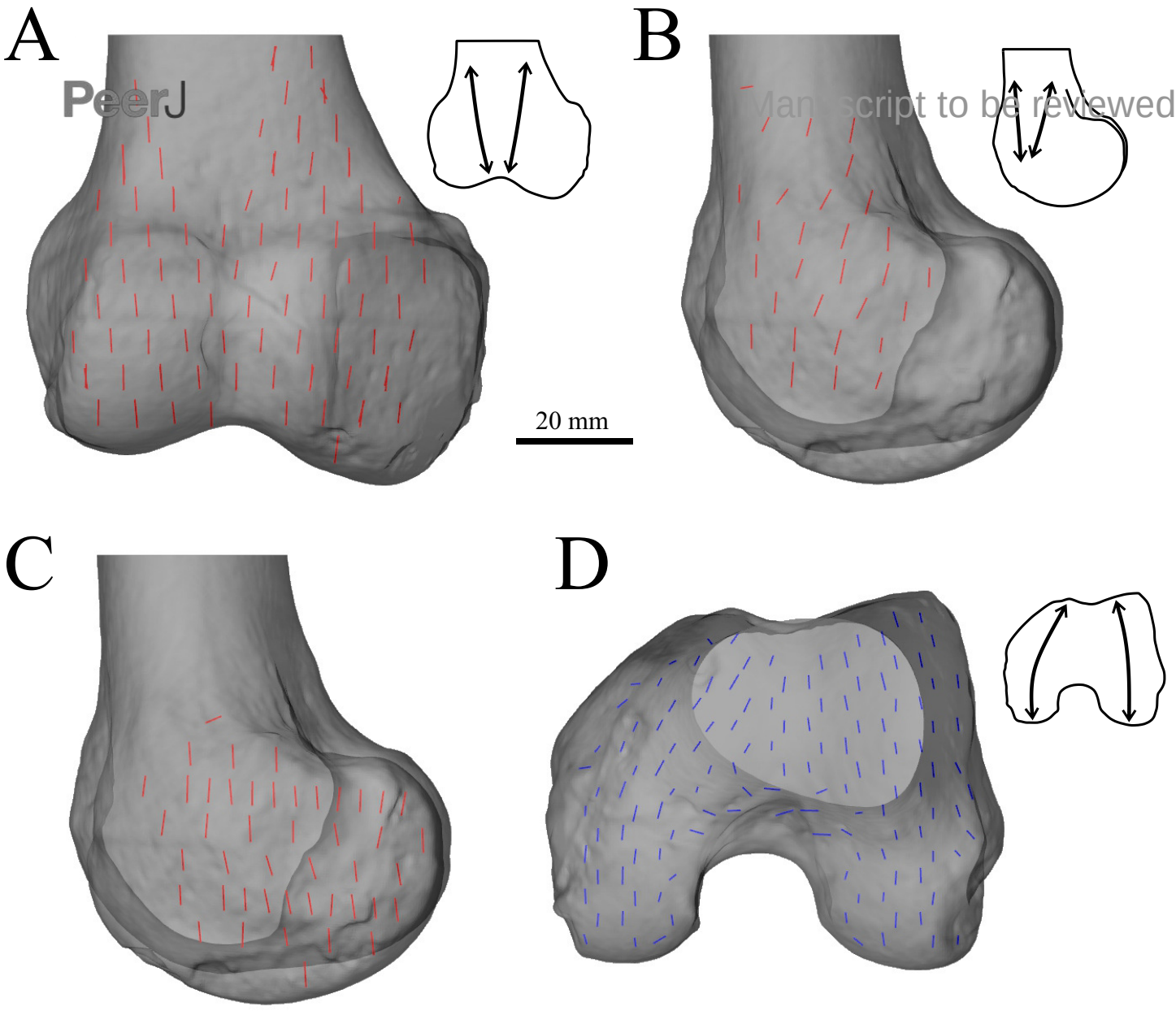

Figure 24(on next page)

The main architectural features of cancellous bone in thedistal femur of birds.

(A) Vector field of $\mathbf{u}_1$ in the central metaphysis of Casuarius casuarius (QMO 30105), in a 3-D slice, parallel to the sagittal plane and between the condyles, shown in lateral view. Note the weakly developed double arcuate pattern. (B, C) Vector field of $\mathbf{u}_2$ in a 3-D slice through the middle of the condyles in Struthio camelus (MV R.2385, B) and Dromaius novaehollandiae (QMO 11685, C), shown in distal view. Note the 'butterfly pattern' in both examples. (D) Isosurface rendering of cancellous bone in the distal condyles of Coturnix japonica (PJB coll.), sectioned in the axial plane; notice the 'butterfly pattern' between the arrows. (E–H) Vector field of $\mathbf{u}_1$ in the medial condyle of Dromaius novaehollandiae (QMO 16140, E, F) and Casuarius casuarius (QMO 30604, G, H), shown in anterior (E, G) and medial (F, H) views. (I, J) Vector field of $\mathbf{u}_1$ in the lateral condyle of Gallus gallus (PJB coll.), shown in anterior (I) and lateral (J) views. (K) Isosurface rendering of cancellous bone in the medial condyle of Porphyrio porphyrio (PJB coll.), sectioned in the sagittal plane. (L) Vector field of $\mathbf{u}_1$ throughout the entire distal femur of Casuarius casuarius (QMO 31137), illustrating increasing obliquity and disorganization of vectors in the proximal metaphysis and transition to the diaphysis (region with braces).

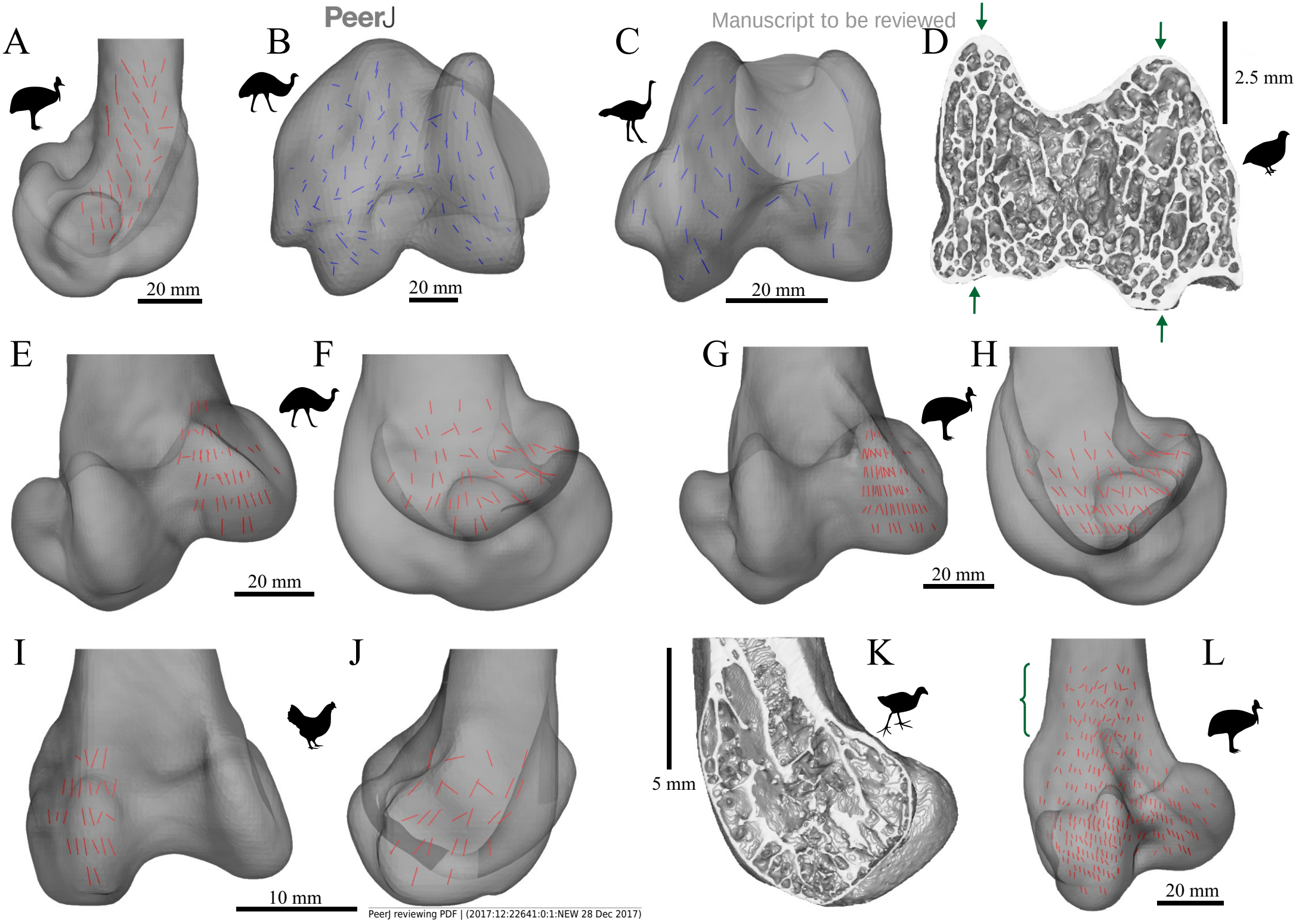
A
B
C
D
2.5 mm
20 mm
20 mm
20 mm
E
F
G
H
20 mm
20 mm
I
J
K
L
10 mm
5 mm
20 mm

Figure 25(on next page)

The main architectural features of cancellous bone in thedistal femur of reptiles.

(A, B) Vector field of $\mathbf{u}_2$ in a 3-D slice through the middle of the condyles in Crocodylus porosus (QMJ 48127, A) and Varanus komodoensis (AM R.106933, B), shown in proximal view. (C, D) Vector field of $\mathbf{u}_1$ in the medial condyle of Crocodylus porosus (QMJ 48127), shown in anterior (C) and medial (D) views. (E, F) Vector field of $\mathbf{u}_1$ in the lateral condyle of Varanus spenceri (QMJ 484416), shown in anterior (E) and lateral (F) views.

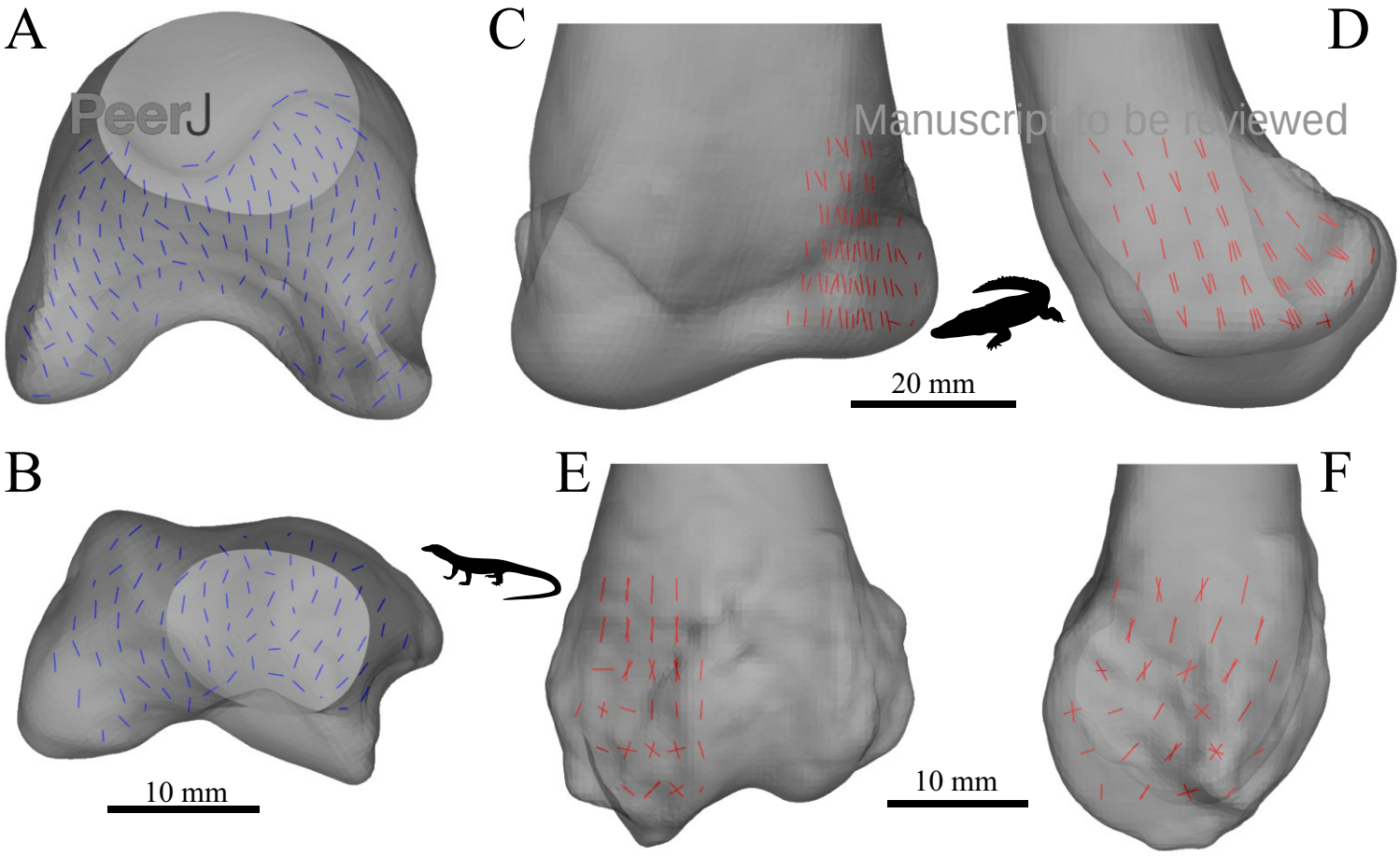

Figure 26(on next page)

The main architectural features of cancellous bone in thedistal femur of both Allosaurus and the tyrannosaurids.

These are illustrated here with a 3-D geometric model of the observed architecture, mapped to the femur of Daspletosaurus torosus (TMP 2001.036.0001). (A–G) **S** even progressive rotations of the bone, in 30° increments, from medial to lateral views (D is a purely anterior view). Note that the architecture of the metaphysis was not observed in the Allosaurus specimens studied, owing to insufficient contrast or resolution in the CT scans failing to reveal any information about the metaphysis. For explanation of the features and colour coding, refer to the main text.

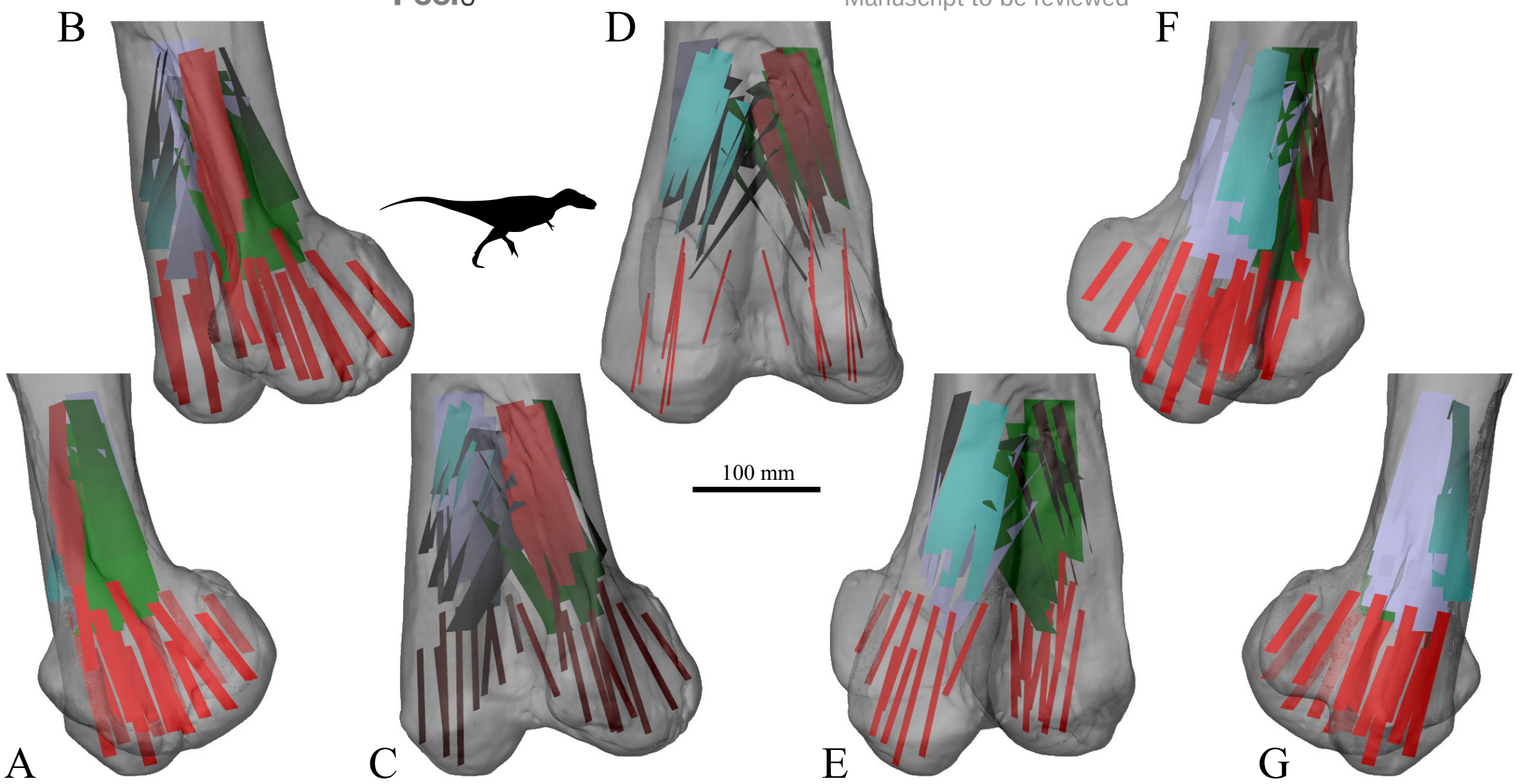
B
D
F
100 mm
A
C
E
G

Figure 27 (on next page)

The main architectural features of cancellous bone in thedistal femur of ornithomimids and caenagnathids.

(A, B) Vector field of $\mathbf{u}_1$ in the lateral condyle of an indeterminate ornithomimid (TMP 99.55.337) in posterior (A) and lateral (B) views. (C, D) Vector field of $\mathbf{u}_1$ in the medial condyle of an indeterminate caenagnathid (TMP 86.36.323) in posterior (C) and medial (D) views. (E, F) Vector field of $\mathbf{u}_1$ (E) and $\mathbf{u}_2$ (F) in the distal femur of an indeterminate ornithomimid (TMP 91.36.569) at the level of the distal condyles, shown in proximal view for a 3-D slice parallel to the axial plane (inset shows location of slice). In A–D, the highlighted yellow vectors in the posterior extremities of the condyles have a much more mediolateral orientation compared to elsewhere in the condyle. This is also seen in E, where vectors that appear longer are more parallel to the axial plane, and vectors that appear shorter are more proximodistally oriented.

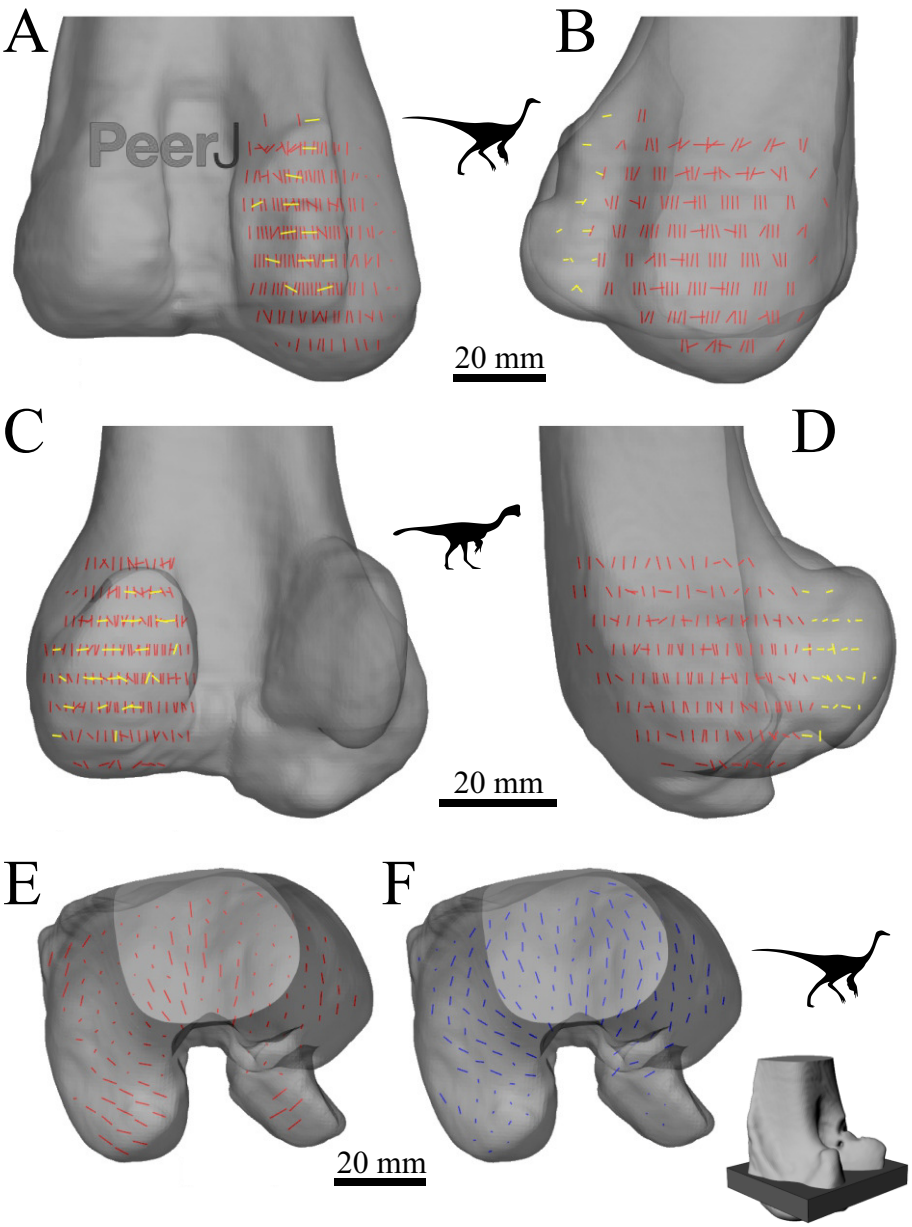

Figure 28(on next page)

The main architectural features of cancellous bone in thedistal femur of Falcarius utahensis and Troodontidaesp .

(A, B) Vector field of $\mathbf{u}_1$ in the medial condyle of Falcarius (UMNH VP 12360) in anterior (A) and medial (B) views. (C) Vector field of $\mathbf{u}_1$ throughout the distal femur of Troodontidae sp. (MOR 553s-7.28.91.239), illustrating increasing obliquity and disorganization of vectors in the proximal metaphysis and transition to the diaphysis (region with braces). (D, E) Vector field of $\mathbf{u}_1$ in the lateral condyle of Troodontidae sp. (MOR 748) in anterior (D) and lateral (E) views. (F) Vector field of $\mathbf{u}_2$ in the condyles of Troodontidae sp. (MOR 748), shown as a 3-D slice through the middle of the condyles in axial view; anterior is toward top of page.

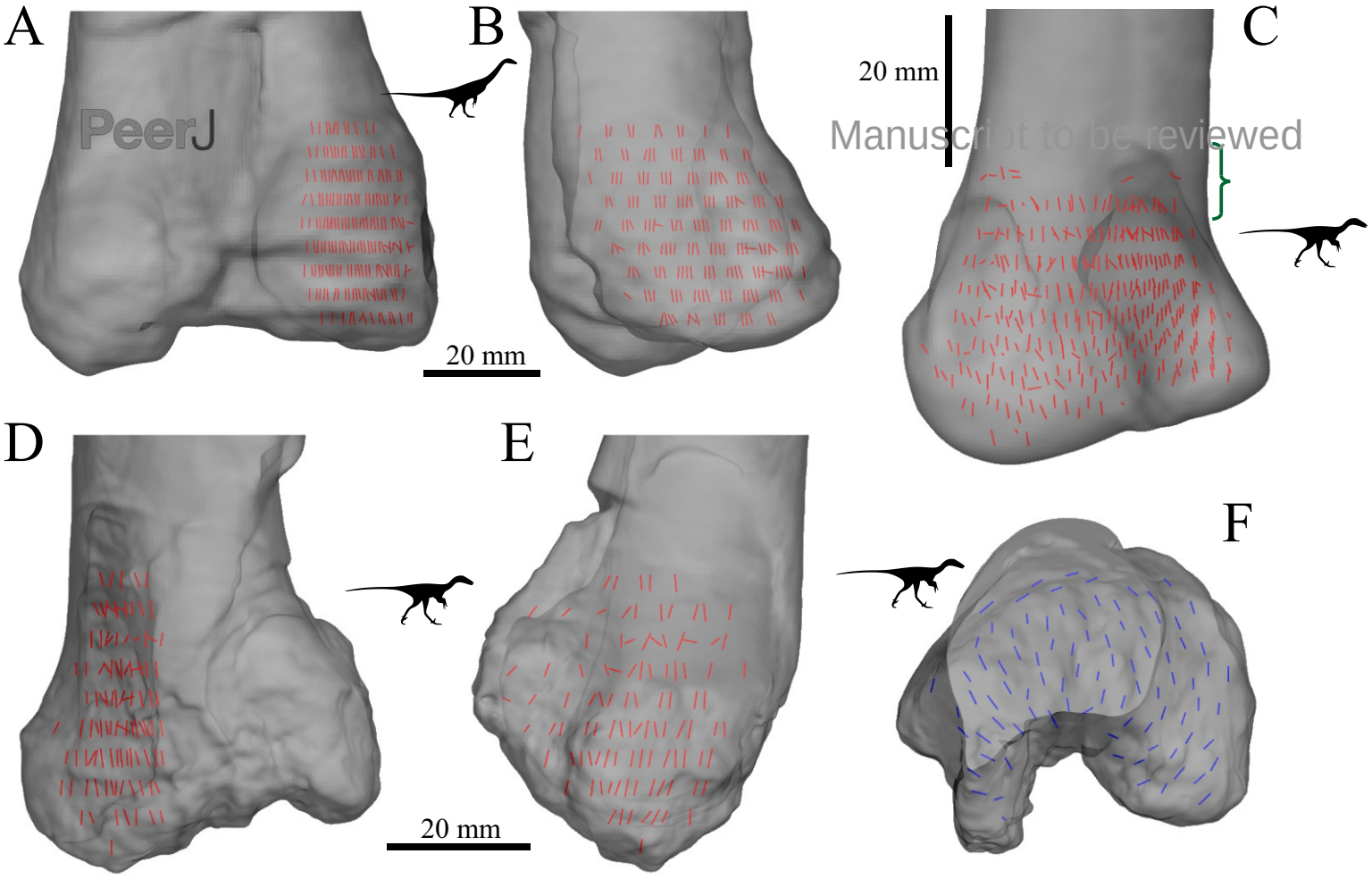

Figure 29 (on next page)

The mean orientation of $\mathbf{u}_1$ in the medial femoral condyle, referenced in the femur anatomical coordinatesystem.

This is plotted on an equal-angle stereoplot, with southern hemisphere projection (using StereoNet 9.5). (A) The results for all specimens analysed; for clarity, only the posteromedial quadrant of the plot is shown. Note that for the fossil specimens, only those that were complete and well-preserved, and enabled an anatomical coordinate system to be defined, were analysed. Colour codes: black = birds, pink = human, blue = Masiakasaurus (FMNH PR 2153, UA 8384), orange = Falcarius , green = Troodontidae sp. , purple = general orientation for Allosaurus and the tyrannosaurids, yellow = indeterminate ornithomimid (TMP 91.36.569), brown = indeterminate caenagnathid, red = mean orientation across birds. (B) Comparison of posterior inclination of $\mathbf{u}_1$ in sagittal plane versus femur length in birds, with major axis regression line (and associated statistics) plotted.

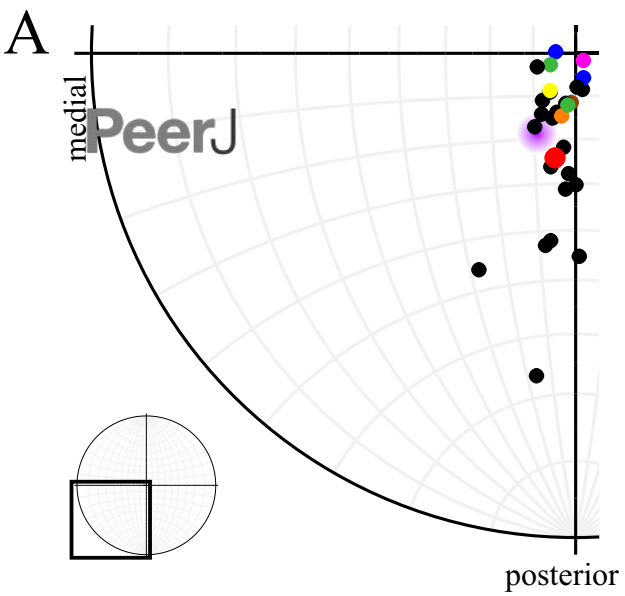

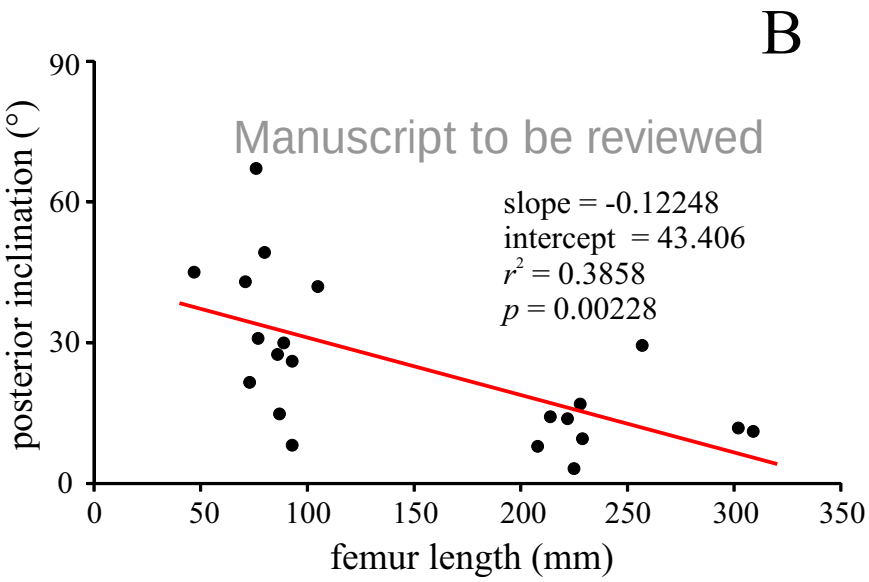

Figure 30(on next page)

The main architectural feature of cancellous bone in thehuman proximal tibia is the gentle posterior inclination of $\mathbf{u}_1$ underneath the medial andlateral condyles.

(A) Vector field of $\mathbf{u}_1$ under the lateral condyle, in lateral view. (B) Vector field of $\mathbf{u}_1$ under both condyles, in anterior view. (C) Vector field of $\mathbf{u}_1$ under the medial condyle, in medial view.

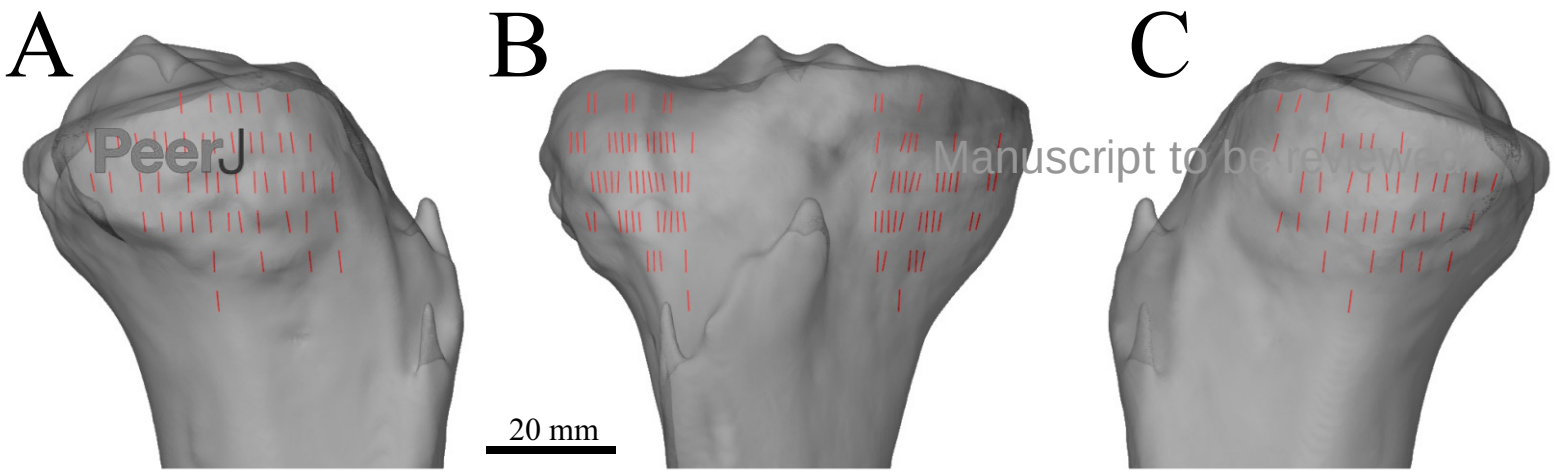

Figure 31(on next page)

The main architectural features of cancellous bone in theproximal tibia of birds.

(A, B) Vector field of $\mathbf{u}_1$ in the anterior (cranial) cnemial crest of Dromaius novaehollandiae (QMO 11686, A) and Meleagris gallopavo (RVC turkey 1, B), shown in medial view. (C, D) Vector field of $\mathbf{u}_1$ in the lateral cnemial crest of Casuarius casuarius (QMO 30105), shown in anterior (C) and lateral (D) views. (E) Isosurface rendering of cancellous bone in the anterior cnemial crest of Threskiornis moluccus (PJB coll., between arrows), sectioned in the sagittal plane. (F) Isosurface rendering of cancellous bone in the lateral cnemial crest of Numida meleagris (PJB coll., between arrows), sectioned in the plane of the crest. (G–J) Vector field of $\mathbf{u}_1$ under the medial condyle of Struthio camelus (MV R.2385, G, H) and Gallus gallus (PJB coll., I, J), shown in posterior (G, I) and medial (H, J) views. (K) Isosurface rendering of cancellous bone under the medial condyle of Eudromia elegans (UMZC 404.e, between arrows), sectioned in the sagittal plane. (L–O) Vector field of $\mathbf{u}_1$ under the lateral condyle of Struthio camelus (MV R.2711, L, M) and Dromaius novaehollandiae (QMO 11686, N, O), shown in posterior (L, N) and lateral (M, O) views. (P) Isosurface rendering of cancellous bone under the lateral condyle of Apteryx owenii (UMZC 378.iii, between arrows), sectioned in the coronal plane. (Q) Vector field of $\mathbf{u}_1$ in a 3-D slice through the middle of the proximal metaphysis, cnemial crests and condyles of Dromaius novaehollandiae (QMO 11686), parallel to the sagittal plane. Schematic inset illustrates the moderately developed double-arcuate pattern present. (R) Vector field of $\mathbf{u}_1$ throughout the entire proximal tibia of Dromaius novaehollandiae (QMO 11686), illustrating increasing obliquity and disorganization of vectors in the distal metaphysis and transition to the diaphysis (region with braces).

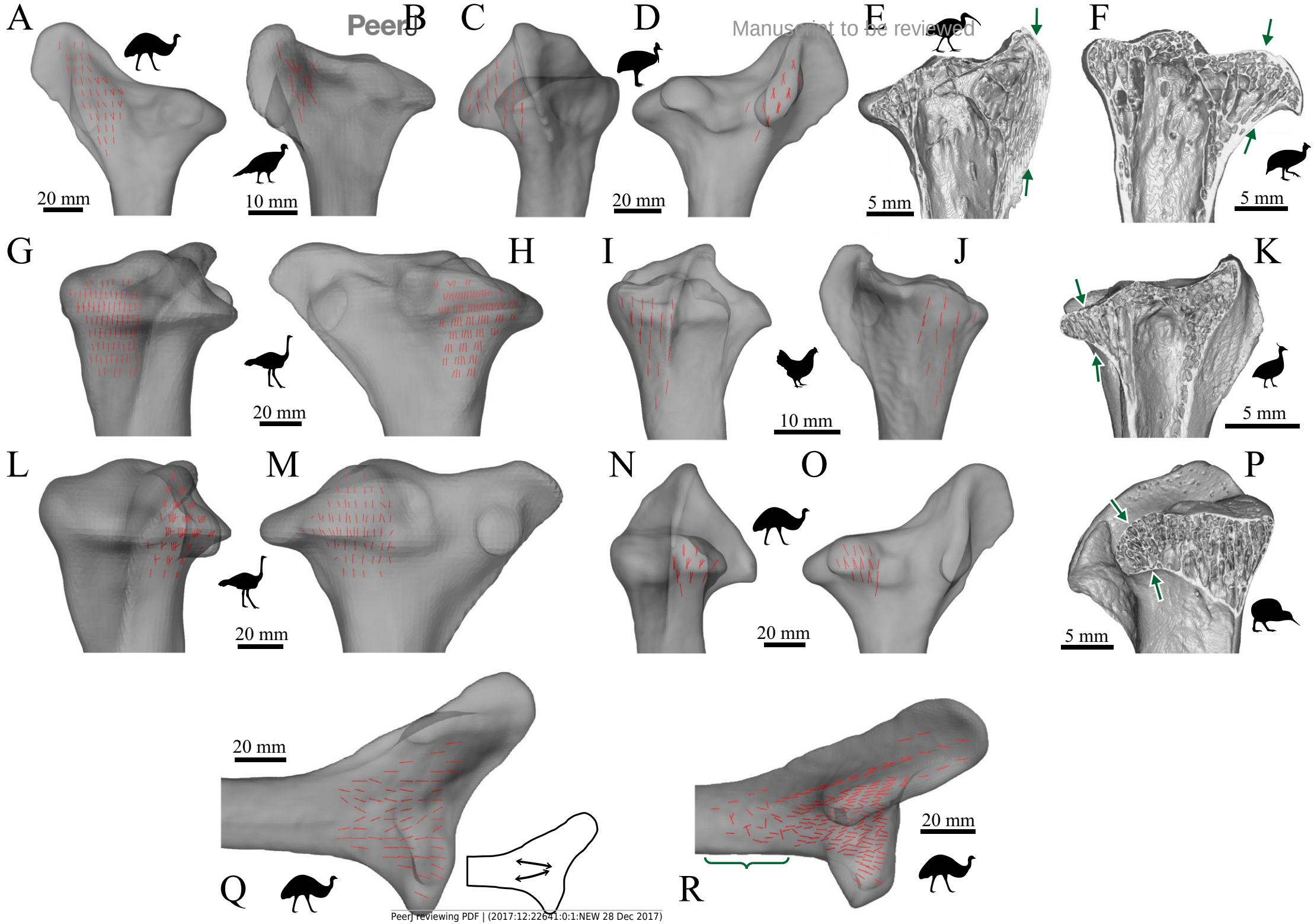

Figure 32 (on next page)

The main architectural features of cancellous bone in theproximal tibia of reptiles, as exemplified by Crocodylus porosus (QMJ 48127).

(A) Vector field of $\mathbf{u}_1$ in anterior view. (B) Vector field of $\mathbf{u}_1$ in medial view.

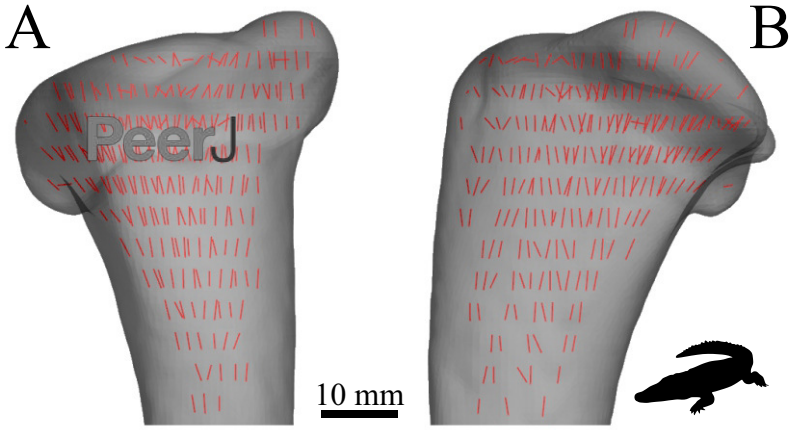

Figure 33 (on next page)

The main architectural features of cancellous bone in theproximal tibia of both Allosaurus and the tyrannosaurids.

These are illustrated here with a 3-D geometric model of the observed architecture, mapped to the tibia of Daspletosaurus torosus (TMP 2001.036.0001). (A) The dominant orientation of cancellous bone in the medial condyle, in medial view. (B) The dominant orientation of cancellous bone in the medial and lateral condyles, in posterior view. (C) The dominant orientation of cancellous bone in the lateral condyle, in lateral view. (D–J) Seven progressive rotations of the bone, in 30° increments, from proximally oblique medial to lateral views. For explanation of the features and colour coding, refer to the main text.

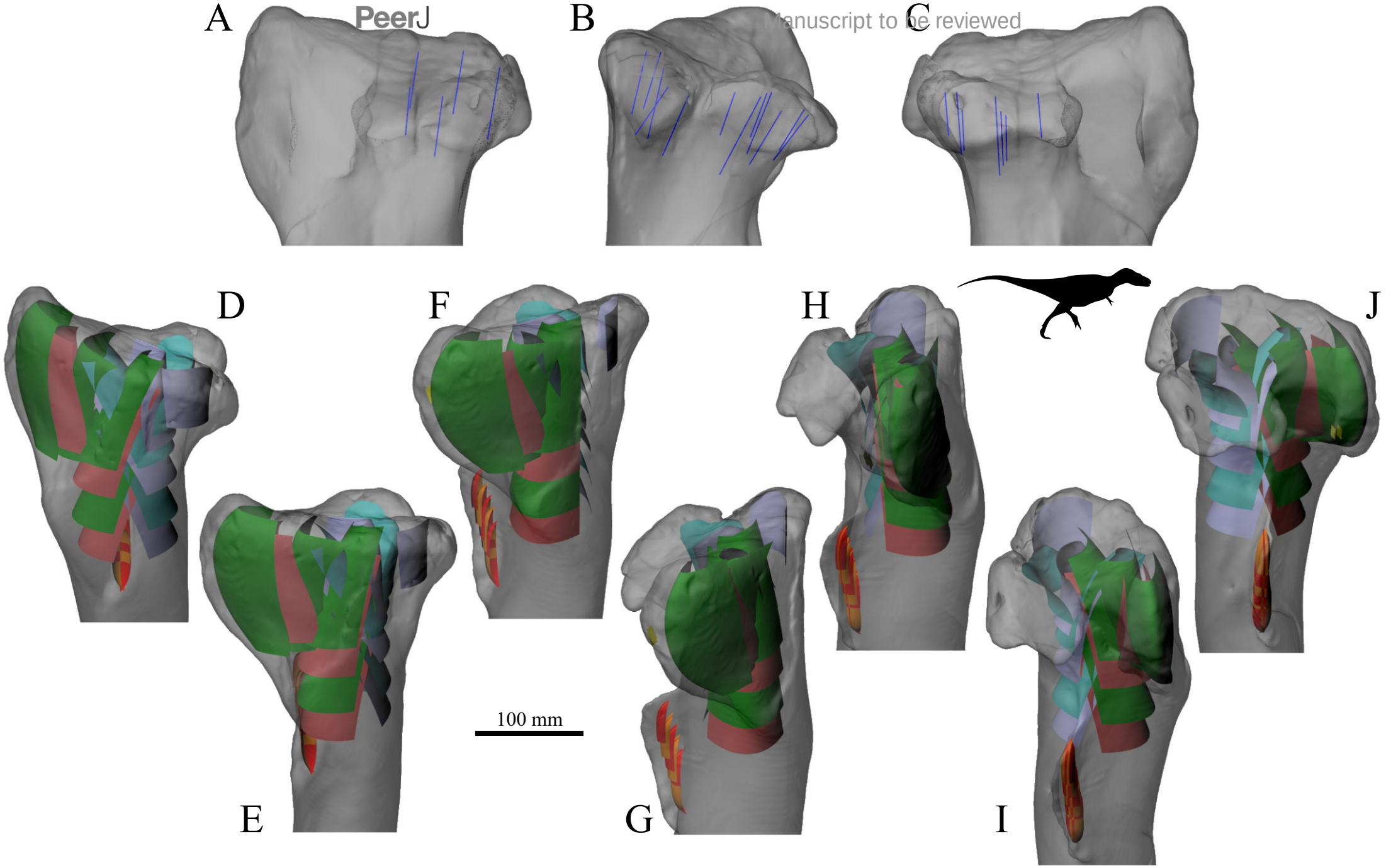

Figure 34(on next page)

The main architectural features of cancellous bone in theproximal tibia of Troodontidae sp. and Saurornitholesteslangstoni .

(A, B) Vector field of $\mathbf{u}_1$ under the medial condyle of Troodontidae sp. (MOR 553s-7.11.91.41) in posterior (A) and medial (B) views. (C, D) Vector field of $\mathbf{u}_1$ under the lateral condyle of Troodontidae sp. (MOR 748) in posterior (C) and lateral (D) views. (E, F) Vector field of $\mathbf{u}_1$ in the cnemial crest of Troodontidae sp. (MOR 748) in lateral (E) and anterior (F) views. (G) Vector field of $\mathbf{u}_1$ in the cnemial crest of Saurornitholestes (MOR 660) in lateral view. (H) Vector field of $\mathbf{u}_1$ in a 3-D slice, parallel to the sagittal plane, through the central metaphysis of Troodontidae sp. (MOR 553s-7.28.91.239), shown in medial view. Schematic inset illustrates the moderately developed double-arcuate pattern present.

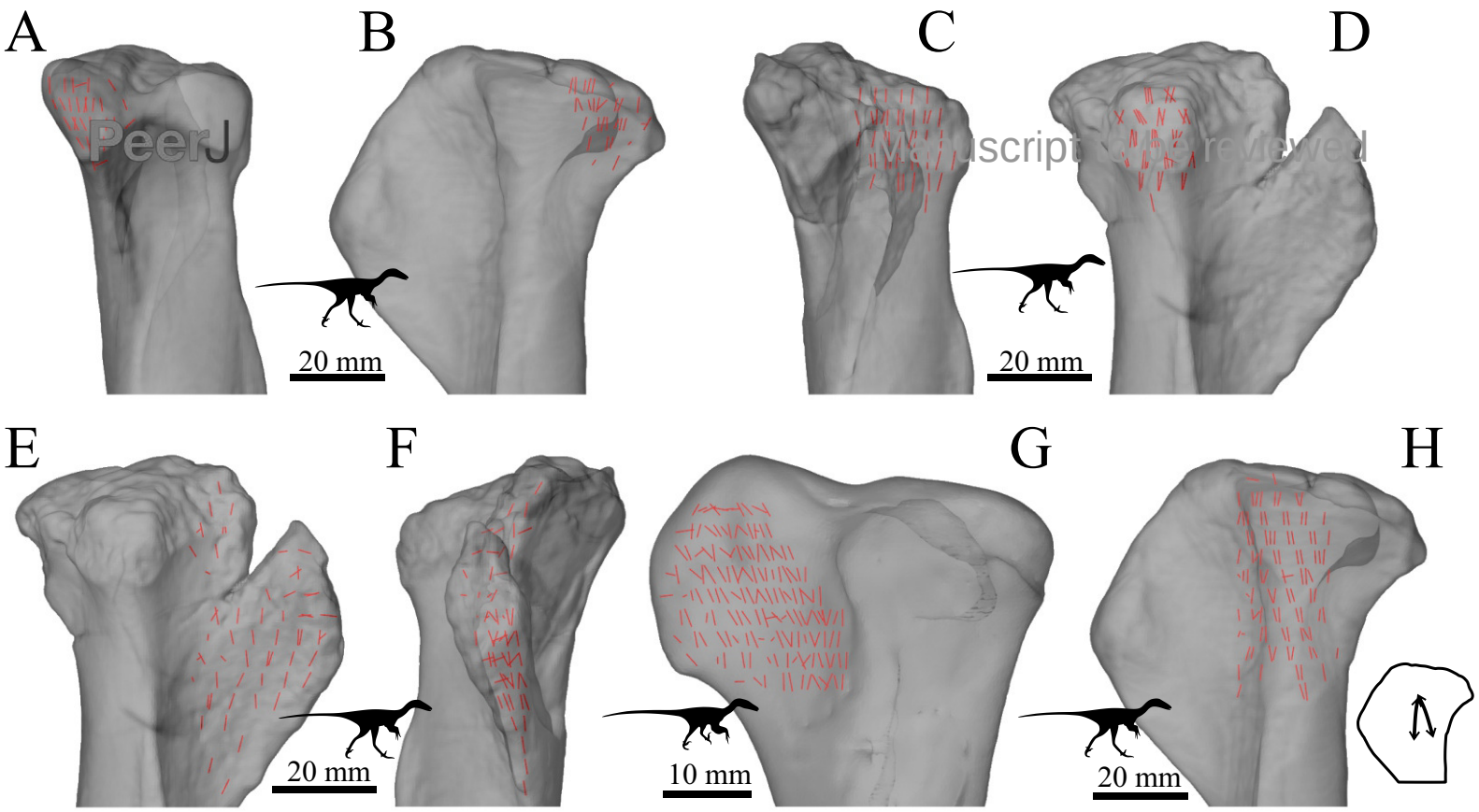

Figure 35(on next page)

The main architectural features of cancellous bone in thehuman distal tibia.

(A) Vector field of $\mathbf{u}_1$ in a 3-D slice, parallel to the coronal plane, through the middle of the bone, shown in anterior view. (B) Vector field of $\mathbf{u}_1$ in a 3-D slice, parallel to the sagittal plane, through the middle of the bone, shown in lateral view. (C) Vector field of $\mathbf{u}_2$ in a 3-D slice, parallel to the axial plane, through the distal end of the bone, shown in proximal view (anterior is toward top of page). Inset shows location of slice.

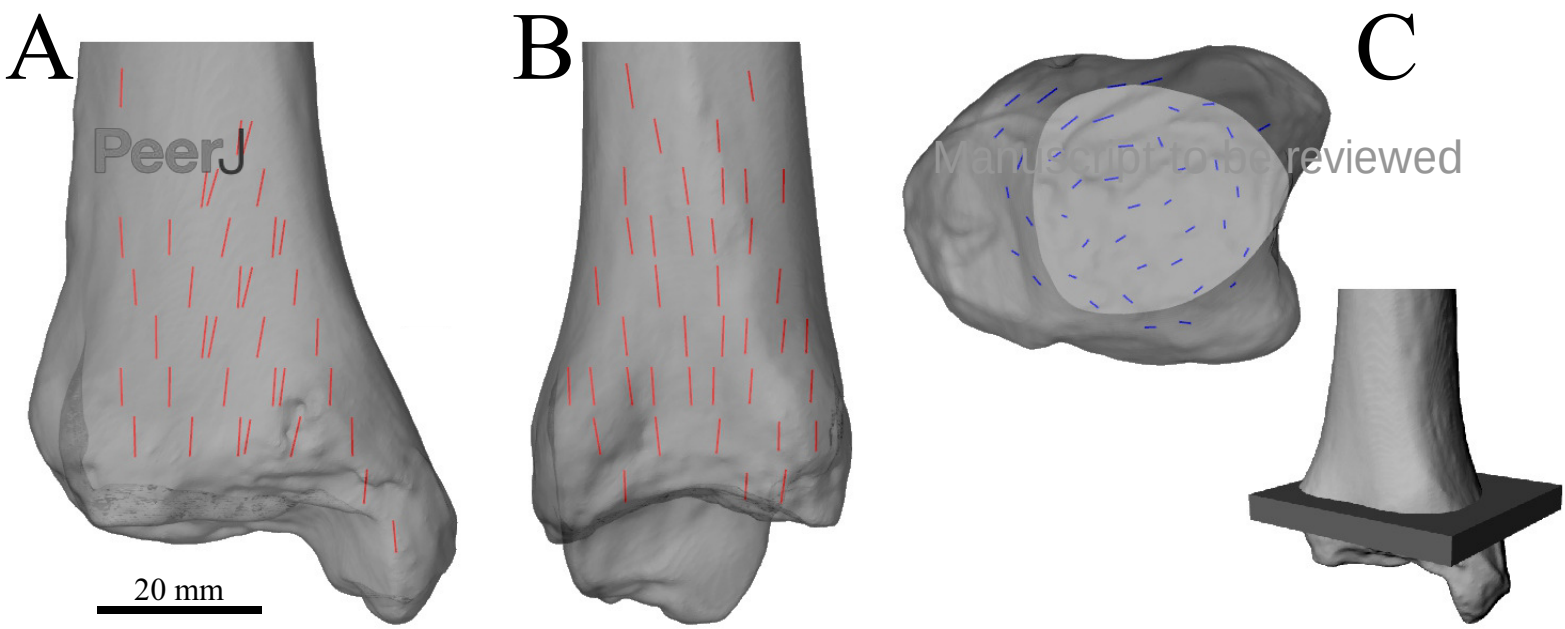

Figure 36(on next page)

The main architectural features of cancellous bone in thedistal tibiotarsus of birds.

(A–D) Vector field of $\mathbf{u}_1$ (A, C) and $\mathbf{u}_2$ (B, D) in the distal tibiotarsus of Dromaius novaehollandiae (QMO 16140) in oblique anterolateral (A, B) and oblique anteromedial (C, D) views. (E) Vector field of $\mathbf{u}_1$ (red) and $\mathbf{u}_2$ (blue) in the condyles of Dromaius novaehollandiae (QMO 16140) in proximal view (anterior is toward top of page). Note how both $\mathbf{u}_1$ and $\mathbf{u}_2$ are strongly aligned parallel to the sagittal plane. This particular specimen exemplifies a very stereotypical pattern that is observed in all large birds; the general pattern illustrated here was also observed in smaller species for which only limited fabric analysis was possible. (F) Isosurface rendering of cancellous bone in the distal tibiotarsus of Casuarius casuarius (QMO 30105), shown in oblique anteromedial view, with multiple cuts through the bone to illustrate 3-D architecture. (G) Isosurface rendering of cancellous bone in the distal tibiotarsus of Ardeotis australis (MVB 20408), shown in oblique anterolateral view, with multiple cuts through the bone to illustrate 3-D architecture. (H) Isosurface rendering of cancellous bone in the distal tibiotarsus of Coturnix chinensis (PJB coll.), sectioned in the axial plane through the middle of the condyles and shown in proximal view (anterior is toward top of page). In F and G, cut surfaces are coloured red to better show the ~~nature of the~~ cancellous bone architecture, in particular, the plate-like ~~nature~~ of many of the trabeculae, largely aligned parallel to the sagittal plane.

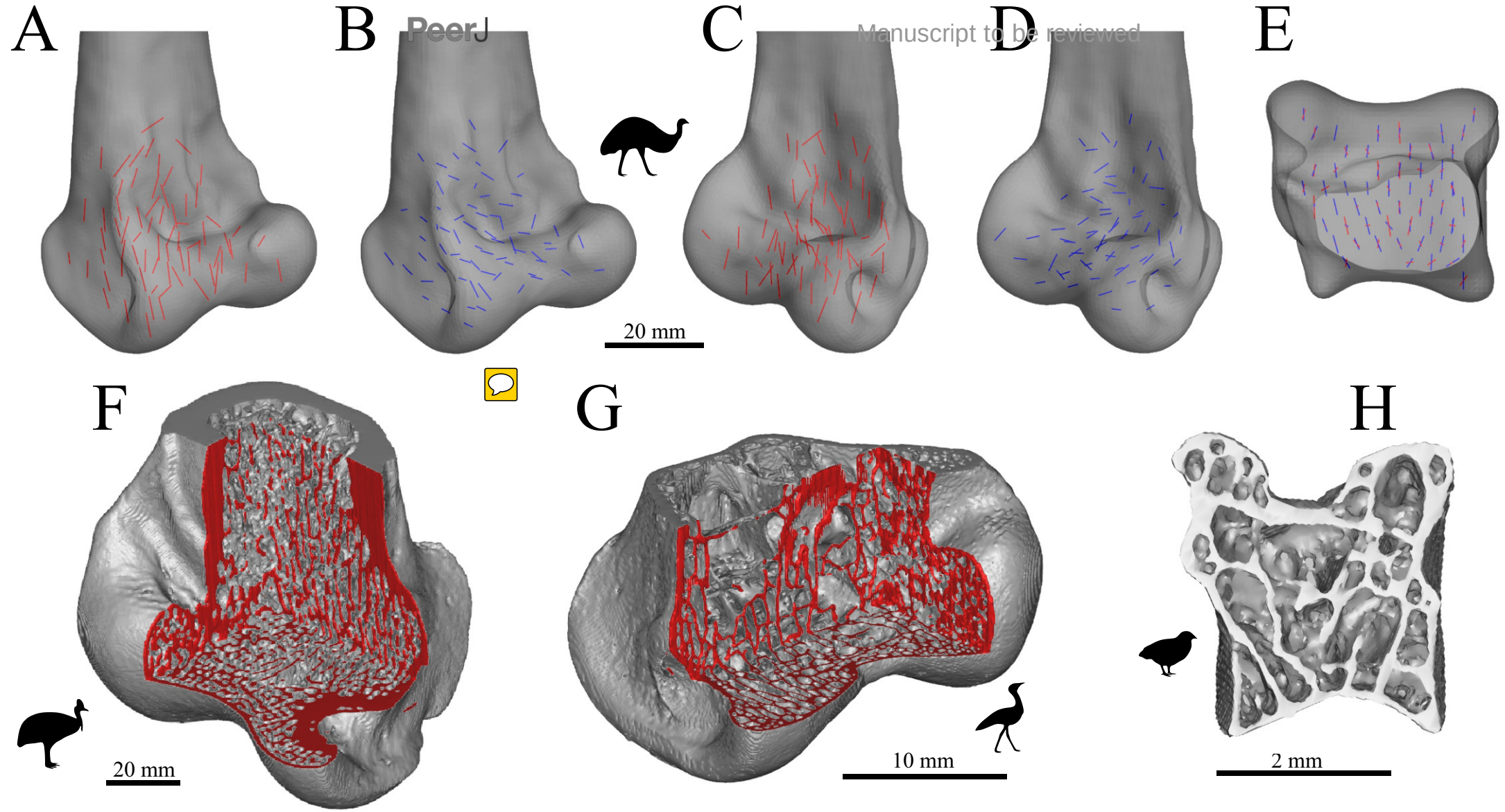

Figure 37 (on next page)

The main architectural features of cancellous bone in thedistal tibiotarsus of reptiles.

(A, B) Vector field of $\mathbf{u}_1$ in Varanus komodoensis (AM R.106933) in anterior (A) and medial (B) views. (C) Vector field of $\mathbf{u}_1$ in Crocodylus porosus (QMJ 48127) in anteromedial view. (D) Vector field of $\mathbf{u}_2$ in a 3-D slice through the distal end of the tibia of Crocodylus porosus (QMJ 48127), shown in proximal view (anterior is toward top of page). Inset shows location of slice.

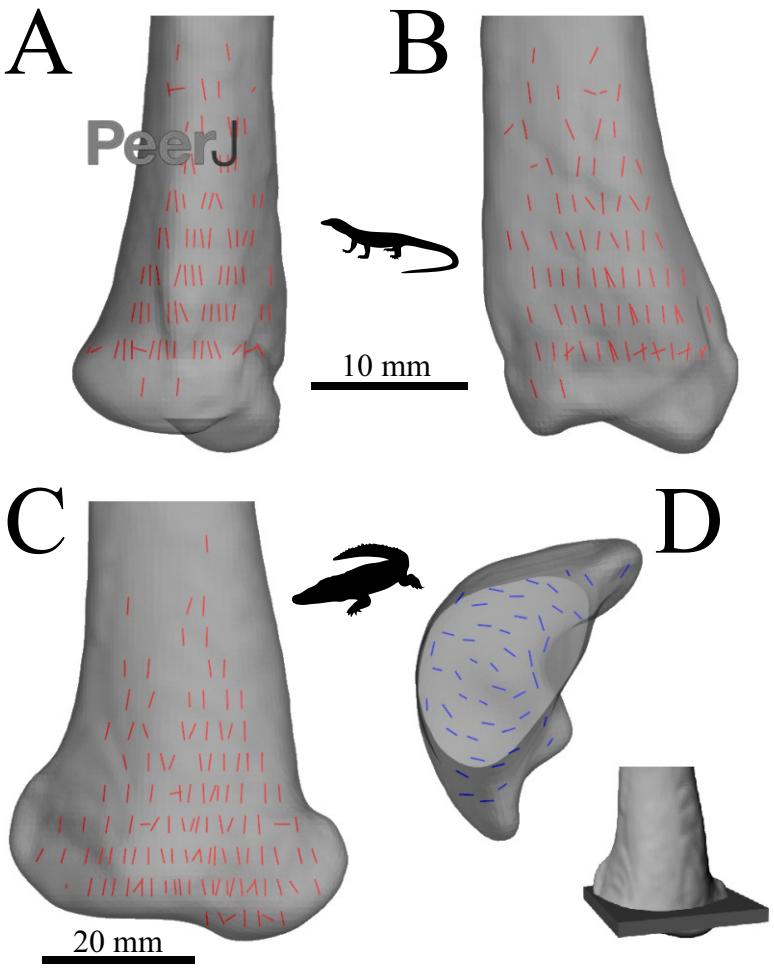

Figure 38(on next page)

The main architectural features of cancellous bone in thedistal tibiotarsus of basal theropods.

These are illustrated here with a 3-D geometric model of the observed architecture, mapped to the tibiotarsus of Daspletosaurus torosus (TMP 2001.036.0001; note that calcaneum was digitally sculpted based on other tyrannosaurid calcanei). (A–G) Seven progressive rotations of the tibia, in 30° increments, from proximally oblique medial to lateral views. Schematic inset in D illustrates generic cross-sectional pattern at the level indicated. (H–J) Three views of the astragalus and calcaneum, corresponding to those in C–E, respectively. The various colours are used to help visualize the various tracts of cancellous bone more clearly.

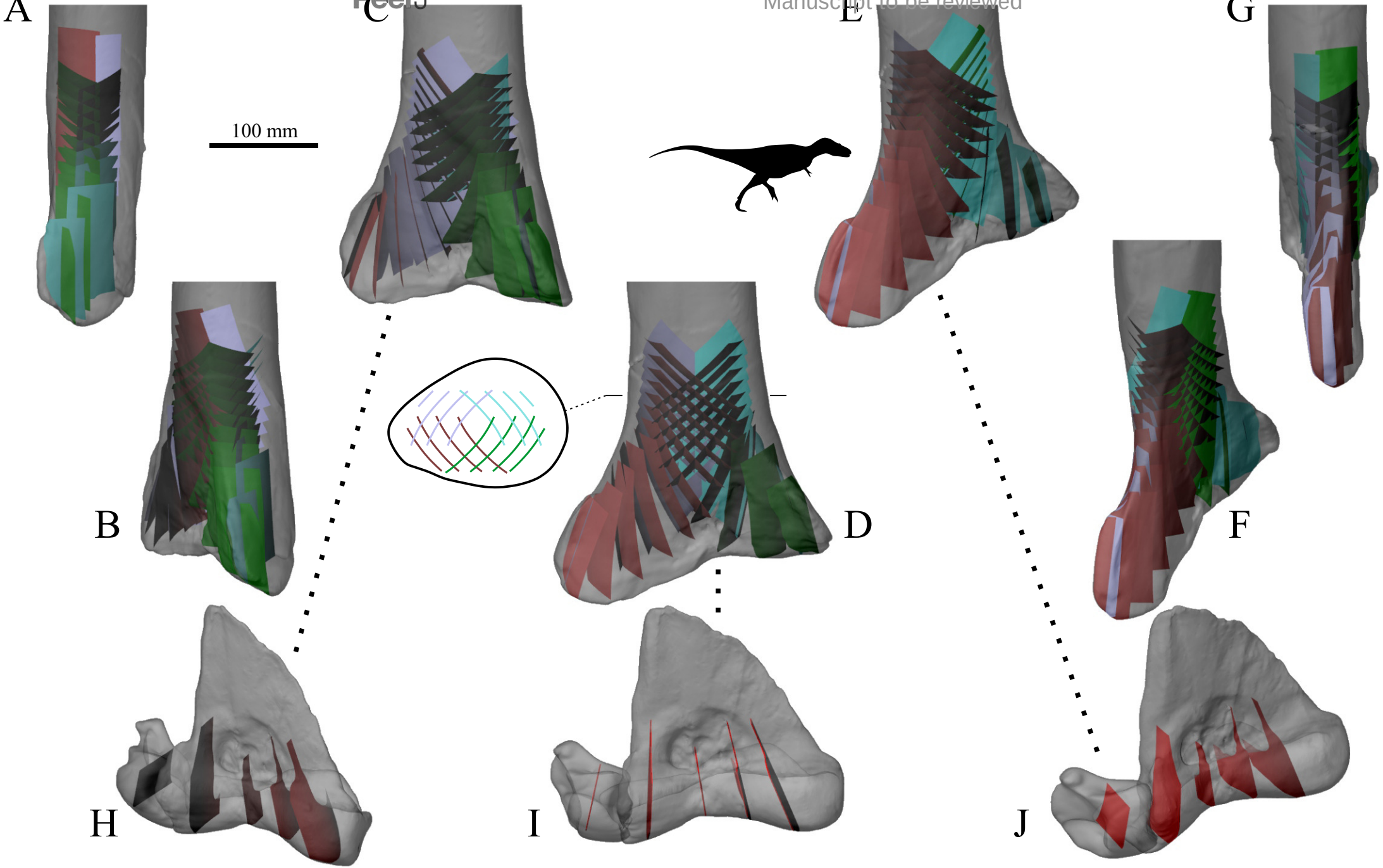

Figure 39(on next page)

The main architectural features of cancellous bone in the distaltibiotarsus of Troodontidae sp. and Saurornitholesteslangstoni .

(A, B) Vector field of $\mathbf{u}_1$ (red) and $\mathbf{u}_2$ (blue) in the distal tibiotarsus of Troodontidae sp. (MOR 748) in anterior (A) and proximal (B) views; in B, anterior is toward top of page. Note how both $\mathbf{u}_1$ and $\mathbf{u}_2$ are generally aligned parallel to the sagittal plane. (C) Isosurface rendering of cancellous bone in the medial distal tibia of Saurornitholestes (MOR 660), shown in oblique anteromedial view, with multiple cuts through the bone (cut surfaces are coloured red) to illustrate 3-D architecture.

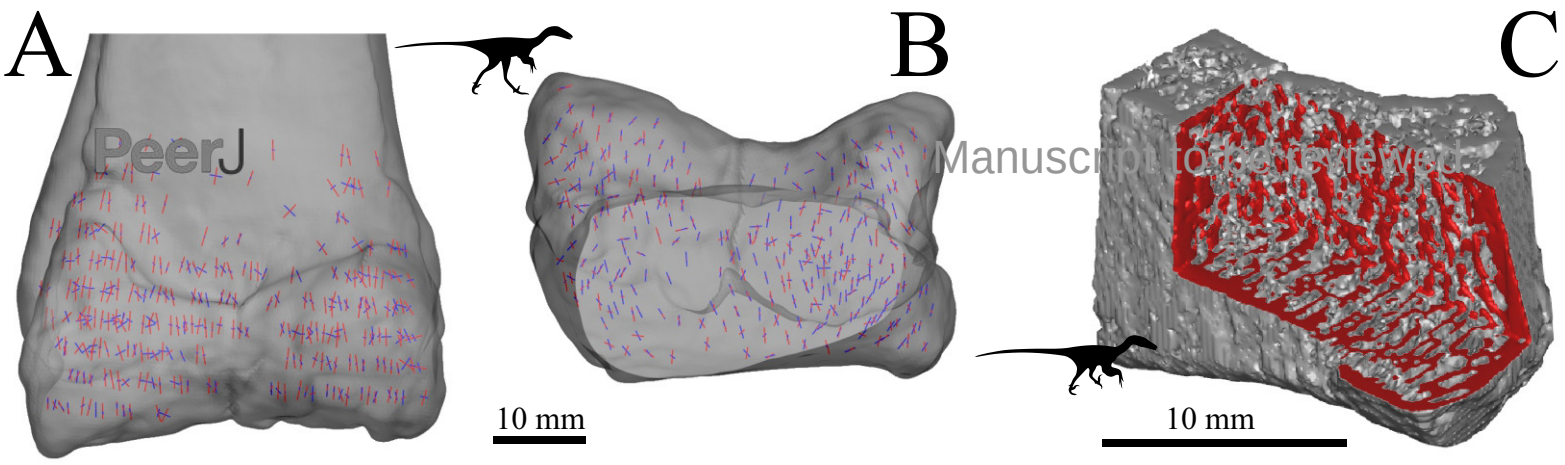

Figure 40(on next page)

The main architectural features of cancellous bone in thefibula.

(A, B) Vector field of $\mathbf{u}_1$ in the human fibula, in anterior (A) and lateral (B) views. (C, D) Vector field of $\mathbf{u}_1$ in Crocodylus johnstoni (QMJ 47916), in anterior (C) and lateral (D) views. (E, F) Vector field of $\mathbf{u}_1$ in Varanus panoptes (QMJ 91981), in anterior (E) and lateral (F) views. (G–I) Vector field of $\mathbf{u}_1$ in the fibular head of Dromaius novaehollandiae (QMO 11686, G), Rhea americana (QMO 23517, H) and Gallus gallus (PJB coll., I), in lateral view. (J, K) Isosurface rendering of cancellous bone in the proximal fibula of Leipoa ocellata (MVB 20194, J) and Coturnix chinensis (PJB coll., K), sectioned in the plane of the head and shown in lateral view. (L, M) The dominant architectural direction of cancellous bone in the fibula of Allosaurus and tyrannosaurids, shown in anterior (L) and lateral (M) views. This is illustrated here with a 3-D geometric model of the observed architecture, mapped to the fibula of Daspletosaurus torosus (TMP 2001.036.0001). (N) Vector field of $\mathbf{u}_1$ in the proximal fibula of Troodontidae sp. (MOR 553s-8.17.92.265), in lateral view.

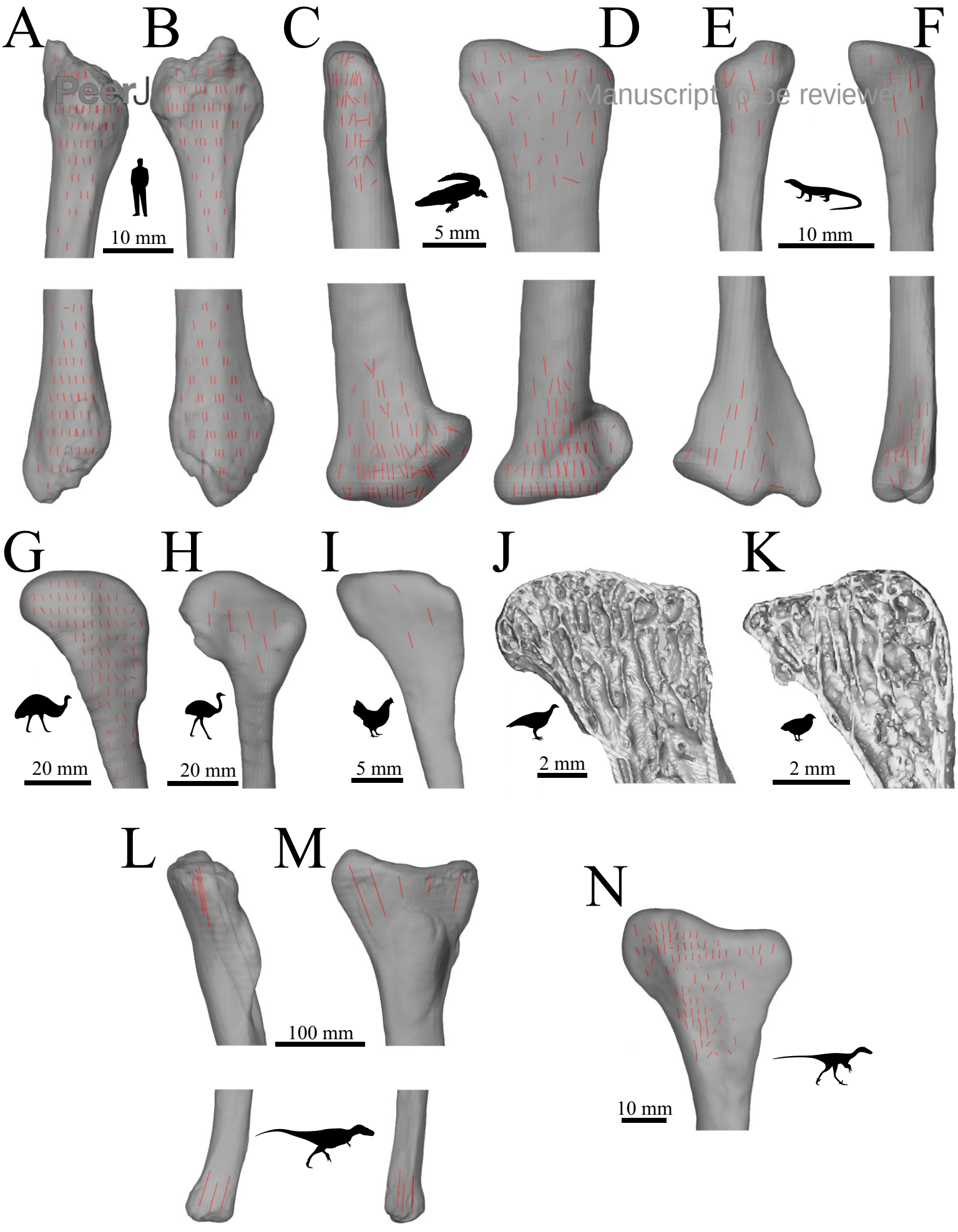

Figure 41 (on next page)

Oblique trabeculae in the diaphyses of birds and reptiles.

These are illustrated here with a number of examples demonstrating the variety of forms the individual trabeculae can assume. (A) Femoral mid-shaft of Dromaius novaehollandiae (QMO 16140). (B) Proximal femoral shaft of Meleagris gallopavo (PJB coll.). (C) Distal femoral shaft of Leipoa ocellata (MVB 20194). (D) Proximal femoral shaft of Dromaius novaehollandiae (QMO 11686). (E) Proximal femoral shaft of Alectura lathami (PJB coll.). (F) Proximal femoral shaft of Eudromia elegans (UMZC 404.e). (G) Femoral mid-shaft of Varanus panoptes (QMJ 91981). (H) Distal femoral shaft of Crypturellus soui (MVB 23647). (I) Tibial mid-shaft of Struthio camelus (MV R.2385). In all figures, proximal is towards the top of the page.

Figure 42 (on next page)

Size-dependent variation in the nature of diaphysealcancellous bone architecture in the femora and tibiae of birds.

These plots compare the results of the categorical scoring of each bone against its length. (A, B) Feature 1 (extent of cancellous bone) in the femur (A) and tibia (B); a higher score indicates greater extent. (C, D) Feature 2 (average orientation of trabeculae) in the femur (C) and tibia (D); a higher score indicates that trabeculae are more perpendicular to the bone's long-axis. (E, F) Feature 3 (degree of association of trabeculae) in the femur (E) and tibia (F); a higher score indicates that trabeculae tend to be more closely associated with other similar trabeculae. Major axis regression lines are also plotted when correlations were statistically significant. N signifies number of species represented, and n signifies number of individuals. Other statistical metrics for each comparison are reported in Table 2.

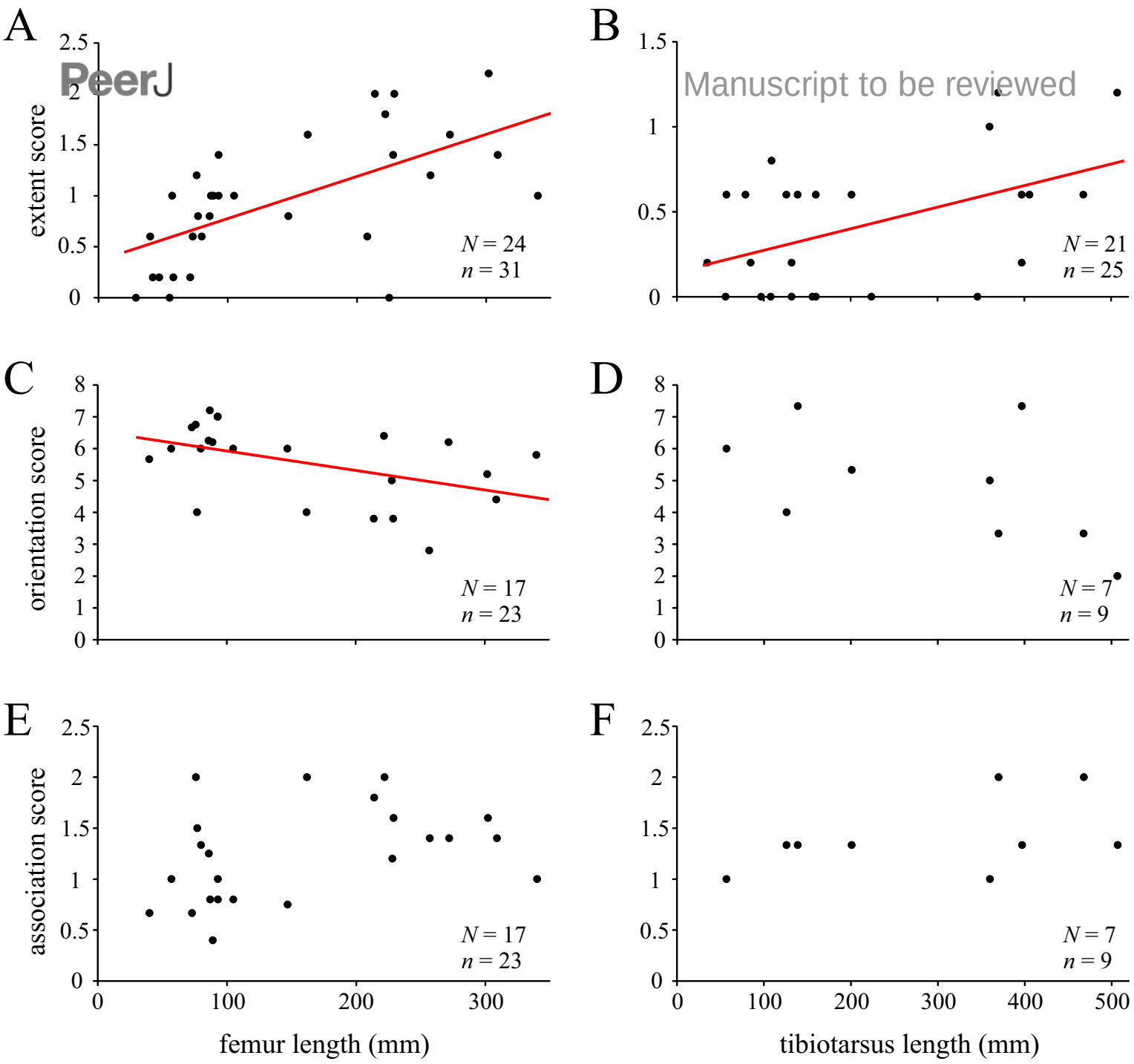

Figure 43(on next page)

Gently oblique trabeculae in the tibial diaphysis of ahuman.

Inset shows location of section relative to the whole bone. Although the trabeculae (or endosteal ‘wrinkles’) are less obliquely oriented compared to the birds or reptiles, they are nonetheless consistently oriented in an oblique fashion.

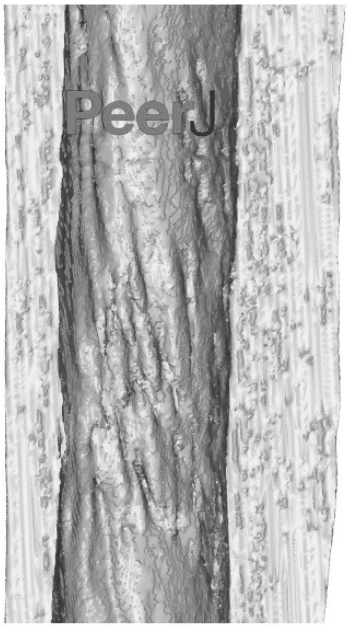

10 mm

Figure 44(on next page)

Schematic demonstrating the effect of differences in thedegree of hip and knee flexion on the joint forces experienced by the femur.

This is illustrated with right lateral views of a human (left) and a typical bird (right) in approximate mid-stance postures. In the more flexed posture of birds, the hip joint force is more anteriorly oriented relative to the long-axis of the femur (dotted line) compared to humans. Further, the knee joint force is more posteriorly oriented relative to the long-axis of the femur compared to humans.